

AN EXPERIMENTAL INVESTIGATION ON FLOW
HYDRODYNAMICS IN PNEUMATIC TRANSPORT OF
SOLID PARTICLES

A MASTER'S THESIS

in

109890

Mechanical Engineering
University of Gaziantep

**T.C. YÜKSEKÖĞRETİM KURULU
DOKÜMANTASYON MERKEZİ**

By

109890

Vedat ORUÇ

January 2001

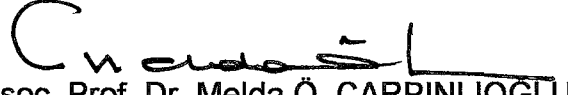
Approval of the Graduate School of Natural and Applied Sciences.



Assoc. Prof. Dr. Ali Rıza TEKİN

Director

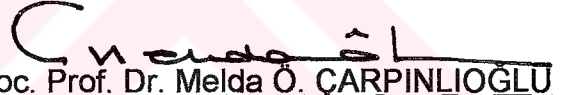
I certify that this thesis satisfies all the requirements as a thesis for the degree of Master of Science.



Assoc. Prof. Dr. Melda Ö. ÇARPINLIOĞLU

Chairman of the Department

I certify that I have read this thesis and that in my opinion it is fully adequate in scope and quality as a thesis for the degree of Master of Science.



Assoc. Prof. Dr. Melda Ö. ÇARPINLIOĞLU

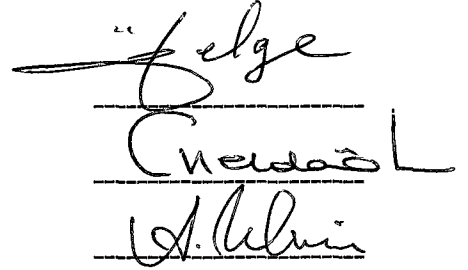
Supervisor

Examining Committee in Charge

Prof. Dr. Tülay A. ÖZBELGE

Assoc. Prof. Dr. Melda Ö. ÇARPINLIOĞLU

Assoc. Prof. Dr. A. Rıza TEKİN



ABSTRACT

AN EXPERIMENTAL INVESTIGATION ON FLOW HYDRODYNAMICS IN PNEUMATIC TRANSPORT OF SOLID PARTICLES

ORUÇ, Vedat

M. S. in Mechanical Engineering

Supervisor: Assoc. Prof. Dr. Melda Ö. ÇARPINLIOĞLU

January 2001, 189 pages

In this thesis, flow frictional characteristics of fully-suspended solid particles in air through transport lines of different angularities were experimentally investigated. The main variables of the study were flow Reynolds number Re , particle loading ratio M_p/M_a , inclination angle of the test section α , and particle physical characteristics.

The particles were Alumina, Fly Ash, and Semolina within a size range of $75.5 \mu\text{m} \leq d_p \leq 275 \mu\text{m}$; a density range of $468 \text{ kg/m}^3 \leq \rho_p \leq 825 \text{ kg/m}^3$. A particle-air loading ratio range of $5\% \leq M_p/M_a \leq 25\%$; and a flow Reynolds number range of $53000 \leq Re \leq 98933$ were used in the experimental study.

The study depended on the measurements of local static pressure gradients along the test section which was used in horizontal and inclined positions with angles of 0° , 10° , 20° , and 30° , respectively. The pipe circumferential static pressure variation was also measured along the test section. The flow friction factor, f was calculated from the measured static pressure gradients along the test section. The effects of specified particle and flow parameters on the frictional behaviour of air-solid suspension flows were determined by means of the proposed correlations.

Key Words: Reynolds number, Air-Particle Flow, Particle Loading Ratio, Local Static Pressure, Circumferential Static Pressure, Transport Line Angularity, Friction Factor.

ÖZET

KATI PARÇACIKLARIN PNÖMATİK TAŞINIMLARINDA AKIŞ HİDRODİNAMİĞİNE YÖNELİK DENEYSEL BİR ARAŞTIRMA

ORUÇ, Vedat
Yüksek Lisans Tezi, Mak. Müh. Böl.
Tez Yöneticisi: Doç. Dr. Melda Ö. ÇARPINLIOĞLU
Ocak 2001, 189 sayfa

Bu tezde, farklı açılardaki taşınım hatları boyunca havada asılı kalan katı parçacıkların akım sürtünme karakteristikleri deneysel olarak araştırılmıştır. Çalışmanın belli başlı değişkenleri akım Reynolds sayısı Re , parçacık yükleme oranı M_p/M_a , deney bölgesinin eğim açısı α ve katı parçacık fiziksel karakterleridir.

Kullanılan parçacıklar; Alumina, Uçucu Kül ve İrmik olup, parçacık büyüklüğü $75.5 \mu m \leq d_p \leq 275 \mu m$, yoğunluğu $468 \text{ kg/m}^3 \leq \rho_p \leq 825 \text{ kg/m}^3$ arasında değişmiştir. Deneysel çalışmada parçacık-hava yükleme oranı $5\% \leq M_p/M_a \leq 25\%$; ve akım Reynolds sayısı $53000 \leq Re \leq 98933$ aralığında kullanılmıştır.

Çalışma yatay ve 10° , 20° , 30° eğimli açılardaki deney bölgesi boyunca yerel statik basınç farklarının ölçümlerine bağlı olmuştur. Ayrıca, borunun çevresel statik basınç değişimi deney bölgesi boyunca ölçülmüştür. Deney bölgesi boyunca ölçülen statik basınç farklarından akımın sürtünme faktörü f , hesaplanmıştır. Parçacık ve akım parametrelerinin sürtünme davranışına etkisi önerilen bağıntılarla belirlenmiştir.

Anahtar Kelimeler: Reynolds sayısı, Hava-Parçacık Akımı, Parçacık Yükleme Oranı, Yerel Statik Basınç, Çevresel Statik Basınç, Taşıma Hattı Açısallığı, Sürtünme Katsayısı.

ACKNOWLEDGEMENTS

I'm grateful to my supervisor Assoc. Prof. Dr. Melda Ö. ÇARPINLIOĞLU for her advice, valuable comments, help and especially for the facilities that she provided for this study.

This study would have never been completed without continuous encouragement of my family. Therefore, I'm indebted for their support and great patience which they had shown during this study.

I want to thank Prof. Dr. Tülay A. ÖZBELGE and Assoc. Prof. Dr. Ali Rıza TEKİN due to discussing and criticizing the manuscript.

I offer my sincerely thanks to Assist. Prof. Dr. Sedat KOLUKISA, Assist. Prof. Dr. Orhan ÇAKIR, and Mr. Haluk KEJANLI from University of Dicle for their encouragement and contributions to this study.

I thank Dr. Yaşar GÜNDOĞDU and Mr. Mustafa ÖZBEY for their valuable ideas and suggestions.

I wish to thank the personnel of the Fluid Machinery Laboratory and workshop of the Mechanical Engineering Department.

The staff of Öz Diyarbakır Travel Agency also deserve my special thanks for making shorter the distances essential for this study.

I would also like to express my thanks to Research Fund of the University of Gaziantep for the research project supported under the code MF: 99-02.

TABLE OF CONTENTS

	Page
ABSTRACT	iii
ÖZET	v
ACKNOWLEDGEMENTS	vii
NOMENCLATURE	xi
CHAPTER 1. INTRODUCTION	1
CHAPTER 2. LITERATURE SURVEY	3
2.1. Introduction	3
2.2. Basics of Pneumatic Conveying of Solid Particles	3
2.3. Properties of Solid Particles	7
2.4. Two-Phase Flow Field Characteristics	8
2.5. Velocity Field Analysis in Two-Phase Flow Fields	13
2.6. Pressure Drop Determination in Two-Phase Flow Fields	22
2.7. Friction Factor Correlations	27
2.8. Conclusions	33
CHAPTER 3. EXPERIMENTAL SET-UP AND MEASUREMENTS	34
3.1. Introduction	34
3.2. Experimental Set-up	34

3.2.1. Blower Unit	35
3.2.2. Settling Tank	36
3.2.3. Pipe System	36
3.2.4. Particle Feeder	37
3.2.5. Cyclone Separator-Bag Filter Assembly	37
3.3. Solid Particles	38
3.4. Measurements and Measuring Devices	40
3.4.1. Pressure Measurement Rings	40
3.4.2. Pitot Tube and Traverse Mechanism	40
3.4.3. Manometers	42
3.5. Experimental Study	43
3.5.1. Setting of Flow Reynolds Number	44
3.5.2. Pressure Measurements	46
3.6. Flow Friction Factor Determination	47
CHAPTER 4. FRICTIONAL BEHAVIOUR OF FLOW	49
4.1. Introduction	49
4.2. Pressure Variation Along The Test Section	50
4.2.1. Local Static Pressure Variation	50
4.2.2. Circumferential Static Pressure Distribution	53
4.3. Frictional Behaviour	57
4.3.1. Friction Factor Variation Along The Test Section	57
4.3.1.1. The Variation of f with x/D	57
4.3.1.2. f - x/D Equations	59
4.3.2. Frictional Flow Resistance Considering Clean Air Flow Resistance	59

4.3.2.1. The Variation of f_{p+a}/f_a with x/D	59
4.3.2.2. The Proposed $f_{p+a}/f_a - x/D$ Equations	62
4.4. Flow Field Velocity Determination	65
4.5. Conclusions	67
CHAPTER 5. FRICTION FACTOR CORRELATIONS	68
5.1. Introduction	68
5.2. The Variation of $(f_{p+a})_r$ with Re	68
5.3. The Variation of $(f_{p+a})_r (M_p/M_a)$ with $Re(d_p/D)$	72
5.4. Resulting Correlations	74
5.5. Conclusions	76
CHAPTER 6. SUGGESTIONS FOR FURTHER INVESTIGATIONS	77
LIST OF REFERENCES	78
APPENDICES	85
Appendix 1: Specifications of The Drive Unit of Blower	86
Appendix 2: Specifications of The Drive Unit of The Particle Feeder	87
TABLES	88
Table 3.1. Physical Characteristics of Solid Particles	89
Table 3.2. Ranges of The Experimental Variables	90
Table 4.1. Sample $f=f(x/D)$ Equations	91
Table 4.2. Sample Equations Concerning S1 and F1 Particles	92
FIGURES	93

NOMENCLATURE

A	cross-sectional area of the pipe, m ²
Ar	Archimedes number
C _D	drag coefficient
d _p	mean particle diameter, μm
dP/dx	local static pressure gradient, Pa/m
D	inside diameter of the pipe, m
f	friction factor
f _a	friction factor of clean air
f _{p+a}	friction factor of particle-air flow
(f _a) _r	friction factor of clean air at x/D=(x/D) _r
(f _{p+a}) _r	friction factor of particle-air flow at x/D=(x/D) _r
f _s	solids friction factor
f _w	wall friction coefficient
Fr	Froude number of the flow, u ² /gD
Fr _s	Froude number based on solid particles, u _s / √gd _p
g	gravitational acceleration, m/s ²
h _{alc}	height of alcohol in the leg of manometer, m
(h _{alc}) _{STP}	height of alcohol in the leg of manometer reduced to standard temperature and pressure condition, m
h _L	head loss, m
L	length of the pipe, m
(L _p /d _p)	particle aspect ratio
M _a	mass flow rate of air, kg/s
M _p	mass flow rate of solid particles, kg/s
M _p /M _a	particle loading ratio
N	rotational speed of the feeder wheel, rpm

P	static pressure, Pa
ΔP_a	pressure drop due to friction of air, Pa
ΔP_T	total pressure drop, Pa
Q	volumetric flow rate, m ³ /s
r	any radius from pipe center, m
R	inside radius of the pipe, m
Re	Reynolds number of the flow, uD/v
Re _p	Reynolds number based on particles, $u_p d_p/v$
Re _{rel}	relative Reynolds number, $u_{rel}D/v$
u	superficial mean gas velocity, m/s
u _a	mean air velocity, m/s
u _f	fluid phase velocity, m/s
u _{gpu}	minimum pick up velocity, m/s
u _{gpu,c}	minimum pick up velocity for a single particle, m/s
u _m	flow velocity of mixture, m/s
u _p	particle velocity, m/s
u(r)	velocity at any radius of the pipe, m/s
u _{rel}	relative or slip velocity, m/s
u _s	solids velocity, m/s
u _{sal}	saltation velocity, m/s
u _t	terminal velocity, m/s
x	distance measured from the particle feeder, m
ρ_a	density of air, kg/m ³
ρ_{alc}	density of alcohol, kg/m ³
ρ_f	density of fluid, kg/m ³
ρ_m	density of mixture, kg/m ³
ρ_p	apparent density of particles, kg/m ³
ν	kinematic viscosity of air, m ² /s
ε	voidage of the particle-air flow
Θ	angle on the pipe circumference, degree
α	inclination angle of the test section, degree
β	inclination angle of the manometer's leg, degree
δ_1	thickness of the laminar sub-layer, m
λ	stress transmission coefficient.

CHAPTER 1

INTRODUCTION

This thesis is an experimental investigation on flow hydrodynamics in pneumatic transport of solid particles. It was aimed to determine the effects of transport line angularity, mass loading ratio M_p/M_a , flow Reynolds number, and particle characteristics such as average particle size and apparent solid density on the flow friction behaviour of air-solid flows.

In Chapter 2, related literature survey is summarized. In general, two-phase flow fields can be obtained by solid-liquid, liquid-liquid, liquid-gas and solid-gas flows. However, literature survey is concerning works on solid-gas flows due to the nature of study. The experimental and theoretical studies in the available literature were mainly ones conducted in horizontal and vertical pipelines.

In Chapter 3, experimental set-up and measurements are presented. The details of the set-up and measurements of local and circumferential static pressures along the test section are given. The methods followed in analysis of experimental data is also explained.

In Chapter 4, measurements on static pressure and calculated friction factors in terms of the influence of variables of the study are described. Functional relationships and correlation studies are given.

The results of a theoretical study of Özbelge [24] on friction factor determination were also applied to the experimental data in order to describe the velocity determination in the flow field. The comparisons between experimental data and theoretical results were made.

In Chapter 5, proposed friction factor correlations are presented in comparison with the related literature. The functional relationships in terms of $(f_{p+a}/f_a)_r$ vs. Re , $(f_{p+a}/f_a)_r \cdot (M_p/M_a)$ vs. $Re(d_p/D)$, $(f_{p+a}/f_a)_r$ vs. Fr_s and $(f_{p+a}/f_a)_r \cdot (M_p/M_a)(\rho_a/\rho_p)$ vs. $Re(d_p/D)(1/Re_{rel})$ are given to find the influence of the related parameters.

Chapter 6 outlines the general conclusions and suggestions for further work.



CHAPTER 2

LITERATURE SURVEY

2.1. INTRODUCTION

The studies related to pneumatic transport of solid particles which is an important industrial process started in 1950 's. However, the details of the flow field are not solved completely.

Literature survey indicated that the previous studies on this subject can be classified as theoretical and experimental ones. The experimental studies are particularly conducted in horizontal or vertical pipelines.

In this chapter, the selected topics are given in the succeeding headings in which results of theoretical and experimental studies are summarized.

2.2. BASICS OF PNEUMATIC CONVEYING OF SOLID PARTICLES

Pneumatic transport technology, otherwise known as pneumatic conveying, is the art of transporting particulate solid materials through a pipeline by a gas medium. Transport phenomena occurring in the pipeline are

very complex depending on the gas velocity, characteristics of the solid particles (size, density and shape), relative weight ratio of gas and solids, pipeline size and configuration (vertical, horizontal or inclined), solids feeding device characteristics and transport direction (upward or downward).

Pneumatic conveying systems are in concept quite simple and are suitable for the transport of materials in factory, site and plant. The basic system requirements are an air mover, a feed device, the conveying pipeline, and a receiver to disengage the conveyed material and carrier gas.

The study of flow characteristics of gas-solids suspensions is of great importance in many fields of mechanical and chemical engineering. It is encountered in fluidized beds, pneumatic conveyings, nuclear reactor cooling, and dust collection. Pneumatic conveying is utilized extensively to transport dry powders and granular materials. Materials handled by this means in industry range from lump coal and crushed ores in the mining industries to pellets and fine powders of polyethylene, PVC and polypropylene in the chemical industries.

The use of pneumatic transport in the chemical, food and metallurgical industries is very widespread. It has been shown that this transport is a very suitable way of introducing a solid phase into various types of reactors and mixers. In recent years there has been an increasing recognition of the use of pneumatic transport for certain new applications such as combustion and gasification of coal and manufacture of non-ferrous metals and special kinds of steels (in the latter case solid particles are pneumatically injected into the molten steel). As the industrial applications become more widely known, more information is needed about the flow behaviour of solid-gas suspensions.

Although pneumatic transport technology has been practised for many years in various industries, principally for loading and unloading dry bulk materials, the design of a pneumatic conveying system remains

empirical. It is safe to say that any dry particulate materials of reasonable particle sizes can be transported pneumatically if the gas velocity is sufficiently high. However, it is important to understand that the optimal design can only be achieved through understanding the phenomena to guarantee not only the reliability of the operation but also to minimize the gas usage, erosion of the pipes, and the power consumption.

Design of a pneumatic transport system is an art rather than a science. For such a complex system, a macroscopic model with some simplifying assumptions has been developed previously by Özbelge [22] to calculate the average solids phase velocity and density, voidage, the external force acting on the solids phase, the relative or drag velocity between the phases. Total pressure drop data was not needed to use this theoretical model

In 1996, Molerus [1] mentioned the following advantages, disadvantages and pitfalls which characterize pneumatic conveying technology :

a) Advantages:

- i) Dust free transportation of a variety of products
- ii) Flexibility in routing, the products can be transported horizontally and vertically by addition of a bend
- iii) Distribution to many different areas in the plants and pick up from several areas

b) Disadvantages:

- i) High power consumption
- ii) Wear and abrasion of equipment
- iii) Incorrect design results in particle degradation

c) Pitfalls:

With changes in the operational parameters, significant effects are observed, sometimes abrupt, and even with the risk of process failure.

The disadvantage of a rather high power consumption restricts the use of pneumatic conveying systems for the conveyance over shorter distances (generally less than 1000 m). The advantages of versatility and flexibility make pneumatic conveying a first choice for the transport of a vast variety of particulate materials.

During the last decades the advantages already mentioned initiated strong development efforts to reduce the power consumption. The results of efforts were dense-phase conveying systems that operate at rather low gas velocities. The pitfalls mentioned last, make it understandable that companies active in the field often more or less specialize in this particular type of industrial equipment.

It is indicated in the study of Çarpınlioğlu and Gündoğdu [19] that since Boothroyd [26] there has been continuing research on the modelling of two-phase particulate flows. However, complete understanding has not been reached yet, and as Coughran [27] has suggested in his paper there is need for more experimental information on gas-solid flow systems. Some of the theoretical and experimental investigations on multiphase flow conducted up to now are given by Rossetti and Pfeffer [28], Yang [29], Rizk and Elghobashi [30], Garner and Kerekes [31]. Furthermore, the handbooks by Govier and Aziz [32] and Hetsroni [33] should be mentioned here.

There have been numerous hydrodynamic studies of gas-solid flows applicable to pneumatic conveyings (Özbelge [22,23]; Yang [29,38]) and fluidized beds (Wen and Galli [39]). In particular, Soo [40] and Hetsroni [33] made considerable contributions to this field. In spite of this, the theory of multi-phase flows cannot yet be considered complete; thus the design of these systems is based on existing experimental data and correlations.

The previous experimental work by Metha et al. [41], Hariu and Molstad [42], and Depew [43] have been devoted to the determination of the average properties of such two-phase systems. They measured the mass fluxes of solids and gas phases, the pressure drop at each different solids loading ratio in the test section, and the weight of solids trapped between the two quick-closing valves in a section of pipe to determine the dispersed solids density. The correlations obtained from the experimental data were partially successful for only limited ranges of parameters.

The later studies required advanced experimental techniques (Boothroyd [44]; Riethmuller [45]; Oki *et al.* [46]) to measure the local properties of two-phase suspension flows, thus in turn, to explain their behaviour. These methods are expensive and they are still in the developmental stages.

2.3. PROPERTIES OF SOLID PARTICLES

When one searches for materials that can be conveyed pneumatically, it soon becomes apparent that the list includes most solid materials one can conceive. It would be easier to complete a list of materials that cannot be conveyed pneumatically. Most notably here are sticky and highly moist powders.

In 1987, Klinzing *et al.* [4] reported that a variety of problems can be encountered during pneumatic conveying that must be addressed. The two extremes in sizes of particles is a problem in most conveying operations; the very fine less than 20 μm and the very large up to 5 cm. The fine particles adhere to themselves and to the pipes, feeders, and collectors. The larger particles need higher velocities for pick up of the solids and require larger pipe diameters for transport. Sticky materials often defy transport at all. Abrasive materials can erode away the pipe walls and bends while also

damaging many types of solid feeder.

In 1990, Marcus *et al.* [2] presented a list of about 300 different products that have been conveyed successfully it ranges from A, like ABS powder, to Z, like zinc powder.

As a result of literature survey, it can be concluded that the parameters concerned with solid particles affecting the two-phase flow field are density, size, shape, stickiness, and chemical structure of them.

2.4. TWO-PHASE FLOW FIELD CHARACTERISTICS

The flow field in a pneumatic particle transport line is highly complicated and is principally dependent on the velocity of the gaseous phase. The broad categories of the flow field as a whole were given as dilute phase, dense phase, moving bed and plug types by Jones and Mills [47]. At low phase densities, the solids tended to be fully suspended in the conveying gas, these dilute phase systems being characterized by high gas velocities. At the lower velocities, non-suspension, dense phase flow could be achieved. The exact nature of dense phase flow depended on the specifications of the solid material and the pipeline, but mostly moving bed and plug type flows occurred. From the view point of fluid dynamics, flow can be further classified as steady or unsteady with respect to its time dependency; laminar, turbulent, transitional related to the nature of the velocity field, and fully developed or developing flows depend upon the flow uniformity based on the phase distribution. Meanwhile the parameters influencing the field can be given as:

a) transport line parameters as configuration of the transport line; horizontal, vertical, inclined; direction of flow; upward or downward in vertical and inclined lines, and the physical constraints of the line moreover its

diameter, wall thickness, material, cross-sectional shape; circular or non-circular, and length etc.;

b) transported solid particle parameters such as particle size, particle density, particle loading ratio, apparent density of the solid, particle shape and flow velocity of the particles;

c) transport medium parameters; viscosity, density, and speed of air.

The deposition of solid particles or droplets from a turbulent suspension flow at the channel walls is a problem of fundamental importance in a number of technical areas. Although a large number of articles on this subject have appeared in the literature, reliable results from carefully planned experiments are scarce and they are mostly related only to the amount of particle deposition at the wall without explaining the mechanisms in the flow that are responsible for the transport of particles towards the wall; e.g. measurements of the deposition of relatively large droplets from gas by Alexander and Coldren [48], and of small solid particles from air by Friedlander and Johnstone [49].

Most theoretical treatment of the subject has adopted the point of view of a conventional three-layer flow structure in the vicinity of the wall -including the viscous sublayer, the buffer zone and the turbulent core- from studies of the single-phase, fully-developed turbulent flow (Friedlander and Johnstone [49]; Lin *et al.* [50]; Beal [51]). In the turbulent core and buffer zone, particles are assumed to be laterally transported by turbulent diffusion in the same way that the scalar quantities, such as heat or the concentration of species, are assumed to be transported in a turbulent stream. Particles reaching the edge of the viscous sublayer as a result of this transport are assumed to coast towards a wall across the sublayer to form deposition.

Fairly recently, there have appeared in the literature three reports on local measurements of flow properties of an upward turbulent dilute flow of air-solid particles in a pipe using non-intrusive laser-Doppler anemometry (Sheen *et al.* [52]; Lee and Durst [53]; Tsuji *et al.* [54]).

The turbulent flow structures in a vertical upward pipe flow of a dilute particle-air suspension were investigated in detail by Sheen *et al.* [52]. They applied a non-intrusive optical method using two-component forward scattering laser Doppler anemometry (LDA) for the flow field study of a polystyrene particle-air two phase suspension flow. Their detailed measurements of the flow structure included two time-mean velocity components of both phases, the volumetric concentration distribution of the particulate phase, and the turbulent properties of the fluid phase. Their experimental results revealed that certain peculiar behaviour of the particles and the fluid which obviously defy the predictions of conventional analyses of turbulent suspension flows. They have concluded that the velocities of fluid and particulate phases in a suspension flow present different characteristics for different particle sizes and mass loadings. Also, the particle's behaviour in a two-phase turbulent pipe flow is basically a two-dimensional motion with longitudinal and radial components.

Yang *et al.* [15] have reported in 1987 that there is no lack of studies on pneumatic transport technology in the literature. However, most of the studies are restricted to pipes less than 75 cm in diameter using particles of relatively narrow size distribution and they emphasize primarily the pressure drop along a pipeline usually less than 15 m in length. Because of the different phenomena occurring in the line, which are not well understood, the data obtained are often inconsistent. Thus, the selection of a set of design equations for the scale-up is difficult. Operational data of actual industrial plants with large, long transport lines and with particle of wide particle size distribution are not generally available. In addition, most of the studies are carried out under ambient temperature and atmospheric pressure. The effect of temperature and pressure on the transport line performance is not well known. Critical phenomena such as saltation in horizontal lines, choking in vertical lines, acceleration length and acceleration pressure drop, and pressure drop around the bends require further studies.

Areas often neglected in pneumatic transport design are the regions of accelerated and non-uniform flows most often seen in the feed regions of the system and in bends.

The concept of flow regimes is often discussed in the literature. However, there is no uniformity in terminology, which adds to the confusion of understanding the phenomena. Dense-phase plugs have been successfully conveyed by a number of commercial firms, but the basic physics has not been fully understood. Along with the dense-phase terminology, the concepts of saltation in horizontal flow and choking in vertical flow create unstable conditions in the transition to a dense-phase regime. The point of transition and its physics are not fully known.

The transport of solids by a gas stream can cause some unique phenomena that often are not seen in gas-liquid flows or single-phase flows. Particles tend to cluster in the dynamic state due to fluid dynamics and adhesion forces. The gas-solid flow systems are complicated due to the occurrence of wall collisions as well as particle-particle collisions where momentum is transferred. The difference between the gas and particle velocities is a result of these multi-particle interactions. With the collisions of dissimilar materials, the work functions of the surfaces are at different levels and as such have the potential to generate electrostatic charges which can significantly offset the flow. The particles, while being characterized by an average size, generally have a wide distribution of size and shapes. The solids in the flow have a tendency to segregate to cause non-uniform concentrations in the regions of feeders and bends. All these happenings are fairly unique to gas solid systems.

In 1985, Lodes *et al.* [3] investigated the rheological behaviour of dilute suspensions of solid particles in air in a vertical cocurrent flow moving upwards. Starting from the experimentally determined dependence of the pressure drop on the concentration of solid particles and the Reynolds number of the carrier medium in the steady flow region, the rheological

parameters were estimated using pseudo-shear diagrams. The investigated dispersed systems have pseudoplastic character, which becomes more pronounced with an increase of concentration, equivalent diameter and density of particles. A statistical treatment of the data obtained from pseudoshear diagrams enabled regression equations for the rheological parameters and critical values of the generalized Reynolds number to be obtained.

A generalized phase diagram was proposed by Klinzing *et al.* [4] to describe pneumatic transport. This generalized theory has been taken a step further in trying to incorporate the pressure loss term into the diagram that can describe the dilute and dense-phase regimes more clearly.

Brown *et al.* [5] examined the development of a tomographic technique for imaging gas-solid flow distributions in pneumatic conveying pipelines. Ultrasonic techniques have been given consideration due to the wealth of knowledge and associated degree of successful application within the fields of non-destructive testing and medical diagnosis.

Wypych and Arnold [6] stated that the method of scaling-up test rig data to full-scale installations, used quite extensively in the design of pneumatic conveying systems, is inadequate in particular applications. They modified two popular forms of definition and three existing empirical relationships for the solids pressure drop component to demonstrate the possible extent of this inadequacy. They obtained steady-state pipeline conveying characteristics from fly ash/cement mixture, PVC powder, and screened coke. In this study, suggested methods to predict air-only pipeline pressure drop (for both single and stepped diameter pipelines) and to generalize pneumatic conveying characteristics for a particular material applicable to any system of length and diameter are also included.

2.5. VELOCITY FIELD ANALYSIS IN TWO-PHASE FLOW FIELDS

The simplest method of obtaining basic information concerning the inner structure of a flow is the experimental determination of velocity profiles. The velocity profile of a flowing fluid is defined as the dependence of the local time-averaged axial velocity component upon the distance from the wall and/or the equipment axis. The shape of the velocity profile of the fluid behind its entry into the equipment changes with the axial distance from the entry. After a certain distance from the entry, the shape of the velocity profile is no longer a function of the axial distance from the entry into the equipment. This state of fluid flow is called "fully developed flow". The axial distance from the entry along which the flow of fluid becomes fully developed is called the entrance length.

When the fluid enters a pipe, an increase in pressure drop, due to a change of kinetic energy and due to friction, is observed. It is known that the length of the entry region depends upon the geometric arrangement of the pipe entrance, the level of turbulence of the entering fluid, Reynolds number and the rheological behaviour of the fluid. The length of the entry region can be determined experimentally in the following way:

- a) on the basis of the distance necessary for the velocity profile to be formed;
- b) on the basis of the distance over which the pressure gradient along the conduit becomes constant.

For the reason that about 95% of the total value of the increment of pressure drop (Bogue [55]) corresponds to the first half of the entry region, the first method is used more often. This explains why the length of the entry region, determined by various authors on the basis of achievement of a constant pressure gradient, is substantially smaller than the length calculated on the basis of the development of the velocity profile.

With regard to experimental problems, only a few sets of data concerning the velocity field in a gas-solid suspension flow are available in the literature. Moreover, these data are inconsistent. For illustration, the following examples can be presented: according to Soo [40], Soo and Terzek [56], and Kolansky *et al.* [57], the presence of particles does not cause a change in the velocity profile of the carrier medium. Boothroyd and Walton [58] and Varga [59] observed a flattening of the velocity profiles. According to Doig and Roper [60] and Drozdová and Lodes [61], the distribution of velocity in the gas phase is more convex in the core region in comparison with the velocity profiles of the pure carrier medium at the same Re ; Drozdová and Lodes [61] have shown the thickness of the boundary layer to be two- or three-fold greater due to the latter observations.

Authoritative reviews about the interaction between solid particles and the turbulence of the carrier fluid in two-phase flow appear at regular intervals (e.g. Soo [40]; Govier and Aziz [32]; Hetsroni [62]). These and later reviews are the best sources for relatively concise descriptions of research on turbulence in two-phase flows. It is well known that data concerning the laws of the velocity field are not convincing enough. These results arise due to the different view points given in the literature for the gas flow past solid particles in 12 various two-phase (solid particles-gas) systems.

Conveying velocity is one of the key parameters in the pneumatic transport of solids. A general procedure to predict the minimum conveying velocity required in dilute-phase systems may be very useful for engineers and designers, since successful design and operation of pneumatic transport systems depend upon the determination of the minimum conveying velocity at which the solids may be conveyed steadily through a pipeline. An unnecessarily high conveying velocity will result in higher energy costs due to an increased pressure drop in the system, solids degradation and pipe erosion, which can result in an economically unattractive operation. On the other hand, system designed with extremely low conveying velocities or extremely high solids flow rates are subject to erratic operation due to the

deposition, or they may become completely inoperable because of blockage in the system. In general, minimum conveying velocity can be defined as the minimum safe gas velocity for the horizontal conveyance of solids. If this gas velocity is set at the beginning of a pneumatic transport system (at the feed point), the rest of the pipeline will operate well above this lower velocity bound, since the gas velocity will increase along the pipeline due to compressibility effects, i.e. density decrease. Keeping gas velocity above minimum conveying velocity in all horizontal sections of a pipeline ensures no deposition of solids in the system and a continuous, steady conveyance of solids.

Although pneumatic transport has been practised for over a century and a considerable amount of work has been done in this field, a general procedure to determine the minimum conveying velocity is not available at the present time. The continuous accumulation of data and correlations demonstrate that there is not yet a thorough understanding of the pick up and saltation mechanisms; therefore theoretical predictions for the pick up and saltation velocities have yet to be developed. The main reason for the diversity of data in pneumatic transport is the variety of materials handled, and today many investigators recommend that the best method of predicting the minimum conveying velocity for a given material is to test it in a pilot plant having features that correspond as closely as possible to those of the plant being designed.

Several terms have been used to refer to minimum conveying velocity: saltation velocity, pick up velocity, suspension velocity, deposition velocity, rolling or sliding velocity, critical velocity, initial mixing velocity, velocity at the minimum pressure point of the general state diagram, etc. Definitions of these terms are based on visual observations and pressure drop measurements, and they are often used to indicate the way in which the particles are moving or begin to move. Although pick up and saltation are often used interchangeably in dilute-phase transport, they represent two completely different mechanisms, creating a controversy on how to define

the minimum conveying velocity. The gas velocity in a horizontal pipeline at which the particles start to drop out of suspension and settle on the bottom of the pipe is usually called saltation velocity. Another similar definition by Rossetti [63] for saltation velocity is the “minimum velocity in a horizontal pipeline that will prevent solids deposition on the bottom of the pipe”. Pick up velocity differs from saltation in relation to the initial position of the particles. Pick up velocity has been defined as the “gas velocity required to resuspend a particle initially at rest on the bottom of the pipe” (Rossetti [63]) or as the “fluid velocity required to initiate sliding, rolling and suspension of particles” (Halow [64]).

A technique for finding the minimum pick up velocity, $U_{g_{pu}}$, of solid particles in horizontal pneumatic conveying was developed by Cabrejos and Klinzing [11] in 1992. They presented a general semi-empirical correlation based on the Archimedes number and a model for the incipient motion of a single particle as:

$$U_{g_{pu}} = (1.27Ar^{-1/3} + 0.036Ar^{1/3} + 0.45) \cdot (0.70Ar^{-1/5} + 1) \cdot U_{g_{puo}} \quad 2.1$$

where $U_{g_{puo}}$ is the minimum pick up velocity for a single particle. This correlation is valid over a range of particle size from 10 to 1000 μm for the prediction of the minimum gas velocity, required to pick up particles. For ‘large spheres’, the size of the particle is considered much larger than the thickness of the laminar sublayer ($d_p \gg \delta_l$). For the velocity of the uniform flow required to initiate motion or to pick up a large single particle lying on the bottom of a horizontal pipe, the following equation was developed:

$$U_{g_{puo}} = \left[1 - \left(\frac{d_p}{D} \right)^{1.5} \right] \sqrt{\frac{4 f_s g d_p}{3 C_D} \left(\frac{\rho_p - \rho_a}{\rho_a} \right)} \quad 2.2$$

It is important to point out that Equation 2.2 is an implicit equation because the drag coefficient is a function of the particle Reynolds number, and thus the gas velocity.

In the case of a 'small sphere' lying on the bottom of a pipe inside the laminar sublayer ($d_p < \delta_l$) the following equation was proposed for $U_{g\text{puo}}$:

$$1.54 \times 10^{-4} \left[1 - \left(\frac{d_p}{D} \right)^{1.5} \right]^{-2} C_D \rho_a d_p^4 \left(\frac{U^7 g \rho_a}{\nu^3 D} \right)^{1/2} = f_s \left[\frac{\pi}{6} g d_p^3 (\rho_p - \rho_a) + 1.302 \times 10^{-6} d_p - 6.35 \times 10^{-3} \rho_a d_p^3 \left(\frac{U^{21} g \rho_a}{\nu^5 D^3} \right)^{1/8} \right] \quad 2.3$$

where f_s is the coefficient of sliding friction between the particle and the wall; ν is the fluid kinematic viscosity. Obviously, Equation 2.3 is an implicit equation and a numerical method should be used in order to solve for the minimum pick up velocity, $U_{g\text{puo}}$, of a small single particle.

In equation 2.1; Ar is the Archimedes number defined by:

$$\text{Ar} = \frac{g (\rho_p - \rho_a) d_p^3}{\nu^2 \rho_a} \quad 2.4$$

Pick up and saltation mechanisms of solid particles have been examined in horizontal pneumatic transport by Cabrejos and Klinzing [12] in 1994. They carried out several experiments to determine pick up, saltation, and particle velocity of a wide variety of materials using different techniques. They presented a simple correlation to predict pick up velocity of coarse particles (above 100 μm diameter) providing alternatives for designers to determine the minimum conveying velocity, U_{gpu} as:

$$\frac{U_{gpu}}{\sqrt{gd_p}} = 0.0428 \text{Re}_p^{0.175} \left(\frac{D}{d_p}\right)^{0.25} \left(\frac{\rho_p}{\rho_a}\right)^{0.75} \quad 2.5$$

This relationship is valid for $25 < \text{Re}_p < 5000$; $8 < (D/d_p) < 1340$; and $700 < (\rho_p/\rho_a) < 4240$.

Saltation in pneumatic conveying is often defined as the condition under which some particles form a stationary or slow-moving layer on the bottom of the horizontal pipe, whilst others continue to move in the upper layer in a well-dispersed flow. The superficial gas velocity at which this behaviour occurs, commonly is called as the saltation velocity and it is a function of solids loading, and of particle and gas properties. It is one of the basic parameters required for the proper design of the conveying system since it represents a change in the flow regime. However, because it is seldom practical to use transparent tubes (and in any event visual observation involves subjective interpretation), the saltation velocity can also be defined in two other ways:

- a) the velocity at which the maximum solids flow occurs when a fixed pressure difference is imposed between the feed and delivery points;
- b) the velocity corresponding to the minimum pressure drop between feed and delivery points for a given solids flow rate.

The saltation velocity is often used as a criterion to distinguish between dilute and dense phase flows. According to Marcus *et al.* [2], the minimum in the pressure drop referred to above does coincide with the deposition in coarse particle systems; for fine particles, however, saltation takes place at velocities above that at which the minimum pressure drop is achieved.

Geldart and Ling [10] have measured saltation velocities for two different fine coals transported in different gases such as nitrogen, carbon

dioxide and hydrogen. They compared experimental values with four published correlations and with one developed from their own extensive high pressure conveying experiments. Their equation, and that of Rizk [65] correlated their data within 15% accuracy, but they have concluded that the Rizk correlation should be preferred because of its much simpler form.

Geldart and Ling [10] expressed Rizk [65] equation in its original form, in terms of the Froude number and solids-gas ratio;

$$\frac{M_p}{M_g} = \frac{1}{10^a} \left(\frac{u}{\sqrt{gD}} \right)^b \quad 2.6$$

where $a = 1440d_p + 1.96$; $b = 1100d_p + 2.5$ and subscript g refers to the gas.

It is more convenient to use Equation 2.6 in the rearranged form to obtain an expression for saltation velocity as:

$$u_{\text{sal}} = \left(\frac{4M_p 10^a g^{b/2} D^{-2+b/2}}{\pi \rho_g} \right)^{1/(b+1)} \quad 2.7$$

The data on which Equation 2.7 based is related to coarse particles of several millimeters in diameter flowing in pipelines up to 55 mm diameter. Below $100\mu\text{m}$, the exponents a and b are virtually constant and equation 2.7 predicts that, for constant solids mass flow rate, M_p , saltation velocity, u_{sal} should be proportional to $1/(\rho_g)^{0.286}$. The Rizk equation is simple and although it is based on limited experimental data, it has been proved to be applicable over a wide variety of conditions.

Ginestet *et al.* [7] investigated pneumatic transport of particles in inclined tube at 72 and 90 degrees with respect to the horizontal plane. They measured solids hold-up, pressure gradient and pressure drop fluctuations as functions of the air velocity and the solids flux. They have also

determined the transition from the dilute to the dense phase in both the vertical and the inclined orientations.

In 1990, Lodes and Mierka [9] estimated velocity profiles in the entry region of a gas-solid suspension flow by means of a two-thermistor anemometer. They have estimated the relationship between entry length and Re number, relative mass fraction and size of solid particles; they have concluded that the entry length decreases with an increase in Re and increases with an increase in both the relative mass fraction and the equivalent diameter of the solid particles.

Slip velocity, the velocity of the carrying fluid relative to the moving solid, is another prime factor in the design of pneumatic transport systems. Its value represents the smallest fluid velocity at which any transport is feasible. When a substantially greater fluid velocity is chosen for practical transport of solid at a specified rate through a vertical conduit, the slip velocity may be used to calculate the solid concentration in the conduit. These in turn may be used to estimate the contributions of solid friction and solid weight to the pressure gradient which must be applied to the motive fluid in order to maintain transport. Such calculations are complicated by doubt over the proper value of slip velocity. It is easy to estimate the terminal settling velocity of a single particle of the solid material, but it is not permissible to identify this result with the slip velocity in vertical transport. The value may be close at low solid loadings in conduits of large diameter, but very substantial differences arise from the effects of proximity of particles and their interactions with one another and with the wall of the conduit.

In 1986, Sankar and Smith [13] presented results of some measurements of slip velocity between solid and gas in vertical pneumatic transport. Their tests covered particles of sand, glass and steel-shot up to 700 μ m in diameter and transport tubes of 12.7 to 38.1 mm in diameter. They measured slip velocity at solid volumetric concentrations up to 10%. They described the countercurrent flow arrangement which permitted easy and

accurate determination of solid velocity from pressure drop data at high concentrations and low solid velocities. Their results indicated that the slip velocity is a strong function of concentration and increases with increasing concentration. They have also concluded that slip velocities are severalfold higher than the corresponding single particle terminal velocities, indicating the possibility of formation of clusters.

At large transport velocities, which often are associated with lower volumetric concentrations, the slip velocity, u_{rel} , is mainly due to solid-wall frictional loss. In such a situation, momentum balance on solid phase results in the following expression proposed by Sankar and Smith [67]:

$$u_{rel} = \left(\frac{8f_s d_p \rho_p}{3C_D D \rho_a} \right)^{1/2} \cdot u_p \quad 2.8$$

where f_s is the solid-wall friction factor. It is seen from Equation 2.8 that slip velocity is proportional to solid velocity at large transport velocities and low concentrations.

One important parameter for the calculation of pressure loss and generally for mathematical modelling of pneumatic transport is the average velocity of the solid particles. Therefore in 1989, Lodes and Mierka [8], investigated average velocity of the dispersed phase in vertical flow of suspensions of solid particles. They have obtained an equation for the calculation of average velocity, u_p , of solid particles as:

$$u_p = u - 0.015 Re^{0.1} (M_p/M_a)^{-0.05} (D/d_p)^{1.1} u_t \quad 2.9$$

where u is the average velocity of continuous phase and u_t is the terminal velocity of particle.

From Equation 2.9, it follows that the average slip velocity increases

with the average velocity of the carrier medium. On the contrary, the average slip velocity decreases (i.e., their average velocity increases) as the solid concentration and equivalent diameter of solids increase. Another expression of particle velocity is given by Hinkle [68] as:

$$u_p = u (1 - 0.044d_p^3 \rho_p^{-0.2} D^{-0.54}) \quad 2.10$$

A modification of Equation 2.10 was made by Institute of Gas Technology, IGT [69] and following relation was obtained:

$$u_p = u (1 - 0.68d_p^{0.92} \rho_p^{0.5} \rho_f^{-0.2} D^{-0.54}) \quad 2.11$$

The velocity of the particles, u_p , can also be evaluated from the correlation proposed by Geldart and Ling [66] as:

$$u_p = u (1 - 0.0638 d_p^{0.3} \rho_p^{0.5}) \quad 2.12$$

It is suggested that $u_p \approx u$ for fine powders.

2.6. PRESSURE DROP DETERMINATION IN TWO-PHASE FLOW FIELDS

The pressure drop for a given fluid-particle combination in pipe flow is an important criterion in designing gas-solid flow systems. A number of empirical correlations are available for some simple flows, e.g., the correlation of Yang [29] for spherical particles greater than 100 μm in vertical dilute gas-solid suspensions. Some of the fluid-particle flow models promise for predicting pressure drop in the simplest kinds of suspension flows.

The problem of mathematically modelling the pneumatic transport of

solid particles in the dilute-phase mode for the purpose of predicting pipeline air pressure drop (for a given set of operating conditions) has been the subject of numerous investigations (Rizk [72], Molerus [73], Yang [74], and Marcus [76]). However, empiricism has been widely used and a unified theory applicable to all materials (especially fine powders) and the numerous configurations of pipeline has yet to be formulated. Theoretical predictions for dense-phase pneumatic transportation have been few in number and the majority are only concerned with straight horizontal pipes.

Chambers and Marcus [75] combined the efforts of a number of researchers to modify slightly the model presented by Marcus [76], and found the difference between predicted and experimental values of total pipeline air pressure drop to be less than a factor of 2.

A theoretical correlation for pressure drop was proposed from the unified theory for dilute-phase pneumatic transport developed by Yang [74]. The approach starts with the material and force balances in a pipe section of length L. The total pressure drop in a horizontal line was given by the following relation:

$$\Delta P_T = \frac{2f_a \rho_a u_a^2 L}{D} + \frac{f_p \rho_p (1 - \varepsilon) u_p^2 L}{2D} \quad 2.13$$

where f_a is the friction of air alone defined by the Fanning equation, ε is the voidage and u_p is the particle velocity given by:

$$\varepsilon = 1 - \frac{4M_p}{\pi \cdot D^2 \rho_p u_p} \quad 2.14$$

$$u_p = u_a - u_t \sqrt{\frac{f_p u_p^2}{2gD} \varepsilon^{-4.7}} \quad 2.15$$

since u_p and f_p are interrelated, a trial and error solution is required to solve Equations 2.14 and 2.15.

By statistical treatment of the experimental data of pressure loss, Lodes *et al.* [77] obtained the following relation:

$$\frac{\Delta P_T - \Delta P_a}{\Delta P_a} = 0.53 \frac{C_D}{f_a} \left(\frac{d_p}{D} \right)^{2/3} \frac{\sqrt{\text{Re}} M_p}{Fr M_a} \quad 2.16$$

in which ΔP_a is the pressure loss due to friction of the carrier medium in the absence of the dispersed phase, f_a is the coefficient of pressure loss due to friction of the pure carrier medium, and C_D is the drag coefficient of the solid particles calculated from the Schiller-Neumann equation, which includes the modified Re_p number:

$$C_D = \frac{24}{\text{Re}_p} (1 + 0.15 \text{Re}_p^{0.687}) \quad 2.17$$

The Reynolds number for particles in Equation 2.17 is defined by

$$\text{Re}_p = \frac{d_p u_p}{\nu_a} \quad 2.18$$

The Froude number involved in Equation 2.16 is defined as follows:

$$Fr = \frac{u_a^2}{gD} \quad 2.19$$

A theoretical expression defining total pressure drop, i.e., due to passage of the air alone, ΔP_a , and due to the excess pressure drop contributed by the collisions of solid particles with the wall was proposed by Michaelides [78] in 1987 as follows:

$$\Delta P_t = \Delta P_a \left[1 + K \frac{M_p \sqrt{Dg}}{M_a u_a f_a} \right] \quad 2.20$$

where K is a constant related with bouncing between the particles and the wall and its order of magnitude is approximately 10^{-1} . In Equation 2.20, gravity plays an important role because it causes collisions of particles with the wall in a horizontal pipe. In a vertical pipe, g will play an important role but for a different reason: it would be the main cause for the presence of slip between the two phases, which contributes to the excess pressure loss. ΔP_a is given by the well-known equality:

$$\Delta P_a = f_a \frac{L \rho_a u_a^2}{D} \quad 2.21$$

Mi and Wypych [14] developed a theoretical expression for the pressure gradient of horizontal slug-flow by applying the principles of powder mechanics to a moving slug. This expression indicates that the air pressure balances the resistive forces due to material weight of the slug and the transmission radial stress caused by the interaction of particles. Based on the theoretical expression of pressure gradient for moving slugs and the experimental results of slug velocity and stress transmission coefficient, following semi-empirical model to predict the total pressure drop along a horizontal pipeline was proposed as follows:

$$\Delta P_T = (1 + 1.084\lambda.Fr^{0.5} + 0.542Fr^{0.5}) \frac{2gf_w M_p L}{A u_{slug}} \quad 2.22$$

where λ is the stress transmission coefficient, f_w is the wall friction coefficient, and A is the cross-sectional area of the pipe. Equation 2.22 can be solved using computer iteration.

Yang *et al.* [15], performed pneumatic transport studies in a horizontal loop using three different elbows and a dead-end tee are described. In this study, preliminary data on line pressure losses are reported. Except for the dead-end tee, the pressure drop around the elbow occurred primarily beyond the elbow rather than at the elbow. The elbow pressure loss was apparently expended for redispersing the solid particles, which are gathered into dense ribbons, beyond the elbow.

In 1986, Lodes and Mierka [18] measured pressure losses and velocity profiles in the air-solid suspension flow in a vertical pipe. From the measurements, they have investigated the entry length parameters. These parameters were found to be the character of the flow and Reynolds number. Their derived mathematical model enabling the estimation of the entry length with accuracy ranging from 10 to 40%.

Saccani [16] carried out some experiments on a pneumatic conveying test plant to verify the predictions obtained by a simulation program. Especially, the pressure loss and the average particle velocity have been simulated. The conveyed solid was sand. Concerning the pressure losses, the author realised several conveying conditions and verified the theoretical predictions by means of pressure taps along the pipe.

The studies by Vaseleski [70] and Radin *et al.* [71] have shown that the pressure drop in liquid-solid suspensions is highly dependent on particle shape. In the experiment of Vaseleski, nylon fibers with aspect ratio (L_p/d_p) on the order of 100 caused a 10% drag reduction in water at a loading ratio, M_p/M_a , of 0.01, while asbestos fibers with $L_p/d_p = 10,000$ gave 70% drag reduction at $M_p/M_a = 0.005$ at $60,000 \leq Re \leq 400,000$. Radin *et al.* [71] tested nylon and rayon fibers with $37 \leq L_p / d_p \leq 105$ in water at $7,000 \leq Re \leq 200,000$. They observed drag reduction up to 25% over $0.002 \leq M_p / M_a \leq 0.04$ and also noted that drag reduction was increased with L_p / d_p of the fiber. No drag reduction was observed for any of the several types of spherical

particles tested in their experiments.

Previous experimental and theoretical works on drag reduction in gas-solid suspensions have been reviewed by Pfeffer and Kane [79]. Drag reduction has been obtained for fine spherical particles at $10000 \leq Re \leq 300000$. Rossetti and Pfeffer [28] reported a 75% drag reduction for one combination of the variables in a vertical tube. On the other hand, Garner and Kerekes [31], in their study of an air suspension of wood pulp fibers, reported a 6% drag reduction over $150,000 \leq Re \leq 300,000$ and $M_p / M_a = 0.21$.

Coughran [27] measured the pressure drop for air suspensions of spherical particles and two types of fibrous particles, all having a mean diameter range of $8 \mu\text{m} \leq d_p \leq 20 \mu\text{m}$ in a pipe having a diameter of 50.42 mm. In that study, a Reynolds number range of $61000 \leq Re \leq 114000$ and a loading ratio range of $0.06 \leq M_p / M_a \leq 0.30$ were investigated. Air-sphere suspensions showed a drag reduction, in agreement with the results of Pfeffer and Kane [79]. Fairly uniform fibers of $L_p/d_p = 75$ gave no drag change and drag increases resulted with "random cut" fibers of mean $L_p/d_p = 31$, contrary to the published results (Vaseleski [70]) for water-fiber suspensions. The author explained the reason of this difference due to the different scales of turbulence in the two fluids, relative to the particle size.

2.7 FRICTION FACTOR CORRELATIONS

In 1987, Michaelides and Roy [17] studied on a project to provide a critical evaluation of many correlations which have appeared in literature and the degree to which these correlations agree with several experimental data sets. These correlations predicted the friction factors in gas-solid pipe flows and they were derived either by dimensional analysis together with non-

linear regression methods or by theoretical models making certain assumptions. Thus, they collected several data sets and arranged them in a way that they may be used to give all the parameters present in the correlations. Then, they have compared each correlation with the available data sets. The expression derived by Michaelides and Roy [17] is;

$$f_{p+a} = f_a + 0.076 \frac{(M_p / M_a)}{\sqrt{Fr}} \quad 2.23$$

One of these correlations proposed by Dogin and Lebedev [80] is given as follows:

$$f_{p+a} = f_a + C \frac{M_p}{M_a} \left(\frac{d_p}{D} \right)^{0.1} \text{Re}^{0.4} Fr^{-0.5} \left(\frac{\rho_p}{\rho_a} \right) \quad 2.24$$

where the constant C has the value 6.6×10^{-6} , as suggested by the authors, or 8×10^{-7} as suggested by Soo [40]. This was treated as two expressions; Dogin & Lebedev (1), based on the first value of C ; and Dogin & Lebedev (2), based on the second value of C .

Another correlation proposed by Hinkle [68] is given in the study of Michaelides and Roy [17] is:

$$f_{p+a} = f_a + \frac{M_p}{M_a} \left(\frac{u_p}{u_a} \right)^2 f_p \quad 2.25$$

where u_p is the solids velocity and f_p is a function of the solid and air properties.

The other correlation mentioned in the study of Michaelides and Roy [17] is that from the study of Pfeffer *et al.* [81]. This work is a source of experimental correlations for pressure drop and for heat-transfer coefficients.

In the study it is recommended that the following expression can be used for:

$$f_{p+a} = f_a \left(1 + \frac{M_p}{M_a} \right)^{0.3} \quad 2.26$$

Considering the study of Michaelides and Roy [17] it was found that Equation 2.26 in general underpredicts the data, a fact corroborated by Soo [40].

Two more expressions were reported by the Pfeffer *et al.* [81] both of which merit consideration. They both emanate from heat-transfer equations after Reynolds analogy has been applied and they are given as follows:

$$f_{p+a} = f_a \left(1 + 4 \text{Re}^{-0.32} \frac{M_p}{M_a} \right), \quad 2.27$$

$$f_{p+a} = 7.6 f_a \left(\frac{M_p}{M_a} \right)^{0.45} \text{Re}^{-0.21} \quad 2.28$$

Rose and Barnacle [82] have proposed following correlation:

$$f_{p+a} = f_a + \frac{\pi}{2} \frac{M_p}{M_a} \left(\frac{\rho_p}{\rho_a} \right)^{0.5} \Psi \quad 2.29$$

where Ψ is a function of the Reynolds number of the flow and is given graphically in their original study. This function was represented by spline polynomials in the computer program used for the work by Michaelides and Roy [17].

The last correlation mentioned in the study of Michaelides and Roy [17] was proposed by Shimizu *et al* [83]:

$$f_{p+a} = f_a \left(1 + 0.379 \frac{M_p}{M_a} \right) \quad 2.30$$

This was suggested as an approximate expression for the friction factor of two-phase flows.

For the friction factor of air flowing alone in the pipe f_a , in Equations 2.23 to 2.30; the following expression was suggested by Michaelides and Roy [17]:

$$f_a = 4(0.0014 + 0.125\text{Re}^{-0.32}) \quad 2.31$$

Michaelides and Roy [17] states that Equation 2.23 is derived from the sets of all the available data and naturally appears to be the best of the group examined in their study.

It was indicated by Michaelides and Roy [17] that one may find in the literature other correlations among others. These correlations were excluded from their study for one or more of the following reasons:

- a) They required knowledge of flow parameters other than those contained in the data sets.
- b) They pertain to a very specific flow regime (e.g. slug flow, dense phase etc.).
- c) The information provided was of a graphical nature which could not be represented easily by spline polynomials.
- d) Their validity was limited to special flows or systems.

Özbelge [22] theoretically analyzed the hydrodynamics of dilute gas-solids suspensions in 1983. She presented a computer program and its algorithm which can be applied to any dilute upward flowing suspension in a vertical pipe. From this study, the relative velocity between the two phases,

the voidage, the external force acting on the solids due to particle-particle and particle-wall interactions can be calculated for different loading ratios.

Özbelge [23] proposed a theoretical correlation in 1984 for solids friction factor in vertical upward pneumatic conveying lines and checked this by using data of Hariu and Molstad [42]. This correlation consisted of easy-to-measure variables which made it quite practical and its accuracy was about $\mp 20\%$. The proposed correlations could be used without the need of any pressure drop data to calculate voidage, drag velocity, solids phase velocity, and density. The proposed correlation for solids friction factor is:

$$f_s = 0.0054 \left(\frac{M_p \rho_a}{M_a \rho_p} \right)^{-0.115} \left(\frac{u_a d_p}{u_{rel} D} \right)^{0.339} \quad 2.32$$

where the solids loading ratio, M_p / M_a is defined by the following relation:

$$\frac{M_p}{M_a} = \frac{u_s \rho_p (1 - \varepsilon)}{u_a \rho_a} \quad 2.33$$

where ε is the voidage and u_s is the solids velocity. In Equation 2.32, u_{rel} is calculated as explained by Özbelge [22]. Equation 2.32 is good to $\mp 20\%$ for 98% of the data by Hariu and Molstad [42] and it can be solved by iteration. The devised trial and error procedure is described by Özbelge [23].

In 1997, Özbelge [24] extended her previous work [23] and she proposed a new correlation for gas-solid mixture friction factors in vertical pipes with an accuracy of $\mp 20\%$ as:

$$f_{p+a} = f_s + 6.33 \left(\frac{1}{Fr_s} \right)^2 \quad 2.34$$

where f_s is found from Equation 2.32, $Fr_s = u_s / \sqrt{gd_p}$. This correlation is valid for the following ranges of the variables: voidage, 0.980-0.999; particle diameter 213-503 μm , superficial gas velocity 6.0-12.5 m/s; pipe diameter 0.00676-0.01354 m. The carrier gas is air and ρ_a is taken as 1.1854 kg/m^3 .

Yang [29] proposed an empirical equation for the horizontal pneumatic conveying as given below:

$$f_{p+a} = 0.0293 \left(\frac{1-\varepsilon}{\varepsilon^3} \right) \left[(1-\varepsilon) \frac{u_a}{\sqrt{gD}} \right]^{-1.15} \quad 2.35$$

where voidage, ε is given by Equation 2.14.

Yang [29] also proposed another correlation for the vertical conveying as follows:

$$f_{p+a} = 0.0315 \frac{1-\varepsilon}{\varepsilon^3} \left[\frac{(1-\varepsilon)u_a}{u_a - u_p} \right]^{-0.979} \quad 2.36$$

Weber [25] theoretically derived friction factor correlations from modified statements, simulation of the measured data and their correlation with or without overlay of errors. This study revealed that the correlation derived from the simulation with an overlaid error corresponds to the real conditions. The proposed correlation with the overlay of errors is:

$$f_{p+a} = 2.98 \left(M_p / M_a \right)^{0.31} Fr^{-0.8} \quad 2.37$$

Çarpınlioğlu and Gündoğdu [20] conducted an experimental two phase flow study in 1999 to determine the development length which is estimated from friction factor variation along the pipeline. They have found that development length is a strong function of Re such that an increase in

Re causes a decrease in the development length while mass loading ratio seems to be of secondary importance.

In 2000, Çarpınlioğlu and Gündoğdu [21] tried to express the experimental data in terms of a correlation based on the development length as:

$$\frac{f_{p+a}}{f_a} Fr \left(M_p / M_a \right)^{-0.175} = -4.2705 + 3.9407 \times 10^{-8} Re^2 \quad 2.38$$

This equation is valid for the following ranges of the parameters: $51500 \leq Re \leq 109000$, $5\% \leq M_p/M_a \leq 20\%$ with $375 \mu\text{m} \leq d_p \leq 825 \mu\text{m}$. The proposed correlation seemed to be appropriate for practical applications in horizontal pneumatic conveyings of solid particles.

2.8 CONCLUSIONS

Under the light of the above given literature survey, the influence of flow angularity on friction factor was studied due to the lack of data in the literature. Therefore, the experiments were performed in horizontal and inclined lines with angularities of 10° , 20° , 30° with the horizontal plane. In addition, circumferential static pressure distribution of the flow was investigated.

Therefore, the main goal of this study is to determine the effect of angularity of transport line used for conveying particles, characteristics of conveying gas and properties of solid particles which primarily influence two-phase flow fields.

CHAPTER 3

EXPERIMENTAL SET-UP AND MEASUREMENTS

3.1. INTRODUCTION

In this chapter, design, construction and calibration of the experimental test set-up and measurement principles of the collaborated devices are presented.

3.2. EXPERIMENTAL SET-UP

In this study, an open circuit blower type set-up designed and constructed by Gündoğdu [34] was used in a modified version with the addition of inclined transport pipeline for obtaining a uniform, steady and fully developed pipe flow. The experimental test set-up was consisted of the following basic parts as shown in Figures 3.1 and 3.2:

1. Blower unit
2. Settling tank
3. Pipe system
4. Particle feeder
5. Cyclone separator-bag filter assembly.

It is seen from Figure 3.1 that, the fluid flow supplied by a centrifugal fan is firstly transferred into the settling tank by means of a flexible duct, and then it continues to flow through plastic PVC pipes into the particle feeding unit. The fluid flow rate is measured by means of a pitot tube and wall static tapping placed just before the particle feeding unit. After the particle feeding unit, flow is fed into the cyclone. The fluid flow from the top of the cyclone is directed into a bag filter by means of a pipe section and a 90° elbow.

3.2.1. Blower Unit

The blower unit is composed of a centrifugal fan coupled to an electric motor and AC motor variable speed control unit. The required head and the maximum air flow rate in the present experimental investigation are 135 mAC and 0.16 m³/sec, respectively.

A vertical shaft centrifugal fan which is capable of providing 0.175 m³/sec of air under a head of 150 mAC when running at 2835 rpm was used to supply air to the set-up. It has an impeller with 420 mm outer and 320 mm inner diameters with 12 backward curved blades. The exit cross-section of the volute casing of fan is a 250 mm x 300 mm rectangle. The fan is driven by a 2.95 HP/2.2 kW, 2835 rpm electric motor. This motor is controlled by an AC motor variable speed control unit which controls the motor speed by controlling the frequency of the mains. The specifications of the motor and speed controller are given in Appendix 1. The speed of motor could be changed safely from 0 to 5000 rpm with the variable speed control unit. Thus the amount of flow rate through the set-up was controlled by controlling the rotational speed of the fan.

3.2.2. Settling Tank

A settling tank removes flow irregularities and reduces the size of the eddies created in the discharged air stream at the blower exit. Therefore, a settling tank of dimensions 800mm x 800mm x 800mm is located at the exit of the blower for this purpose. Hence the flow velocity is very small inside the settling tank with respect to the test pipe and a uniform steady air flow free from disturbances induced by the blower is obtained.

The acceptable measurements can be achieved if the flow is virtually free from swirl. The flow must be symmetrical across the pipe axis and is fully developed at a short distance downstream. Thus, a special flow straightener according to BS 1042 [35], a honeycomb is installed at the exit of the settling tank.

3.2.3. Pipe System

A PVC tube of inner diameter $D=106$ mm is used in the piping. The 600 cm of the pipe downstream of the settling tank is called the entrance pipe section, providing sufficient length to have a fully developed turbulent flow of clean air in the test section. The test section along which the pressure measurements are taken has a length of 535 cm downstream of the solid particle feeder.

The inclination of the test section is achieved with an 90° -elbow rotated about w axis and α degree inclination is obtained as shown in Figure 3.2. The elbow was fitted just after the particle feeder and the desired angle was between test section and z axis.

3.2.4. Particle Feeder

A celled wheel particle feeder was used to induce solid particles. The feeding unit mainly consists of a celled wheel, a particle storage tank, an electric motor driven with direct or belt, and an AC motor speed controller. The operation procedure of the particle feeder may be summarized as follows:

A definite amount of the particle is filled into the particle storage tank and then the top cover of storage tank is closed when the particle exit mouth of the storage tank which is placed at the bottom of the storage tank is closed. After setting the required rotational speed of the celled wheel which was calibrated previously experimentally, the particle exit mouth of the storage tank is opened. Thus, the particles were taken with a definite mass flow rate from the particle storage tank and transferred into the fluid flow.

The desired particle-air loading ratio is obtained by controlling air mass flow rate in the pipe by an AC motor variable speed controller which is linked on the electric motor of the blower unit and by feeding the solid particles also at a controlled rate by an another AC motor variable speed controller which is linked on the electric motor of the particle feeder. The specifications of the electric motor and speed controller of the particle feeder unit are given in Appendix 2. A uniform particle feeding into the flow is provided by means of a mixer mounted on the particle feeder.

3.2.5. Cyclone Separator-Bag Filter Assembly

A cyclone separator- bag filter assembly was used at the end of the test section. The induced solid particles are conveyed with air through test section and finally they are collected in the cyclone where the air-particle mixture entered tangentially. Then a swirling flow structure is generated, thus the particles collapse at the bottom of the cyclone and clean air rises

upward. Fine particles which cannot be collected by the cyclone separator are carried with the clean air and they are collected in a bag filter. A schematic view of the cyclone is given in Figure 3.3.

3.3. SOLID PARTICLES

Alumina, Semolina, and Fly Ash particles were used to see the effect of type and size of these particles on two-phase flows. Characteristics of them are given in Table 3.1. The apparent density was measured according to ASTM B212-76 [36]. The particle size distribution was determined by weighing the sieved quantities of particles using Endecotts' EFL 2 MK 3 test sieve shaker. The average particle diameter, d_p , taken as the one corresponding to 50% weight of sieved particles.

Among the solid particles, Alumina had a single size range while Semolina and Fly Ash were grouped into three different size ranges. These ranges were represented by the symbols A1, S1, S2, S3, F1, F2, and F3, respectively.

The loading ratio of solid particles was calibrated by plotting M_p (kg/s) vs f (Hz) curves. The mass flow rate, M_p of solid particles is determined as follows: The mass of sample is measured, then it is placed into the particle feeder. A reference frequency of the particle feeder is chosen. When the flow of solid particles is started, a stopwatch is started to run simultaneously and when the particle feeder is free from the particles, the stopwatch is paused and the time covered between starting and pausing of the stopwatch is recorded. Then the mass measured already is divided by the recorded time. Thus, the mass flow rate of a sample at a specific frequency can be determined. After that, the rotational speed of the particle feeder is changed to a different value, the elapsed time is measured and mass flow rate is evaluated. All these processes are repeated for different

frequencies and the data from these measurements are obtained. Then, the calibration curve of a sample is plotted in terms of M_p vs f (Hz). If it is desired to plot this curve in terms of M_p and rotational speed of the feeder wheel, N ; frequency, f (Hz) should be converted into N . Thus, the resulting curves will be M_p vs N as shown in Figure 3.4.

After the calibration curves of all samples were plotted, particle-air mass loading ratio, M_p/M_a could be set to a required value. It is known that, $M_a = Q \cdot \rho_{air}$, where M_a is the mass flow rate of air, Q is the volumetric flow rate and ρ_{air} is the density of air. Q can be found from the relation:

$$Q = A * \bar{u}_a \quad 3.1$$

where, A is the cross-sectional area of the pipe ($A = \pi \cdot R^2$) and \bar{u}_a is the mean air flow velocity perpendicular to this area. Then the following equation can be written:

$$M_a = \pi \cdot R^2 \cdot \bar{u}_a \cdot \rho_{air} \quad 3.2$$

Now, if any M_p/M_a value at a specific velocity is required, this value is multiplied by M_a calculated from Equation 3.2. Thus, the mass flow rate of solid particles, M_p can be obtained. Then by referring to M_p (kg/s) vs. f (Hz) curves, the frequency of the particle feeder for any sample is determined. When these determined f (Hz) values are set into the speed control unit of the particle feeder, it is known that there is a desired M_p/M_a ratio in the flow at a given velocity.

3.4. MEASUREMENTS AND MEASURING DEVICES

3.4.1. Pressure Measurement Rings

In this experimental investigation, local static pressure and circumferential pressure measurement around the pipe were conducted separately. The local static pressure and circumferential pressure were determined by means of pressure rings covering the pipe circumference installed according to BS 1042 [35]. The section views of the pressure rings are given in Figures 3.5 and 3.6, respectively.

3.4.2. Pitot Tube and Traverse Mechanism

The details of flow velocity and flow direction measurement by using pressure probes have been described by Bryer and Punkhurst [37]. An L-shaped copper pitot tube of 2.2 mm OD and 1.1 mm ID located at 30 cm upstream of the particle feeder together with a wall static pressure tapping were used to measure the mean velocity at the reference station. The pitot tube was traversed across the pipe cross-section with an accuracy of ± 0.025 mm by means of a traverse mechanism to find the position of the pitot tube at which the mean velocity was measured. The traverse mechanism is shown in Figure 3.7. Since the average velocity is measured approximately at the same distance from the pipe wall for fully developed turbulent flows, which is also verified by Figure 3.8, the position of pitot tube from the pipe wall is determined once as follows:

At a specific frequency of the blower unit, pitot tube is traversed across the pipe cross-section. The velocity corresponding to each traversed point is measured with an inclined leg alcohol manometer. As expected, velocity at the center of the pipe, i.e. $r/R = 0$, reaches its maximum value and velocity at the wall of the pipe, i.e. $r/R = 1$, is zero which can be seen from

Figure 3.8. After traversing is completed, the velocity distribution $u(r)$ of the flow is obtained by fitting the data to a curve. The volume flow rate inside the pipe is calculated from Equation 3.1:

$$Q = A * \bar{u}_a$$

If $u(r)$ is the velocity at any radius r ; the flow δQ through an annular element of radius r and thickness δr will be,

$$\delta Q = 2\pi r \cdot \delta r \cdot u(r)$$

and, hence

$$Q = 2\pi \int_0^R u(r) \cdot r \cdot dr \quad 3.3$$

where r is any radius from pipe center and R is the full radius of the pipe. Pipe center is assumed to be 0. This integration can easily be evaluated since velocity distribution has already been obtained.

The mean velocity, \bar{u}_a defined as volume flow rate, Q divided by the cross-sectional area A normal to the flow is obtained after calculating Q from Equation 3.3; thus \bar{u}_a is given by:

$$\bar{u}_a = \frac{2\pi \int_0^R u(r) \cdot r \cdot dr}{\pi R^2} \quad 3.4$$

After mean velocity is calculated from Equation 3.4, it is inserted into the velocity distribution function to determine the radial distance. The calculation yields $r/R = 0.73$ which corresponds to $r = 38.7$ mm for the pipe

with a radius of 53 mm. Then, the tip of the pitot tube is placed at a radial distance, $R-r= 14.3$ mm from the pipe wall. After fixing that point, all the experimental measurements were taken at this reference position of the pitot tube. The mentioned calibration is used to simplify the experiments. Thus, required average fluid velocity within the pipe is directly calibrated by means of an AC motor variable speed control unit and an inclined tube micro-manometer without changing the radial position of pitot tube, with an accuracy of $\pm 0.5\%$.

3.4.3. Manometers

An inclined micro-manometer, the manometer fluid being alcohol, was used in collaboration with the pitot tube. The pressure measurement sensitivity was such that the pressures as low as 0.35 Pa could be measured.

Local static pressures and circumferential pressure magnitudes were measured by means of an inclined multi-tube alcohol manometer. Each of the tapping on the pressure rings was connected to a leg of the manometer separately with flexible pressure tubes. The pressure read on a leg was not affected by pressures applied on the remaining legs due to the property of multi-tube manometers.

The atmospheric pressure and the ambient temperature were measured during each experiment; because all experimental data was taken under varying atmospheric conditions. In order to avoid the effect of ambient temperature and atmospheric pressure changes on the manometer readings; all readings were converted to the ones at standard temperature and pressure, S. T. P. condition. Figure 3.9 was used to correct the manometer readings to S. T. P. condition.

3.5. EXPERIMENTAL STUDY

The experimental study was composed of 224 test cases in the horizontal line, 672 test cases in the inclined line for which the local and circumferential static pressure measurements were made.

The variables of the experiments are flow Re number, particle loading ratio, M_p/M_a , particle type, particle size, d_p , measurement stations, x/D , and inclination angle of the pipe system, α . The ranges of the covered experimental variables are given in Table 3.2.

The local static pressure measurements were taken along the test section at the following distances from the particle feeder such as $x=3.44D$, $x=10.47D$, $x=17.50D$, $x=24.45D$, $x=31.48D$, and $x=39.90D$ for horizontal line. For inclined line, the distances were $x=3.77D$, $x=10.82D$, $x=17.87D$, $x=27.14D$, $x=34.19D$, and $x=39.52D$.

The particle loading ratio, M_p/M_a , was varied between 5% to 25% for the horizontal line and 5% to 20% for the inclined line. The flow velocities were $\bar{u}_a=7.5$ m/s, $\bar{u}_a=10$ m/s, $\bar{u}_a=12.5$ m/s, and $u_a=14$ m/s. Re number is determined for pipe flows, from the following equation:

$$Re = \bar{u}_a \cdot D / \nu \quad 3.5$$

where \bar{u}_a is the mean air flow velocity, D is inside diameter of the pipe and ν is kinematic viscosity of the air. According to Equation 3.5, Reynolds numbers corresponding to the above given velocities were $Re=53000$, $Re=70667$, $Re=88333$, and $Re=98933$, respectively.

3.5.1. Setting of Flow Reynolds Number

The following procedure was used for setting the flow Reynolds number:

First of all, the ambient pressure was measured by means of a mercury barometer, and ambient temperature was measured with an alcohol thermometer. This was necessary for recording the coefficient, c , for alcohol. Because, alcohol was used in the manometers to measure pressures. From the correction chart of alcohol (Figure 3.9), the c value is found corresponding to the measured ambient pressure and temperature. The alcohol height is reduced to STP conditions from the ratio;

$$h_{\text{alc}} / (h_{\text{alc}})_{\text{STP}} = c,$$

$$(h_{\text{alc}})_{\text{STP}} = h_{\text{alc}}/c \quad 3.6$$

The alcohol height in the inclined manometer leg for a specific flow velocity was determined as follows:

As the blower unit is running at an unknown velocity, the alcohol level in the manometer had shows a value, but this is random. The required height is found with respect to the required velocity. The value read on the manometer-leg corresponds to the difference of total pressure and static pressure. Because, the pressure sensed by the pitot tube is sum of the static and dynamic pressure of the flow and this total pressure is applied on the reservoir of the manometer. The static pressure from the wall static pressure tapping is applied to the leg of the manometer. That is, the pressure from the pitot tube is increasing the alcohol height while that from the tapping decreases the alcohol height in the manometer-leg. Thus, the resulting height of the alcohol is the difference between the total and static pressure. In other words, this height represents the dynamic pressure of the flow. So;

$$P_{\text{Total}} - P_{\text{Static}} = P_{\text{Dynamic}}$$

$$\Delta P = P_{\text{dynamic}} \quad 3.7$$

The dynamic pressure is also expressed by the relation;

$$P_{\text{dynamic}} = \rho_{\text{air}} \cdot u^2 / 2 \quad 3.8$$

where, density of air, ρ_{air} is in kg/m^3 , flow velocity u in m/s and pressure, P is in Pascal.

The difference between total and static pressure, ΔP in the manometer-leg in terms of alcohol height, h_{alc} is given by:

$$\Delta P = \rho_{\text{alc}} \cdot g \cdot h_{\text{alc}}$$

where, ρ_{alc} is the density of alcohol in kg/m^3 . Taking into consideration manometer's inclination angle, β and h_{STP} from Equation 3.6, following equation is obtained:

$$\Delta P = \rho_{\text{alc}} \cdot g \cdot (h_{\text{alc}}/c) \cdot \sin\beta \quad 3.9$$

Substituting Equations 3.8 and 3.9 into Equation 3.7, following relation was obtained:

$$\rho_{\text{alc}} \cdot g \cdot (h_{\text{alc}}/c) \cdot \sin\beta = (\rho_{\text{air}} \cdot u^2 / 2) \quad 3.10$$

It is seen that h_{alc} can be evaluated from Equation 3.10, since all the parameters in this equation are known. Therefore, the required velocity together with the other parameters are inserted into Equation 3.10 and h_{alc} can be calculated. Thus, the frequency of the blower's motor is regulated with the speed control unit (it is increased or decreased) until calculated

alcohol height from Equation 3.10 is achieved.

3.5.2. Pressure Measurements

After setting the flow Re number by using Equation 3.5, the local static pressure measurements from pressure rings as shown in Figure 3.5 are taken by means of a multi-tube alcohol manometer. Before running the blower, the alcohol levels in the legs of multi-tube manometer are marked. On running the blower, static pressures at pressure ring stations push down these levels; the final levels are also marked. Then, the difference between two marked levels is measured. These measurements are also converted to STP conditions, applying Equation 3.6. The STP reduced heights, h_{STP} from each station are then converted into pressure magnitudes with the following relation:

$$P = \rho_{alc} \cdot g \cdot h_{STP} \cdot \sin\beta \quad 3.11$$

The procedures mentioned above are related with only clean air flow. If air-particle flow is considered, the particle loading ratio, M_p/M_a , plays an important role. Previously the frequencies of the particle feeder corresponding to any velocity and any loading ratio had been determined with the aid of Equations 3.1 and 3.2 in collaboration with Figure 3.4. At a specific flow velocity, the required M_p/M_a for a specific particle type was provided by regulating the frequency of the particle feeder to the determined value. The local static pressure measurements in two-phase flow were evaluated by following a similar procedure to that of clean air flow.

Pressure measurements around the pipe circumference were taken by using pressure ring which has six holes located at 60° , 120° , 180° , 240° , 300° , and 360° as shown in Figure 3.6. These measurements were conducted along the test section at distances from the particle feeder as $x=2.17D$, $x=20.83D$, and $x=39.51D$ for the horizontal line. In the inclined line,

these distances were $x=4.25D$, $x=22.60D$, and $x=41.50D$.

All the procedures for recording the circumferential pressures were the same as those in the local static pressure measurements. The experiments were performed for all types of particles given in Table 3.1, for all loading ratios and Re numbers given in Table 3.2. After completing the experiments in horizontal line, the test section was inclined to $\alpha=10^\circ$, $\alpha=20^\circ$, and $\alpha=30^\circ$, respectively as shown in Figure 3.2. The inclination was given by simply rotating the elbow around w-axis and then the pressure measurements in the inclined line were made with the same methods cited previously.

3.6. FLOW FRICTION FACTOR DETERMINATION

Friction factor of the flow was calculated from the local pressure gradients. It is known that frictional head loss of the pipe is given by:

$$h_L = f (L/D)(u^2/2g) \quad 3.12$$

where f is the friction factor, L is the length of the pipe, u is the flow velocity, D is the pipe diameter and g is gravitational acceleration. h_L can also be expressed by:

$$h_L = \Delta P / \rho_{\text{air}} g \quad 3.13$$

where ΔP is the static pressure difference between the two stations. From Equation 3.13 and Equation 3.12, f can be derived as:

$$f = (\Delta P/L)(2D/\rho_{\text{air}} u^2)$$

$(\Delta P/L)$ term in the last equation can be approximated as $(-dP/dx)$, then

equation describing friction factor, f becomes:

$$f = (-dP/dx)(2l) / \rho_m u^2 \quad 3.14$$

In equation 3.14, pressure gradient $(-dP/dx)$, can be calculated by using the static pressure measurements along the pipe. For this reason, the static pressure variation in terms of $P = P(x/D)$ was obtained by fitting curves to P - x/D data. P (Pa) magnitudes at different stations were measured and recorded previously and P vs. x/D curves were plotted easily.

The fitted curves are in terms of exponential expressions as:

$$P = a.e^{-b.(x/D)} \quad 3.15$$

where a and b are constants, e is the base of natural logarithm and P is the pressure in Pascal.

The $(-dP/dx)$ term in Equation 3.14 is obtained by taking the derivative of Equation 3.15 with respect to x as:

$$(dP/dx) = -a.(b/D).e^{-b.(x/D)} \quad 3.16$$

The result obtained from Equation 3.16 is a constant magnitude in N/m^3 and this is inserted into Equation 3.14. Thus, friction factor values, f at any location in the test section can be obtained.

CHAPTER 4

FRICTIONAL BEHAVIOUR OF FLOW

4.1. INTRODUCTION

In this chapter, the results of the local static pressure measurements along the flow line and those of circumferential static pressure measurements are discussed.

Based on the flow friction factor, the results which are determined from the local static pressure measurements along the flow line are discussed by considering the effects of particle size, density, particle-air loading ratio, Reynolds number, and pneumatic line configuration on the frictional resistance behaviour.

The relationship between f and x/D ; f_{p+a}/f_a and x/D are presented in terms of linear equations. Calculations for the velocity determination of the flow field, based on a force balance in the theoretical approach by Özbelge [22] are also given.

4.2. PRESSURE VARIATION ALONG THE TEST SECTION

4.2.1. Local Static Pressure Variation

The local static pressures are measured as explained in Chapter 3 and the ranges of variables are given in Table 3.2.

In this section, pressure variation along the pipe line is described by means of P (Pa) versus x/D graphs. In order to be concise, only sample graphs are given starting from Figure 4.1 to Figure 4.17.

Figures 4.1 to 4.4 correspond to the horizontal line case ($\alpha=0^\circ$) at different Re numbers for all particles; Alumina (A1), Semolina (S1, S2, S3) and Fly Ash (F1, F2, F3), while Figures 4.5 to 4.9, 4.10 to 4.13 and 4.14 to 4.17 correspond to $\alpha=10^\circ$, $\alpha=20^\circ$, and $\alpha=30^\circ$ cases, respectively.

A superficial inspection of these figures results in the following conclusions:

- a) magnitude of pressure decreases with the length of the test section,
- b) pressure values for clean air flow are always greater than those for air-particle flow,
- c) as Re increases, pressure values also increase,
- d) as M_p/M_a increases, magnitude of pressures decrease slightly,
- e) pressure variation with x/D seems to be a strong function of M_p/M_a , particle type, Re number, and inclination angle, α of the test section. It is very difficult to differentiate the strongest parameter among all these variables. It can also be estimated that all these parameters are interrelated.

Furthermore following detailed explanation of these figures can be appropriate to understand the subject:

In Figure 4.1, pressure variation with x/D along horizontal line for A1 is plotted for Re number of 53000, 70667, 88333, and 98933 taking into consideration of particle-air mass loading ratio, M_p/M_a . It can be said that M_p/M_a has no considerable effect on P variation at Re=53000. However, it becomes effective for Re>53000, particularly at Re=98933. The magnitude of pressure at the first measurement station ($x/D=3.44$) of that case is approximately 1000 Pa for $M_p/M_a=5\%$. This value decreases to 860 Pa for $M_p/M_a=20\%$.

The slope of pressure variation for each M_p/M_a remains nearly constant. At Re=70667 and Re=88333, pressure variation with x/D for $M_p/M_a>10\%$ can be considered by a single curve that is M_p/M_a becomes ineffective for these cases.

Figure 4.2 gives pressure variation with x/D along horizontal line at Re=53000 for three different sizes of Semolina; S1, S2 and S3. From this figure it can be concluded that particle size has no great effect on the local pressure magnitudes. For example when $M_p/M_a=10\%$, the magnitude of pressure for S1 is 310 Pa at $x/D=3.44$. At the same conditions, this value is 315 Pa for S3. The difference between these values is only 5 Pa and this is not a great difference. However, it can be said that for a specific type of particle the magnitude of pressure for smaller sized particles is slightly greater than that for larger sized particles.

M_p/M_a seems to be effective on pressure variation with x/D for S1, S2, and S3. For these particles and these conditions the maximum pressure magnitude, i.e., that measured at the first station is in the order of 330 Pa and the minimum pressure magnitude, i.e., that measured at the last station is in the order of 300 Pa for $M_p/M_a=5\%$.

Figures 4.3 and 4.4 give pressure variation with x/D for three size of Fly Ash; F1, F2, and F3 along horizontal line at $Re=70667$ and $Re=88333$, respectively. The behaviour observed from these two figures seems to be the same except for the pressure magnitudes due to the effect of Re number. M_p/M_a is also effective on the pressure variation, but particle size does not affect it significantly.

As can be seen from Figure 4.5 to Figure 4.17, inclined flow line cases are considered. It is apparent that M_p/M_a starts to lose its effect along inclined lines as can be seen clearly from Figure 4.5.c,d, Figure 4.6, Figure 4.9, Figure 4.10.a,b,c, Figure 4.11, and Figure 4.14.a. In particular M_p/M_a becomes ineffective if $M_p/M_a > 5\%$ for all particles with α inclination.

If pressure variation with x/D along horizontal and inclined lines are compared; it is seen that pressure magnitudes along horizontal line are greater than those along inclined lines. This is true for both clean air and two-phase flows. For example if only clean air is considered, from Figure 4.1.b for $Re=70667$ along horizontal line for A1, pressure value is 610 Pa at the first measurement station. However, from Figure 4.5.b for $Re=70667$ along inclined line, $\alpha=10^\circ$ for A1, pressure value is 460 Pa. The difference between them cannot be neglected. So, effect of inclination of test section results in excess pressure drop with respect to the horizontal test section. If two-phase flow is considered for above conditions and $M_p/M_a=10\%$, pressure is 490 Pa along the horizontal line and 370 Pa for $\alpha=10^\circ$. In this case, the conclusion drawn is again valid. In fact, this conclusion is not surprising because as it is known that the resistance of flow in horizontal line should be smaller than that of the inclined line. Then, this theory is confirmed by the experimental results.

The radical difference in behaviour between horizontal flow line and inclined flow at $\alpha=10^\circ$ is not seen in the lines with $\alpha > 10^\circ$. For the case of S2 particles in air flow at $Re=70667$ and $M_p/M_a=15\%$, the pressure magnitudes

at the last measurement stations are 260Pa, 325 Pa, and 315 Pa corresponding to $\alpha=10^\circ$, 20° , 30° , respectively as seen in Figures 4.6, 4.11, and 4.46. It can be concluded that the difference between inclination angles is not as high as that observed between horizontal and inclined lines in terms of measured pressure magnitudes.

Another conclusion can be drawn by the comparison of horizontal and inclined lines is that particle-air mass loading ratios may be increased up to 25% in horizontal flow which is seen from Figures 4.1.b, 4.1.c, 4.2, 4.3, and 4.4. However in inclined flow, loading ratio of 25% cannot be reached as can be seen from Figures 4.5 to Figure 4.17. Then, it can be said that although the higher M_p/M_a ratios can be reached in horizontal line, along inclined flow line $M_p/M_a < 25\%$ can be transported.

4.2.2. Circumferential Static Pressure Distribution

Literature survey indicated that there is almost no experimental investigation on circumferential pressure distribution in pneumatic transport lines. In order to fill this gap, static pressures along pipe circumference are measured by using a pressure ring which has six holes at angles of $\theta_1=60^\circ$, $\theta_2=120^\circ$, $\theta_3=180^\circ$, $\theta_4=240^\circ$, $\theta_5=300^\circ$, and $\theta_6=360^\circ$ (Figure 3.6) as it is described in Chapter 3. The variables for performed measurements are listed in Table 3.2. Circumferential pressure distribution indicates mainly:

a) particle distribution in pipe cross-section, since pressure measurements are based on the amount of sensed air. If particle concentration at a location is increased, static pressure is decreased locally in accordance with the increasing concentration,

b) flow uniformity.

Due to the nature of experiments, influence of M_p/M_a , particle type, Re number, and inclination angle (α) on flow; particle distribution can be determined by means of P (Pa) vs. θ plots. In order to find influence of pneumatic transport as was done in local static pressure measurements, the reference case of clean air flow circumferential pressure measurements were also taken. Simple plots are given from Figure 4.18 to Figure 4.33. By referring to these figures, the general behaviour of circumferential pressure distribution can be explained as follows:

a) as distance from the particle feeder increases, magnitudes of the sensed pressures decrease as it is also observed in local static pressure variation with x/D .

b) circumferential pressure variation is not at high levels with clean air. There is no angularity effect and the flow uniformity is seen (Figures 4.18, 4.22, 4.26, 4.30).

c) circumferential pressure variation is at higher levels with two-phase flows. Angularity effect is observed and flow is not as uniform as the case for clean air flow.

Figures 4.19, 4.20, 4.21 show circumferential pressure distributions for loading of A1, S1, F3 particles. Figure 4.20 which is for loading of S1 at $x=2.17D$ and $Re=70667$ along the horizontal line, gives a clear information of circumferential pressure distribution such that the particles are mostly concentrated at the angles between 120° and 240° along the contour of the pipe. In other words concentration of the particles occurring at the bottom of the pipe is high. Furthermore, the pressure distribution of this section is uniform which is indicated by the same pressure magnitude sensed in this section. However, between 0° to 120° and 240° to 360° , the behaviour is not similar to this behaviour. The magnitude of pressure remains constant up to $\theta=60^\circ$, and then starts to decrease towards $\theta=120^\circ$. It remains again constant between $\theta=120^\circ$ and $\theta=240^\circ$. For $\theta>240^\circ$, it shows an increasing trend up to $\theta=300^\circ$. Then it remains constant again up to $\theta=360^\circ$.

If the influence of particle-air mass loading ratio on circumferential pressure distribution is considered, it can be concluded by referring to the same sample figure (Figure 4.20) that M_p/M_a does not affect this behaviour seriously. The same argument is valid at $M_p/M_a=5\%$, 10% , 15% , and 20% . In fact, the pressure decrease is not so large. This can be verified by considering the worst condition, i.e., the case for which the highest pressure decrease or increase is observed. In Figure 4.20, this case seems to be valid at $M_p/M_a=10\%$. The magnitude of pressure between $\theta=0^\circ$ and $\theta=60^\circ$ is 557.5 Pa. It is decreased to 553.5 Pa at $\theta=120^\circ$. The difference between these pressure values is only 4 Pa which corresponds to 0.7% of the pressure decrease between $\theta=0^\circ$ and $\theta=120^\circ$. While between $\theta=240^\circ$ and $\theta=360^\circ$, the increase of the pressure results in the same amount. As one may accept that this percentage amount would not influence the flow field seriously, but it should be known that there is a decrease and/or increase of pressure around the pipe contour, it does not remain same implying the importance of loading.

From Figure 4.18 to 4.21, behaviour of the circumferential pressure distribution along horizontal test section is indicated. Along inclined test section which is shown by the Figures 4.22 to 4.33, the behaviour mentioned for horizontal line seems to be different indicating that inclination of the test section influences the results. As can be seen from Figure 4.23 for the case of F3 loading along 10° inclined test section for $Re=88333$, at $x/D=4.25$, the circumferential pressure variation with θ is as follows:

The magnitude of pressure at $M_p/M_a=15\%$ is 524.5 Pa at $\theta=0^\circ$. It is uniformly decreased to 520.5 Pa at $\theta=120^\circ$. Then from $\theta=120^\circ$ to $\theta=180^\circ$ it is increased to 522.5 Pa. Then, a decrease in the pressure is seen from $\theta=180^\circ$ to $\theta=300^\circ$ and the pressure reaches to that of $\theta=120^\circ$. From $\theta=300^\circ$ to $\theta=360^\circ$, the pressure is again increased to 524.5 Pa. So, inclination of test section may have an effect on circumferential pressure distribution.

The similar behaviour is observed for the lines with $\alpha=20^\circ$ and $\alpha=30^\circ$ shown in the sample Figures 4.27 to 4.29 and 4.31 to 4.33, respectively. That is pressure around the pipe circumference does not continuously remain constant; it may decrease, increase or remain constant between certain angles of θ .

Examining the figures related with circumferential pressure distribution, it may be said that increasing Re does not affect the behaviour seriously as well as particle type and size. In fact this result is also true whether the test section is horizontal or inclined. The percentage increase or decrease in pressure along inclined test section is the same as that mentioned in the horizontal test section.

The distance from the particle feeder does not have an important effect on the behaviour. This can be seen from Figures 4.27, 4.28, and 4.29 corresponding to $x=4.25D$, $x=22.60D$, and $x=41.50D$, respectively. After examining these figures a certain conclusion cannot be reached that as the distance from the particle feeder increases, the distribution of circumferential pressure is affected. This can be said also for particle type. It can be seen from Figures 4.19, 4.28 and 4.32 corresponding to A1 ($\alpha=0^\circ$), F2 ($\alpha=20^\circ$), and S1 ($\alpha=30^\circ$), respectively, that as the particle type is changed, the circumferential pressure distribution behaviour is not affected seriously.

By referring to the previously mentioned figures (Figure 4.18-4.33) it may be concluded that the circumferential pressure distribution is not uniform with constant magnitudes but it fluctuates in small amounts (maximum increase or decrease is noted as 1%). The main cause of this fluctuation is not any of the parameters which are α , Re, M_p/M_a , particle type, and the distance from the particle feeder, but it is the characteristics of the flow field as a whole. Meanwhile, this can also be considered as a confirmation for the developed uniform flow at the test section.

4.3. FRICTIONAL BEHAVIOUR

4.3.1. Friction Factor Variation Along The Test Section

4.3.1.1. The Variation of f with x/D

The calculation procedure of friction factor, f was explained in Chapter 3 (Section 3.6). These calculations were based on the pressure measurements and the results of them are shown in terms of f vs. x/D plots as given in Figure 4.34 to Figure 4.59.

As can be seen from Figure 4.33.a,b,c,d for loading of A1 at $Re=53000$, there exists some influence of line inclination. Along horizontal line, the curves concerning M_p/M_a are separated from each other. However, along inclined lines with $\alpha=10^\circ$, $\alpha=20^\circ$, and $\alpha=30^\circ$; these curves start to join together. That is as α increases, the effect of M_p/M_a decreases for cases above $M_p/M_a=15\%$.

As expected, friction factors of air-particle flow (f_{p+a} magnitudes) are greater than those of clean air (f_a values). As can be seen from Figure 4.34.b, f_a is equal to 0.022 at $x/D=3.44$. When the particles are induced, for example at $M_p/M_a=10\%$, this value is increased to 0.037 at the same location. The difference between them is clearly seen as high as 68%.

There is little dependence of f_a on x/D ; because the slope of f_a with x/D is close to zero. For example, if Figure 4.34.b is considered, the f_a value corresponding to initial measurement station is 0.022 and this value at the last measurement station is 0.020. However, flow of air-particle is dependent on location, x/D downstream of the particle feeder. As x/D increases, f_{p+a} decreases. This is confirmed by Figure 4.34.d; f_{p+a} values at $M_p/M_a=15\%$ are decreasing starting from initial measurement station as 0.036, 0.035, 0.034, 0.032, 0.031, and 0.029 respectively.

The loading of particles has an effect in such a way that as M_p/M_a increases, the magnitude of f_{p+a} increases as can be seen from Figures 4.34.a,b,c,d. For example if Figure 4.34.a is examined, f_{p+a} values at the last measurement station are 0.022, 0.024, and 0.028 corresponding to $M_p/M_a=5\%$, 10%, and 15% respectively.

Another conclusion drawn from Figures 4.34.a,b,c,d is that f values along inclined test section are greater than that along horizontal line. If Figure 4.34.a (the case for horizontal line) and Figure 4.34.c (the case for inclined line, $\alpha=20^\circ$) are compared at $M_p/M_a=10\%$, f value at $x/D=3.44$ is 0.027 for the first case and 0.040 for the latter case corresponding to the same conditions. Thus, this behaviour confirms the above mentioned argument.

The last conclusion derived from Figures 4.34.a,b,c,d is that the f_{p+a} values are more separated from f_a values for the inclined line in comparison with horizontal line. This may be explained by the numerical values read from this figure. The minimum loading of particles is at 5% as known. From Figure 4.34.a which is the case for horizontal line f_a and f_{p+a} for $M_p/M_a=5\%$ at $x/D=3.44$ are 0.0195 and 0.025 respectively. The deviation of f_{p+a} from f_a is 28.2%. From Figure 4.34.b which is the case for inclined line, $\alpha=10^\circ$ f_a value is equal to 0.022 and f_{p+a} value for $M_p/M_a=5\%$ is equal to 0.036 at $x/D=3.44$. Then deviation of f_{p+a} from f_a is corresponding to 63.64%. From Figure 4.34.c which is the case for $\alpha=20^\circ$ f_a and f_{p+a} values are found to be 0.022 and 0.038 respectively for the same conditions. Then the deviation of f_{p+a} from f_a is 72.73%.

Thus, the difference between horizontal line and inclined line is evident considering the deviation of f_{p+a} from f_a .

All the conclusions drawn from the sample figure of Figure 4.34.a,b,c,d for loading of A1 particles at $Re=53000$ along different test section inclinations, are also valid for the remaining cases shown in Figures

4.35 to 4.59. In these figures, the different parameters with respect to Figure 4.34. a,b,c,d are Re of 70667, 88333, 98933 and particle types of S1, S2, S3 and F1, F2, F3. Changing these parameters does not yield a different conclusion. Only the magnitudes are different for these cases, but the behaviour of friction factor, mentioned previously in Figure 4.34. a,b,c,d, does not change.

4.3.1.2. f - x/D Equations

In this section the relationship between f and x/D is introduced with proposed equations and the sample ones are given in Table 4.1. These equations were derived from Figure 4.34 to Figure 4.59 for only the cases where the curves representing the relationship between f and x/D seem to be coincided irrespective of M_p/M_a . The proposed equations are in the following form:

$$f = a(x/D) + b$$

where a and b are constants.

4.3.2. Frictional Flow Resistance Considering Clean Air Flow Resistance

4.3.2.1. The Variation of f_{p+a}/f_a with x/D

In order to express the frictional behaviour of air-particle flows in comparison with clean air flow, variations of f_{p+a}/f_a with x/D were searched as can be seen from the sample figures given in Figures 4.60 to 4.77.

The similar plots were performed for all the experimental cases. A classification of the related parameters was used in these representations such that one of them was kept constant, the others were varied to see the

influences on f_{p+a}/f_a vs. x/D . For this reason, for a specified Re and M_p/M_a , the effect of particle type was investigated for the particles; A1, S1, S2, S3, F1, F2, F3 (Figures 4.60 to 4.71).

Then, for a selected particle type at a specified Re , different M_p/M_a were taken (Figures 4.72 to 4.77). Furthermore, the effect of α was also observed by considering all of these representations along $\alpha=0^\circ$, 10° , 20° , and 30° .

Inspection of the above mentioned figures results in the following conclusions:

In certain cases, loading of any particle type does not make any difference. In those cases, two or more types of particles exhibit a unique behaviour (Figure 4.64.b). Another conclusion drawn from this figure together with Figure 4.64.a,c,d is that the slope of f_{p+a}/f_a versus x/D along the horizontal line (shown in Figure 4.64.a) is less than that along the inclined line (shown in Figure 4.64.b,c,d). This conclusion can be expressed by numerical quantities more clearly. In Figure 4.64.a, along horizontal line, f_{p+a}/f_a value of S2 starts with 1.18 and it decreases with x/D up to 1.15 corresponding to a drop of 2.5%. However, in Figure 4.64.c, along the inclined line with $\alpha=20^\circ$, initial and final f_{p+a}/f_a values for S2 particles are 1.60 and 1.45, respectively. The corresponding drop for these values is 9.4%. Thus the difference in slopes of f_{p+a}/f_a versus x/D along horizontal and inclined lines justifies the mentioned conclusion.

Furthermore, the combination of the curves corresponding to different particles occurs more along inclined test section. In Figure 4.64.a only the curves concerning S1 and F2 particles are coincided along $\alpha=0^\circ$. On the other hand, as mentioned previously, all the particle types are combined along the inclined line, $\alpha=10^\circ$ as shown in Figure 4.64.b. Curves of four types of particles; A1, S3, F1, and F2 are combined in Figure 4.64.c along the inclined line, $\alpha=20^\circ$. In Figure 4.64.d, however, curves of six types

of particles; A1, S2, S3, F1, F2, and F3 are combining along $\alpha=30^\circ$ line.

The last interpretation that may be made from observation of Figure 4.64.a,b,c,d is that f_{p+a}/f_a values are increasing with the increasing inclination of the test section, which can be clarified as follows: The f_{p+a}/f_a values at the first measurement stations corresponding along horizontal line and inclined lines of $\alpha=10^\circ$, 20° , 30° for S1 particles are 1.12, 1.47, 1.55, and 1.58 respectively. The similar behaviour is also indicated by the inspection of remaining figures; Figures 4.60.a,b,c,d to Figure 4.71. The differences arising between these figures may be due to the magnitudes of the parameters.

It can be seen from the sample figure for F3 along horizontal line (Figure 4.74.a,b,c,d) that as M_p/M_a increases f_{p+a}/f_a values also increase. For example, at $Re=53000$, the f_{p+a}/f_a values at the first measurement stations at $M_p/M_a=5\%$, 10% , 15% and 20% are 1.255, 1.265, 1.275, and 1.295 respectively. The increasing behaviour of these values with M_p/M_a is also valid for the other Re numbers.

It is also clear that f_{p+a}/f_a values decrease with increasing x/D at $Re=70667$; f_{p+a}/f_a value is starting from 1.250 and decreasing with x/D taking the values of 1.245, 1.235, 1.225, 1.220, and 1.210 respectively.

The effect of Re number on f_{p+a}/f_a cannot be determined clearly by examining the Figures 4.72-4.77. Since as Re increases, magnitude of f_{p+a}/f_a sometimes decreases or increases. This is verified by interpreting two sample figures for A1 along horizontal line (Figure 4.72.a,b,c,d) and for S2 along inclined line, $\alpha=10^\circ$ (Figure 4.75.a,b,c,d) at $M_p/M_a=15\%$ as follows:

In Figure 4.72.a which is at $Re=53000$, the value of f_{p+a}/f_a just after the particle feeder corresponding to $M_p/M_a=15\%$ is 1.65. When Re is increased to 70667 (Figure 4.72.b), f_{p+a}/f_a is decreased to 1.47 for the same conditions. However, at $Re=88333$ (Figure 4.72.c), the value is increased to

1.57 in this case. Then it has decreased to 1.51 at Re=98933 (Figure 4.72.d).

The above situation is also observed in Figure 4.75.a,b,c,d which is plotted for S2 particles along inclined line of $\alpha=10^\circ$ such that initial f_{p+a}/f_a values just after the particle feeders are 1.70, 1.57, 1.69, and 1.68 corresponding to Re of 53000, 70667, 88333, and 98933 respectively.

Thus, variation in Re influences the magnitudes of f_{p+a}/f_a along the line, but it is difficult to estimate the form of the relationship between f_{p+a}/f_a and Re.

4.3.2.2. The Proposed f_{p+a}/f_a - x/D Equations

In this section the equations proposed for the variation of f_{p+a}/f_a with x/D are given in the following form:

$$f_{p+a} / f_a = \alpha(x / D) + b$$

The equations fitted to the data and obtained for S1 and F1 particles along horizontal and inclined lines of $\alpha=10^\circ, 20^\circ, 30^\circ$ for all the covered Re numbers and M_p/M_a ratios are introduced and the sample ones are listed in Table 4.2. The curves representing the behaviour of all equations are shown in the Figures 4.78 and 4.79. The particles of S1 and F1 were selected since their sizes were remaining within the particle size range studied by Hariu and Molstad [42].

The similar equations were derived for the situations where the curves expressing the variation of f_{p+a}/f_a with x/D for different type of particles seemed to be coincide. Furthermore, the following ten equations satisfied by the experimental data can be proposed as:

$$f_{p+a} / f_a = -0.0029x / D + 1.5306 \quad 4.1$$

Equation 4.1 is valid at $Re=53000$ and $M_p/M_a=5\%$ along $\alpha=20^\circ$ (Figure 4.60.b). In this case F1, F2, F3, S1, and S3 particles indicate the same behaviour that is they are all together.

$$f_{p+a} / f_a = -0.0031x / D + 1.413 \quad 4.2$$

In Equation 4.2, the curves for A1, S1, S2, F1, and F3 particles are coincided at $Re=70667$, $M_p/M_a=5\%$ and $\alpha=10^\circ$ (Figure 4.63.b).

$$f_{p+a} / f_a = -0.0033x / D + 1.4688 \quad 4.3$$

Equation 4.3 is valid at $Re=70667$, $M_p/M_a=10\%$ and $\alpha=30^\circ$. In this case A1, S2, S3, F1, F2, and F3 particles indicate the same behaviour (Figure 4.64.d)

$$f_{p+a} / f_a = -0.0044x / D + 1.5575 \quad 4.4$$

Equation 4.4 is valid for the particles of A1, S1, S2, S3, F2, and F3 at $Re=70667$; $M_p/M_a=15\%$, and $\alpha=10^\circ$ (Figure 4.65.b)

$$f_{p+a} / f_a = -0.0048x / D + 1.6132 \quad 4.5$$

Equation 4.5 is valid for the concentration of data for A1, S2, S3, F1, and F2 particles at $Re=88333$, $M_p/M_a=10\%$, and $\alpha=10^\circ$ (Figure 4.67.b).

$$f_{p+a} / f_a = -0.0045x / D + 1.6685 \quad 4.6$$

In Equation 4.6, data for A1, S1, S2, and F3 particles seems to be coincided at $Re=88333$, $M_p/M_a=15\%$, and $\alpha=20^\circ$ (Figure 4.68.c).

$$f_{p+a} / f_a = -0.0024x / D + 1.6471 \quad 4.7$$

Equation 4.7 is valid for the combination of data for A1, S1, S2, S3, and F2 particles at $Re=88333$, $M_p/M_a=20\%$, $\alpha=0^0$ (Figure 4.69.a).

$$f_{p+a} / f_a = -0.0069x / D + 1.8017 \quad 4.8$$

Equation 4.8 is valid for combination of data for S1, S2, S3, F2, and F3 particles at $Re=88333$, $M_p/M_a=20\%$, and $\alpha=10^0$ (Figure 4.69.b).

$$f_{p+a} / f_a = -0.0048x / D + 1.6883 \quad 4.9$$

In Equation 4.9, the combination of data for A1, S1, S2, S3, and F3 particles is seen at $Re=88333$, $M_p/M_a=20\%$, and $\alpha=20^0$ (Figure 4.69.c).

$$f_{p+a} / f_a = -0.0065x / D + 1.7548 \quad 4.10$$

The last one, Equation 4.10 is valid for coinciding of data for A1, S1, S2, F1, F2, and F3 particles at $Re=98933$, $M_p/M_a=15\%$, $\alpha=10^0$ (Figure 4.71.b).

Inspection of proposed equations (Equation 4.1 to 4.10) results in the following conclusions:

1. The relationship between f_{p+a}/f_a is similar indicating the general character of flow friction in air-particle suspensions.
2. The a and b constants in the form of proposed equations exhibit a variety for the covered cases such that $0.0024 \leq a \leq 0.0069$ and $1.413 \leq b \leq 1.8017$ ranges were observed. These parameter ranges are a strong function of α , Re , M_p/M_a and particle type. However, it is difficult to determine their importance on the relationship.

Finally, the following 3 equations concerning the combination of data for all particles (A1, S1, S2, S3, F1, F2, F3) can be introduced as:

$$f_{p+a} / f_a = -0.0042x / D + 1.480 \quad 4.11$$

Equation 4.11 is related to the case of $\alpha=10^0$ at $Re=70667$, and $M_p/M_a=10\%$ (Figure 4.64.b).

$$f_{p+a} / f_a = -0.0041x / D + 1.546 \quad 4.12$$

Equation 4.12 is valid at $Re=70667$, $M_p/M_a=15\%$, and $\alpha=30^0$ (Figure 4.65.d).

$$f_{p+a} / f_a = -0.0048x / D + 1.606 \quad 4.13$$

Equation 4.13 is valid at $Re=98933$, $M_p/M_a=10\%$, and $\alpha=10^0$ (Figure 4.70.b).

4.4. FLOW FIELD VELOCITY DETERMINATION

In the study of Özbelge [22] in 1983, a theoretical analysis for the hydrodynamics of dilute upward flowing air-solid suspensions in vertical pipes was presented. This analysis is based on the macroscopic momentum balances along the axial direction for both of the phases. In this analysis, the voidage, mass fluxes of gas and solid phases were determined by using continuity equation together with the momentum principle. Therefore superficial gas velocity, relative velocity, and dispersed solid density, ρ_m were determined.

In 1984 Özbelge [23] indicated that solids friction factor is affected mainly by the external force on solids phase, drag velocity, terminal velocity and pressure drop due to solids friction. Then she had proposed Equation 2.32 which is based on a force analysis. Thus, this equation eliminates the

necessity of pressure drop data. She compared the proposed equation with the data of Hariu and Molstad [42] and she concluded that 98% of that data was satisfied by that equation in an error range of $\pm 20\%$. The comparison covered experimental data points with mean particle diameter ranging from 213 μm to 503 μm , particle density from 2600 kg/m^3 to 2700 kg/m^3 , voidage from 0.98 to 0.999, pipe diameter from 6.76×10^{-3} m to 13.54×10^{-3} m, superficial gas velocity from 6 m/s to 12.5 m/s. ρ_a was taken as 1.185 kg/m^3 .

In 1997 Özbelge [24] proposed another relationship between f_{p+a} and f_s in terms of a correlation given by Equation 2.34. The experimental data collected in this study was evaluated in Reference [85] and summarized by Çarpınlioğlu *et al.* [84] in terms of the theoretical method of Özbelge [22,23,24] to determine the voidage ε , mixture density ρ_m , velocity of solids phase u_s , velocity of fluid phase u_f , velocity of mixture u_m and drag velocity of solids u_{rel} . The following definitions were used for these calculations:

$$\text{Density of mixture, } \rho_m = \rho_p(1 - \varepsilon) + \rho_a\varepsilon \quad 4.14$$

$$\text{Flow velocity of mixture, } u_m = u + u_p \quad 4.15$$

$$\text{Fluid phase speed, } u_f = u / \varepsilon \quad 4.16$$

$$\text{Solids speed, } u_s = u_p / (1 - \varepsilon) \quad 4.17$$

$$\text{Relative velocity between phases, } u_{rel} = u_f - u_s \quad 4.18$$

The theoretical calculations were done by Çarpınlioğlu *et al.* [84] by using Equations 4.14 to 4.18 and the range of voidage ε , was found to be between 0.98-0.999 for the covered magnitudes of M_p/M_a . The calculated magnitudes of ρ_m (Table 1) were independent of Re and M_p/M_a .

The average flow velocity of mixture u_m and fluid phase velocity u_f were found to be in the order of superficial air velocity, u_a with a maximum and minimum amount of deviations 0.63% and 0.011% respectively. Thus u_a can be used as u_m or u_f without influencing the accuracy since superficial air velocity is effective in dilute phase. The calculations for the solid particle velocity u_s and relative drag velocity u_{rel} were indicated that u_{rel}/u_s is constant for different Re and varying only with M_p/M_a independent of angularity of the test section. It was observed that as M_p/M_a increases the magnitude of u_{rel}/u_s decreases.

4.5. CONCLUSIONS

In this chapter the variation of local static pressures with x/D and distribution of circumferential static pressure of the test section were explained. Then behaviour of friction factor which is determined from local static pressure variations is presented and friction factor correlations were proposed and such correlations were not encountered in the available literature. The theoretical results concerning flow field velocity (u_f , u_s , u_{rel} , u_m), mixture density, ρ_m and voidage, ε were also discussed.

CHAPTER 5

FRICION FACTOR CORRELATIONS

5.1.INTRODUCTION

In this chapter to describe the influence of α , Re , M_p/M_a , ρ_a , ρ_p , d_p , and D parameters on flow friction factor, the proposed correlations are given as a result of a trial-error approach.

5.2. THE VARIATION OF $(f_{p+a}/f_a)_r$ with Re

$(f_{p+a})_r$ and $(f_a)_r$ are the f_{p+a} and f_a values at $x/D=40$. This was state due to the need to define a single value in correlations. The parameter $(f_{p+a}/f_a)_r$ ratio is introduced indicating the discrepancy of f_{p+a} from f_a . Then the variation of $(f_{p+a}/f_a)_r$ with Re is shown as in Figures 5.1.a,b,c,d; 5.2.a,b,c,d; and 5.3.a,b,c,d along different test section inclinations. If these figures are inspected, it can be observed that as Re increases, particle type loses its effect on $(f_{p+a}/f_a)_r$. Figure 5.1.b is a good example to confirm this conclusion such that at $Re=53000$, $(f_{p+a}/f_a)_r$ is varying between 1.15 and 1.5. Increasing Re to 70667, the range of $(f_{p+a}/f_a)_r$ for all particle types is varied between 1.18 and 1.35. Finally $(f_{p+a}/f_a)_r$ magnitude for all particles is varied from 1.22 to 1.30 for $Re=98933$.

Also it can be said that as α increases, $(f_{p+a}/f_a)_r$ becomes independent of the particle type again (Figure 5.1.a,b,c,d). The flow behaviour for $\alpha=0^0$ and $\alpha=10^0$ seems to be almost the same. However, for $\alpha>10^0$ shows a different behaviour. For example $(f_{p+a}/f_a)_r$ values vary between 1.18 and 1.35 for all particles at $Re=70667$ along $\alpha=10^0$ test section. The magnitudes of $(f_{p+a}/f_a)_r$ are varying between 1.23 and 1.3 along $\alpha=20^0$ at the same Re .

In Figure 5.1.a which is along horizontal line, the particles seem to be separate from each other. They don't show a combination behaviour. The magnitudes of $(f_{p+a}/f_a)_r$ vary between 1.02 and 1.25; 1.08 and 1.33; 1.10 and 1.42; 1.15 and 1.30 corresponding to Re of 53000, 70667, 88333, and 98933 respectively. Therefore it can be said that the state in which all of the particles seem to be combined corresponds to $Re=98933$ since the least fluctuation in the magnitudes of $(f_{p+a}/f_a)_r$ is seen at that condition. Furthermore, it is observed that at $Re=70667$ and $Re=88333$, A1 particles are more separated from the other particles.

As previously stated $\alpha=10^0$ case does not differ from $\alpha=0^0$ case in a serious manner as shown in Figure 5.1.b. The particles are not still concentrated at $Re=53000$, the magnitude of $(f_{p+a}/f_a)_r$ varies between 1.15 and 1.50. At $Re=70667$, this range is noted to be fluctuate between 1.18 and 1.35 for all particles. It should be emphasized here that at $Re=70667$ and $\alpha=10^0$ case S3 particles contradict to the coinciding of all particles. If these particles are not considered, the remaining ones seem to be concentrated such that the magnitudes of $(f_{p+a}/f_a)_r$ change between 1.28 and 1.35. However, at $Re=88333$, it can be said that the particles are concentrated since the range of magnitude of $(f_{p+a}/f_a)_r$ changes between 1.25 and 1.35. As an average value, the magnitude of $(f_{p+a}/f_a)_r$ can be taken as 1.30 considering all of the particles. This means that at $Re=88333$, $M_p/M_a=5\%$ along $\alpha=10^0$, loading of any type of particle causes 30% excess friction in comparison with

clean air flow. At $Re=98933$, the particles seem to be combined and the average magnitude of $(f_{p+a}/f_a)_r$ can be given as 1.25.

In Figure 5.1.c which is the case for $\alpha=20^\circ$ and $M_p/M_a=5\%$, it can be observed that the particles are combined. At $Re=53000$, A1 particles seem to be contrary to the concentration of particles, however, at $Re=88333$ S1 particles are separated from the other particles. If the mentioned particles considered to be in the same group of other particles, average magnitudes of $(f_{p+a}/f_a)_r$ can be estimated as 1.42, 1.25, and 1.30 corresponding to Re of 53000, 70667, and 88333 respectively.

The particles still seem to be concentrated as shown in Figure 5.1.d along $\alpha=30^\circ$. The scattering of them is not resulted in a serious manner since the magnitudes of $(f_{p+a}/f_a)_r$ change between 1.40 and 1.53; 1.20 and 1.32 corresponding to Re of 53000 and 70667 respectively.

If the remaining figures 5.2.a,b,c,d and 5.3.a,b,c,d considering only M_p/M_a change in comparison with 5.1.a,b,c,d inspected, it can be said that if M_p/M_a is increased to 10% (Figure 5.2.a,b,c,d) the similar conclusion can be drawn, but the magnitudes of $(f_{p+a}/f_a)_r$ are changed with respect to behaviour of those at $M_p/M_a=5\%$ (Figure 5.1.a,b,c,d) such that along $\alpha=0^\circ$ the magnitude is changing between 1.1 and 1.3 for all covered particles at $Re=53000$. Along $\alpha=30^\circ$ $(f_{p+a}/f_a)_r$ takes values between 1.55 and 1.65 at $Re=53000$. This is seen also along $\alpha=20^\circ$ and $\alpha=30^\circ$. That is the range of values for $(f_{p+a}/f_a)_r$ changes as M_p/M_a changes. This is also valid for the case given in Figure 5.3.a,b,c,d in which $M_p/M_a=15\%$. The magnitude of $(f_{p+a}/f_a)_r$ takes different values corresponding to each Re .

If the case for which $M_p/M_a=10\%$ (Figure 5.2.a,b,c,d) is extensively investigated, a different behaviour can be observed in comparison with $M_p/M_a=5\%$ case (Figure 5.1.a,b,c,d). The concentration of particles is more evident in this case. The magnitudes of $(f_{p+a}/f_a)_r$ vary from 1.10 to 1.30, 1.10

to 1.37, 1.30 to 1.48, and 1.23 to 1.45 corresponding to Re of 53000, 70667, 88333, and 98933 respectively along $\alpha=0^\circ$ (Figure 5.2.a). However the magnitudes are changing between 1.19 and 1.52 at Re=53000 along $\alpha=10^\circ$ (Figure 5.2.b). At Re=70667 all of the particle types seem to be concentrated and the magnitude of $(f_{p+a}/f_a)_r$ can be given as an average value of 1.32 which means that in this case loading of any particle type causes an increase of friction by 32% in respect of clean air flow. At Re=88333, only S1 particles are separated from the group of others and the magnitude of $(f_{p+a}/f_a)_r$ may be given as 1.38.

The magnitudes of $(f_{p+a}/f_a)_r$ take values between 1.41 and 1.63; 1.27 and 1.42 corresponding to Re=53000 and Re=70667 respectively, however the magnitude may be given as an average value of 1.45 at Re=88333 along $\alpha=20^\circ$ (Figure 5.2.c). Along $\alpha=30^\circ$ which is the case as shown in Figure 5.2.d the particles seem to be combined and average magnitudes of $(f_{p+a}/f_a)_r$ are 1.60 and 1.35 corresponding to Re=53000 and Re=70667 respectively.

If $M_p/M_a=15\%$ case (Figure 5.3.a,b,c,d) is inspected, the magnitudes of $(f_{p+a}/f_a)_r$ take values from 1.12 to 1.53; 1.22 to 1.39; 1.39 to 1.53; and 1.32 to 1.49 corresponding to Re=53000, Re=70667, Re=88333, and Re=98933 respectively along $\alpha=0^\circ$ case (Figure 5.3.a). On the other hand, this range is varying between 1.20 and 1.57 at Re=53000 along $\alpha=10^\circ$ (Figure 5.3.b). Meanwhile, at Re=70667, except for F1 particles and Re=98933, except for S3 particles, a combination of all particles is observed. For these cases, the average magnitude of $(f_{p+a}/f_a)_r$ can be given as 1.38 and 1.52 respectively. The magnitudes take values between 1.38 and 1.55 at Re=88333.

The average magnitudes of $(f_{p+a}/f_a)_r$ for all covered particles are 1.58, 1.37 and 1.52 corresponding to Re=53000, Re=70667, and Re=88333 respectively along $\alpha=20^\circ$ (Figure 5.3.c). However, these magnitudes are 1.55 at Re=53000 and 1.38 at Re=70667 along $\alpha=30^\circ$ (Figure 5.3.d).

It can be concluded that there is a critical Re for which concentration of particles takes place. This Re can be determined by referring to Figures 5.1.a,b,c,d; 5.2.a,b,c,d; and 5.3.a,b,c,d simultaneously. The critical Re is determined as 70667 after examining these figures. It is valid for independent of M_p/M_a and α , because for $Re > 70667$, the magnitudes of $(f_{p+a}/f_a)_r$ for all particles seem to be combined at $M_p/M_a = 5\%, 10\%, 15\%$ and $\alpha = 0^\circ, 10^\circ, 20^\circ, 30^\circ$.

5.3. THE VARIATION OF $(f_{p+a}/f_a)_r$ (M_p/M_a) with $Re(d_p/D)$

In this section, in order to see the effects of the parameters M_p/M_a , Re, d_p , and D on friction factor in non-dimensional form, $(f_{p+a}/f_a)_r$ (M_p/M_a) vs. $Re(d_p/D)$ graphs are plotted as given from Figure 5.4 to Figure 5.6 under the light of Section 5.2. In these figures, particle type and M_p/M_a are effective on the relationship between $(f_{p+a}/f_a)_r$ (M_p/M_a) and $Re(d_p/D)$, and the relationship is noted to be semi-logarithmic. It can also be realized that the inclination of test section influences the relationship.

In Figure 5.4, variation of $(f_{p+a}/f_a)_r$ (M_p/M_a) with $Re(d_p/D)$ is given for all covered particles along $\alpha = 0^\circ$. It can be said that as M_p/M_a increase, the scattering of the data increase. For example if F1, F2, F3 particles are considered, $(f_{p+a}/f_a)_r$ (M_p/M_a) seems to be constant for all data at $M_p/M_a = 5\%$ and taking the value of 0.4 without influencing change in Re. However, if M_p/M_a is increased to 20% for these particles, the magnitude of $(f_{p+a}/f_a)_r$ (M_p/M_a) does not remain constant any more. In fact it fluctuates surprisingly between 0.240 and 0.320 as Re is changed. This is also true for S1, S2, S3 and A1 particles.

In Figure 5.5.a,b,c variation of $(f_{p+a}/f_a)_r$ (M_p/M_a) with $Re(d_p/D)$ is given for S1, S2, S3 particles along $\alpha = 10^\circ, 20^\circ, 30^\circ$. It can be concluded that the

behaviour of the parameters is affected with α such that as α increases, the scattering of data also increases. For example along $\alpha=10^\circ$ the data corresponding to $M_p/M_a=15\%$ is concentrated and shows a linear relationship between the parameters. However, if $\alpha=30^\circ$ case is examined for $M_p/M_a=15\%$, the data scatters and a relationship cannot be determined between the parameters. The same conclusion is also valid for F1, F2, F3 particles as shown in Figure 5.6.a,b,c; that is as inclination angle of the test section is increased, the data becomes more scattered.

In order to obtain a correlation describing the effect of α , some trials were done as can be seen in Figure 5.7 by only using the data taken with the particles A1, S1, and F1 and the variation of $(f_{p+a}/f_a)_r (M_p/M_a)$ with $Re(d_p/D)\cos\alpha$ was investigated. It can be seen from the plot drawn using the data with A1, the behaviour is influenced by changing of α .

The previous conclusions drawn from Figures 5.4, 5.5.a,b,c and 5.6.a,b,c related to variation of $(f_{p+a}/f_a)_r (M_p/M_a)$ with $Re(d_p/D)$ are confirmed with Figure 5.7. However, a single correlation cannot be proposed at this state since properties of particles seem to be effective on the behaviour.

Concentrating Figure 5.7 for S1 and F1 particles, Figure 5.8 was obtained. It can be said that as M_p/M_a increases, the scattering of data increases. For example at $M_p/M_a=5\%$, $(f_{p+a}/f_a)_r (M_p/M_a)$ remains constant approximately at 0.06 independent of $Re(d_p/D)\cos\alpha$. However it changes between 0.12 and 0.16 at $M_p/M_a=10\%$; 0.18 and 0.24 at $M_p/M_a=15\%$. So, from this figure, still a resulting correlation couldn't be obtained.

5.4. RESULTING CORRELATIONS

In this section resulting correlations are proposed by referring to the Figures 5.9 and 5.10. In Figure 5.9, variation of $(f_{p+a}/f_a)_r$ with Fr_s at $M_p/M_a=5\%$, 10% , 20% along $\alpha=0^\circ$, 10° , 20° , 30° for F1, S1, S2 particles is presented. Fr_s was calculated from Özbelge's [24] approach as:

$$Fr_s = u_s / \sqrt{gd_p} \quad 5.1$$

where u_s was described in Section 4.4.

From Figure 5.9 it can be concluded that the functional relationship is affected by the angularity of test section. The variation between $(f_{p+a}/f_a)_r$ and Fr_s seems to be more uniform along $\alpha=0^\circ$ and $\alpha=10^\circ$ in comparison to the cases with $\alpha>10^\circ$. Along $\alpha=20^\circ$ and $\alpha=30^\circ$ test sections the data exhibit a scattering tendency. Therefore angularity of test section has a considerable influence on the functional relationship between $(f_{p+a}/f_a)_r$ and Fr_s .

On the $\alpha=0^\circ$ case, all data can be represented by a single line sketched whose equation is given as:

$$(f_{p+a} / f_a)_r = 0.0054Fr_s + 1.0016 \quad 5.2$$

This means that the relationship is a linear one. The experimental data scatters from Equation 5.2 within an error band of $\pm 13\%$.

On the $\alpha=10^\circ$ case, data concentration is such that a logarithmic relationship exists between $(f_{p+a}/f_a)_r$ and Fr_s which can be proposed as follows:

$$\left(f_{p+a} / f_a\right)_r = 0.1835 \ln(Fr_s) + 0.6797 \quad 5.3$$

The experimental data scatters from Equation 5.3 with an error band of $\pm 11\%$ and this equation can be used to determine $(f_{p+a}/f_a)_r$ in terms of Fr_s for F1, S1, and S2 particles at $M_p/M_a=5\%$, 10% , 20% for Re of 53000, 70667, 88333 along $\alpha=10^\circ$ test section.

Considering Equation 2.32 and all the parameters mentioned in Section 5.1, a final correlation can be proposed in the form of Figure 5.10. In this figure, variation of $(f_{p+a}/f_a)_r(M_p/M_a)(\rho_a/\rho_p)$ with $Re(d_p/D)(1/Re_{rel})$ is given for the data of F1 and S1 particles at $M_p/M_a=5\%$, 10% , 20% for $Re=53000$, 70667 , 88333 along $\alpha=0^\circ$, 10° , 20° , 30° . The relationship between these two parameters seems to have a logarithmic expression as:

$$\left(f_{p+a} / f_a\right)_r \left(M_p / M_a\right) \left(\rho_a / \rho_p\right) = 0.001 \ln \left[Re \left(d_p / D \right) \left(1 / Re_{rel} \right) \right] + 0.0062 \quad 5.4$$

where $Re_{rel} = u_{rel} D / \nu$

In Figure 5.10, the most scattering of data is observed for horizontal test section and a deviation of $\pm 50\%$ from Equation 5.4 is recorded. However, the data related to test sections inclined with 10° , 20° , 30° angles seems to be coincided and a deviation of $\pm 15\%$ from Equation 5.4 exists.

In fact, there is a critical magnitude of $Re(d_p/D)(1/Re_{rel})$ that causes two different behaviours to be existed. This magnitude can be noticed from Figure 5.10 as 0.0035. Because up to this value the data seems to exhibit a relationship and after this value. The remaining data seems to have another relationship between them. However to simplify the result, a single correlation was proposed as given by Equation 5.4.

5.5. CONCLUSIONS

In this chapter a trial and error approach was used to obtain friction factor correlations. For this reason, $(f_{p+a}/f_a)_r$ vs. Re graphs were plotted initially. Then variations of $(f_{p+a}/f_a)_r(M_p/M_a)$ with $Re(d_p/D)$ and $(f_{p+a}/f_a)_r(M_p/M_a)$ with $Re(d_p/D)\cos\alpha$ were investigated. It was realized that these trials were not efficient for describing resulting correlations since particle type and angularity of the test section were effective on the behaviour.

Then variation of $(f_{p+a}/f_a)_r$ with Fr_s was investigated and two correlations were proposed from this relationship.

Finally the variation of $(f_{p+a}/f_a)_r(M_p/M_a)(\rho_a/\rho_p)$ with $Re(d_p/D)(1/Re_{rel})$ was investigated and a correlation was proposed representing this relationship.

These correlations are depended on all the parameters that affect two-phase flow fields and the advantage of them is that if $(f_{p+a}/f_a)_r$ is known, Fr_s or Re_{rel} which are directly related to solids velocity can be calculated with these correlations, thereby particle velocities can be determined.

As deriving these correlations, clean air density was considered. However mixture density ρ_m should be used since the magnitudes of ρ_m were different from the clean air density in deviations from 28% to 40% influencing the correlations.

CHAPTER 6

SUGGESTIONS FOR FURTHER INVESTIGATIONS

In this chapter suggestions for further investigations are given as follows:

1. The particles having different sizes and properties should be used .
2. A test section having different diameter and length with respect to that used in this study should be used.
3. There is a need to repeat the experiments along test sections for $\alpha > 30^\circ$, particularly along $\alpha = 45^\circ$ and $\alpha = 90^\circ$ as a following of this study.
4. The investigations must be done to confirm the results of experimental studies with those obtained from detailed theoretical studies.
5. An investigation should be performed to determine the flow characteristics (laminar, transitional, turbulent) since this is required for comprehensive velocity measurements.
6. An experimental set-up should be designed and constructed for loading of particles up to 50% at very high velocities.

LIST OF REFERENCES

1. Molerus, O., 1996. "Overview: Pneumatic Transport of Solids", Powder Technology, Vol. 88, pp. 309-321.
2. Marcus, R. D., Leung, L. S., Klinzing, G. E. and Rizk, F., 1990. "Pneumatic Conveying of Solids", Chapman and Hall, London.
3. Lodes, A., Mierka, O., and Micak, J., 1985. "Rheological Behaviour of Two-Phase Flow of Solid Particles in a Gas", Rheol Acta, Vol. 24, pp. 611-616.
4. Klinzing, G. E., Rohatgi, N.D., Zaltash, A., and Myler, C. A., 1987. "Pneumatic Transport - a Review: Generalised Phase Diagram Approach to Pneumatic Transport", Powder Technology, Vol. 51, pp. 135-149.
5. Brown, G. J., Reilly, D., and Mills, D., 1996. "Development of an Ultrasonic Tomography System for Application in Pneumatic Conveying", Meas. Sci. Technol., Vol. 7, pp. 396-405.
6. Wypych, P. W. and Arnold, P. C., 1987. "On Improving Scale-up Procedures for Pneumatic Conveying Design", Powder Technology, Vol. 50, pp. 281-294.
7. Ginestet, A., Guigon, P. and Large, J. F., 1993. "Hydrodynamics of a Flowing Gas-Solids Suspension in a Tube at High Angles of Inclination", The Canadian Journal of Chemical Engineering, Vol. 71, pp. 177-182.
8. Lodes, A. and Mierka, O., 1989. "Particle Velocities in Two-Phase Solid-Gas Flow", Powder Technology, Vol. 58, pp. 163-168.
9. Lodes, A. and Mierka, O., 1990. "The Velocity Field in a Vertical Gas-Solid Suspension Flow", Int. J. Multiphase Flow, Vol. 16, pp. 201-209.

10. Geldart, D. and Ling, S. J., 1992. "Saltation Velocities in High Pressure Conveying of Fine Coal", Powder Technology, Vol. 69, pp. 157-162.
11. Cabrejos, F. J. and Klinzing, G. E., 1992. "Incipient Motion of Solid Particles in Horizontal Pneumatic Conveying", Powder Technology, Vol. 72, pp. 51-61.
12. Cabrejos, F. J. and Klinzing, G. E., 1994. "Pickup and Saltation Mechanisms of Solid Particles in Horizontal Pneumatic Transport", Powder Technology, Vol. 79, pp. 173-186.
13. Sankar, S. R. and Smith, T. N., 1986. "Slip Velocities in Pneumatic Transport, Part-I", Powder Technology, Vol. 47, pp. 167-177.
14. Mi, B. and Wypych, P. W., 1994. "Pressure Drop Prediction in Low Velocity Pneumatic Conveying", Powder Technology, Vol. 81, pp. 125-137.
15. Yang, W. C., Anestis, T. C., Gizzie, R. E., and Haldipur, G. B., 1987. "Pneumatic Transport in a 10-cm Pipe Horizontal Loop", Powder Technology, Vol. 49, pp. 207-216.
16. Saccani, C., 1996. "Solid Speed and Pressure Loss in Pneumatic Conveying Plants: Simulation and Experimental Measurements", Bulk Solids Handling, Vol. 16, No.3, pp. 383-390.
17. Michaelides, E. E. and Roy, I., 1987. "Evaluation of Several Correlations Used For The Prediction of Pressure Drop in Particulate Flows", Int. J. Multiphase Flow, Vol. 13, No. 3, pp. 433-442.
18. Lodes, A. and Mierka, O., 1986. "Calculation of The Entry Length in a Suspension Flow of Solid Particles-Gas Mixture", Chemical Engineering Science, Vol. 41, No. 1, pp. 195-198.
19. Çarpınlioğlu, M. Ö. and Gündoğdu, M. Y., 1998. "An Experimental Approach for Determination of Development Length in Particulate Flows", Int. J. Multiphase Flow, Vol. 24, No. 2, pp. 347-353.
20. Çarpınlioğlu, M. Ö. and Gündoğdu, M. Y., 1999. "Effect of Particle Size and Loading on Development Region in Two-Phase Flows", Tr. J. of Engineering and Environmental Science, Vol. 23, pp. 27-37.
21. Çarpınlioğlu, M. Ö. and Gündoğdu, M. Y., 2000. "Correlation for Development Length of Fully-Suspended Flows in Horizontal Pneumatic Conveying", Powder Handling & Processing, Vol. 12, No. 2, pp. 145-151.

22. Özbelge, T. A., 1983. "An Algorithm for Hydrodynamics of Turbulent Upward Flowing Dilute Gas-Solids Suspensions", Int. J. Multiphase Flow, Vol. 9, No. 4, pp. 437-446.
23. Özbelge, T. A., 1984. "Solids Friction Factor Correlation for Vertical Upward Pneumatic Conveying", Int. J. Multiphase Flow, Vol. 10, No. 4, pp. 459-465.
24. Özbelge, T. A., 1997. "A New Mixture Friction Factor Correlation for Vertical Pneumatic Conveying of Solid Particles", Tr. J. of Engineering and Environmental Sciences, Vol. 21, pp. 253-255.
25. Weber, M., 1991. "Friction of the Air and Air-Solid Mixture in Pneumatic Conveying", Bulk Solids Handling, Vol. 11, No. 1, pp. 99-102.
26. Boothroyd, R. G., 1966. "Pressure Drop in Duct Flow of Gaseous Suspensions of Fine Particles", Trans. Inst. Chem. Eng., Vol. 44, pp. 306-313.
27. Coughran, M. T., 1988. "The Effect of Particle Shape on Pressure Drop in Turbulent Pipe Flow of a Gas-Solid Suspension", Trans. ASME, J. Fluids Eng., Vol. 110, pp. 222-225.
28. Rossetti, S. J. and Pfeffer, R., 1972. "Drag Reduction in Dilute Flowing Gas-Solid Suspensions", AIChE J., Vol. 18, No. 1 pp. 31-39.
29. Yang, W. C., 1978. "A Correlation for Solid Friction Factor in Vertical Pneumatic Conveying Line", AIChE J., Vol. 24, pp. 548-551.
30. Rizk, M. A. and Elghobashi, S. E., 1989. "A Two-Equation Turbulence Model for Dispersed Dilute Confined Two-Phase Flows", Int. J. Multiphase Flow, Vol. 15, pp. 119-133.
31. Garner, R. G. and Kerekes, R. J., 1980. "Flow Regimes of Wood-Pulp Fibers in Air Suspensions", Tappi, Vol. 63, No. 6, pp. 103-107.
32. Govier, G. W. and Aziz, K., 1972. "The Flow of Complex Mixtures in Pipes", Van Nostrand Reinhold, New York, 1st edn.
33. Hetsroni, G., 1982. "Handbook of Multiphase Systems", McGraw-Hill, New York.
34. Gündoğdu, M. Y., 1995. "Swirling Flow Generators and Swirling Flow Separators", Ms Thesis, Gaziantep University, Turkey.
35. BS 1042, Part 2A, 1973. "British Standard Methods for the Measurement of Fluid Flow in Pipes", British Standard Institution.

36. ASTM B212-76, "Standard Test Method for Apparent Density of Free Flowing Metal Powders", ANSI/ASTM American National Standard, New York.
37. Bryer, D. W. and Punkhurst, R. C., 1971. "Pressure Probe Methods for Determining the Wind Speed at Flow Direction", NPL Her Majesty's Stationary Office, London.
38. Yang, W. C., 1974. "Correlations for Solid Friction Factors in Vertical and Horizontal Pneumatic Conveyings", AIChE J., Vol. 20, pp. 605-607.
39. Wen, C. Y. and Galli, A. F., 1971. "Fluidization" (Edited by J. F. Davidson and D. Harrison), Academic Press, London.
40. Soo, S. L., 1967. "Fluid Dynamics of Multiphase Systems", Blaisdell, Waltham, Mass.
41. Metha, N. C., Smith, J. M., and Comings, E. W., 1957. "Pressure Drop in Air-Solid Flow Systems", Ind. Engng. Chem., Vol. 49, pp. 986-992.
42. Hariu, O. H. and Molstad, M. C., 1949. "Pressure Drop in Vertical Tubes in Transport of Solids by Gases", Ind. Engng. Chem., Vol. 41, pp. 1148-1160.
43. Depew, C. A., 1960. "Heat Transfer to Flowing Gas-Solids Mixtures in a Vertical Circular Duct", Ph. D. Thesis, University of California, Berkeley, U.S.A.
44. Boothroyd, R. G., 1971. "Flowing Gas-Solids Suspensions", Chapman and Hall, London.
45. Riethmuller, M. L., 1973. "Optical Measurement of Velocity in Particulate Flows, *Measurements of Velocities in Single and Two-Phase Flows*", von Karman Inst. For Fluid Dyn. Lecture Series, Vol. 54.
46. Oki, K., Walawender, W. P. and Fan, L. T., 1977. "The measurement of Local Velocity in Solid Particles", Powder Technol., Vol. 18, pp. 171-178.
47. Jones, M. G. and Mills, D., 1990. "Product Classification for Pneumatic Conveying", Powder Handling and Processing, Vol. 2, pp. 117-122.
48. Alexander, L. G. and Coldren, C. L., 1951. "Droplet Transfer from Suspending Air to Duct Wall", Ind. Engng. Chem., Vol. 45, pp. 1325-1331.

49. Friedlander, S. K. and Johnstone, H. F., 1975. "Deposition of Suspended Particles from Turbulent Gas Streams", Ind. Engng. Chem, Vol. 49, pp. 1151-1156.
50. Lin, C. S., Moulton, R. W., and Putnam, G. L., 1953. "Mass Transfer Between Solid Wall and Fluid Streams", Ind. Engng. Chem, Vol. 45, pp. 667-678.
51. Beal, S.K., 1968. "Transport of Particles in Turbulent Flow to Channel or Pipe Walls", Bettis Atomic Power Lab. Westinghouse Electric Corp., Pittsburgh, PA, U.S.A., Report No. WAPDTM-765.
52. Sheen, H. J., Chang, Y. Z., and Chiang, Y. S., 1993. "Two-Dimensional Measurements of Flow Structure in a Two-Phase Vertical Pipe Flow", Proc. Natl. Sci. Counc. ROC (A), Vol. 17, No. 3, pp. 200-213.
53. Lee, S. L. and Durst, F., 1982. "On the Motion of Particles in Turbulent Duct Flows", Int. J. Multiphase Flow, Vol. 8, pp. 125-146.
54. Tsuji, Y., Moorikawa, Y., and Shiomi, H., 1984. "LDV Measurements of an Air-Solid Two-Phase Flow in a Vertical Pipe", J. Fluid Mechanics, Vol. 139, pp. 417-434.
55. Bogue, D. C., 1959. "Entrance Effects and Prediction of Turbulence in non-Newtonian Flow", Ind. Engng Chem, Vol. 51, pp. 874-878.
56. Soo, S. L. and Terzek, G. J., 1966. "Turbulent Pipe Flow of Magnesia Particles in Air", Ind. Engng Chem. Fundam., Vol. 5, pp. 388-392.
57. Kolansky, M. S., Weinbaum, S., and Pfeffer, R., 1976. "Pneumatic Transport of Solids in Pipes", Proc. 3rd Int. Conf. On Pneumatic Transport, British Hydrodynamics Research Ass. Fluid Engineering, Cranfield, Beds., pp. C1-20.
58. Boothroyd, R. G. and Walton, P. I., 1973. "Fully Developed Turbulent Boundary Layer Flow of a Fine Solid Particle-Gaseous Suspension", Ind. Engng Chem. Fundam., Vol. 12, pp. 75-82.
59. Varga, M., 1978. "Hydrodynamics of Two-Phase Flow", Ph. D. Thesis, Faculty of Chemical Technology, Bratislava.
60. Doig, I. A. and Roper, G. H., 1967. "Air Velocity profiles in the Presence of Cocurrently Transported Particles", Ind. Engng Chem. Fundam., Vol. 6, pp. 247-256.
61. Drozdová, M. and Lodes, A., 1986. "Velocity Profiles in the Vertical Flow of Dilute Suspension Particles-Gas in Pipes", In Collection of the Scientific Works of the CHTF, 1979-1981, pp. 179-186.

62. Hetsroni, G., 1989. "Particles Turbulence Interaction", Int. J. Multiphase Flow, Vol. 15, pp. 735-746.
63. Rossetti, S. J., 1983. "Concepts and Criteria for Gas-Solids Flow", Handbook of Fluids, Ann Arbor Science/Butterworths, Boston, Ch. 24, pp. 635-652.
64. Halow, J., 1973, Chem. Eng. Sci., Vol. 28, pp. 1.
65. Rizk, F., 1976, April. Proc. Pneumotransport 3, BHRA Fluid Eng., Cranfield, pp. D4.
66. Geldart, D. and Ling, S. J., 1990. Powder Technol., Vol. 62, pp. 241.
67. Sankar, S. R. and Smith, T. N., 1986. "Slip Velocities in Pneumatic Transport, Part-II", Powder Technology, Vol. 47, pp. 179-194.
68. Hinkle, B. L., 1953. Ph. D. Thesis, Georgia Institute of Technology, Atlanta, GA.
69. Institute of Gas Technology, Oct. 1978, Dept. Of Energy Contract, FE2286-32.
70. Vaseleski, R. C., 1972. "Drag Reduction in the Turbulent Flow of Fiber Suspensions", M. S Thesis. University of Delaware, Newark.
71. Radin, I., Zakin, J. L., and Fatterson, G. K., 1975. "Drag Reduction in Solid-Fluid Systems", AIChE Journal, Vol. 21, No. 2, pp. 358-371.
72. Rizk, F., 1982. Bulk Solids Handling, Vol. 2, pp.235.
73. Molerus, O., 1981. Chem. Eng. Sci., Vol. 36, pp. 1977.
74. Yang, W. C., 1977. J. Powder and Bulk Solids Technol., Vol. 1, pp.89.
75. Chambers, A. J. and Marcus, R. D., 1986. Proc. 2nd Int. Conf. On Bulk Materials Storage Handling and Transportation, Univ. of Wollongong, pp. 49-52.
76. Marcus, R. D., 1983. Notes for Short Course on Pneumatic of Bulk Solids, Univ. of Newcastle, N.S.W., Australia.
77. Lodes, A., Mierka, O., and Micák, J., 1986. Chem. Eng. Commun., Vol. 41, pp. 151.
78. Michaelides, E. E., 1987. "Motion of Particles in Gases: Average Velocity and Pressure Loss", Transactions of ASME, Vol. 109, pp. 172-178.

79. Pfeffer, R. and Kane, R. S., 1974. "A Review of Drag Reduction in Dilute Gas-Solid Suspension Flow in Tubes", Int. Conf. On Drag Reduction, Paper F1 and Discussion, BHRA Fluid Engineering.
80. Dogin, M. E. and Lebedev, V. P., 1962. "Dependence of the Resistance in Pneumatic Conveying Pipelines on the Fundamental Parameter of the Two-Phase Flow", Ind. Engng. Chem., Vol. 2, pp. 64.
81. Pfeffer, R., Rosetti, S., and Licklein, S., 1966. "Analysis and Correlation of Heat Transfer Coefficient and Heat Transfer Data for Dilute Gas-Solid Suspensions", Report NASA. TN-D 3603.
82. Rose, H. E. and Barnacle, H. E., 1957. "Flow of Suspensions of non-cohesive Spherical Particles in Pipes", Engineer, June, pp. 898.
83. Shimuzu, A., Echigo, R., Hasegawa, S., and Hishida, M., 1978. "Experimental Study on Pressure Drop and Entry Length of the Gas-Solid Suspension Flow in a Circular Tube", Int. J. Multiphase Flow, Vol. 4, pp. 53-64.
84. Çarpınlioğlu, M. Ö., Özbelge, T. A., and Oruç, V. "Flow Frictional Resistance in Pneumatic Conveying of Solid Particles Through Inclined Lines" Accepted for presentation and publication for 4th International Conference on Multiphase Flow May 27-June 1, 2001 Tulane University, New Orleans, Louisiana.
85. "Theoretical Calculations in a Pneumatic Flow Field", ME 499 Graduation Project conducted by Çiledağ, Ö. H., B. S. Student of Mechanical Engineering Department, University of Gaziantep, Supervised by Çarpınlioğlu, M. Ö. December 2000.



APPENDICES

APPENDIX 1

SPECIFICATIONS OF THE DRIVE UNIT OF BLOWER

The drive unit of fan consists of an electric motor and the AC motor variable speed controller which have the following specifications:

Electric motor

Input: 3 \emptyset , 220/380 V, 50 Hz

Power rating: 2.95 HP/2.2 kW

Rotational speed: 2835 rpm

Protection class: IP 44 B

AC speed controller

Controller specification: Simovert P. 6SE2008-3AA00

Input: 3 \emptyset , 380/500 V \mp 10%, 14/12 A, 47-63 Hz

Output: 3 \emptyset , 380/500 V, 12/11 A, 0-400 Hz

Power rating: 8.3 kVA, motor: 7.5 HP/5.5 kW

Protection class: IEC 529 IP 20

Temperature range: 0-40 $^{\circ}$ C.

APPENDIX 2

SPECIFICATIONS OF THE DRIVE UNIT OF PARTICLE FEEDER

The drive unit of particle feeder consists of an electric motor and an AC motor variable speed controller which have the following specifications:

Electric motor

Input: 3Ø, 220/380 V, 50 Hz

Power rating: 0.8 HP/0.6 kW

Rotational speed: 1375 rpm

Protection class: KR 80. 1/4 TA III (Made in Germany)

AC speed controller

Controller specification: Simovert P. 6SE2001-1AA00

Input: 1Ø, 220/240 V \pm 10%, 7A, 50-60 Hz

Output: 3Ø, 0-220/240 V, 2.5A, 0-120 Hz

Power rating: 0.7 kVA, motor: 0.5 HP/0.37 kW

Protection class: IEC 529 IP 20

Temperature range: 0-40°C



TABLES

Table 3.1 Physical Characteristics of Solid Particles

Material	Material Code	Particle Size Range (μm)	Average Particle Diameter, d_p (μm)	Apparent Density ρ_p (kg/m^3)	Mixture Density ρ_m (kg/m^3)	Shape
Alumina	A1	45-150	97.5	824.17	2.0229	Spherical
Semolina	S1	250-300	275	579.92	1.7787	Irregular
Semolina	S2	150-250	200	544.51	1.7433	Irregular
Semolina	S3	63-150	106.5	467.75	1.6665	Irregular
Fly Ash	F1	150-300	225	538.47	1.7372	Spherical
Fly Ash	F2	106-150	128	642.72	1.8415	Spherical
Fly Ash	F3	45-106	75.5	750.33	1.9491	Irregular

Table 3.2 Ranges of the experimental variables.

Material Code	Re				M_p/M_a (%)				Local Pressure Measurement Stations (x/D)	Circumferential Pressure Measurement Stations (x/D)
	$\alpha=0^\circ$	$\alpha=10^\circ$	$\alpha=20^\circ$	$\alpha=30^\circ$	$\alpha=0^\circ$	$\alpha=10^\circ$	$\alpha=20^\circ$	$\alpha=30^\circ$		
A1	53000	53000	53000	53000	5,10,15,20	5,10,15	5,10,15	5,10,15	$\alpha=0^\circ$	$\alpha=0^\circ$
	70667	70667	70667	70667	5,10,15,20,25	5,10,15	5,10,15	5,10,15		
	88333	88333	88333	-	5,10,15,20,25	5,10,15,20	5,10,15,20	-		
	98933	98933	-	-	5,10,15,20	5,10,15,20	-	-		
S1	53000	53000	53000	53000	5,10,15,20,25	5,10,15,20	5,10,15,20	5,10,15	$\alpha=10^\circ$	$\alpha=10^\circ$
	70667	70667	70667	70667	5,10,15,20,25	5,10,15	5,10,15	5,10,15		
	88333	88333	88333	-	5,10,15,20	5,10,15,20	5,10,15,20	-		
	98933	98933	-	-	5,10,15,20	5,10,15,20	-	-		
S2	53000	53000	53000	53000	5,10,15,20,25	5,10,15,20	5,10,15,20	5,10,15	$\alpha=20^\circ$	4.25
	70667	70667	70667	70667	5,10,15,20,25	5,10,15,20	5,10,15,20	5,10,15,20		
	88333	88333	88333	-	5,10,15,20	5,10,15,20	5,10,15,20	-		
	98933	98933	-	-	5,10,15,20	5,10,15,20	-	-		
S3	53000	53000	53000	53000	5,10,15,20	5,10,15	5,10,15	5,10,15	$\alpha=30^\circ$	20.83
	70667	70667	70667	70667	5,10,15,20,25	5,10,15,20	5,10,15,20	5,10,15,20		
	88333	88333	88333	-	5,10,15,20	5,10,15,20	5,10,15,20	-		
	98933	98933	-	-	5,10,15,20	5,10,15,20	-	-		
F1	53000	53000	53000	53000	5,10,15,20	5,10,15	5,10,15	5,10,15	3.44	3.77
	70667	70667	70667	70667	5,10,15,20,25	5,10,15,20	5,10,15,20	5,10,15		
	88333	88333	88333	-	5,10,15,20	5,10,15	5,10,15	5,10,15		
	98933	98933	-	-	5,10,15,20	5,10,15,20	-	-		
F2	53000	53000	53000	53000	5,10,15,20	5,10,15	5,10,15	5,10,15	10.47	10.82
	70667	70667	70667	70667	5,10,15,20,25	5,10,15,20	5,10,15,20	5,10,15,20		
	88333	88333	88333	-	5,10,15,20,25	5,10,15,20	5,10,15,20	5,10,15,20		
	98933	98933	-	-	5,10,15,20	5,10,15,20	-	-		
F3	53000	53000	53000	53000	5,10,15,20	5,10,15	5,10,15	5,10,15	17.50	17.87
	70667	70667	70667	70667	5,10,15,20,25	5,10,15,20	5,10,15,20	5,10,15,20		
	88333	88333	88333	-	5,10,15,20,25	5,10,15,20	5,10,15,20	5,10,15,20		
	98933	98933	-	-	5,10,15,20,25	5,10,15,20	5,10,15,20	5,10,15,20		
F3	53000	53000	53000	53000	5,10,15,20,25	5,10,15,20	5,10,15,20	5,10,15	24.45	27.14
	70667	70667	70667	70667	5,10,15,20	5,10,15	5,10,15	5,10,15		
	88333	88333	88333	-	5,10,15,20,25	5,10,15,20	5,10,15,20	5,10,15,20		
	98933	98933	-	-	5,10,15,20,25	5,10,15,20	5,10,15,20	5,10,15,20		
F3	53000	53000	53000	53000	5,10,15,20,25	5,10,15,20	5,10,15,20	5,10,15	31.48	34.19
	70667	70667	70667	70667	5,10,15,20	5,10,15	5,10,15	5,10,15		
	88333	88333	88333	-	5,10,15,20,25	5,10,15,20	5,10,15,20	5,10,15,20		
	98933	98933	-	-	5,10,15,20,25	5,10,15,20	5,10,15,20	5,10,15,20		
F3	53000	53000	53000	53000	5,10,15,20,25	5,10,15,20	5,10,15,20	5,10,15	39.90	39.52
	70667	70667	70667	70667	5,10,15,20	5,10,15	5,10,15	5,10,15		
	88333	88333	88333	-	5,10,15,20,25	5,10,15,20	5,10,15,20	5,10,15,20		
	98933	98933	-	-	5,10,15,20,25	5,10,15,20	5,10,15,20	5,10,15,20		

Table 4.1 Sample $f=f(x/D)$ equations.

Equation	Particle Type	Inclination Angle of The Test Section, α	Re	M_p/M_a (%)	Referred Figure	Data Scattering
$f = -7E-5x/D + 0.0238$	A1	0°	88333	5, 10, 15	4.48.a	±6%
$f = -0.0002x/D + 0.0375$	A1	10°	53000	5, 10, 15	4.34.b	±10%
$f = -0.0002x/D + 0.0404$	A1	20°	53000	5, 10, 15	4.34.c	±5%
$f = -0.0002x/D + 0.0367$	S1	10°	88333	10, 15, 20	4.51	±5%
$f = -0.0002x/D + 0.0373$	S1	20°	70667	5, 10, 15	4.42.c	±10%
$f = -0.0002x/D + 0.0349$	S2	10°	98933	10, 15, 20	4.58	±5%
$f = -0.0002x/D + 0.0423$	S2	20°	53000	5, 10, 15, 20	4.36.c	±10%
$f = -0.0002x/D + 0.0330$	S3	10°	53000	5, 10, 15	4.37.b	±3%
$f = -0.0002x/D + 0.0376$	S3	30°	53000	5, 10, 15	4.37.d	±10%
$f = -0.0001x/D + 0.0291$	F1	10°	53000	5, 10, 15	4.38.b	±10%
$f = -0.0002x/D + 0.0330$	F1	10°	88333	5, 10, 15	4.52	±9%
$f = -0.0002x/D + 0.0341$	F2	10°	53000	5, 10, 15	4.39.b	±5%
$f = -0.0002x/D + 0.0352$	F2	10°	70667	5, 10, 15	4.46.b	±8%
$f = -6E-5x/D + 0.0233$	F3	0°	70667	10, 15, 20, 25	4.47.a	±5%
$f = -0.0002x/D + 0.0356$	F3	30°	53000	5, 10, 15	4.40.d	±4%

Table 4.2 Sample equations concerning S1 and F1 particles.

Equation	Particle Type	Inclination Angle of The Test Section, α	Re	M_p/M_a (%)	Referred Figure
$f_{p+a}/f_a = -0.0007x/D + 1.2065$	S1	0°	53000	5	4.60.a
$f_{p+a}/f_a = -0.0015x/D + 1.4123$	S1	0°	98933	15	4.71.a
$f_{p+a}/f_a = -0.0031x/D + 1.4130$	S1	10°	70667	5	4.63.b
$f_{p+a}/f_a = -0.0048x/D + 1.6883$	S1	20°	88333	20	4.69.c
$f_{p+a}/f_a = -0.0049x/D + 1.8122$	S1	30°	53000	10	4.61.d
$f_{p+a}/f_a = -0.0019x/D + 1.4055$	F1	0°	53000	15	4.62.a
$f_{p+a}/f_a = -0.0067x/D + 1.7915$	F1	10°	70667	20	4.66.b
$f_{p+a}/f_a = -0.0065x/D + 1.7548$	F1	10°	98933	15	4.71.b
$f_{p+a}/f_a = -0.0055x/D + 1.7861$	F1	20°	88333	15	4.68.c
$f_{p+a}/f_a = -0.0030x/D + 1.5452$	F1	30°	53000	5	4.60.d



FIGURES

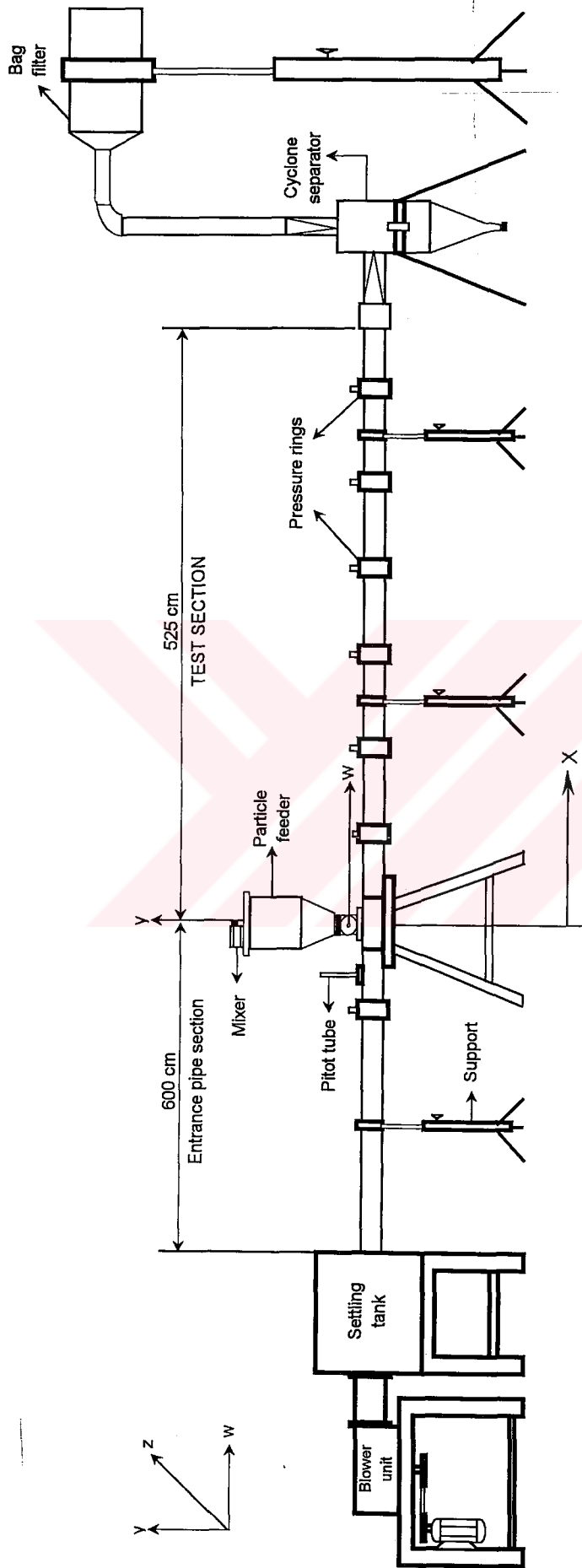


Figure 3.1 Sketch of set-up with horizontal test section.

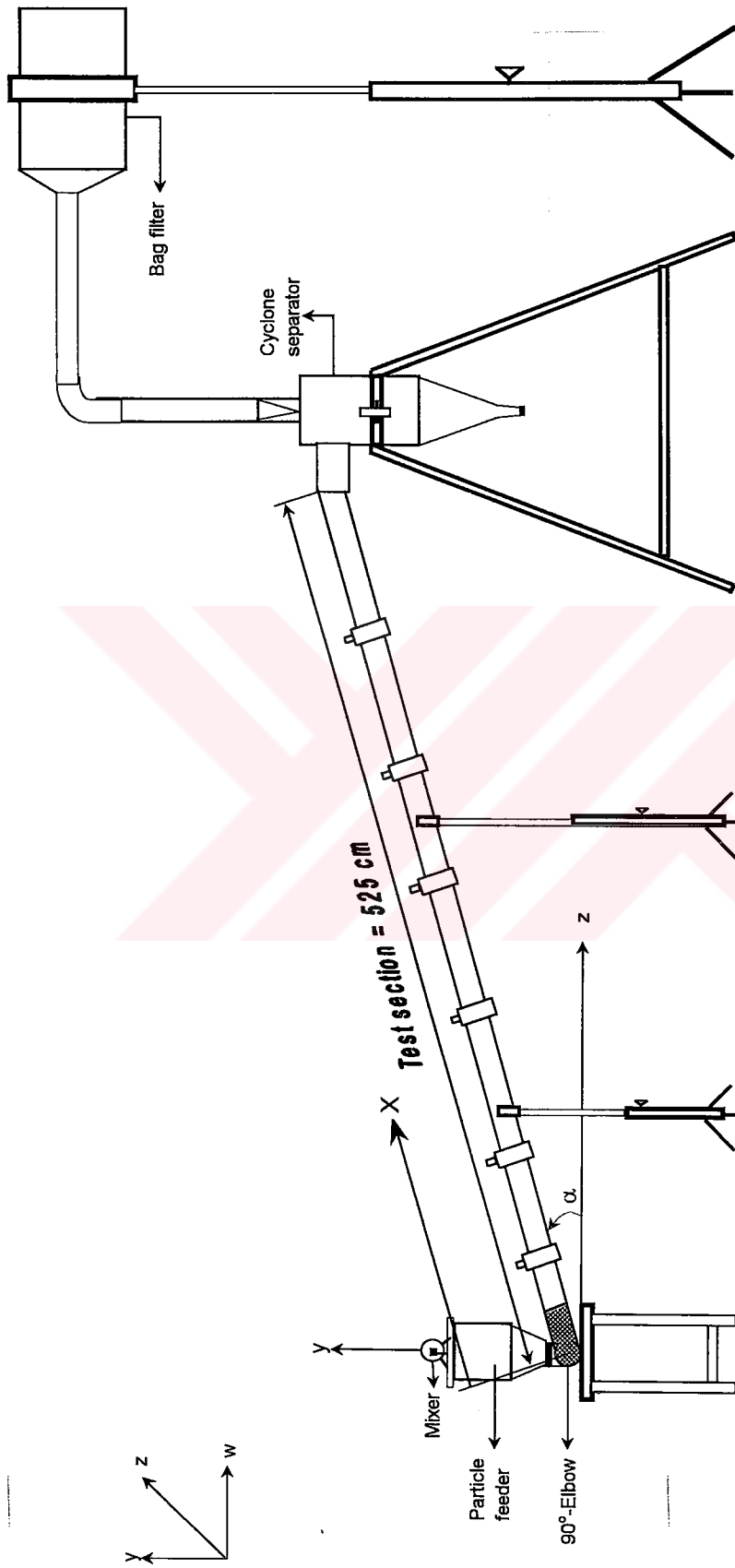


Figure 3.2 Sketch of set-up with inclined test section.

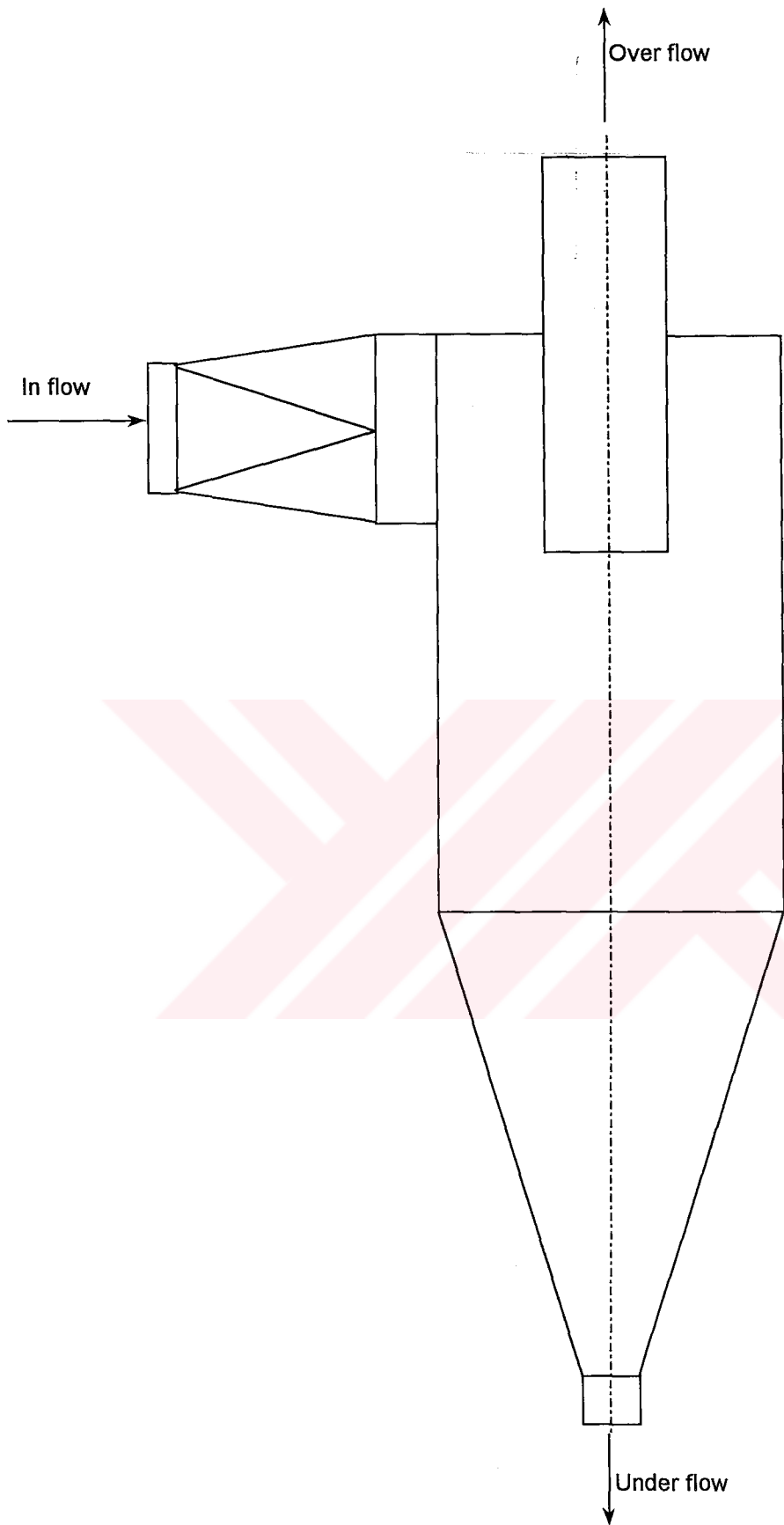


Figure 3.3 A section view of the cyclone separator.

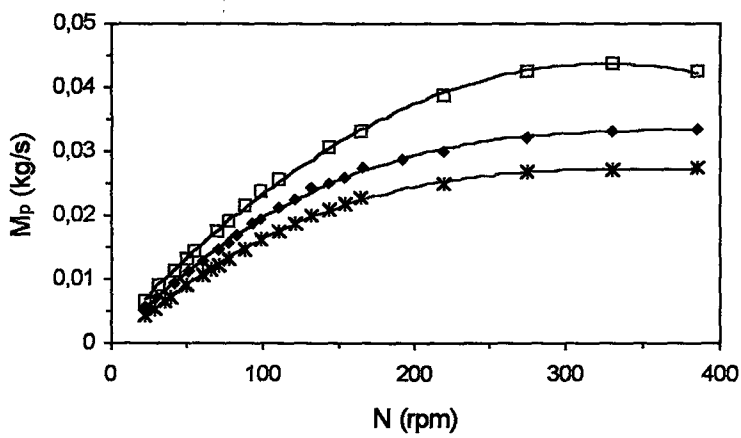
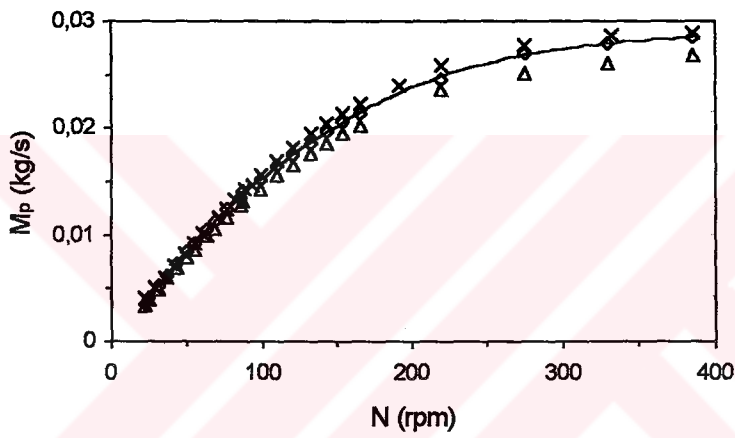
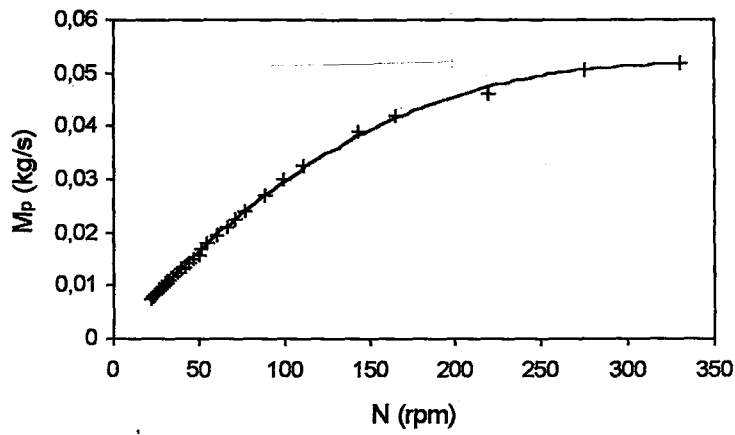


Figure 3.4 Calibration curves of the particle feeder wheel.

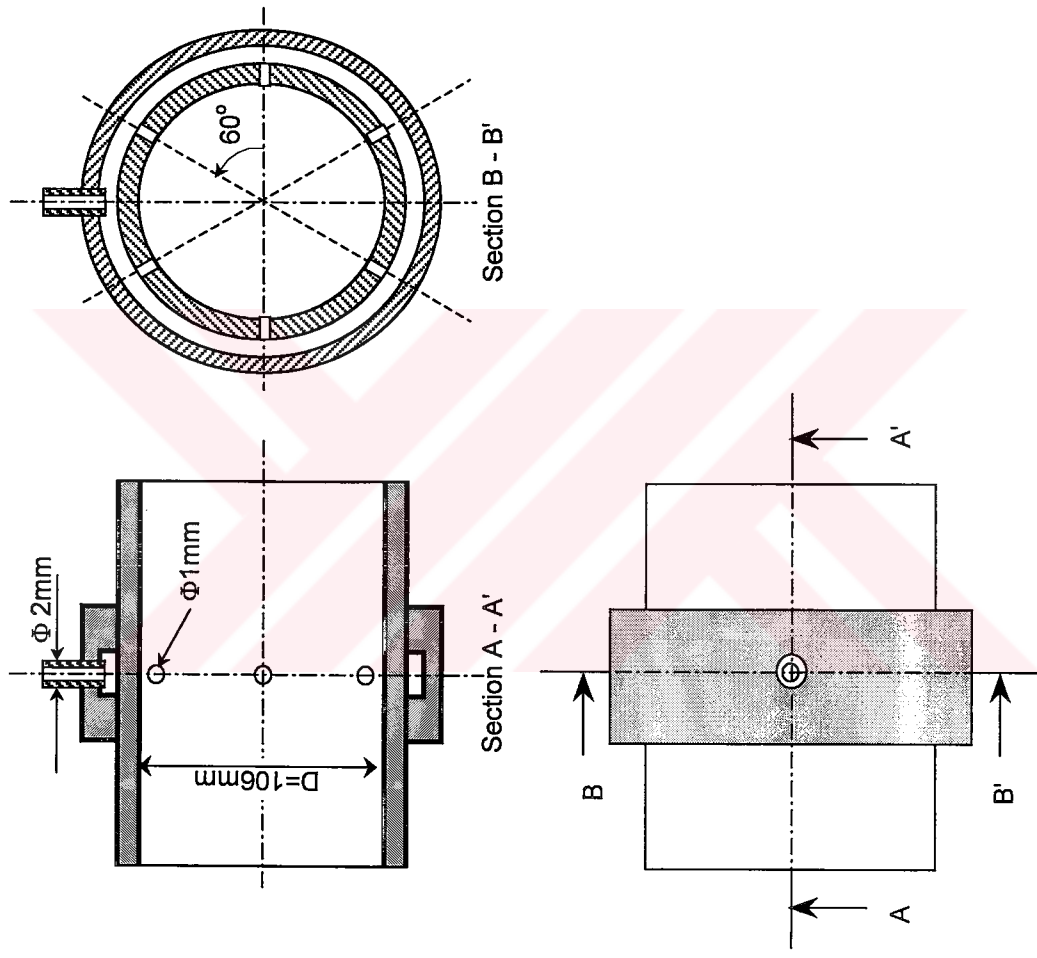


Figure 3.5 Pressure ring used for local static pressure measurement.

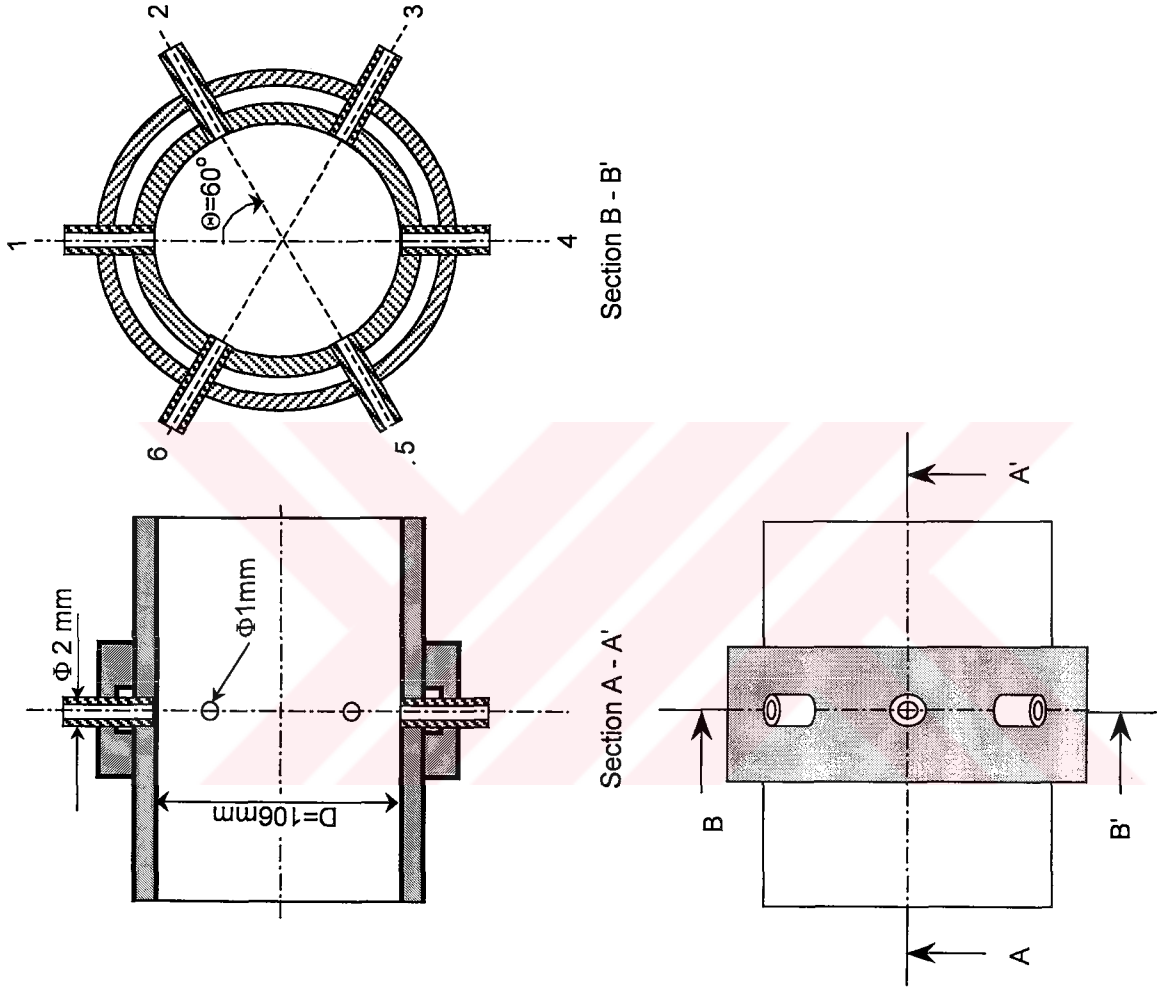


Figure 3.6 Pressure ring used for circumferential pressure measurement.

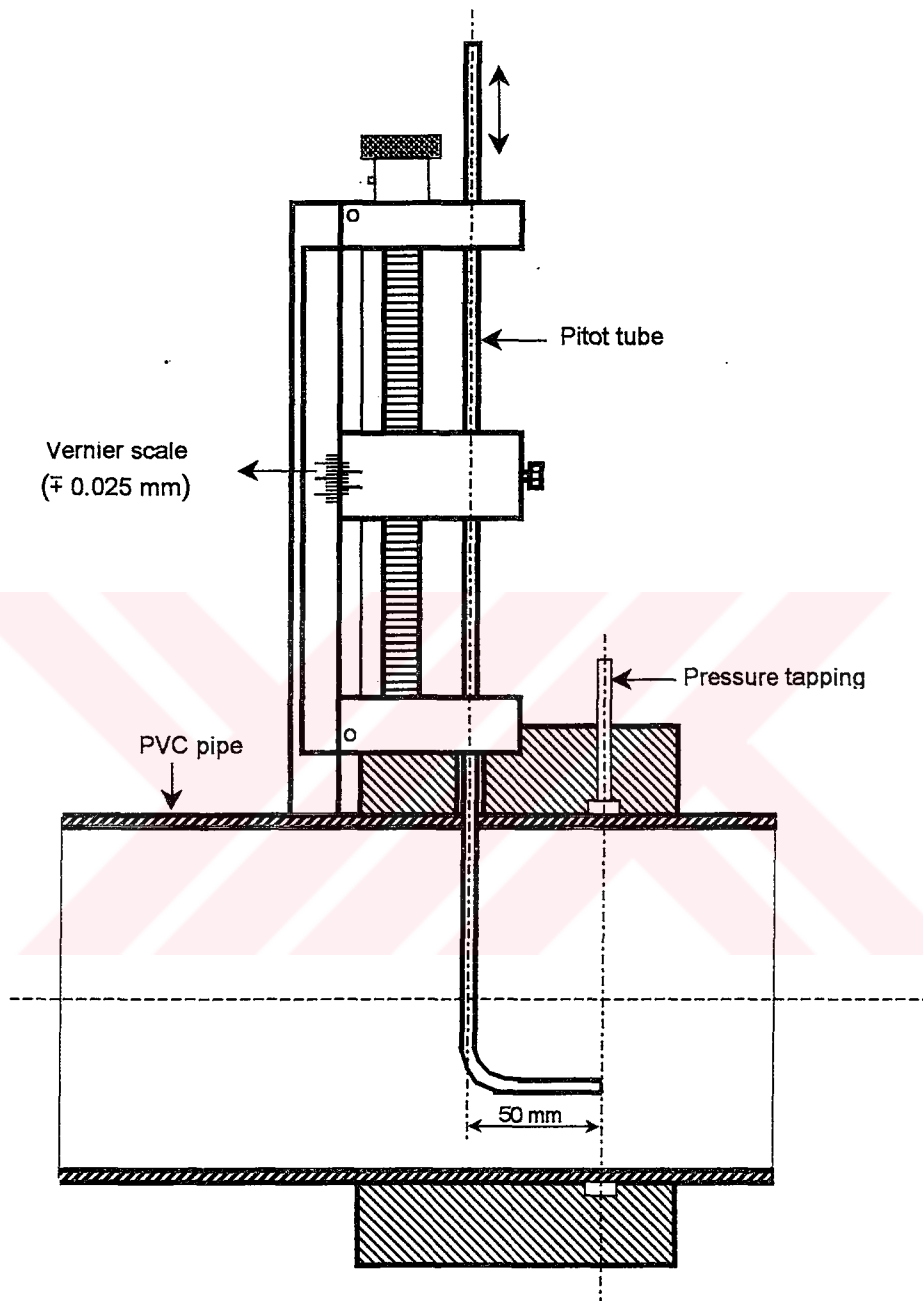


Figure 3.7 Pitot tube and traverse mechanism.

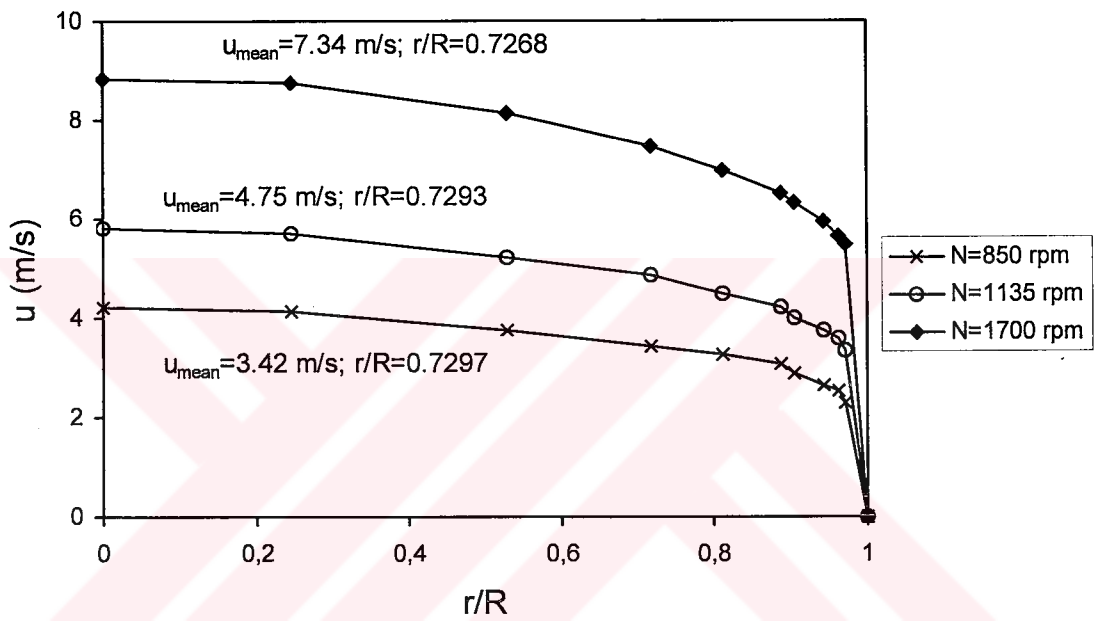


Figure 3.8 Velocity profiles for calibration of pitot tube at different rotational speeds of the blower unit.

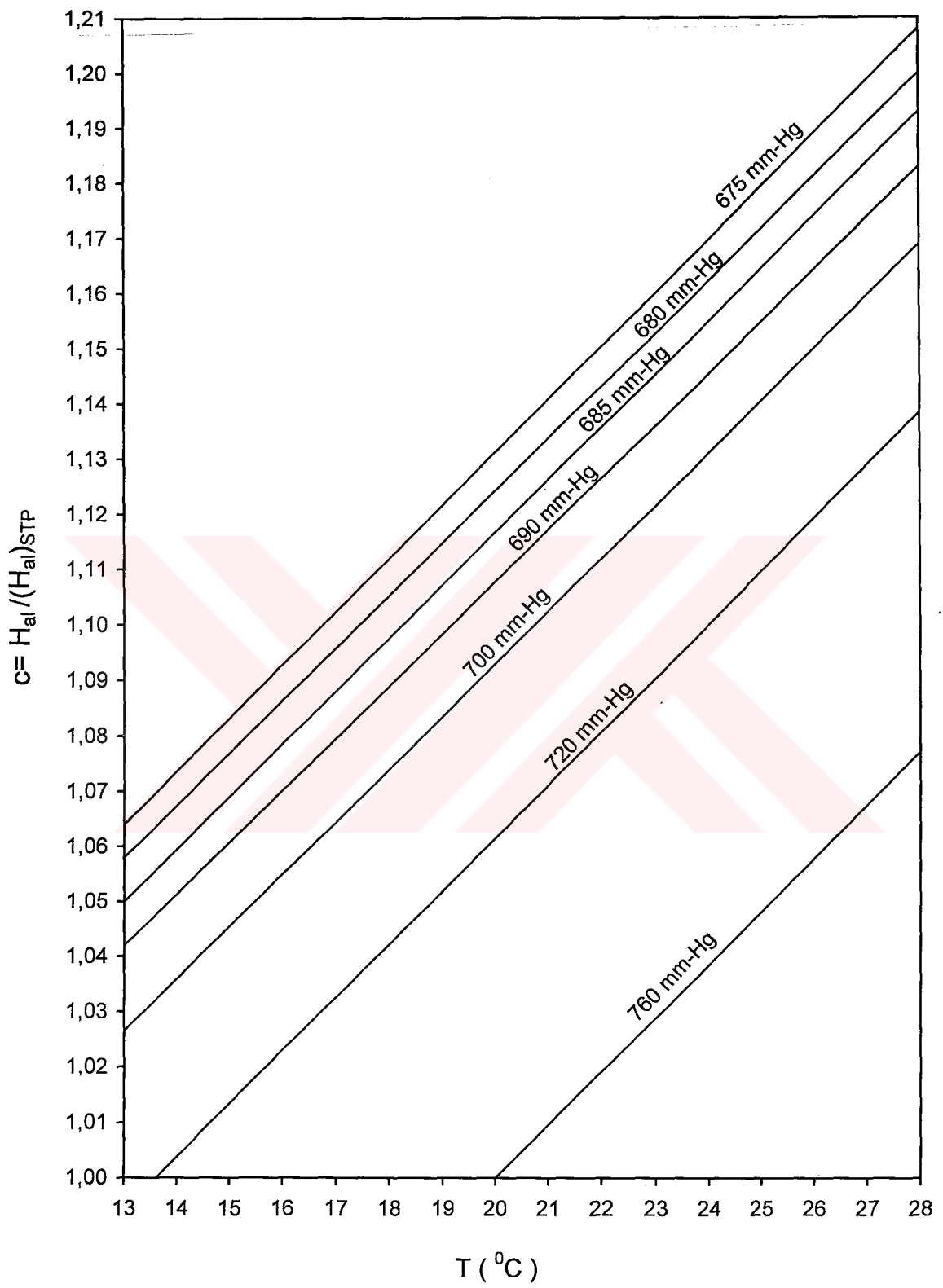
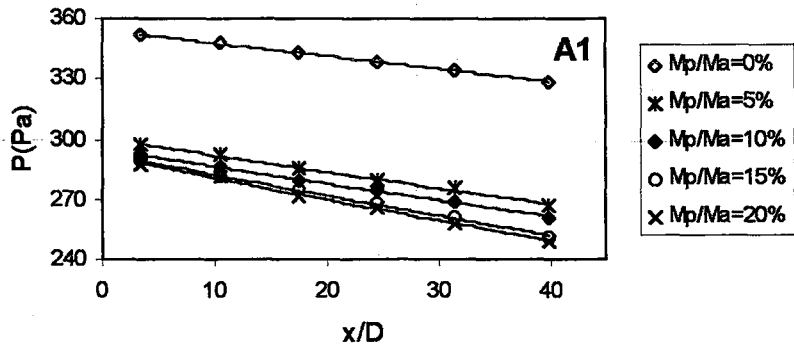
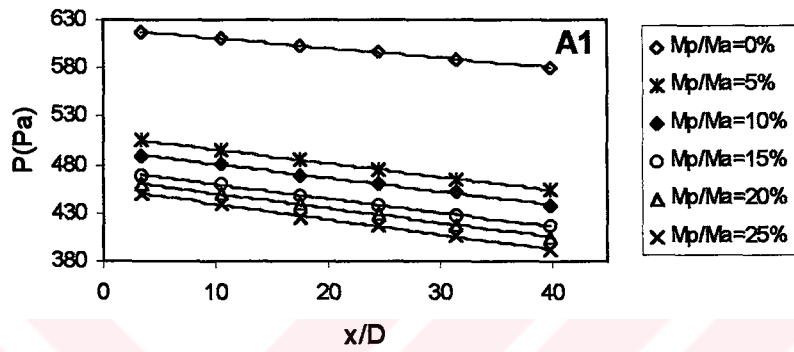


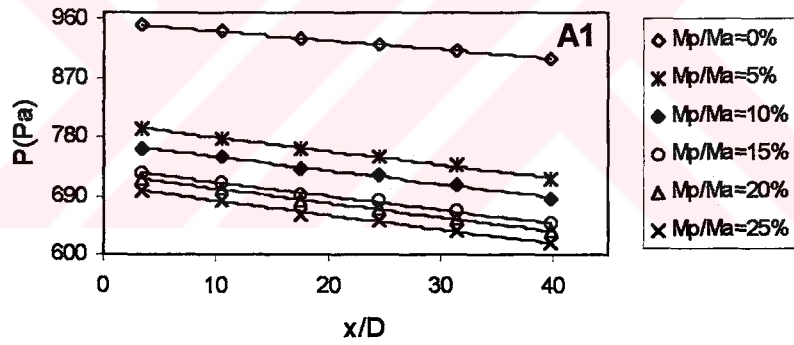
Figure 3.9 Correction Chart for the Head of Alcohol



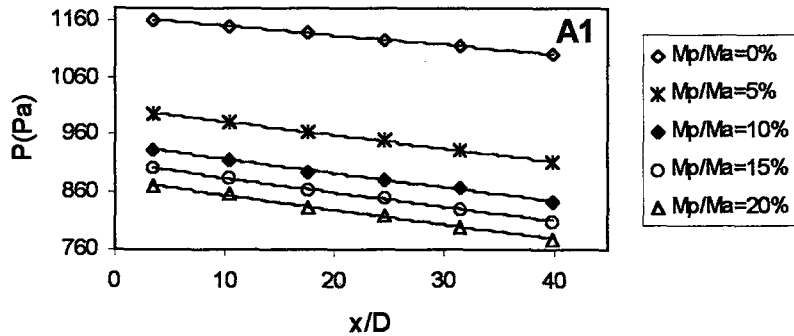
a) $Re=53000$



b) $Re=70667$



c) $Re=88333$



d) $Re=98933$

Figure 4.1.a, b, c, d Variation of pressure with x/D for A1 at different Re numbers along horizontal line.

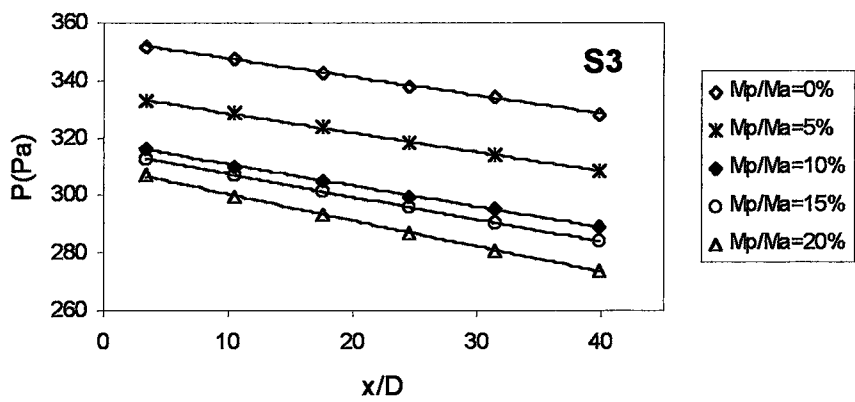
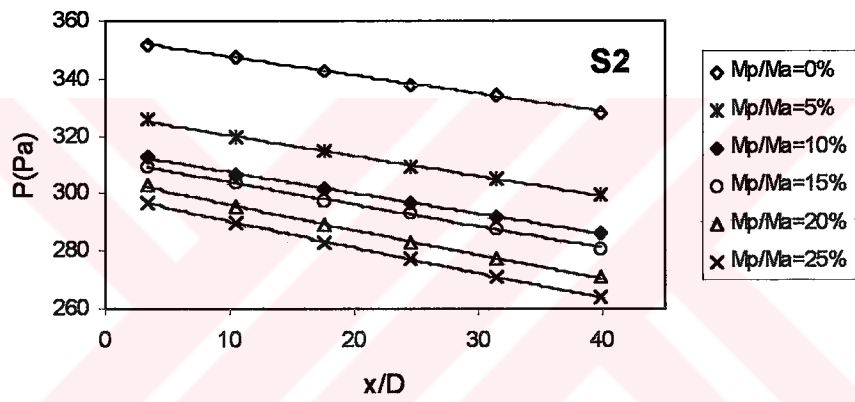
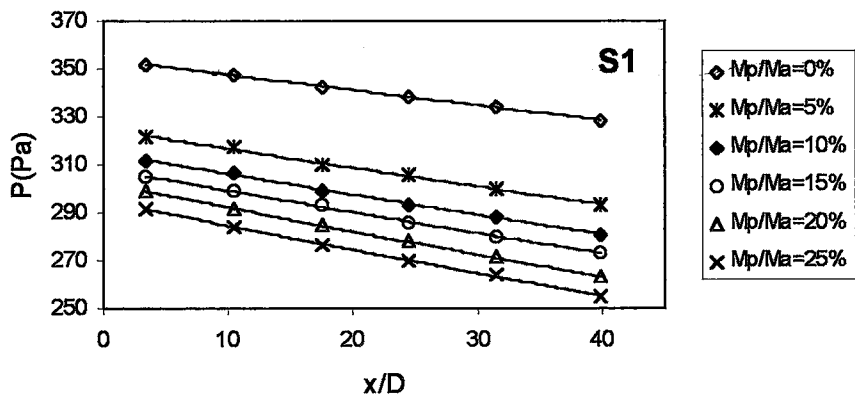


Figure 4.2 Variation of pressure with x/D for S1, S2, S3 at $Re=53000$ along horizontal line.

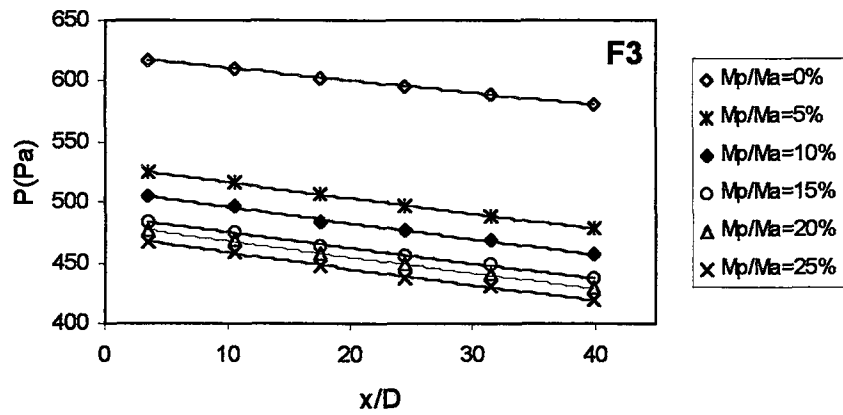
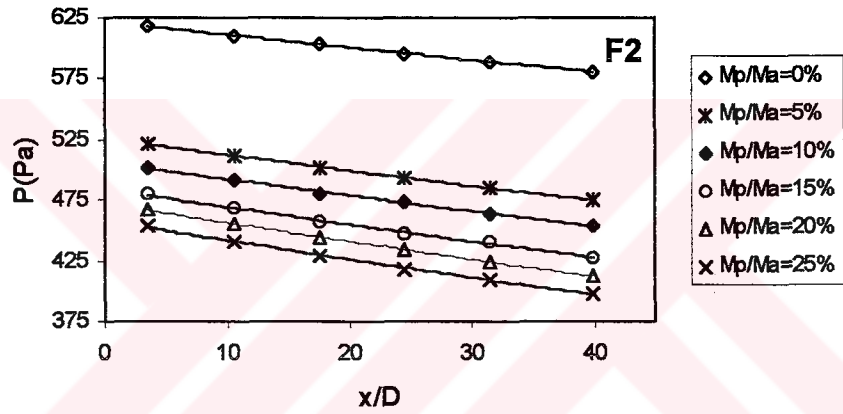
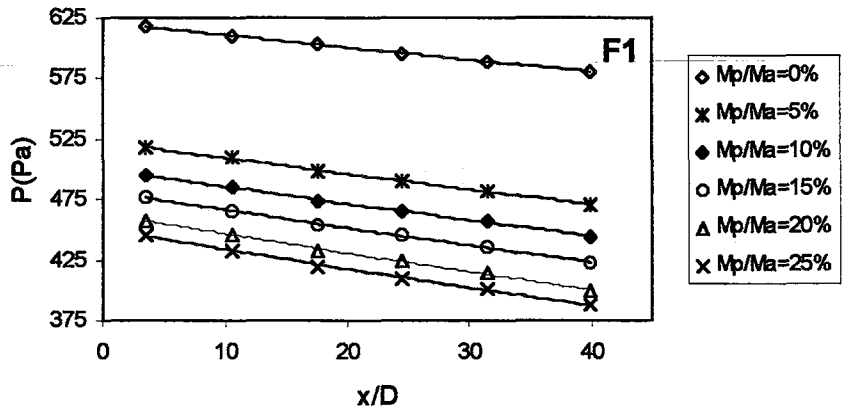


Figure 4.3 Variation of pressure with x/D for F1, F2, F3 at $Re=70667$ along horizontal line.

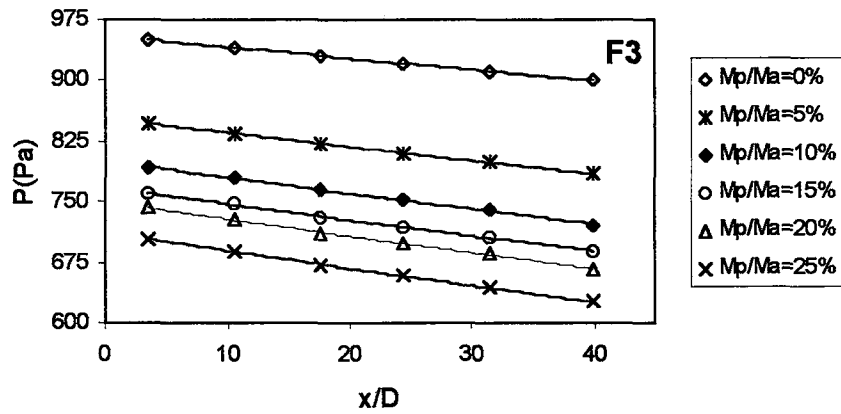
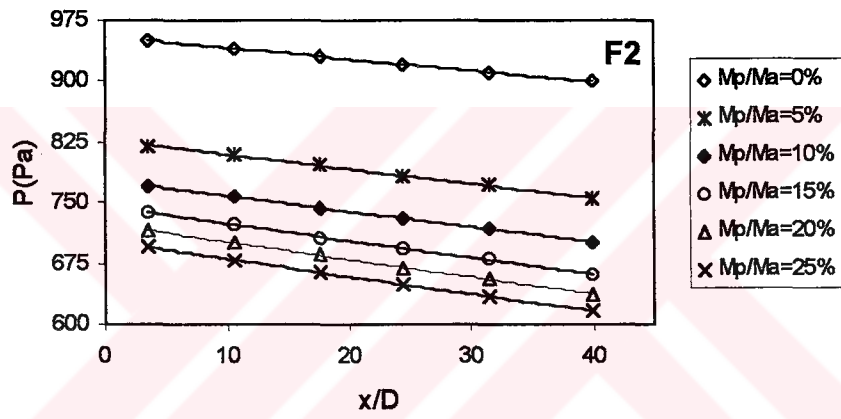
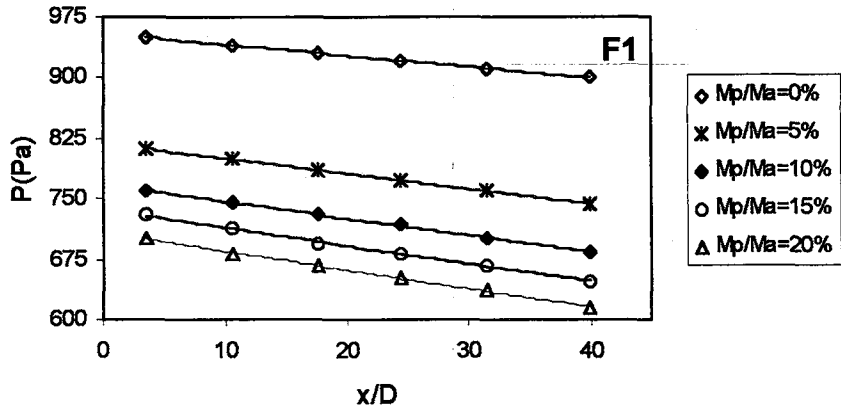
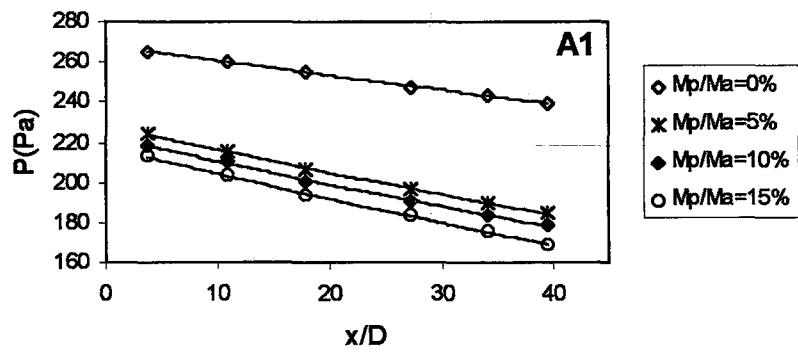
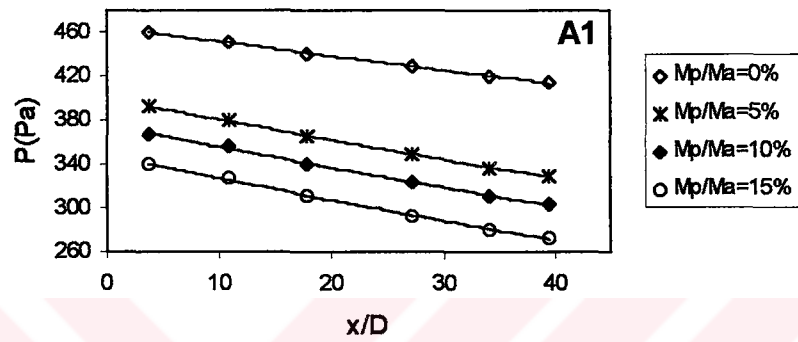


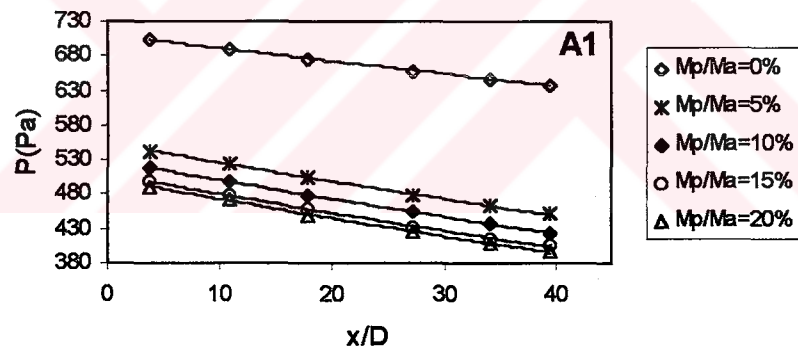
Figure 4.4: Variation of pressure with x/D for F1, F2, F3 at $Re=88333$ along horizontal line.



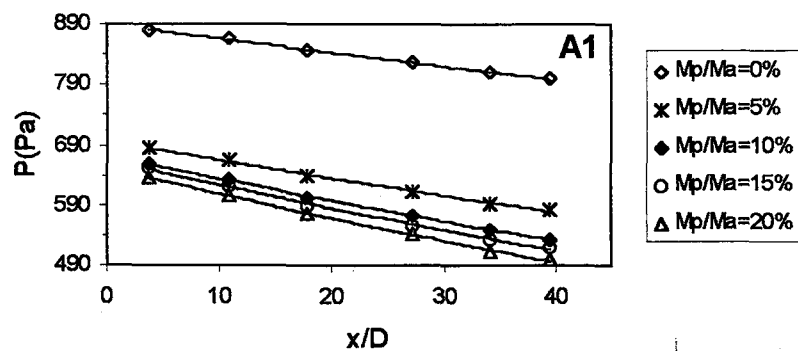
a) $Re=53000$



b) $Re=70667$



c) $Re=88333$



d) 98933

Figure 4.5. a, b, c, d Variation of pressure with x/D for A1 at different Re numbers along inclined line, $\alpha=10^\circ$.

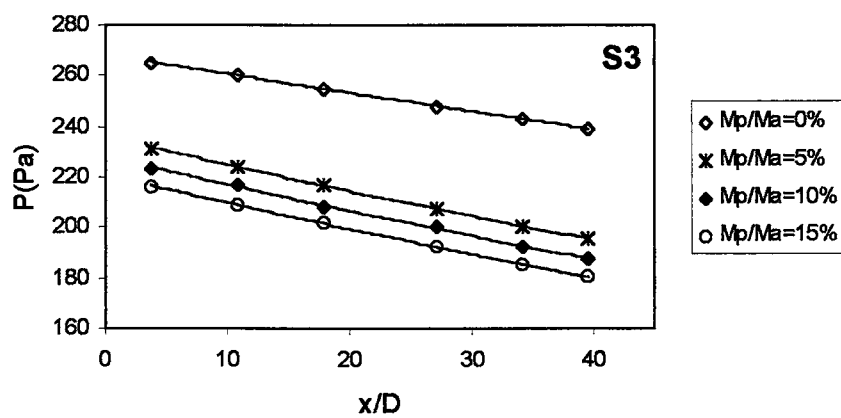
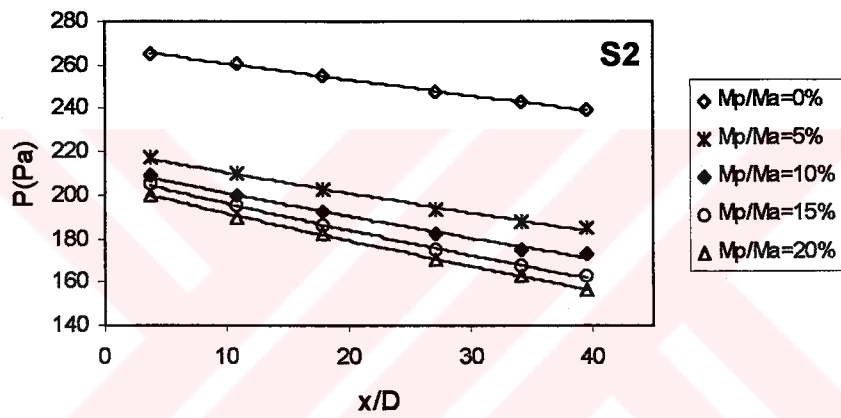
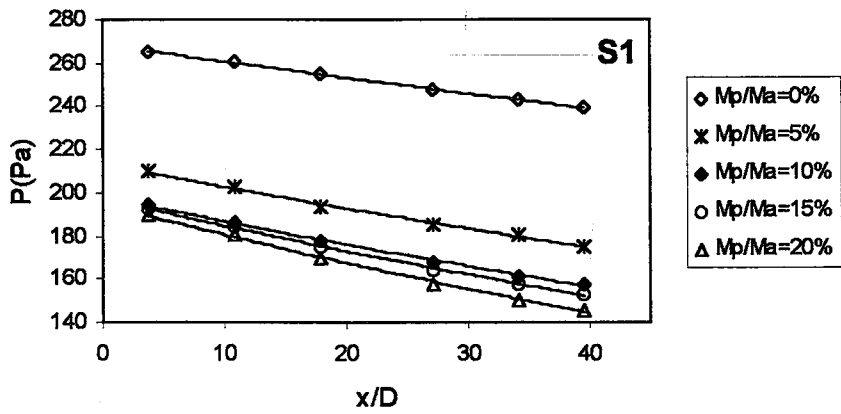


Figure 4.6 Variation of pressure with x/D for S1, S2, S3 at $Re=53000$ along inclined line, $\alpha=10^\circ$.

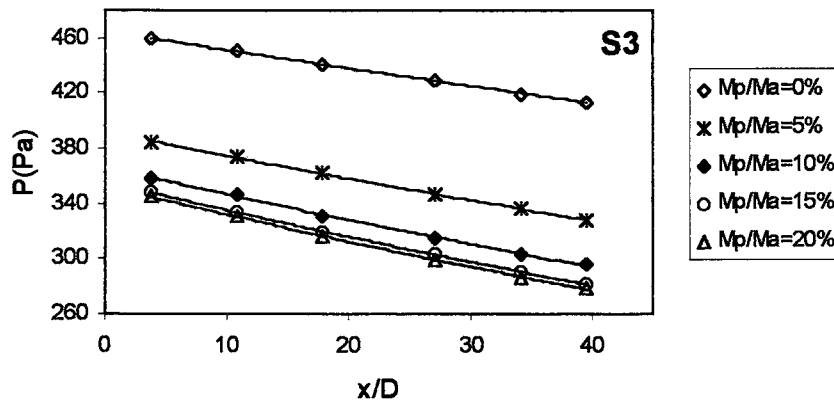
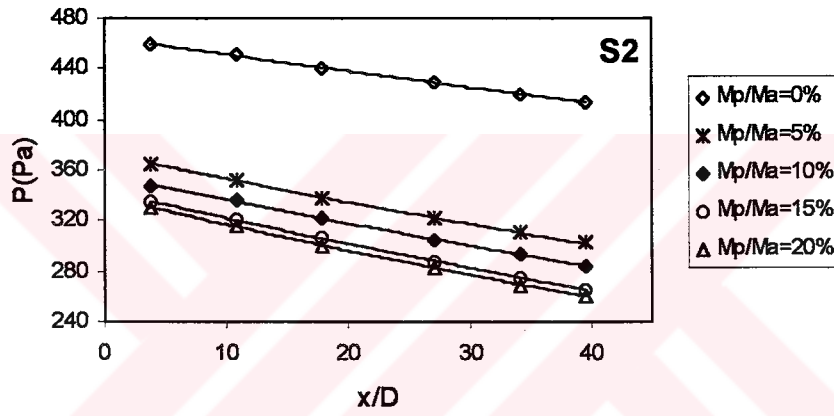
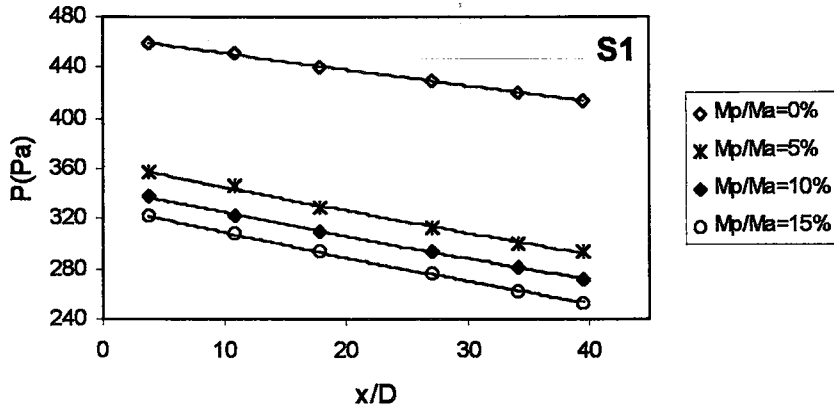


Figure 4.7 Variation of pressure with x/D for S1, S2, S3 at $Re=70667$ along inclined line, $\alpha=10^\circ$.

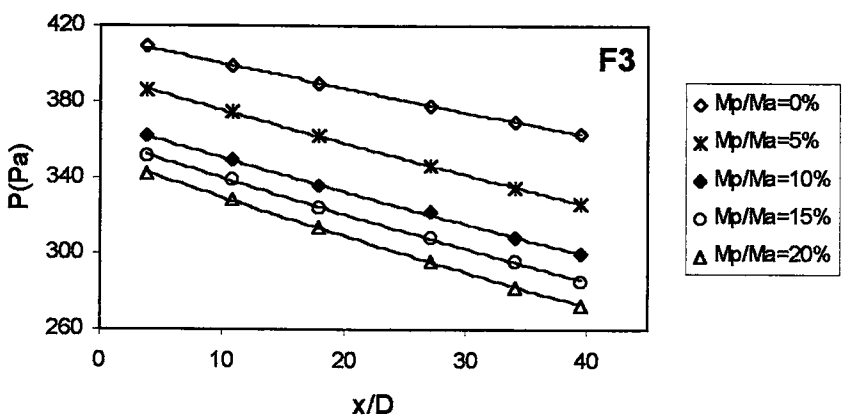
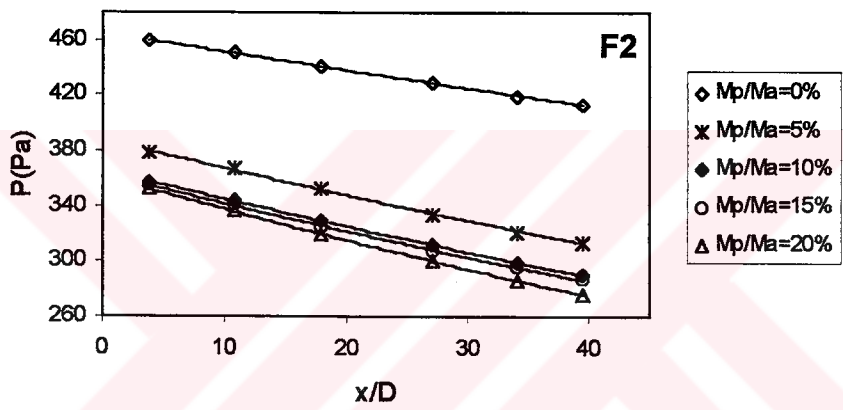
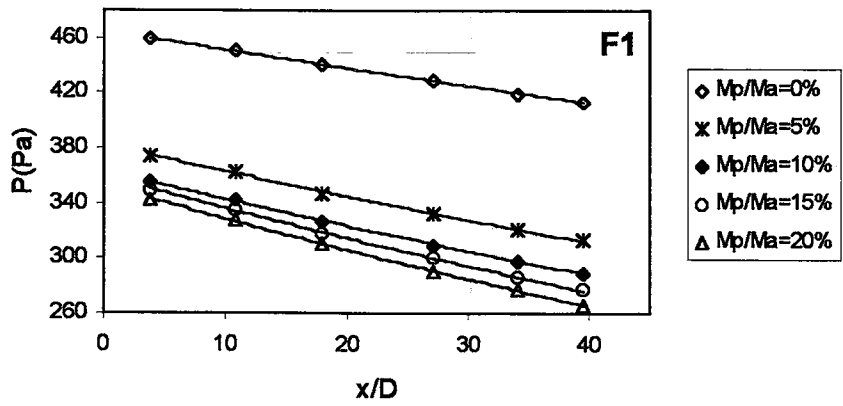


Figure 4.8 Variation of pressure with x/D for F1, F2, F3 at $Re=70667$ along inclined line, $\alpha=10^\circ$.

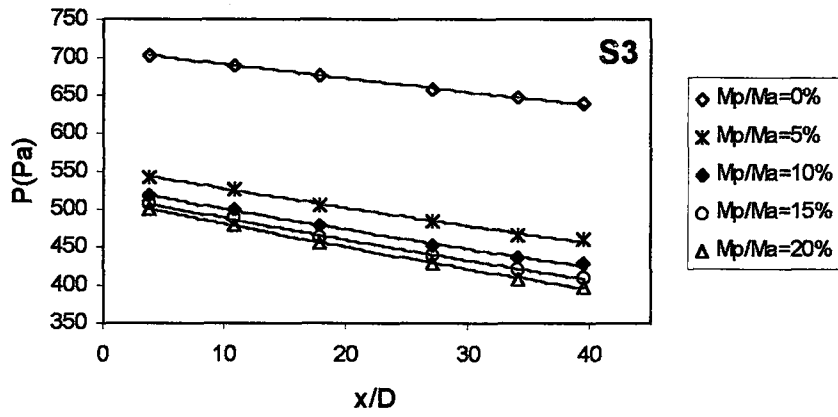
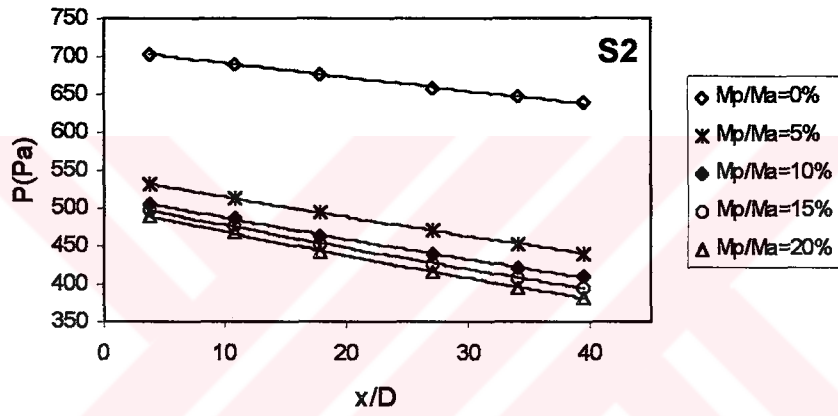
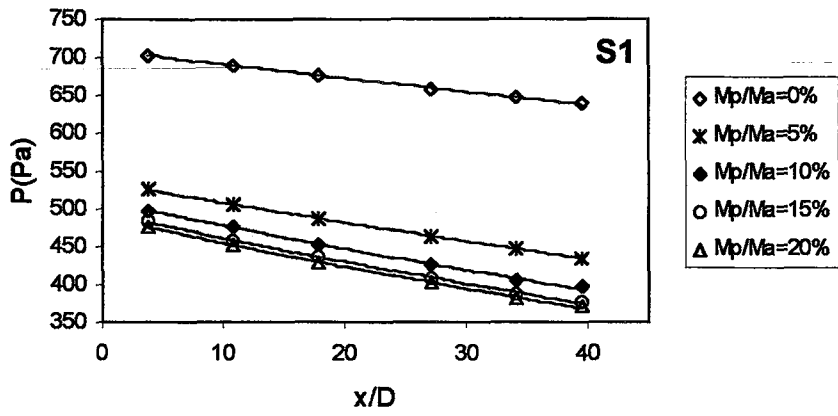
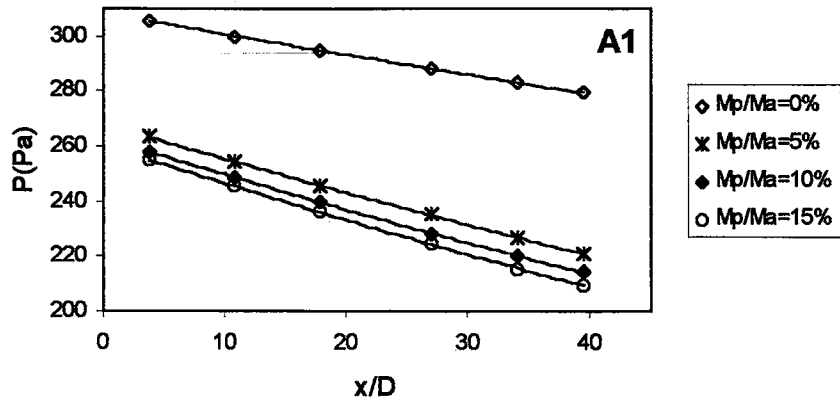
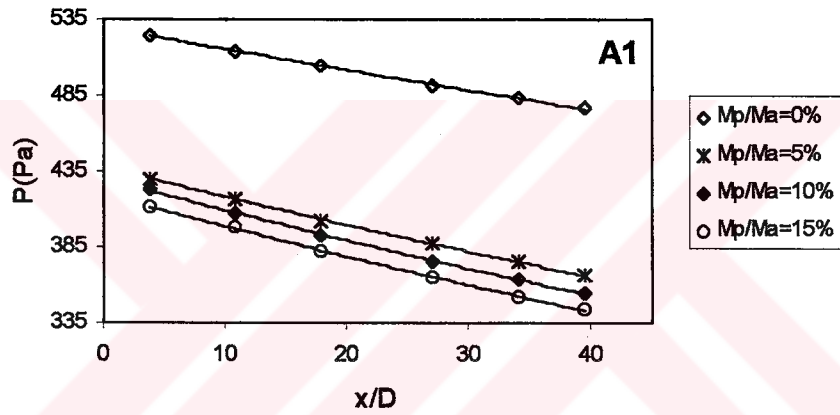


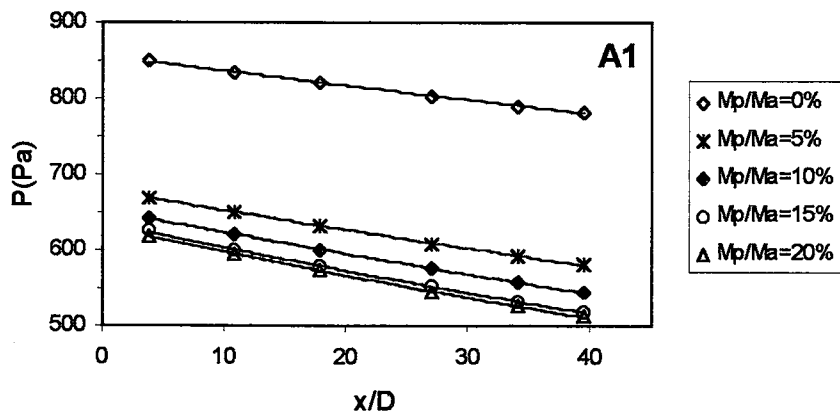
Figure 4.9 Variation of pressure with x/D for S1, S2, S3 at $Re=88333$ along inclined line, $\alpha=10^\circ$.



a) Re=53000



b) Re=70667



c) Re=88333

Figure 4.10.a, b, c Variation of pressure with x / D for A1 at different Re numbers along inclined line, $\alpha=20^\circ$.

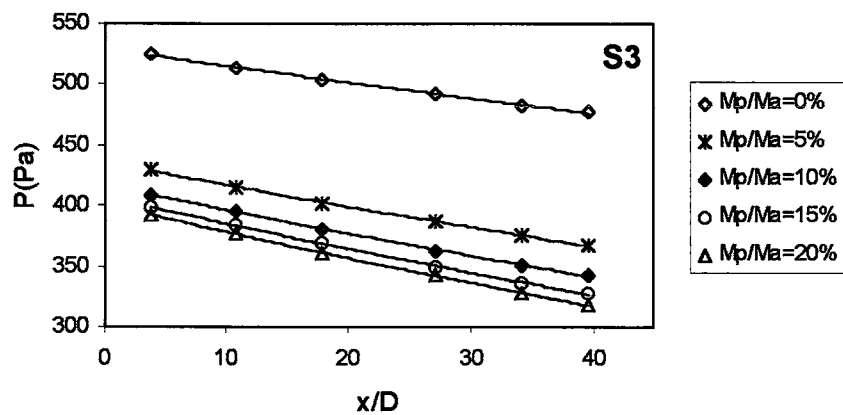
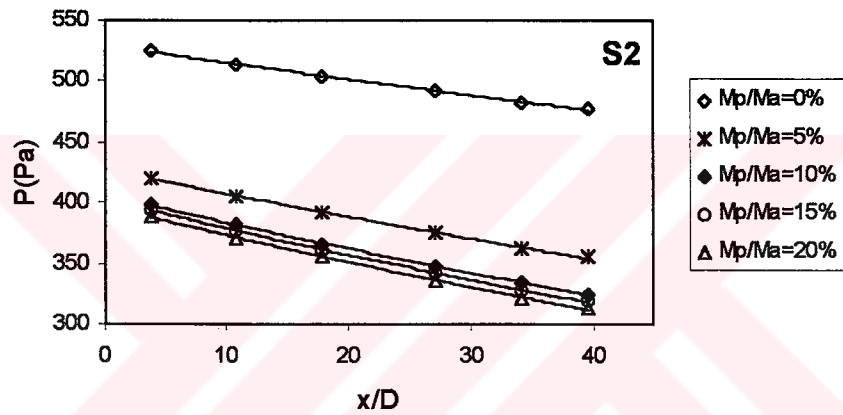
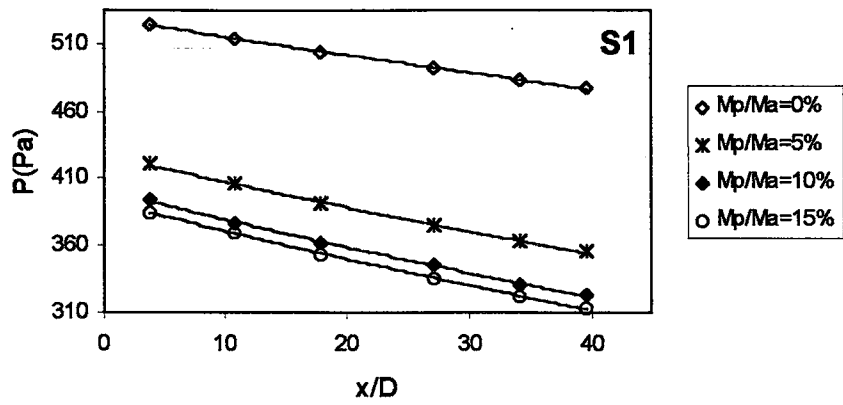


Figure 4.11 Variation of pressure with x/D for S1, S2, S3 at $Re=70667$ along inclined line, $\alpha=20^\circ$.

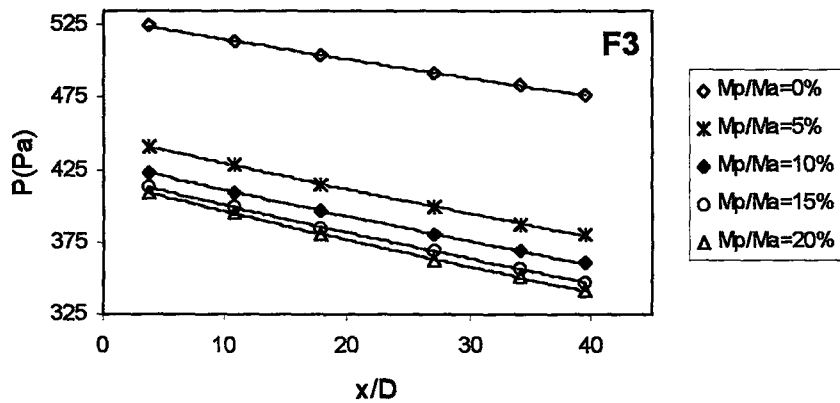
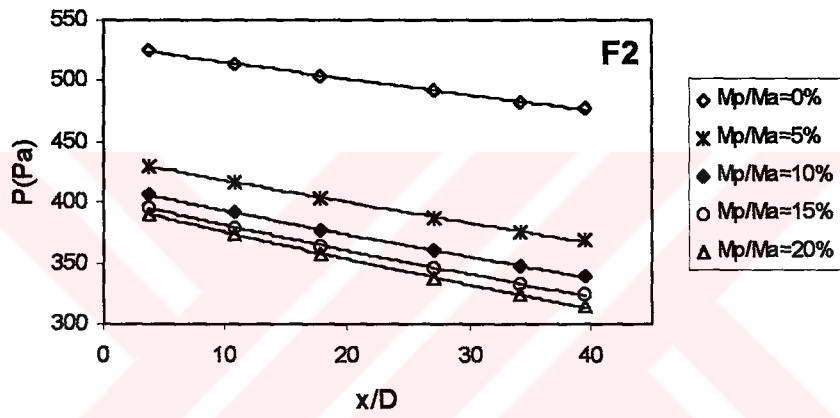
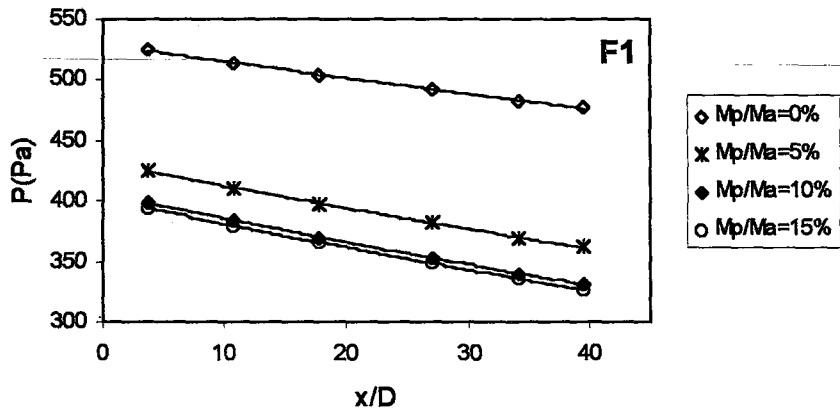


Figure 4.12 Variation of pressure with x/D for F1, F2, F3 at $Re=70667$ along inclined line $\alpha=20^\circ$.

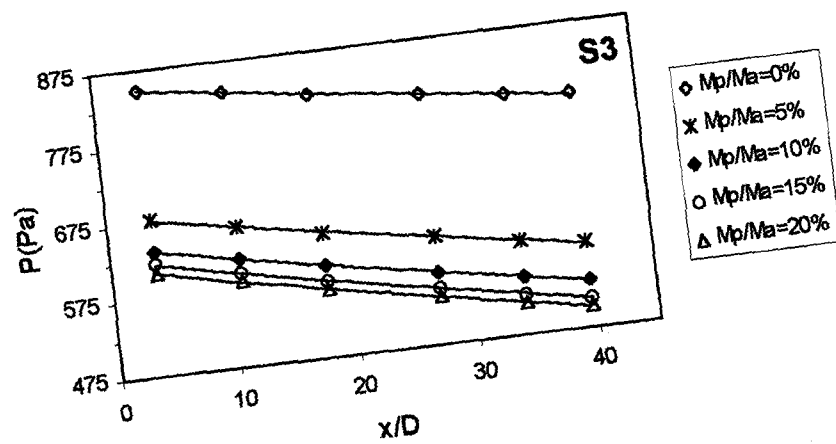
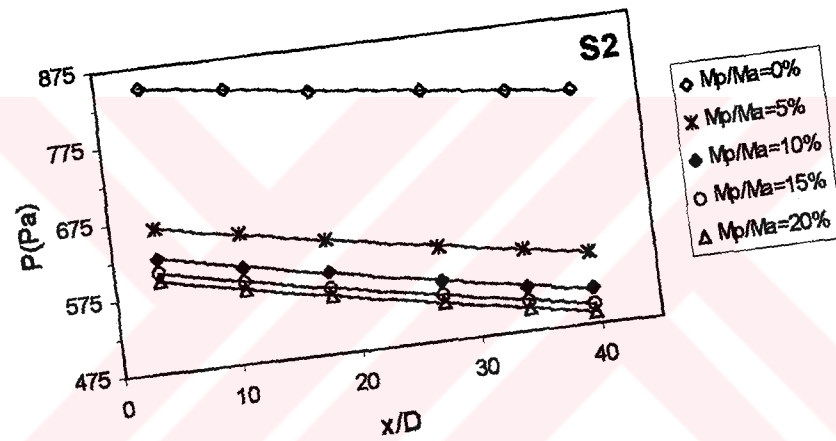
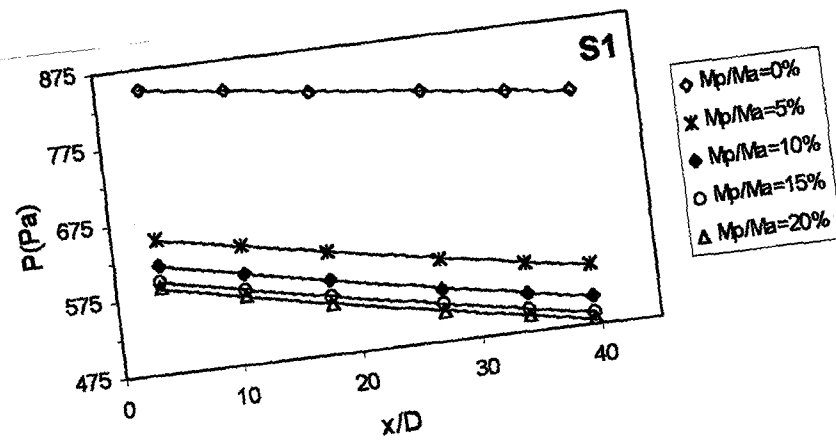
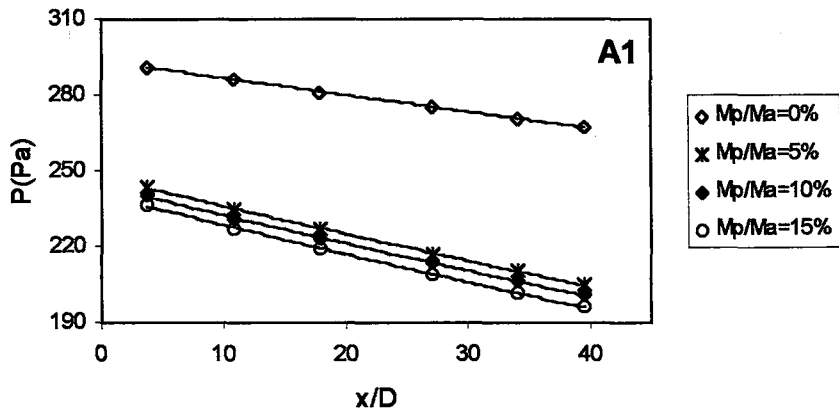
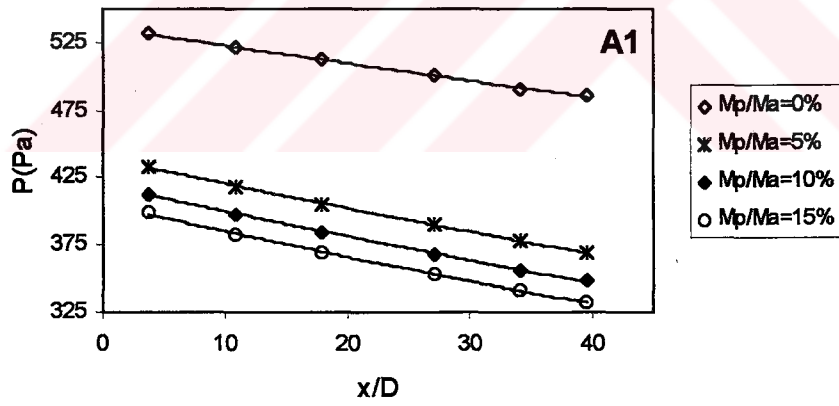


Figure 4.13 Variation of pressure with x/D for S1, S2, S3 at $Re=88333$ along inclined line, $\alpha=20^\circ$.



a) $Re=53000$



b) $Re=70667$

Figure 4.14.a, b Variation of pressure with x/D for A1 at different Re numbers along inclined line, $\alpha=30^\circ$.

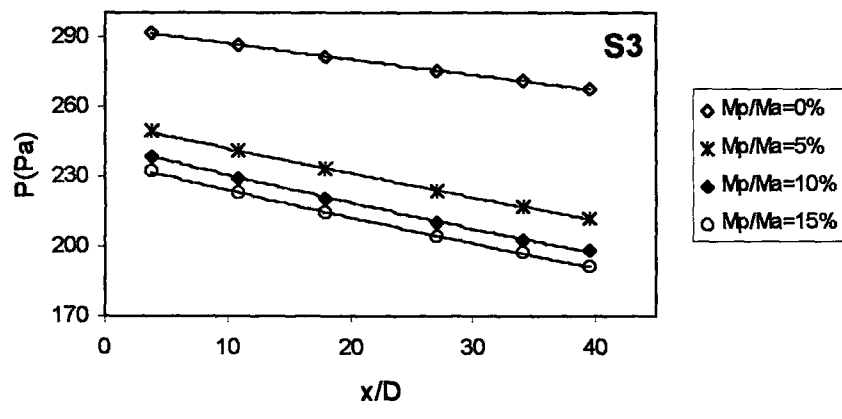
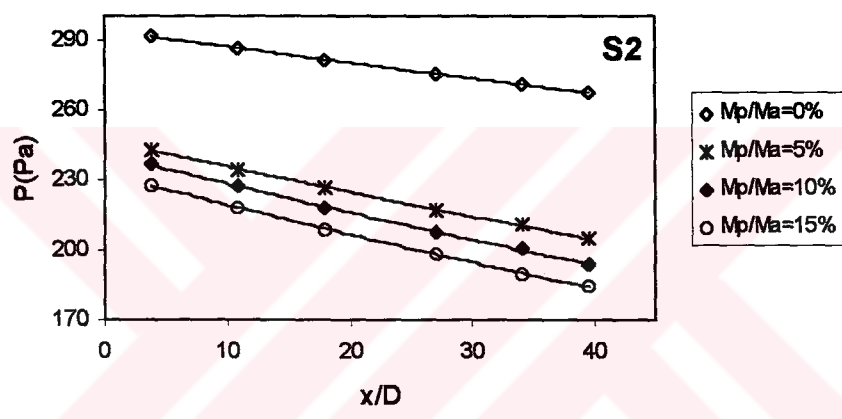
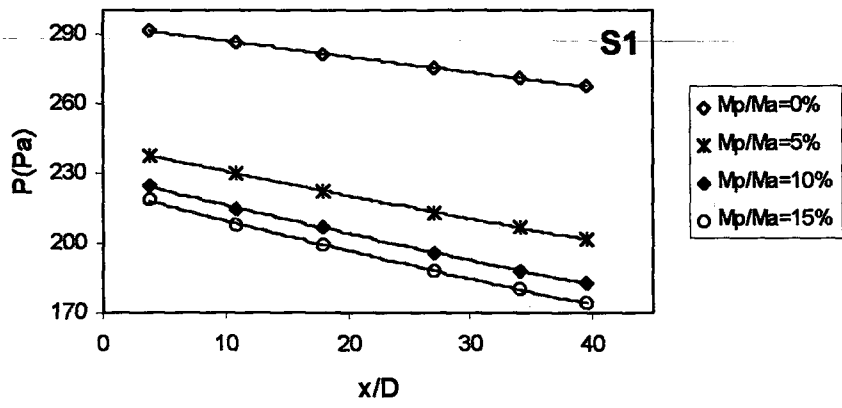


Figure 4.15 Variation of pressure with x/D for S1, S2, S3 at $Re=53000$ along inclined line, $\alpha=30^\circ$.

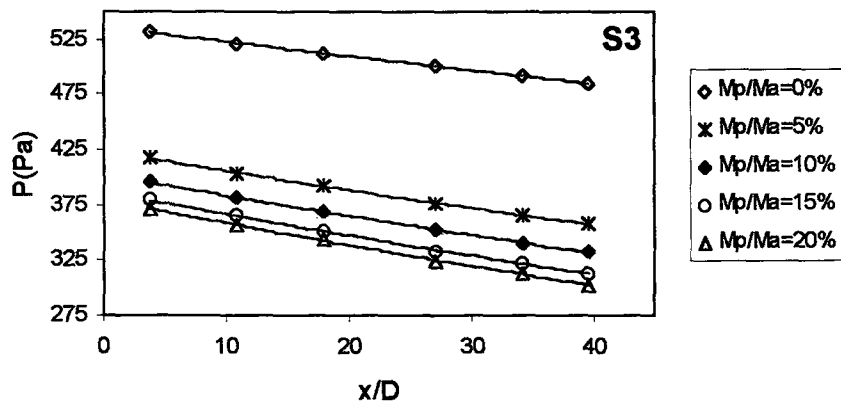
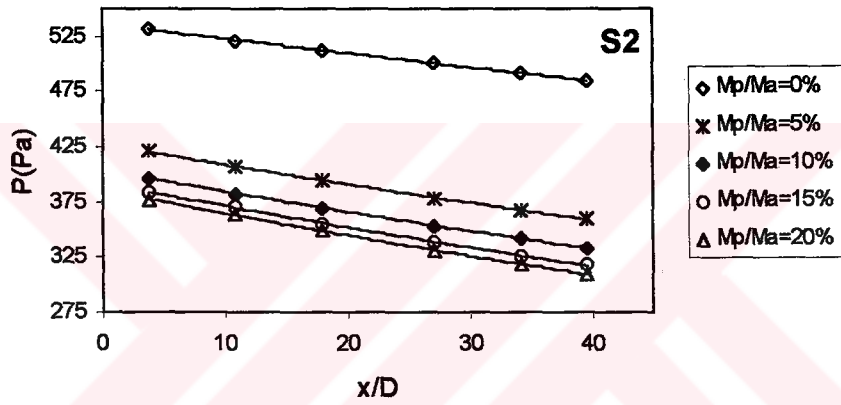
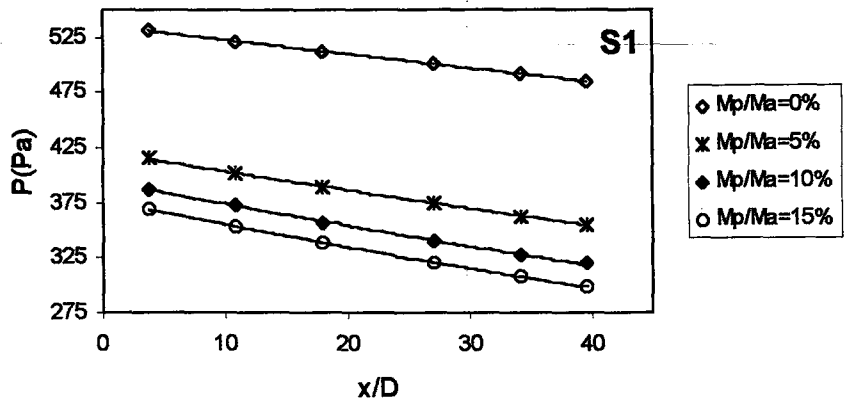


Figure 4.16 Variation of pressure with x/D for S1, S2, S3 at $Re=70667$ along inclined line, $\alpha=30^\circ$.

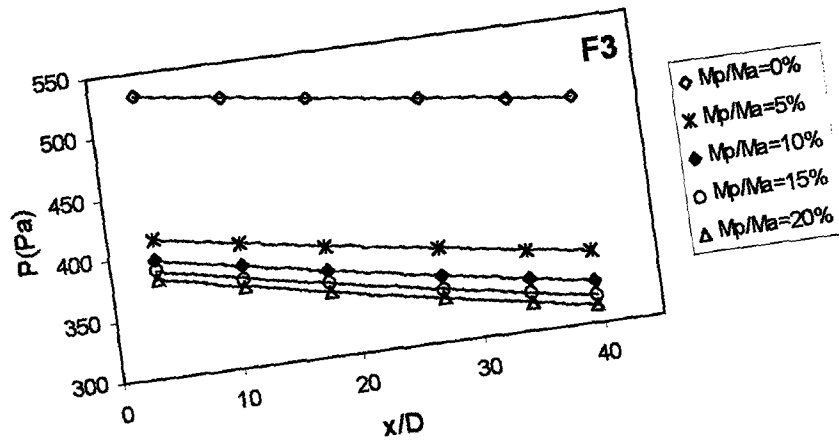
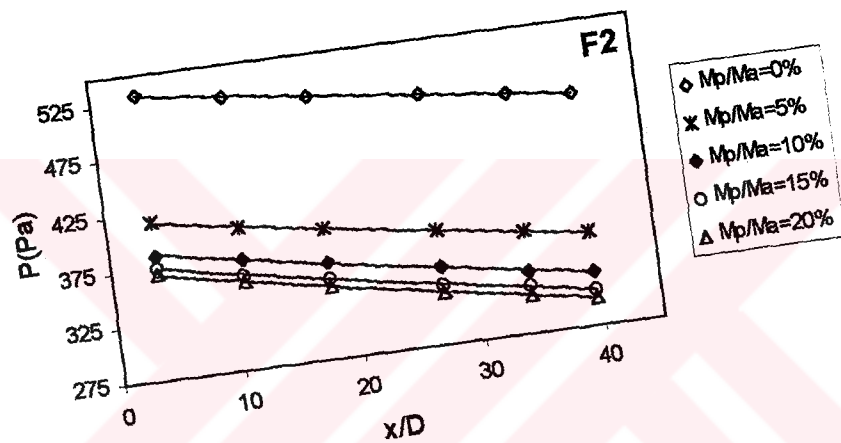
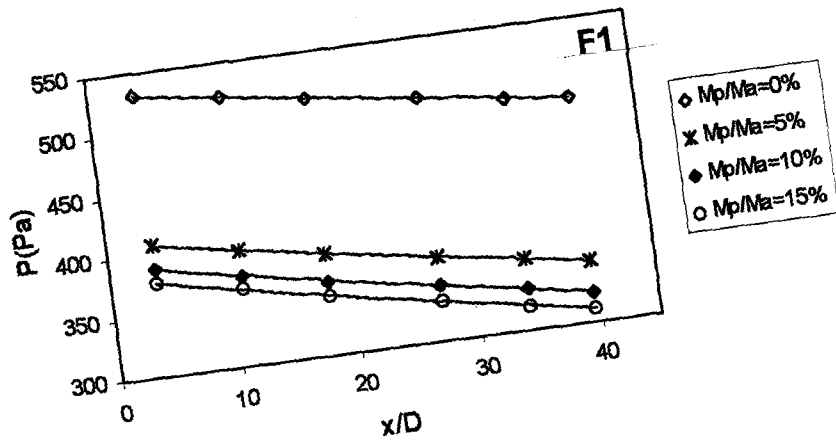


Figure 4.17 Variation of pressure with x/D for F1, F2, F3 at $Re=70667$ along inclined line, $\alpha=30^\circ$.

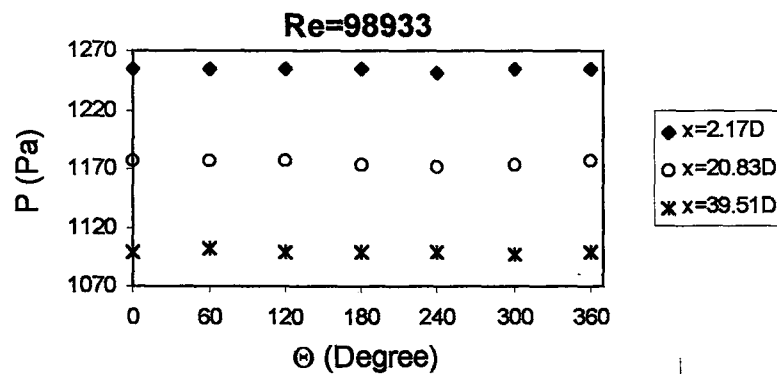
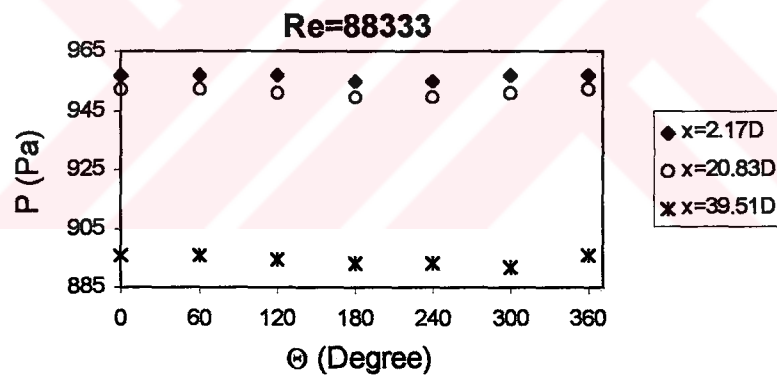
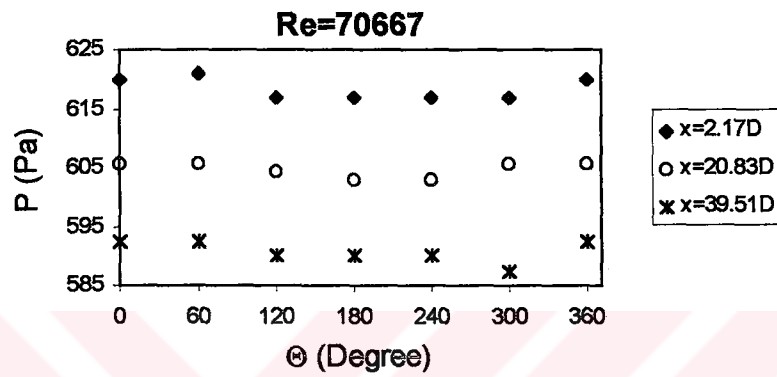
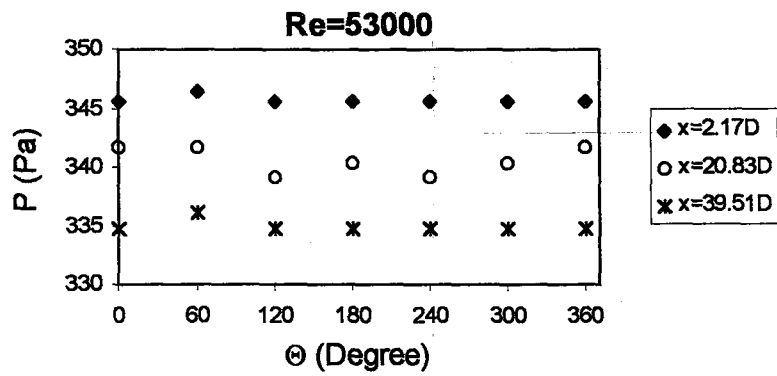


Figure 4.18 Variation of circumferential pressure with Θ for $M_p/M_a=0\%$ at different Re numbers along horizontal line, $\alpha=0^\circ$.

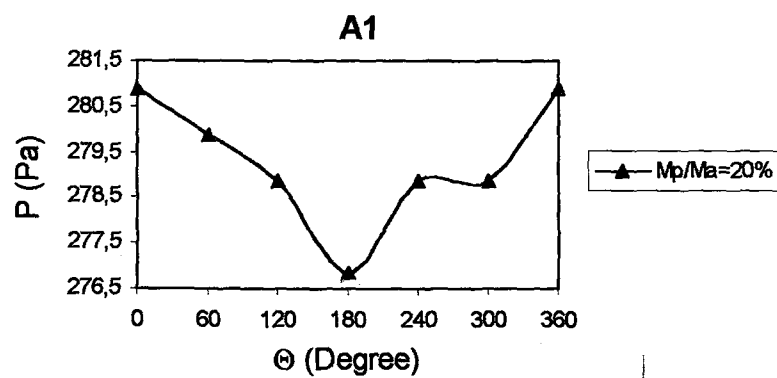
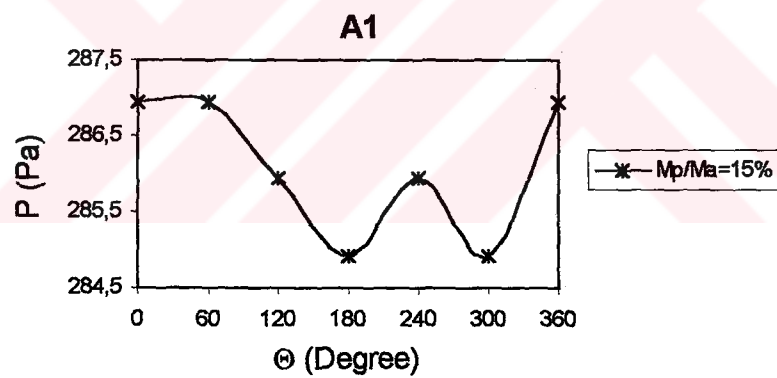
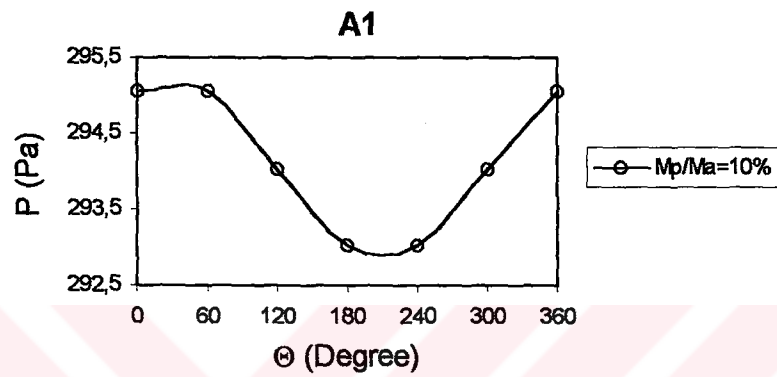
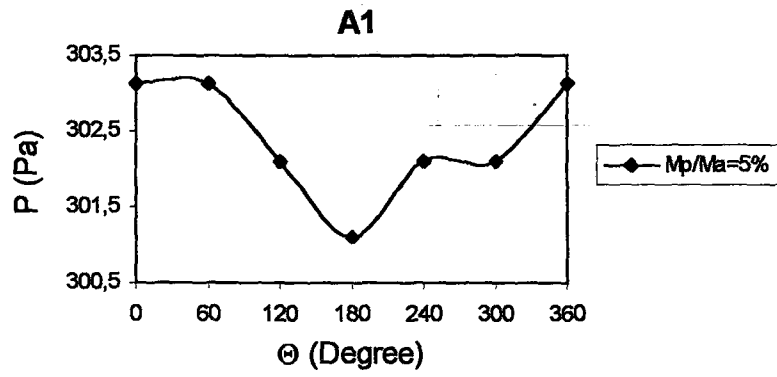


Figure 4.19 Variation of circumferential pressure with Θ for A1 at $x=2.17D$ and $Re=53000$ along horizontal line, $\alpha=0^\circ$.

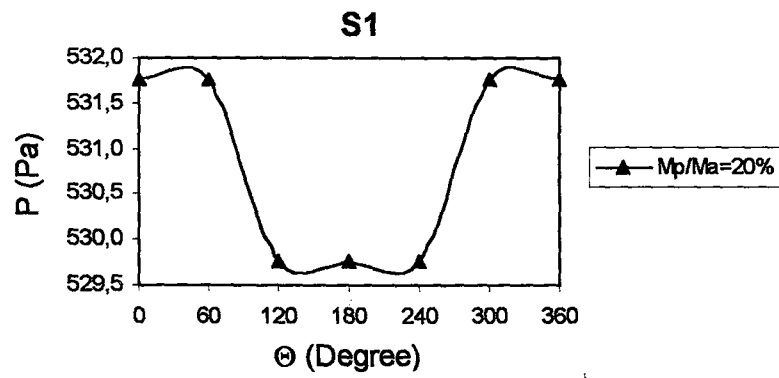
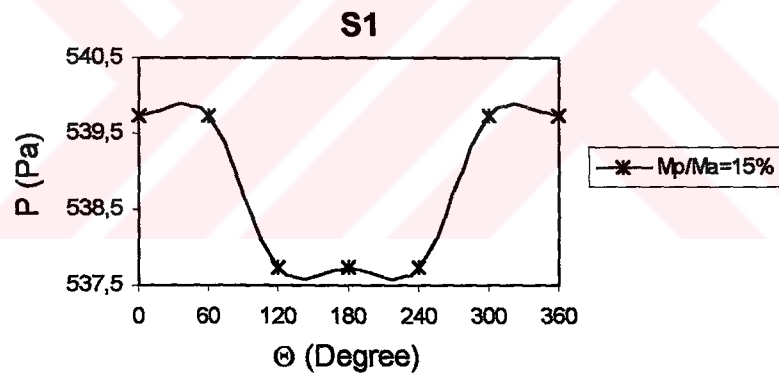
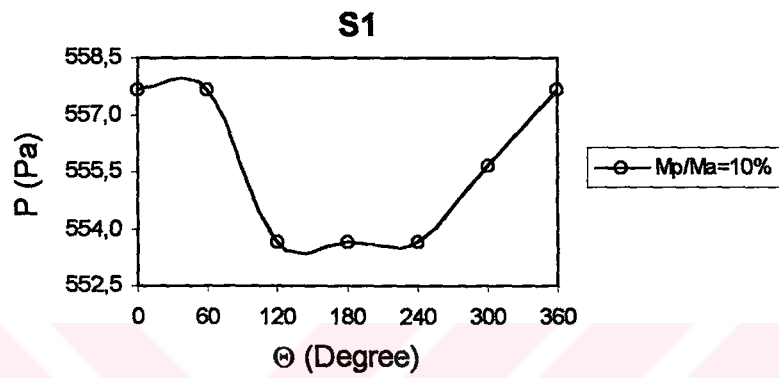
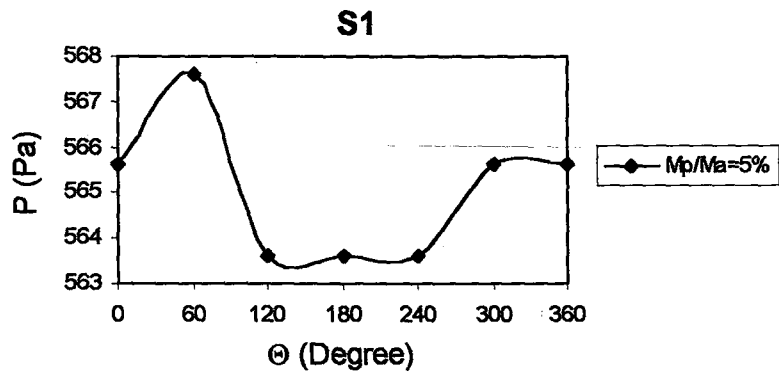


Figure 4.20 Variation of circumferential pressure with Θ for S1 at $x=2.17D$ and $Re=70667$ along horizontal line, $\alpha=0^\circ$.

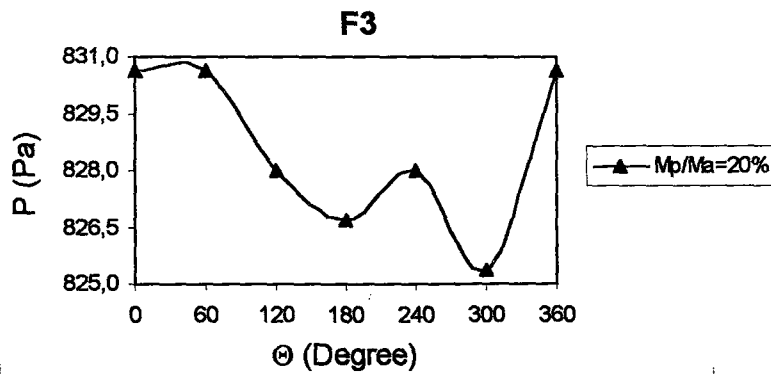
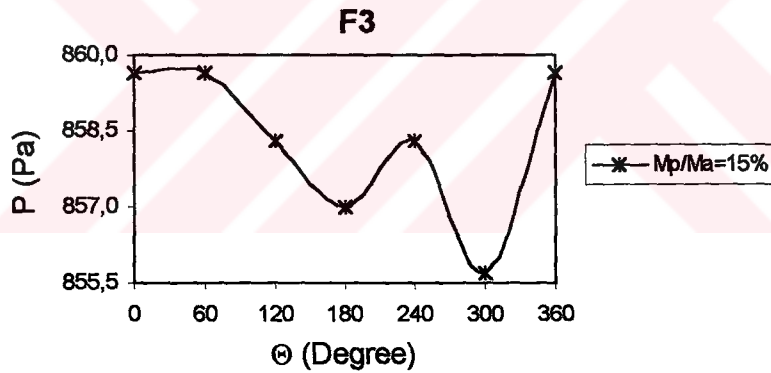
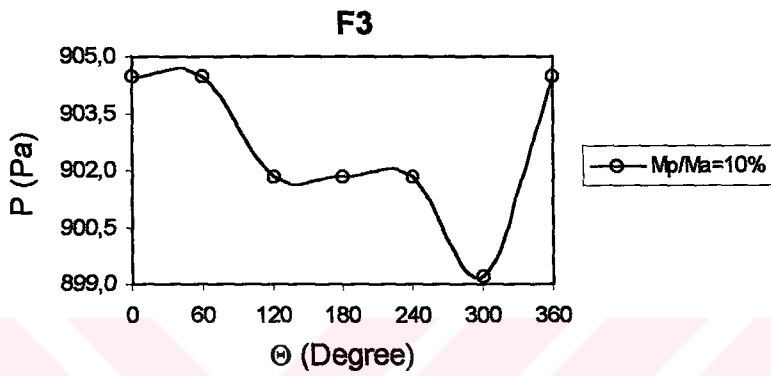
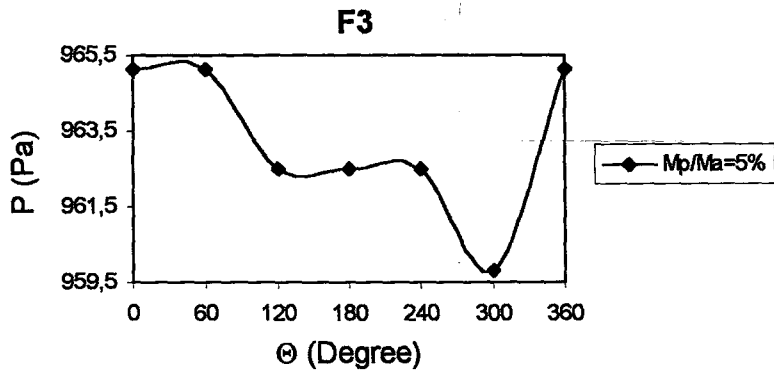


Figure 4.21 Variation of circumferential pressure with Θ for F3 at $x=39.51D$ and $Re=98933$ along horizontal line, $\alpha=0^\circ$.

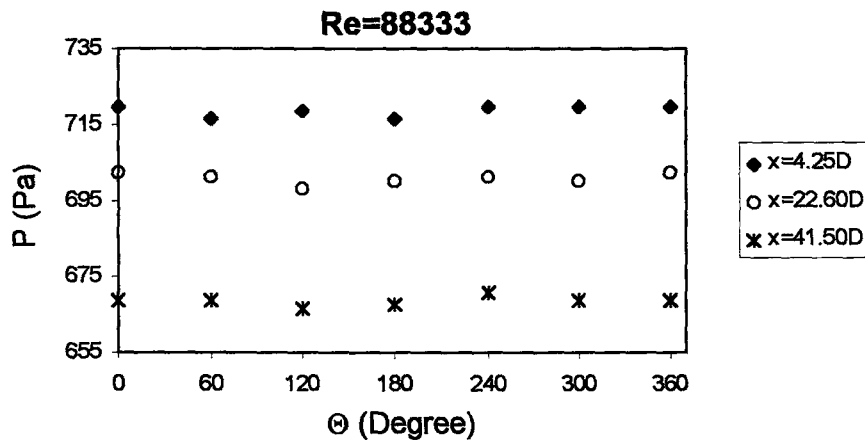
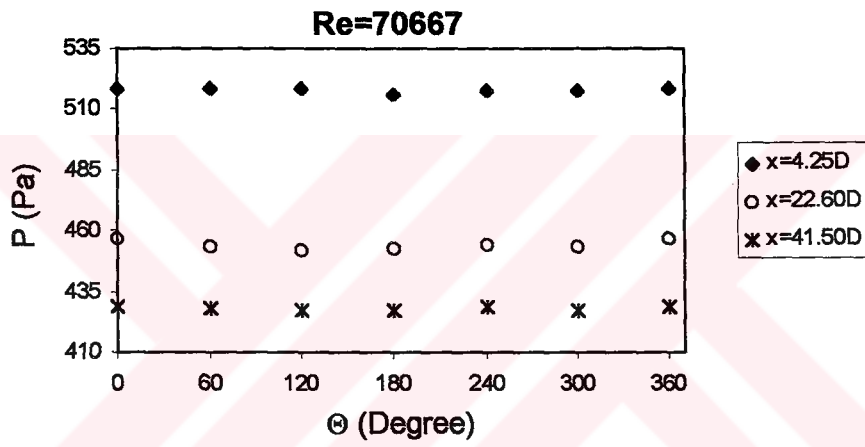
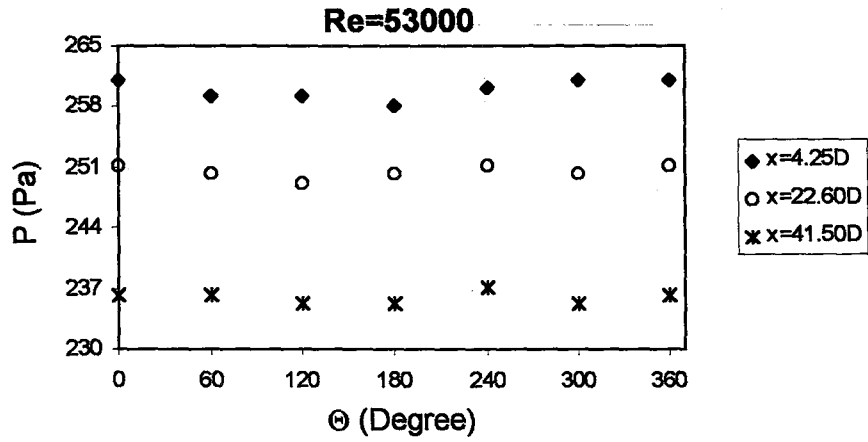


Figure 4.22 Variation of circumferential pressure with Θ for $M_p/M_a=0\%$ at different Re numbers along inclined line, $\alpha=10^\circ$.

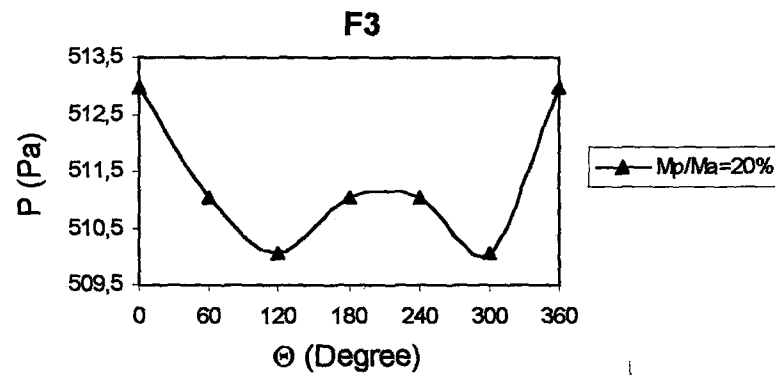
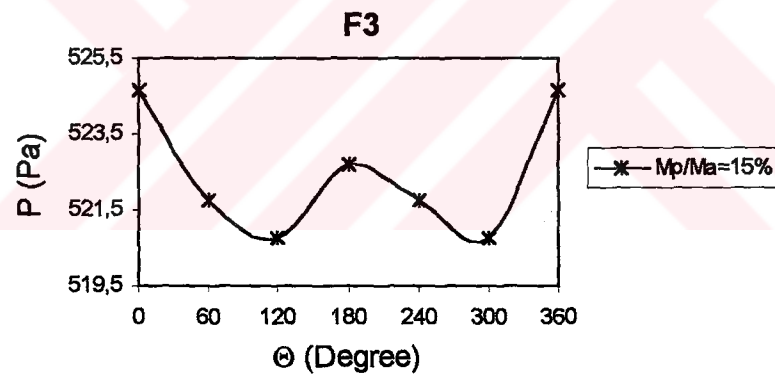
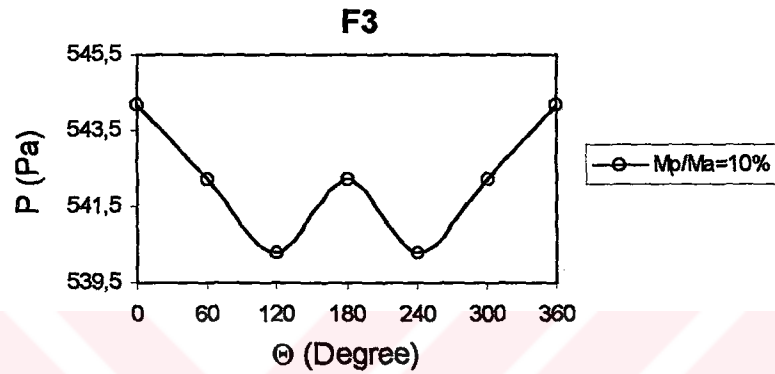
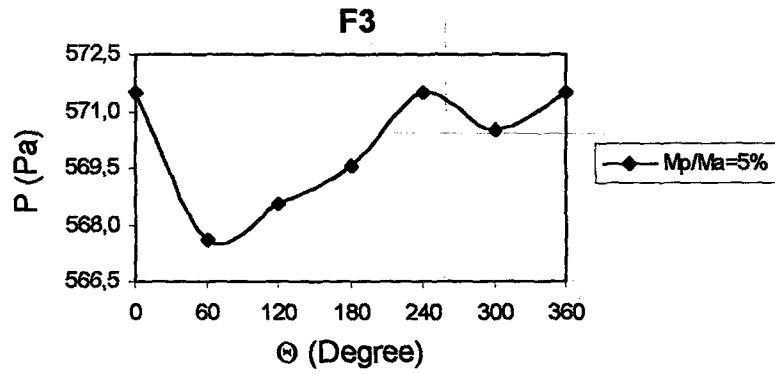


Figure 4.23 Variation of circumferential pressure with Θ for F3 at $x=4.25D$ and $Re=88333$ along inclined line, $\alpha=10^\circ$.

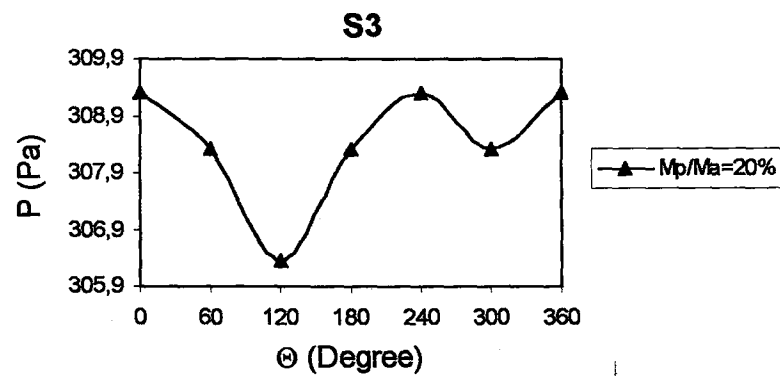
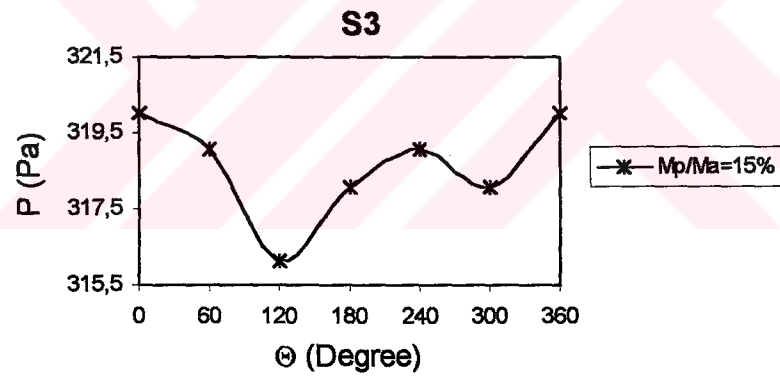
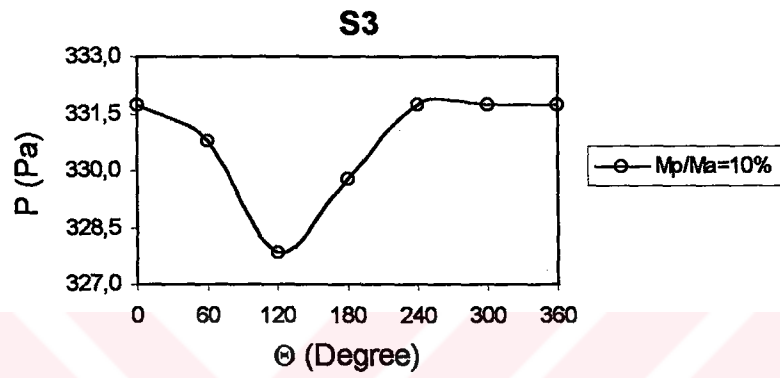
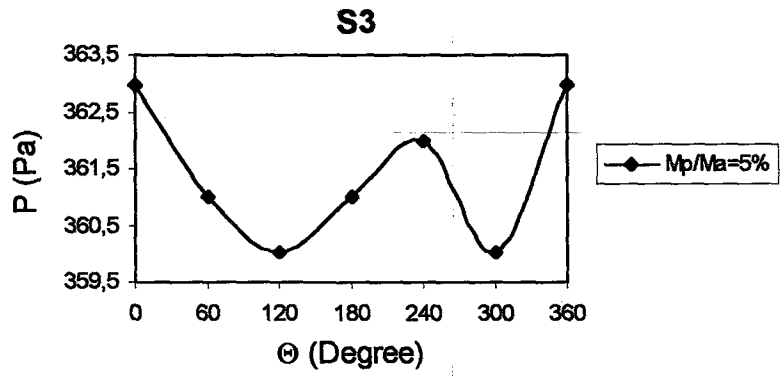


Figure 4.24 Variation of circumferential pressure with Θ for S3 at $x=22.60D$ and $Re=70667$ along inclined line, $\alpha=10^\circ$.

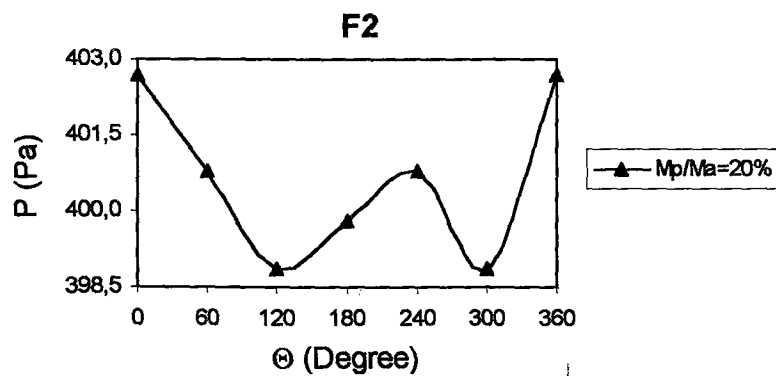
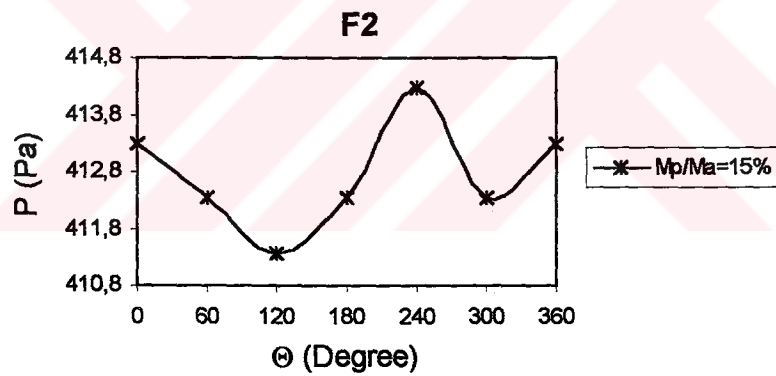
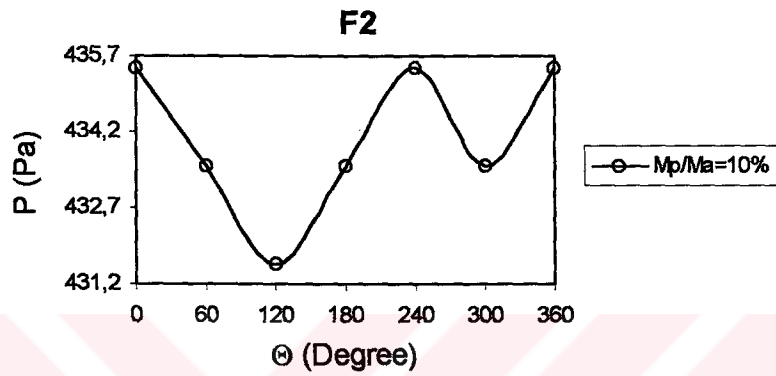
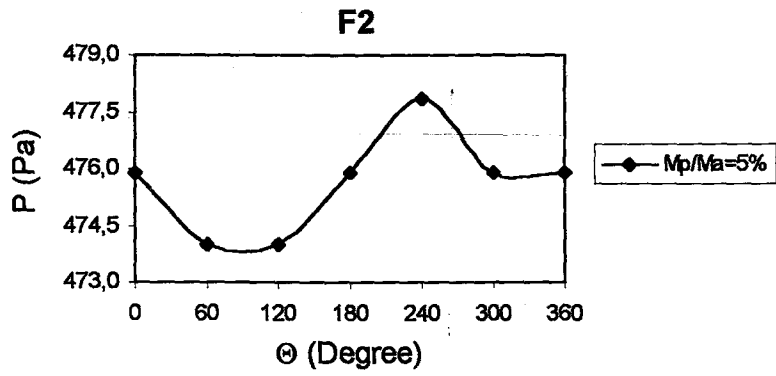


Figure 4.25 Variation of circumferential pressure with Θ for F2 at $x=41.50D$ and $Re=88333$ along inclined line, $\alpha=10^\circ$.

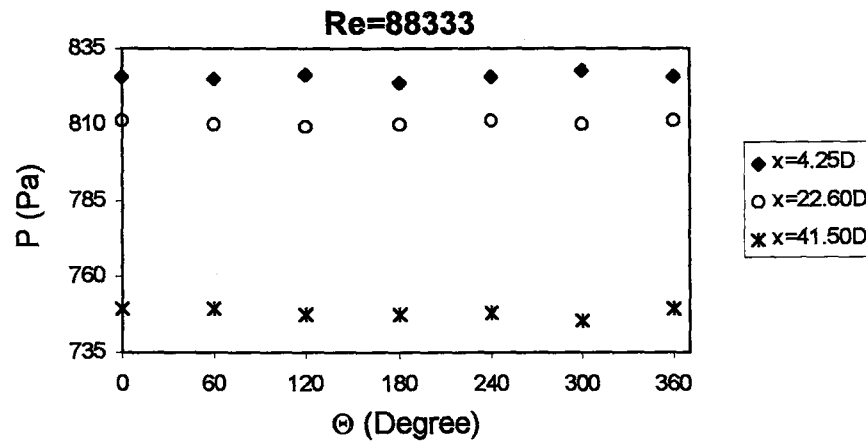
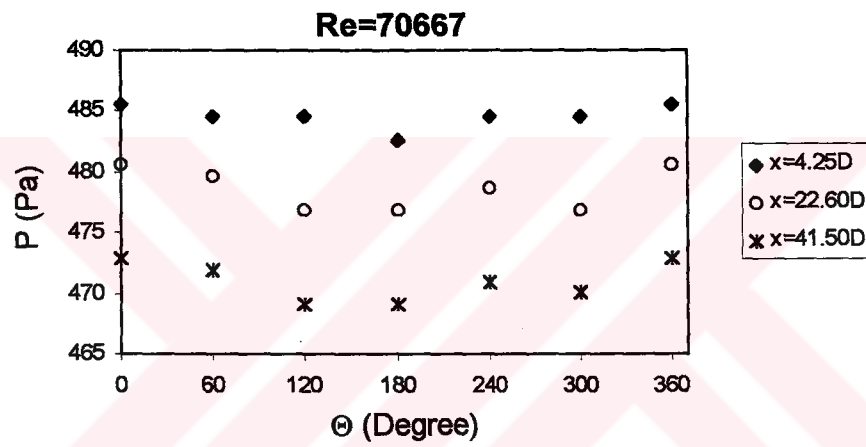
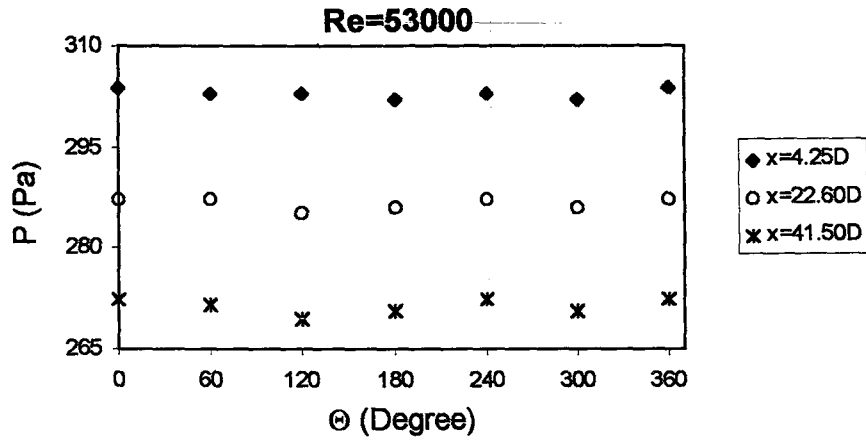


Figure 4.26 Variation of circumferential pressure with Θ for $M_p/M_a=0\%$ at different Re numbers along inclined line, $\alpha=20^\circ$.

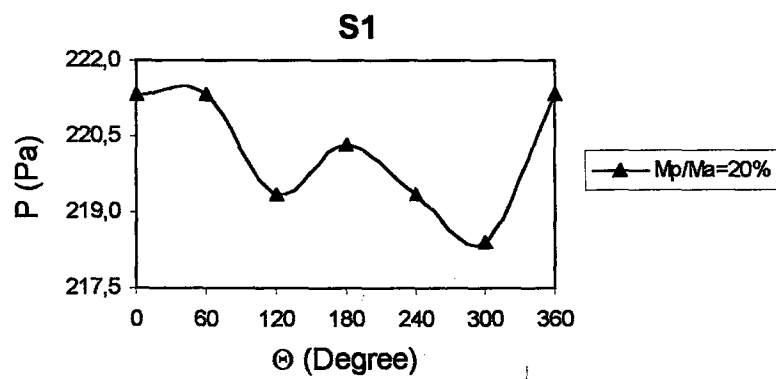
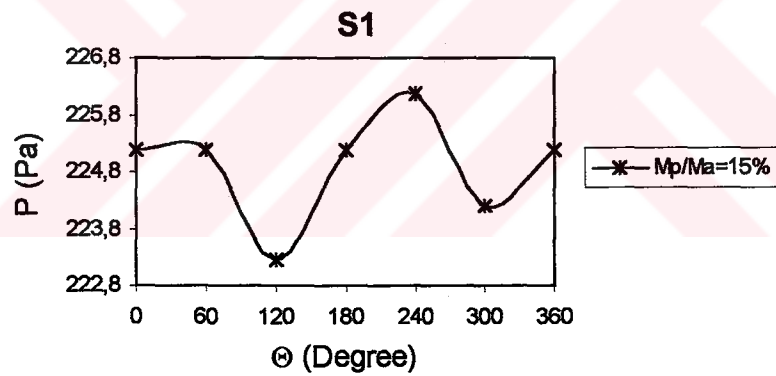
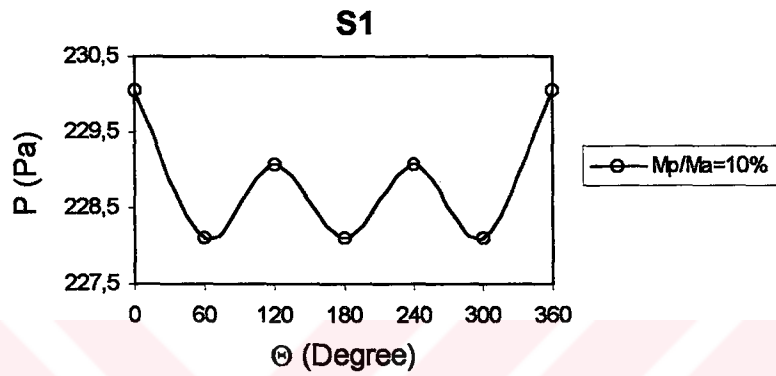
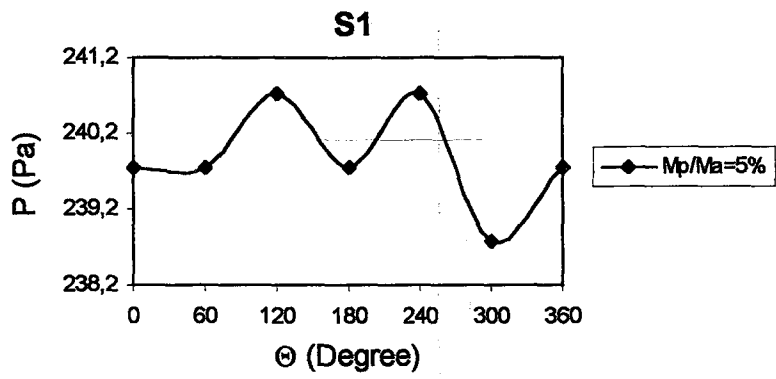


Figure 4.27 Variation of circumferential pressure with θ for S1 at $x=4.25D$ and $Re=53000$ along inclined line, $\alpha=20^\circ$.

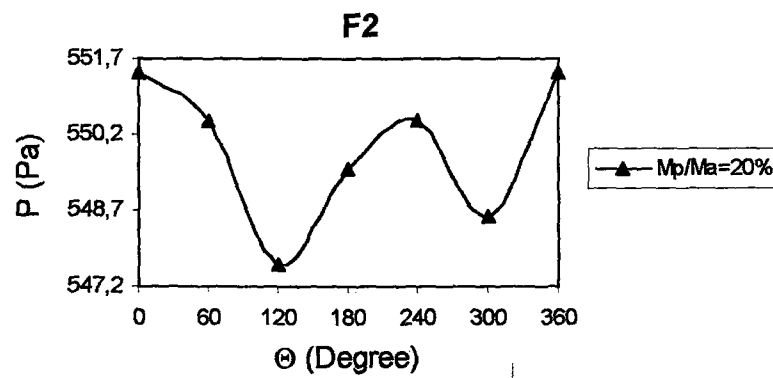
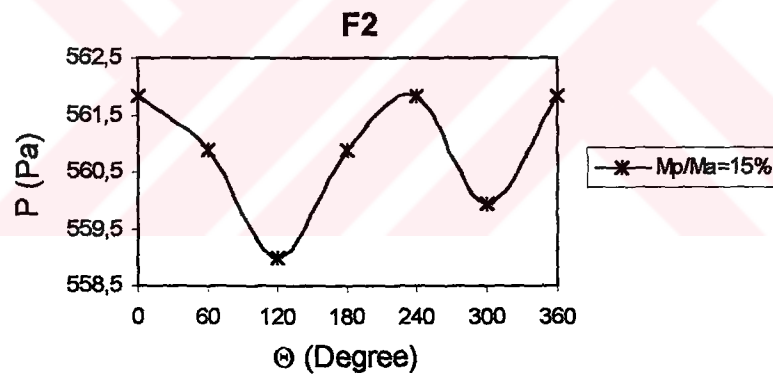
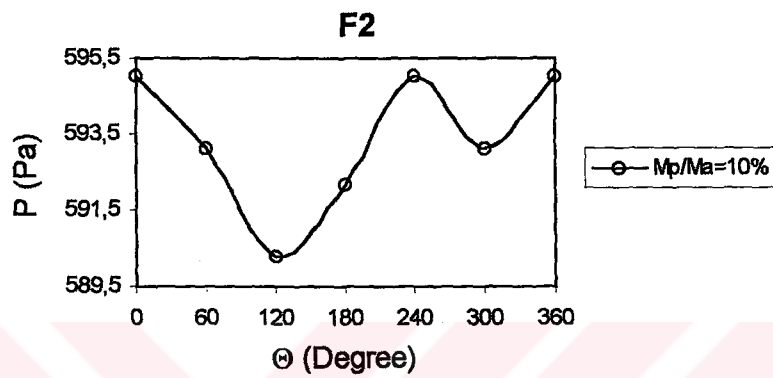
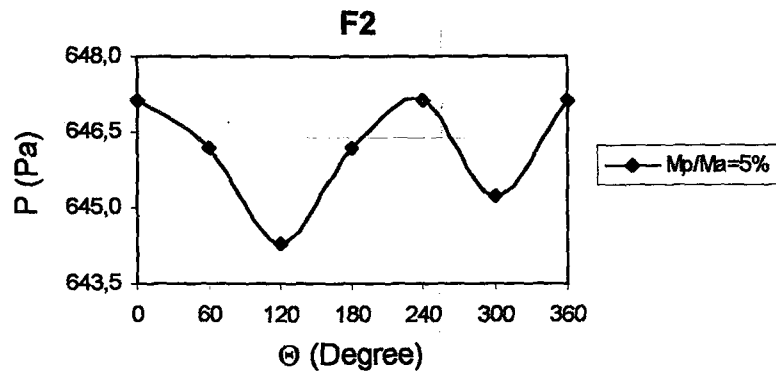


Figure 4.28 Variation of circumferential pressure with \ominus for F2 at $x=22.60D$ and $Re=88333$ along inclined line, $\alpha=20^\circ$.

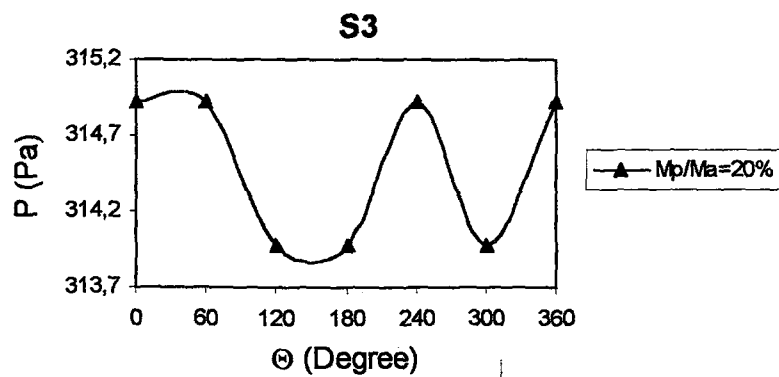
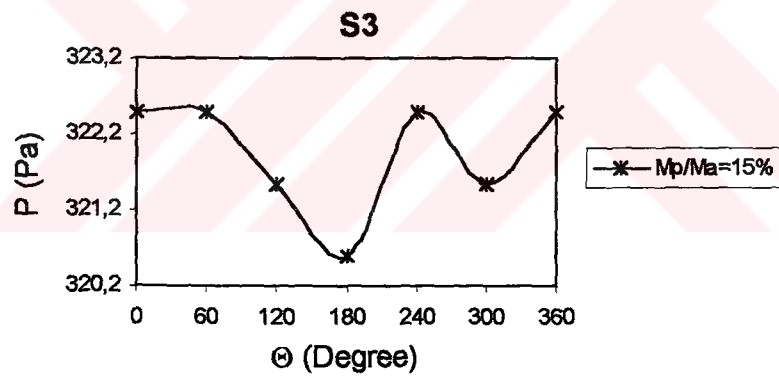
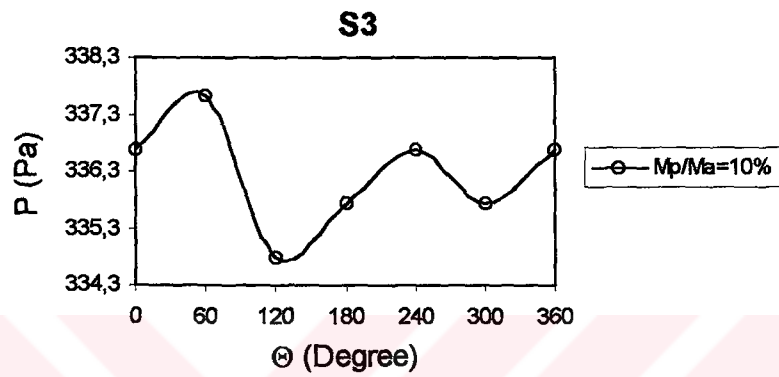
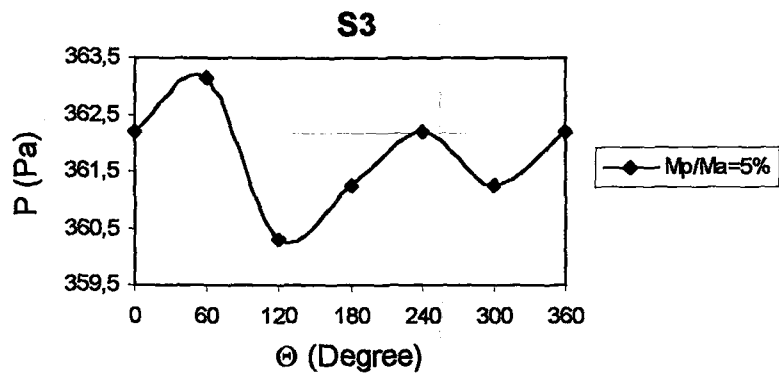


Figure 4.29 Variation of circumferential pressure with Θ for S3 at $x=41.50D$ and $Re=70667$ along inclined line, $\alpha=20^\circ$.

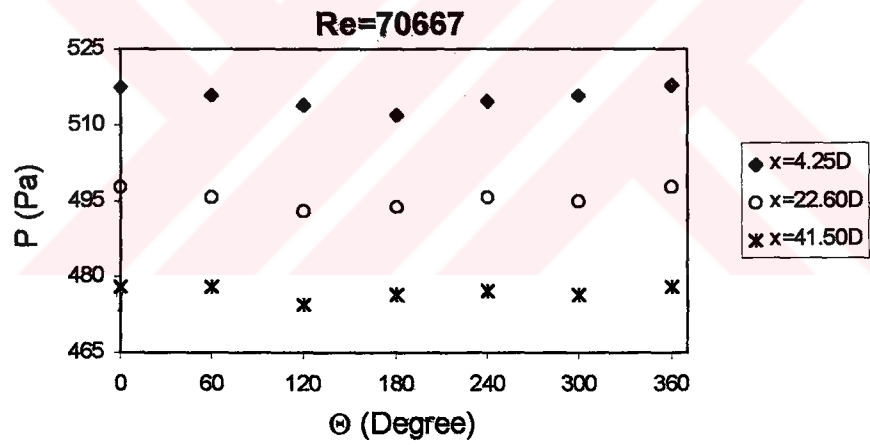
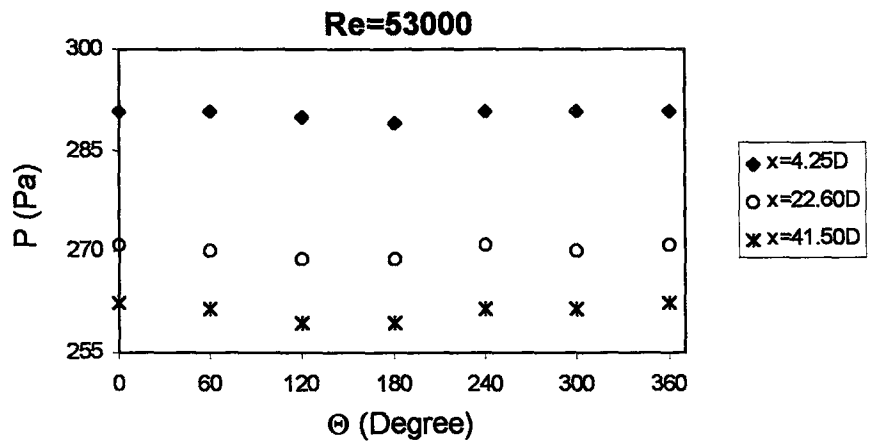


Figure 4.30 Variation of circumferential pressure with Θ for $M_p/M_a=0\%$ at different Re numbers along inclined line, $\alpha=30^\circ$.

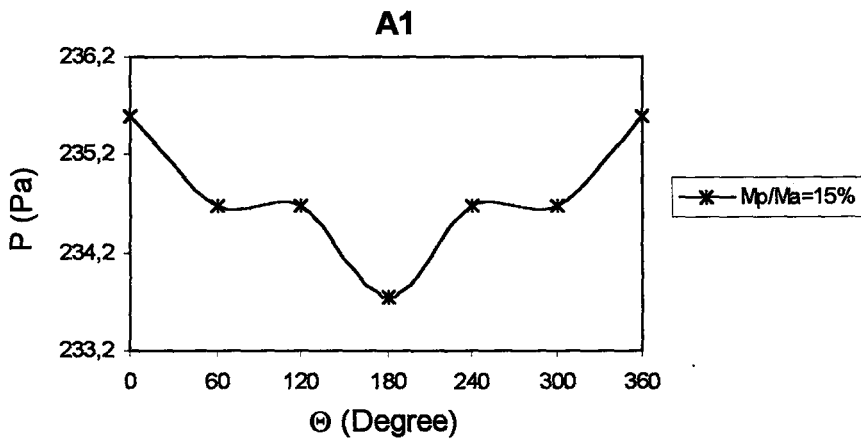
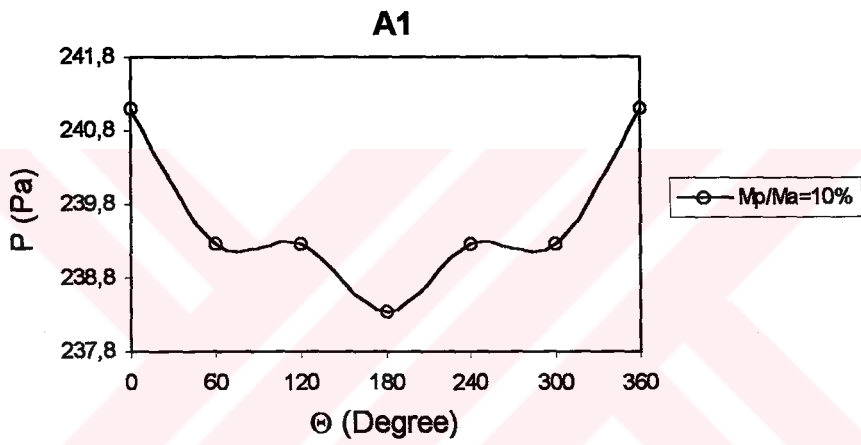
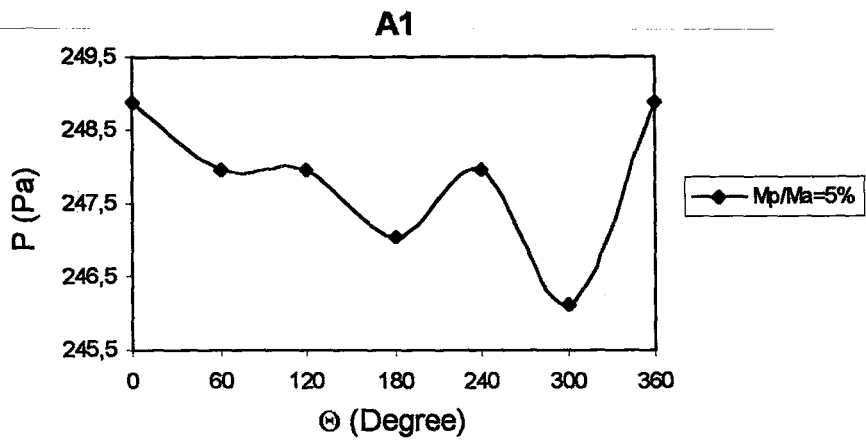


Figure 4.31 Variation of circumferential pressure with Θ for A1 at $x=4.25D$ and $Re=53000$ along inclined line, $\alpha=30^\circ$.

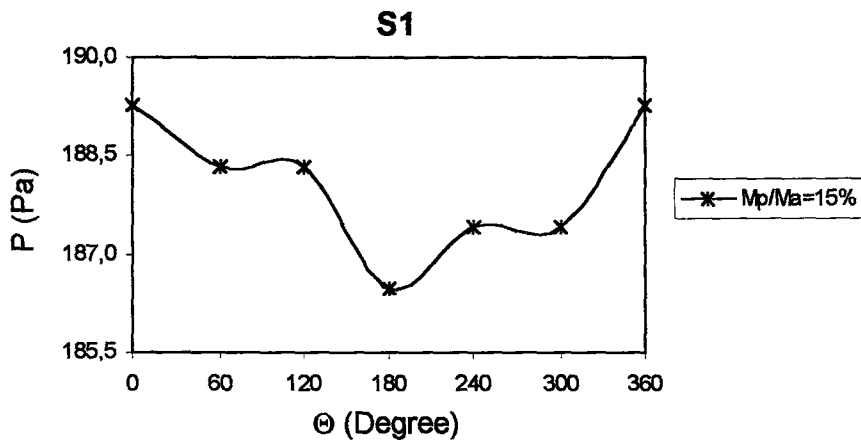
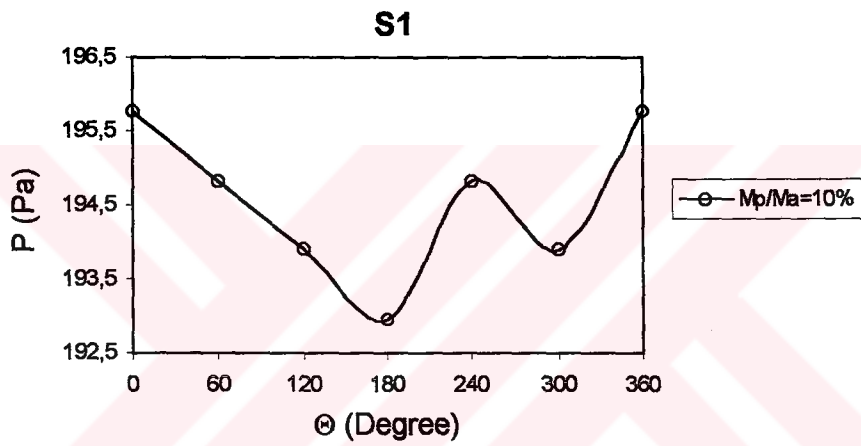
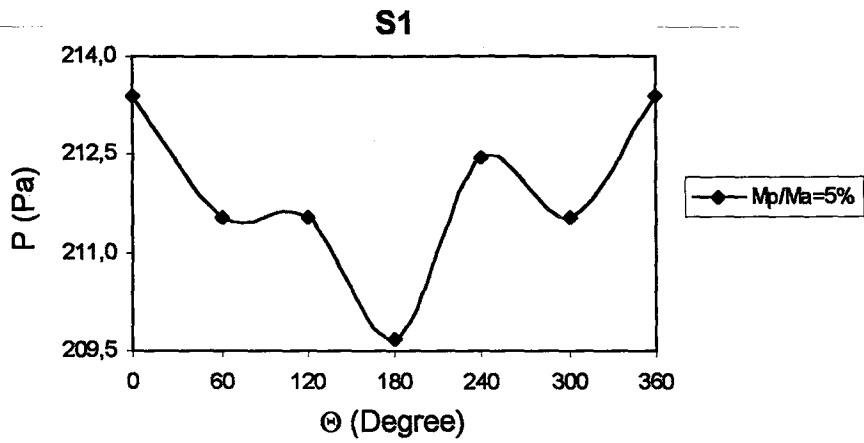


Figure 4.32 Variation of circumferential pressure with Θ for S1 at $x=22.60D$ and $Re=53000$ along inclined line, $\alpha=30^\circ$.

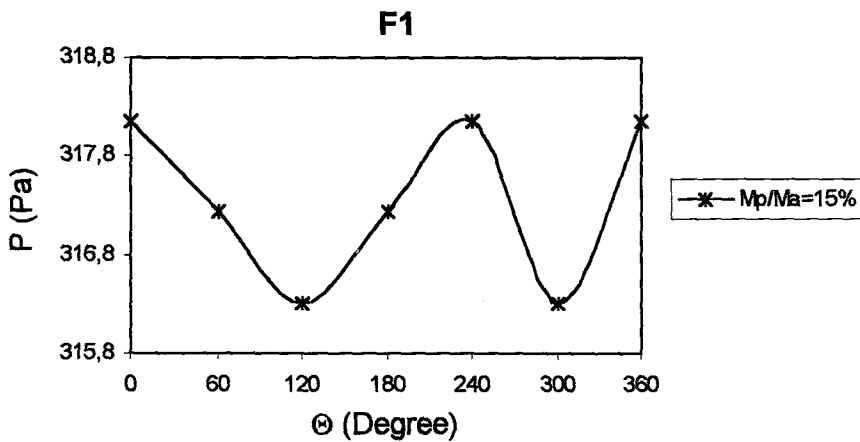
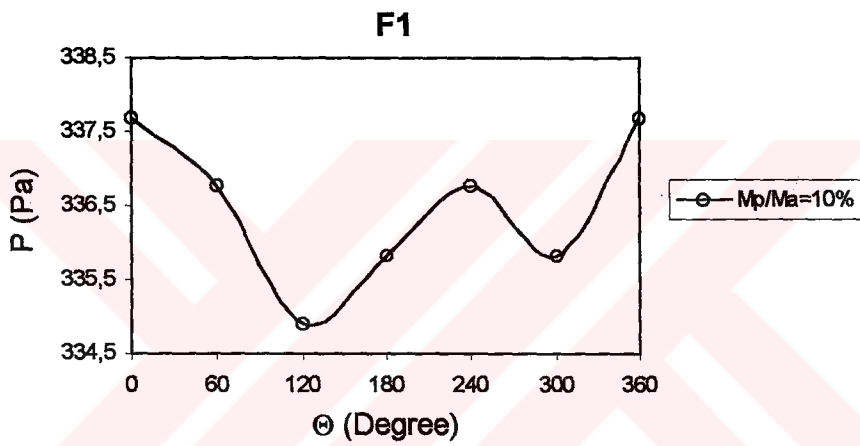
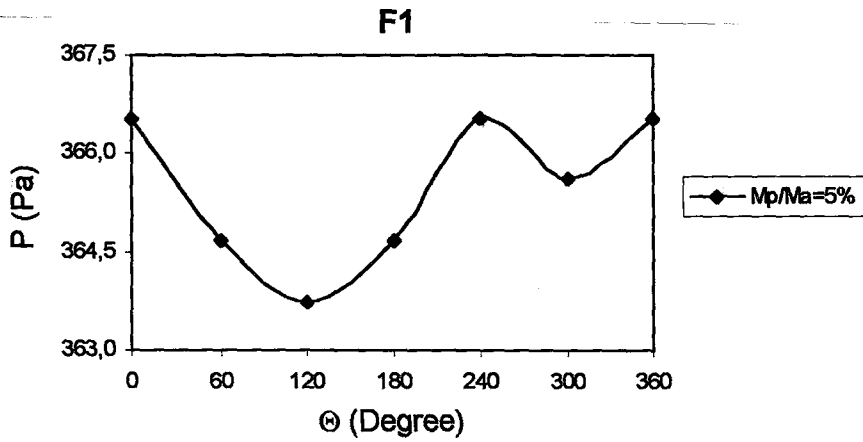
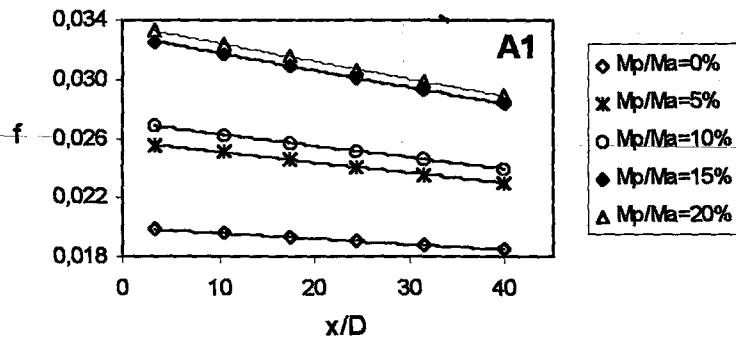
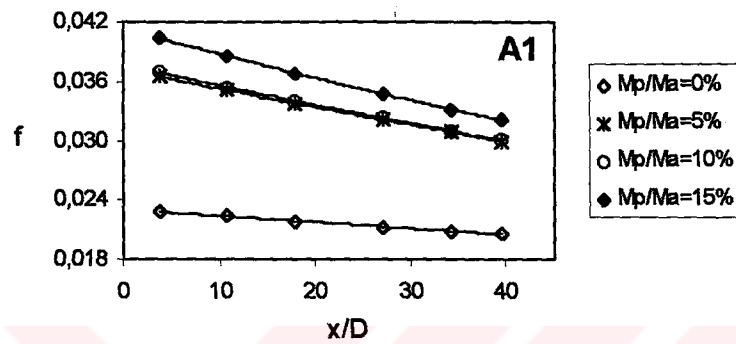


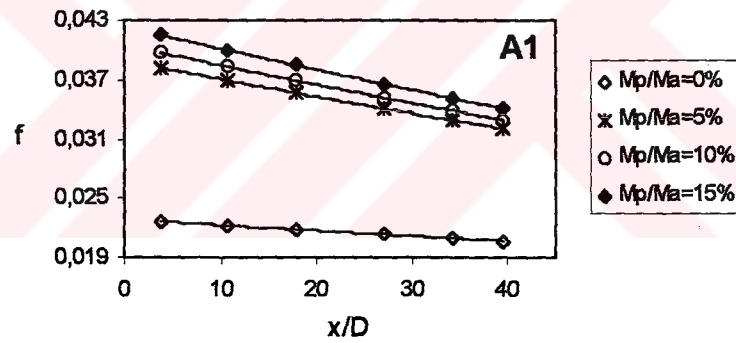
Figure 4.33 Variation of circumferential pressure with Θ for F1 at $x=41.50D$ and $Re=70667$ along inclined line, $\alpha=30^\circ$.



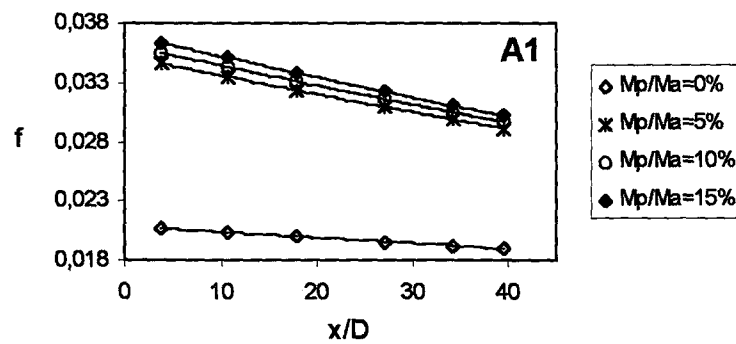
a) $\alpha=0^\circ$ (Horizontal Line)



b) $\alpha=10^\circ$

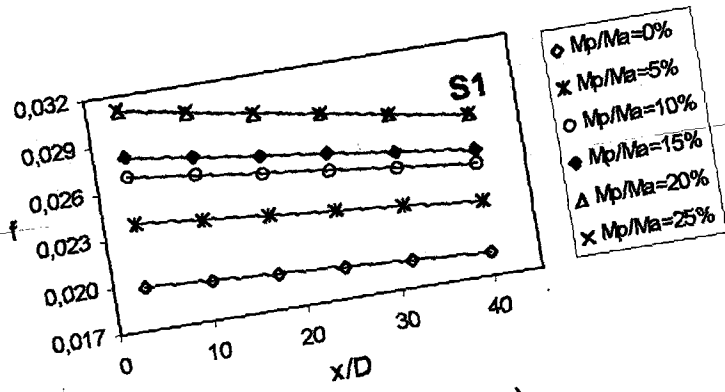


c) $\alpha=20^\circ$

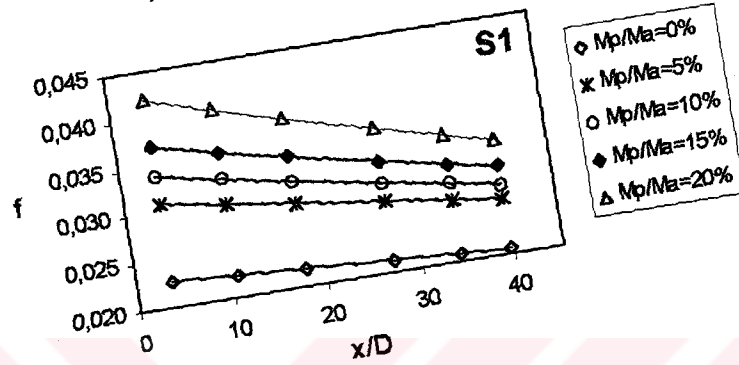


d) $\alpha=30^\circ$

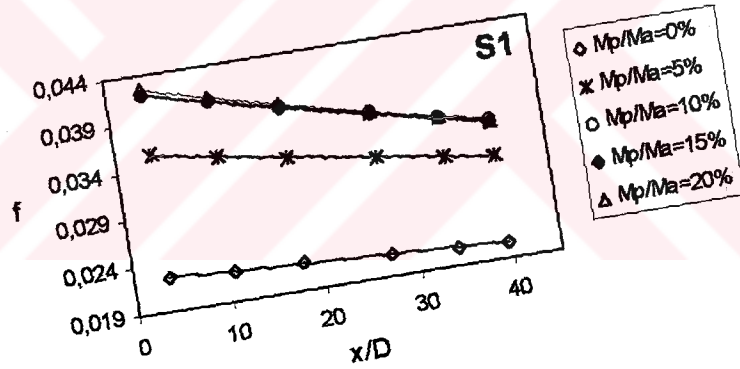
Figure 4.34. a, b, c, d Variation of friction factor f with x/D for A1 at $Re=53000$ along different test section inclinations.



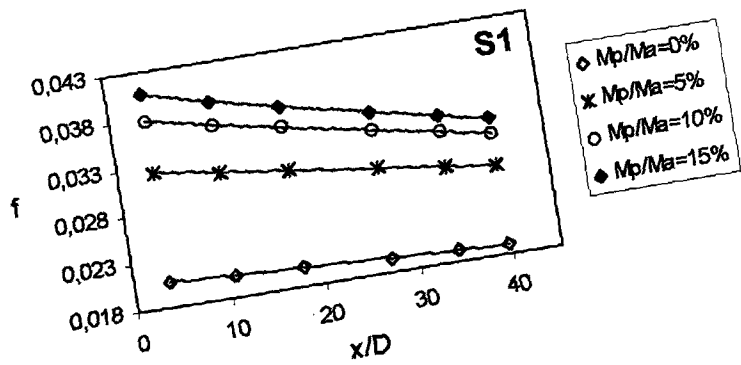
a) $\alpha=0^\circ$ (Horizontal Line)



b) $\alpha=10^\circ$

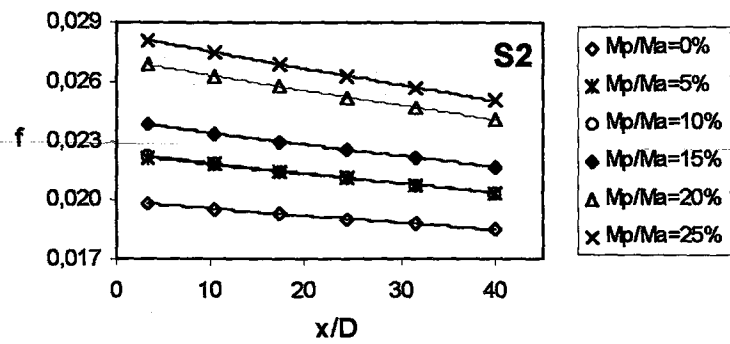


c) $\alpha=20^\circ$

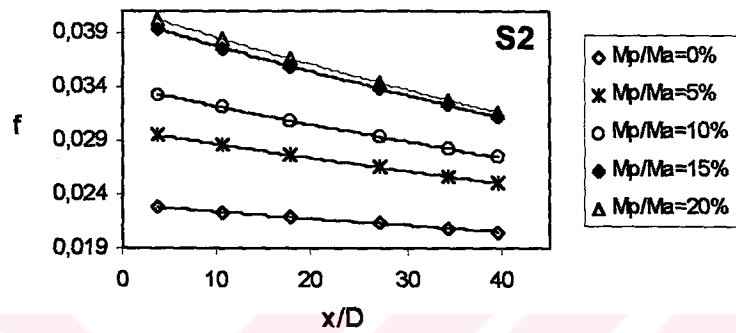


d) $\alpha=30^\circ$

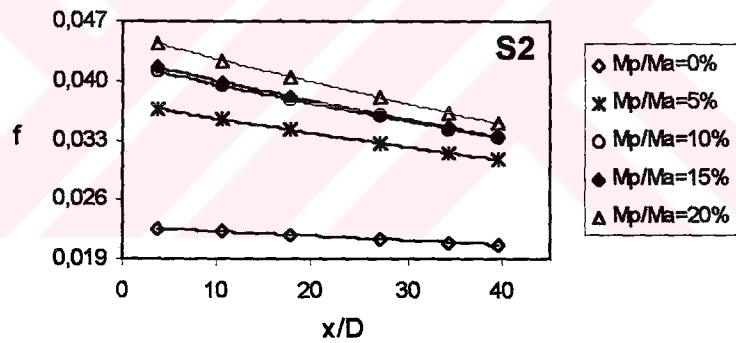
Figure 4.35. a, b, c, d Variation of friction factor f with x/D for S1 at $Re=53000$ along different test section inclinations.



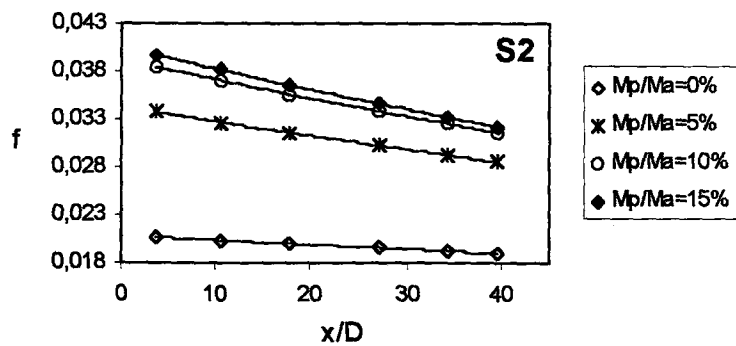
a) $\alpha=0^\circ$ (Horizontal Line)



b) $\alpha=10^\circ$

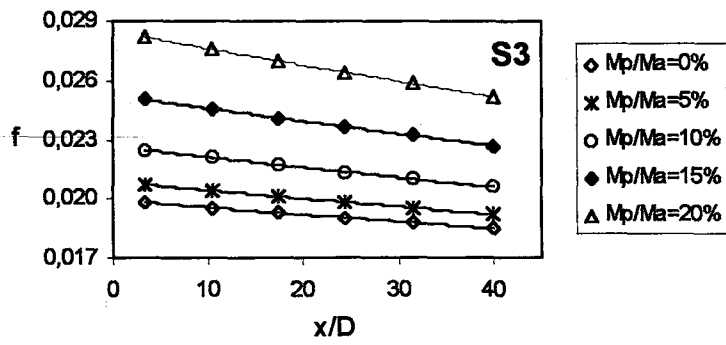


c) $\alpha=20^\circ$

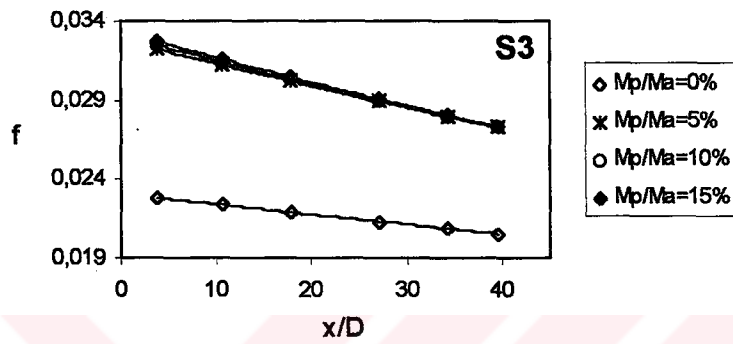


d) $\alpha=30^\circ$

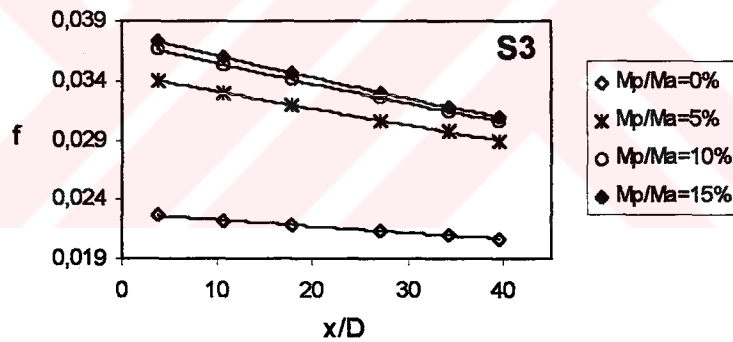
Figure 4.36. a, b, c, d Variation of friction factor f with x/D for S2 at $Re=53000$ along different test section inclinations.



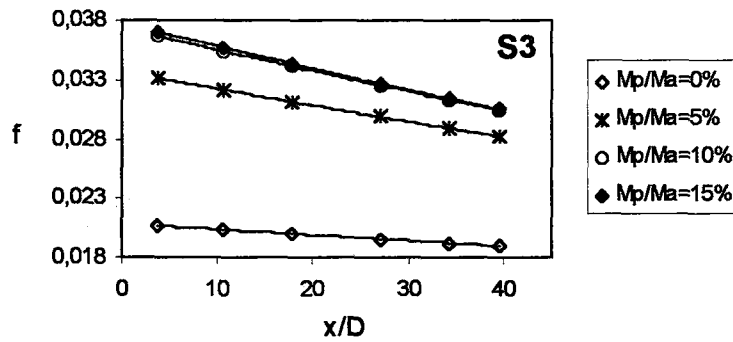
a) $\alpha=0^\circ$ (Horizontal Line)



b) $\alpha=10^\circ$

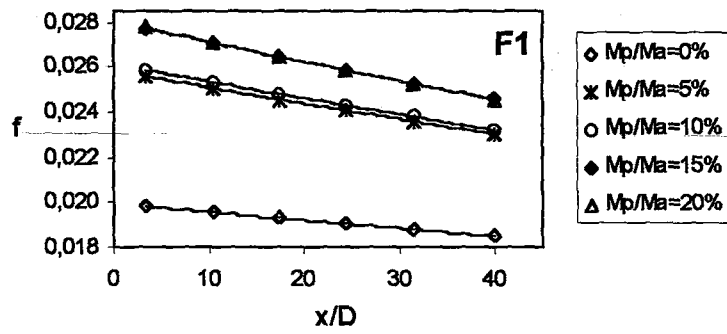


c) $\alpha=20^\circ$

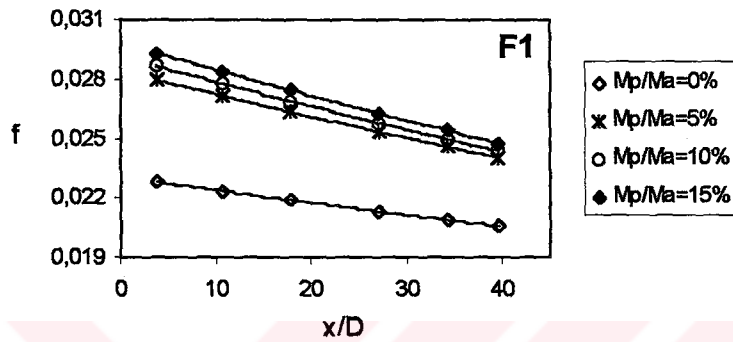


d) $\alpha=30^\circ$

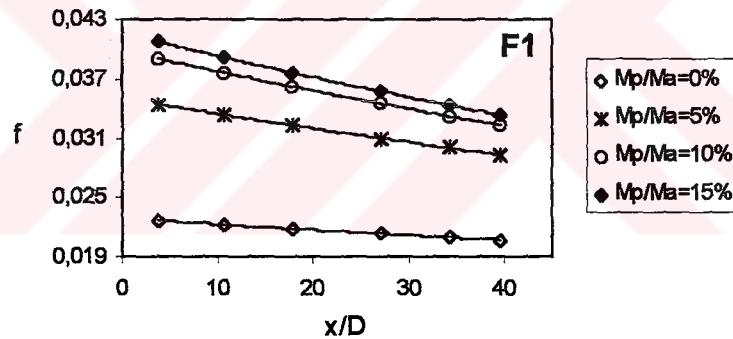
Figure 4.37. a, b, c, d Variation of friction factor f with x/D for S3 at $Re=53000$ along different test section inclinations.



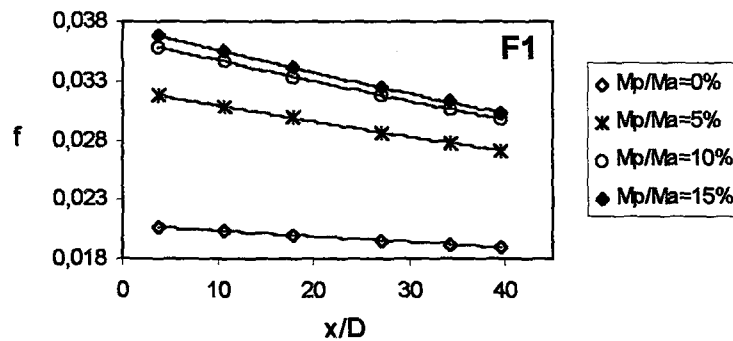
a) $\alpha=0^\circ$ (Horizontal Line)



b) $\alpha=10^\circ$

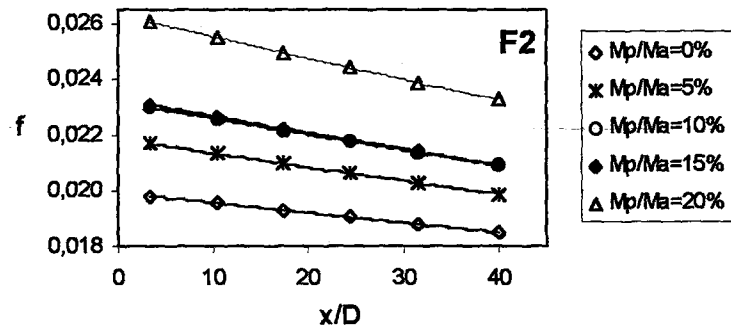


c) $\alpha=20^\circ$

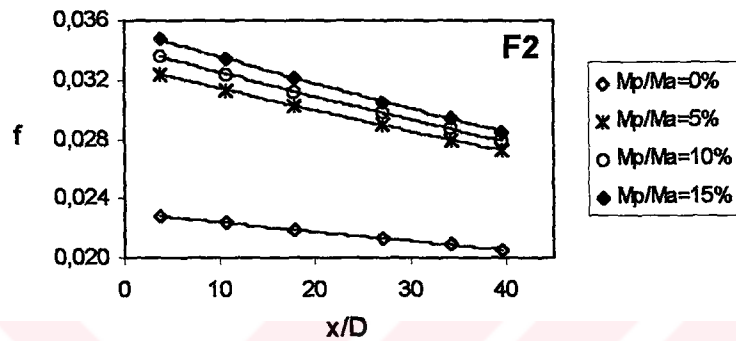


d) $\alpha=30^\circ$

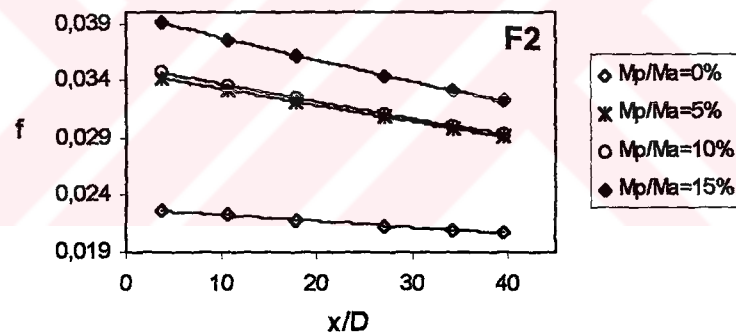
Figure 4.38. a, b, c, d Variation of friction factor f with x/D for F1 at $Re=53000$ along different test section inclinations.



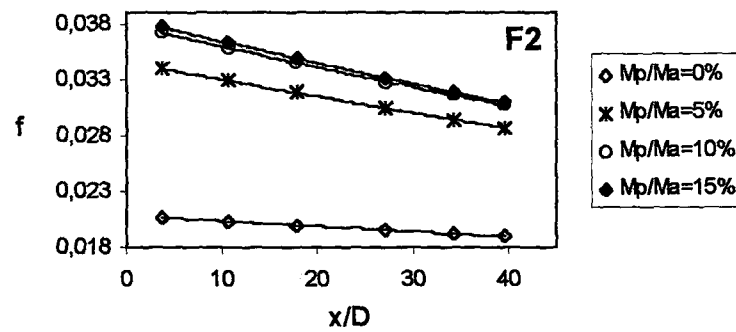
a) $\alpha=0^\circ$ (Horizontal Line)



b) $\alpha=10^\circ$

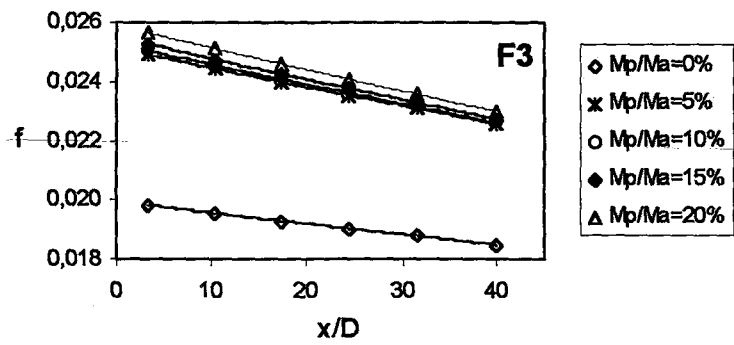


c) $\alpha=20^\circ$

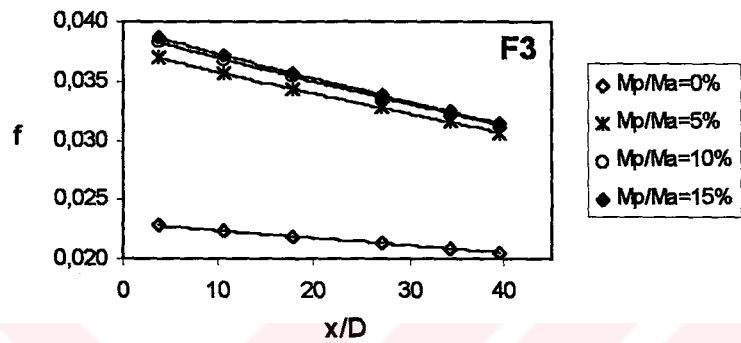


d) $\alpha=30^\circ$

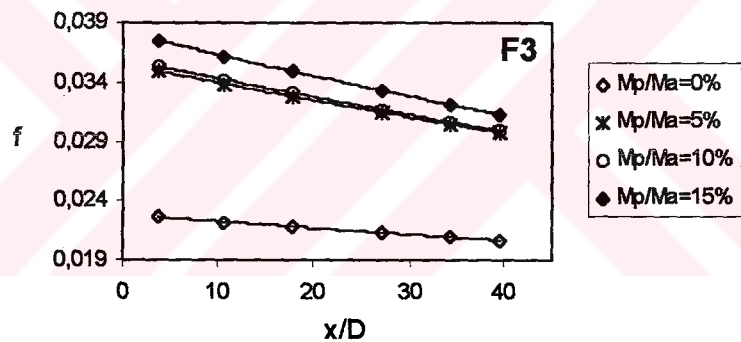
Figure 4.39. a, b, c, d Variation of friction factor f with x/D for F2 at $Re=53000$ along different test section inclinations.



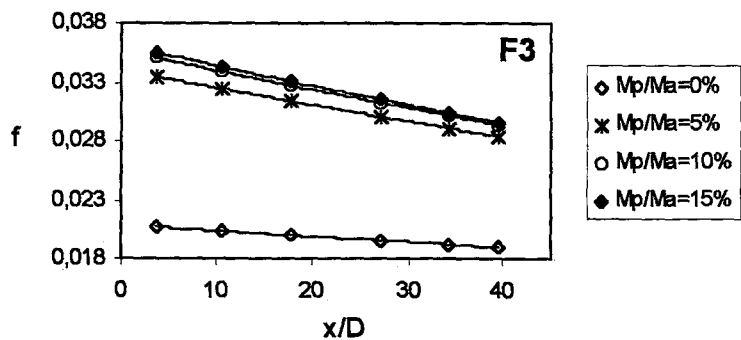
a) $\alpha=0^\circ$ (Horizontal Line)



b) $\alpha=10^\circ$

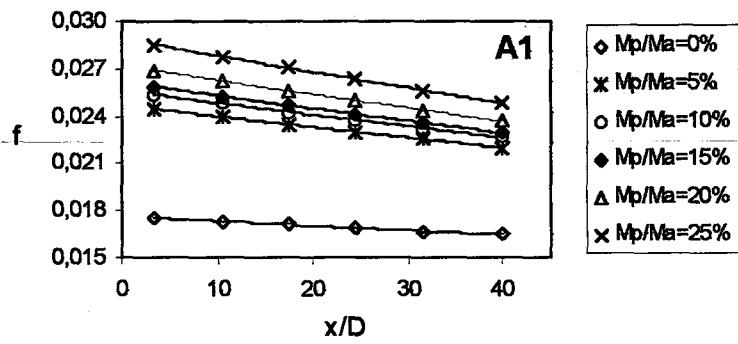


c) $\alpha=20^\circ$

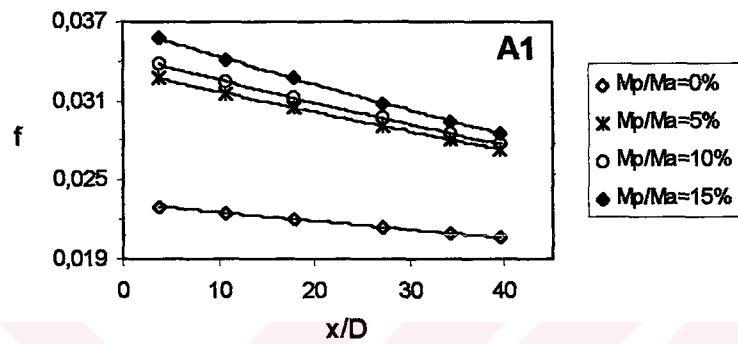


d) $\alpha=30^\circ$

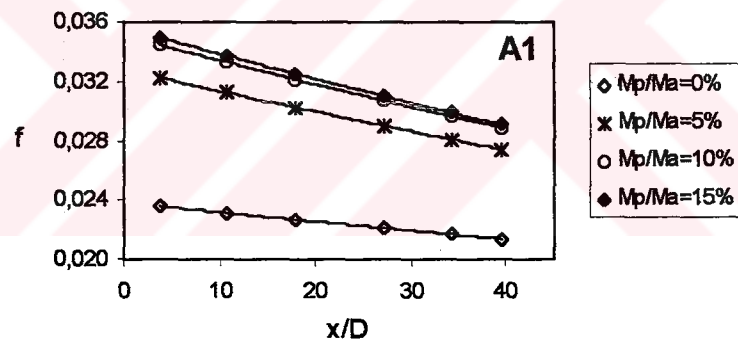
Figure 4.40. a, b, c, d Variation of friction factor f with x/D for F3 at $Re=53000$ along different test section inclinations.



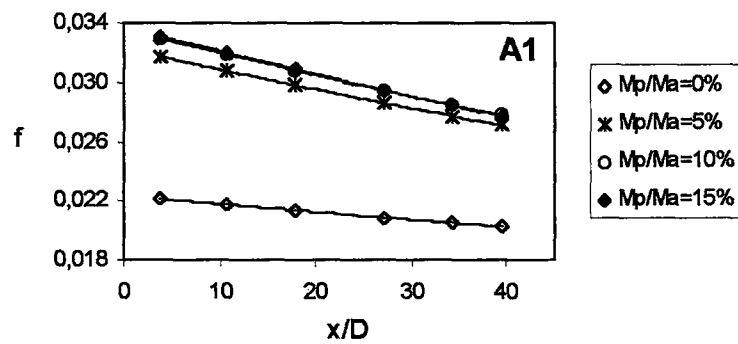
a) $\alpha=0^\circ$ (Horizontal Line)



b) $\alpha=10^\circ$

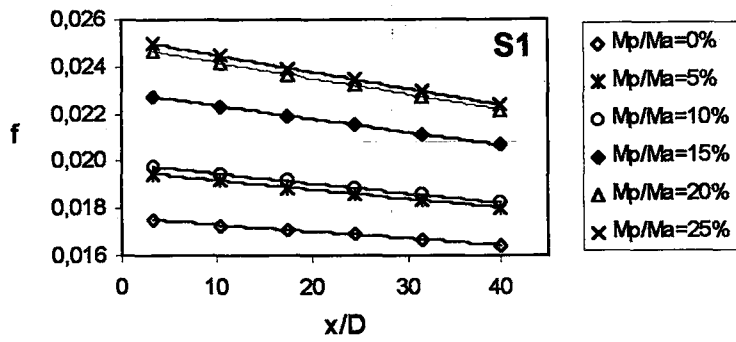


c) $\alpha=20^\circ$

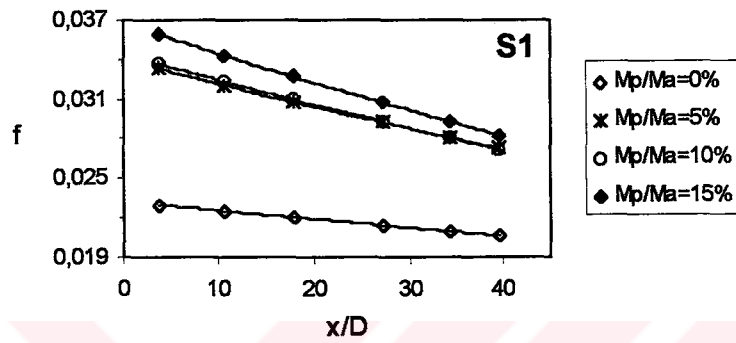


d) $\alpha=30^\circ$

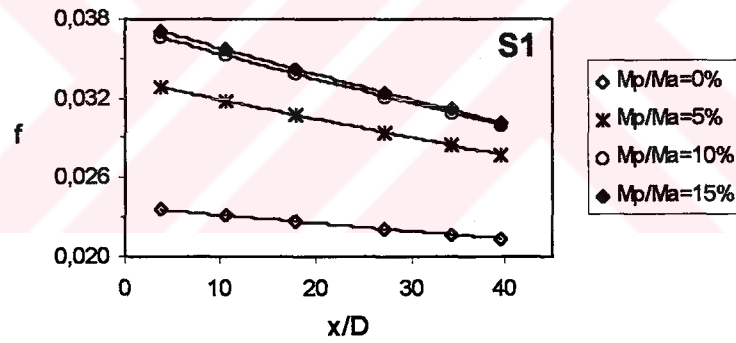
Figure 4.41. a, b, c, d Variation of friction factor f with x/D for A1 at $Re=70667$ along different test section inclinations.



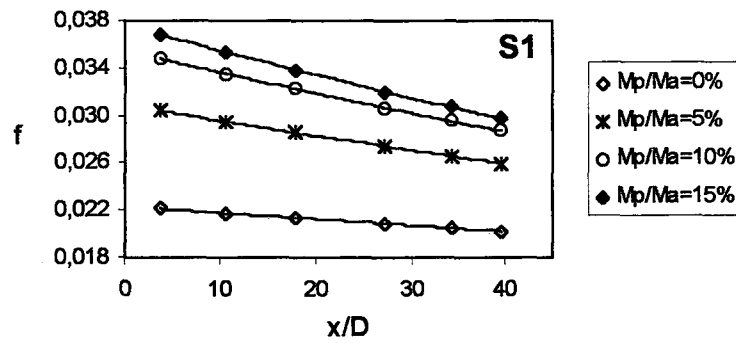
a) $\alpha=0^{\circ}$ (Horizontal Line)



b) $\alpha=10^{\circ}$

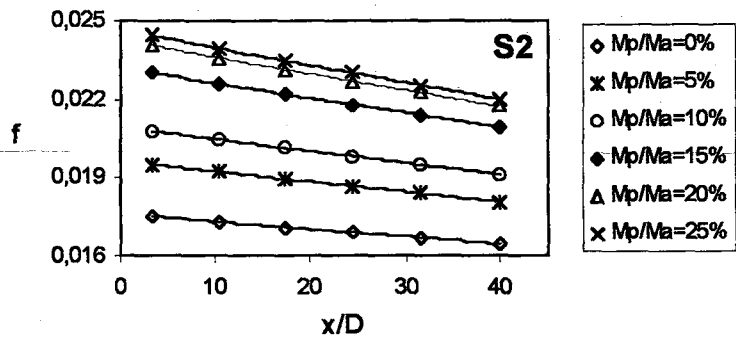


c) $\alpha=20^{\circ}$

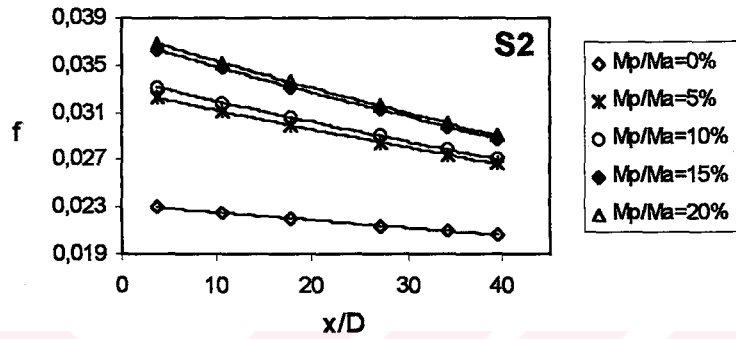


d) $\alpha=30^{\circ}$

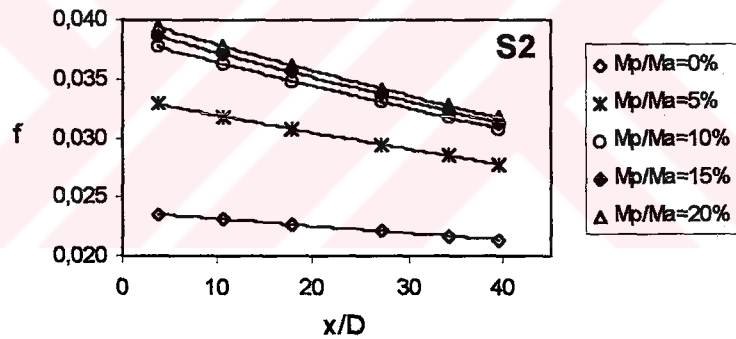
Figure 4.42.a, b, c, d Variation of friction factor f with x/D for S1 at $Re=70667$ along different test section inclinations.



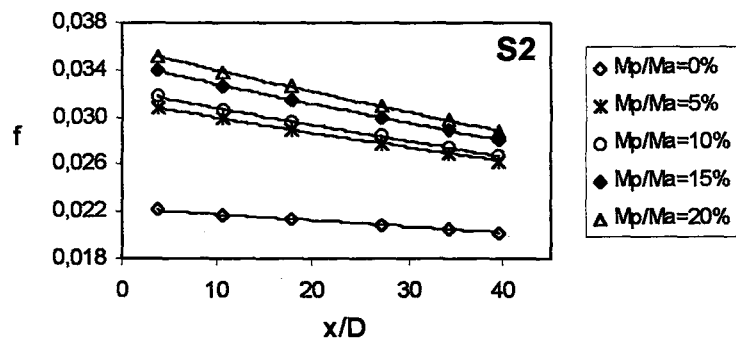
a) $\alpha=0^\circ$ (Horizontal Line)



b) $\alpha=10^\circ$

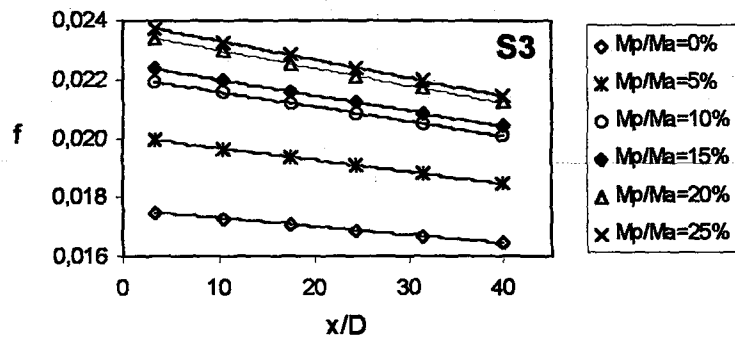


c) $\alpha=20^\circ$

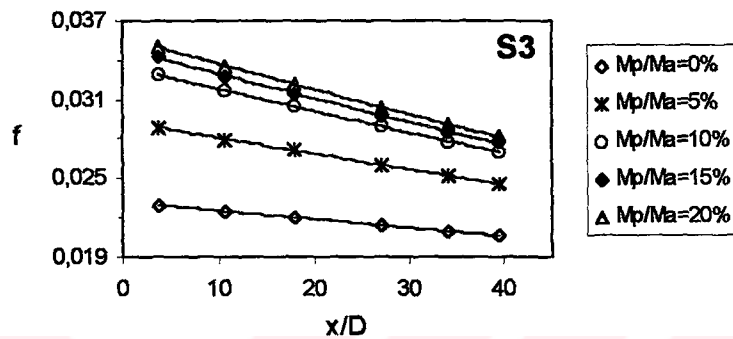


d) $\alpha=30^\circ$

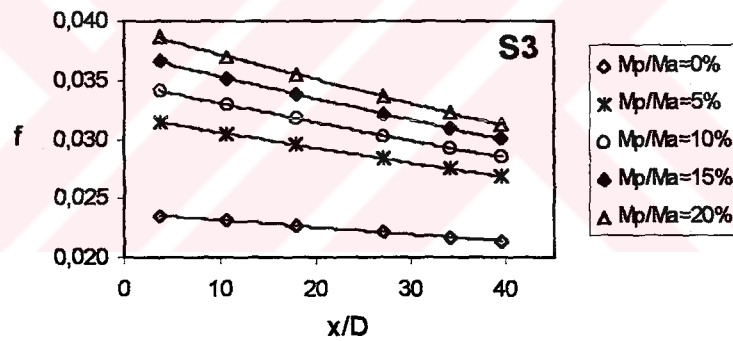
Figure 4.43. a, b, c, d Variation of friction factor f with x/D for S2 at $Re=70667$ along different test section inclinations.



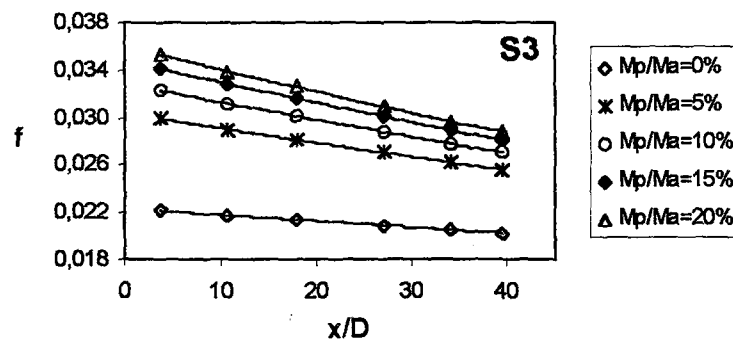
a) $\alpha=0^\circ$ (Horizontal Line)



b) $\alpha=10^\circ$

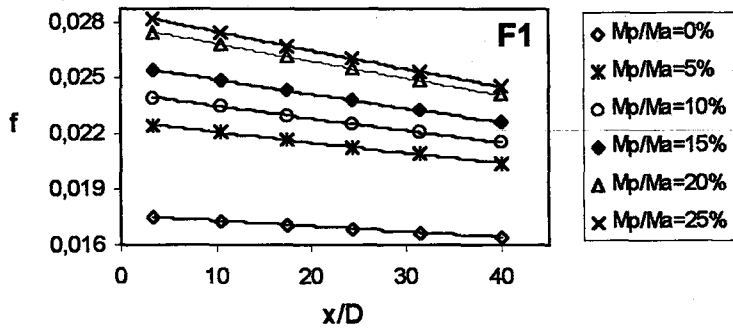


c) $\alpha=20^\circ$

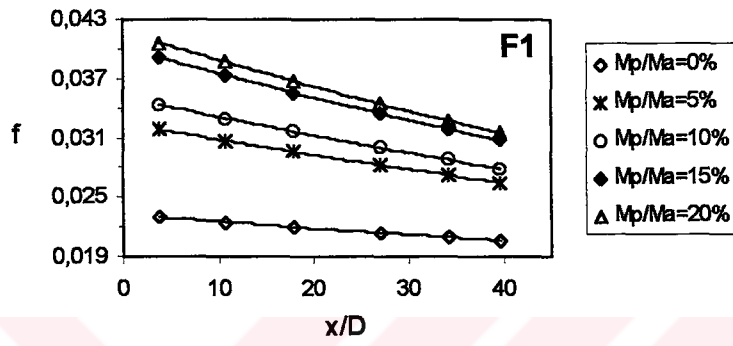


d) $\alpha=30^\circ$

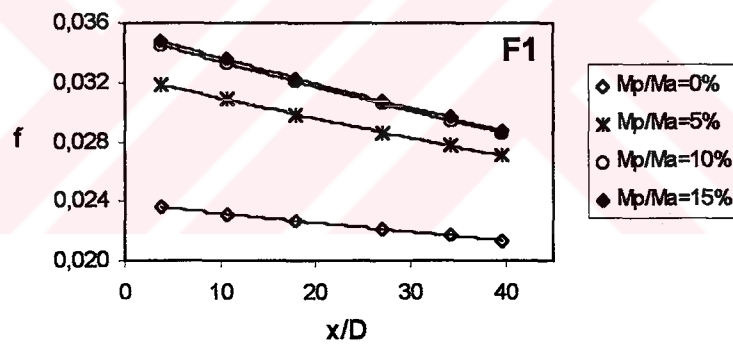
Figure 4.44. a, b, c, d Variation of friction factor f with x/D for S3 at $Re=70667$ along different test section inclinations.



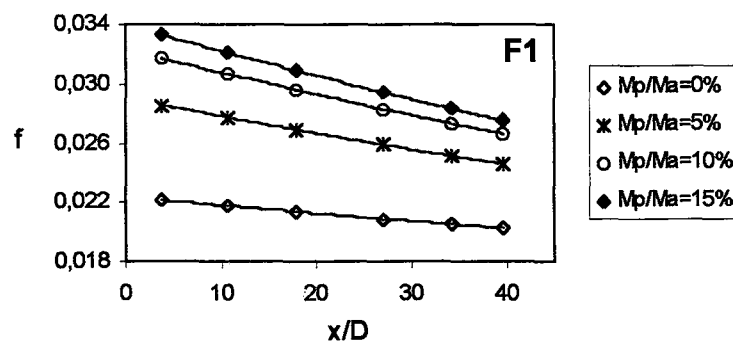
a) $\alpha=0^\circ$ (Horizontal Line)



b) $\alpha=10^\circ$

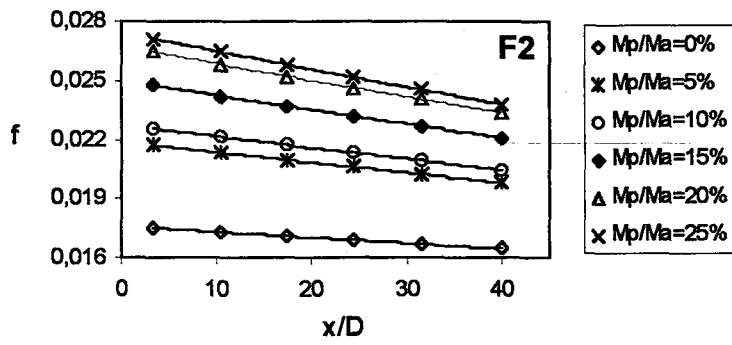


c) $\alpha=20^\circ$

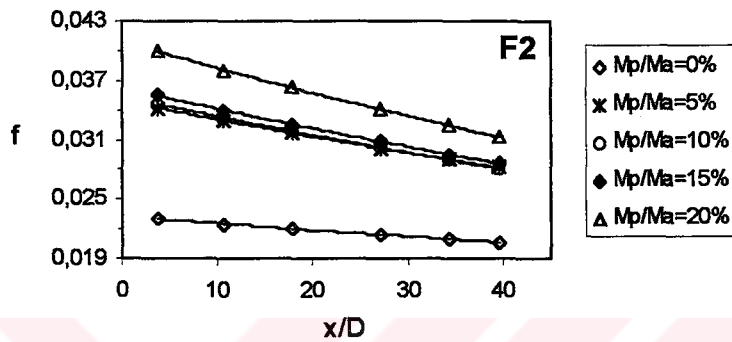


d) $\alpha=30^\circ$

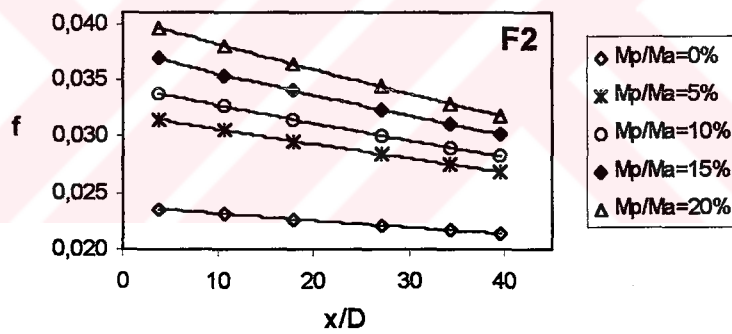
Figure 4.45. a, b, c, d Variation of friction factor f with x/D for F1 at $Re=70667$ along different test section inclinations.



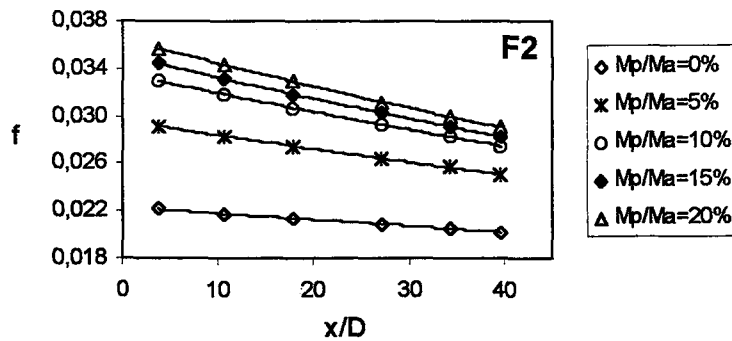
a) $\alpha=0^\circ$ (Horizontal Line)



b) $\alpha=10^\circ$

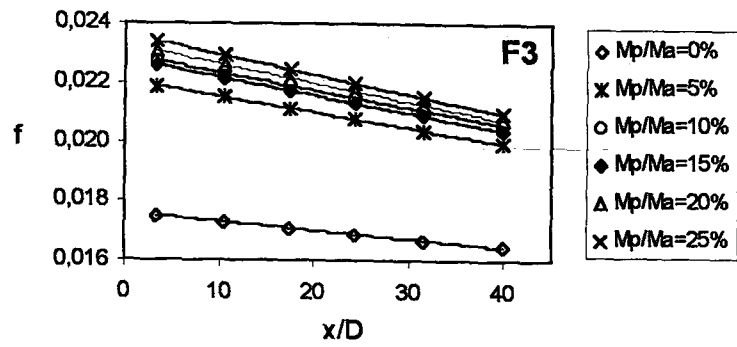


c) $\alpha=20^\circ$

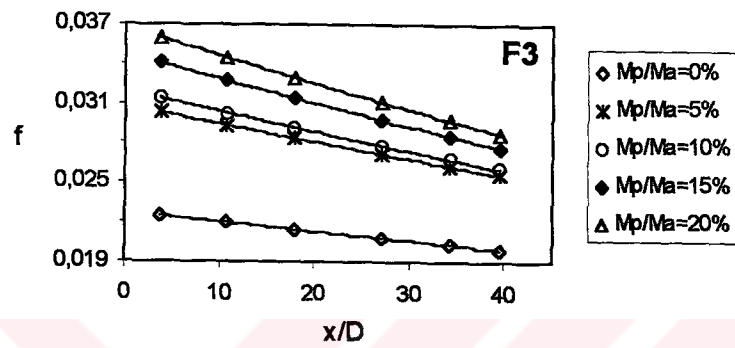


d) $\alpha=30^\circ$

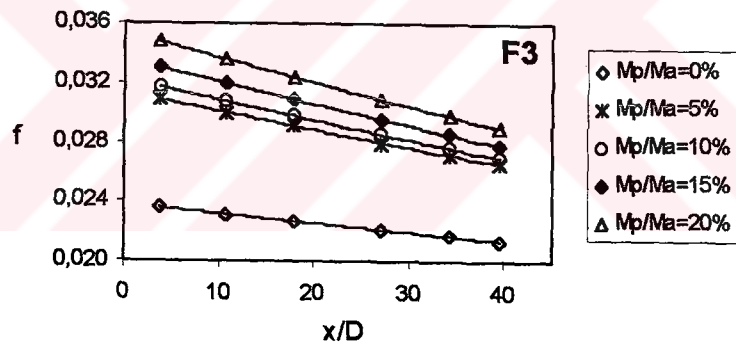
Figure 4.46.a, b, c, d Variation of friction factor f with x/D for F2 at $Re=70667$ along different test section inclinations.



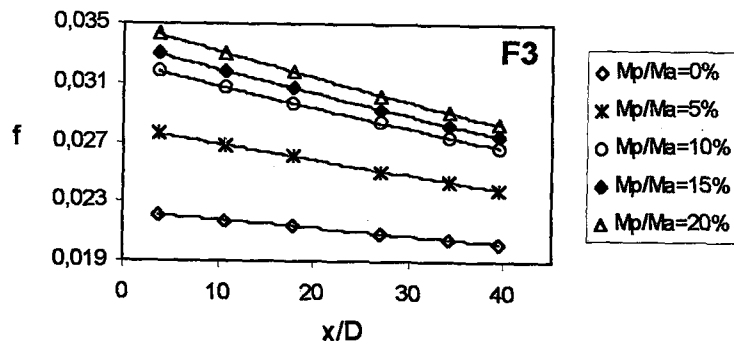
a) $\alpha=0^\circ$ (Horizontal Line)



b) $\alpha=10^\circ$

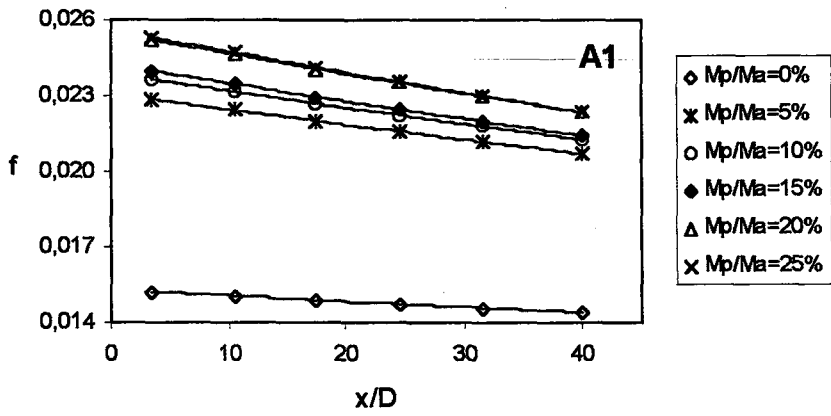


c) $\alpha=20^\circ$

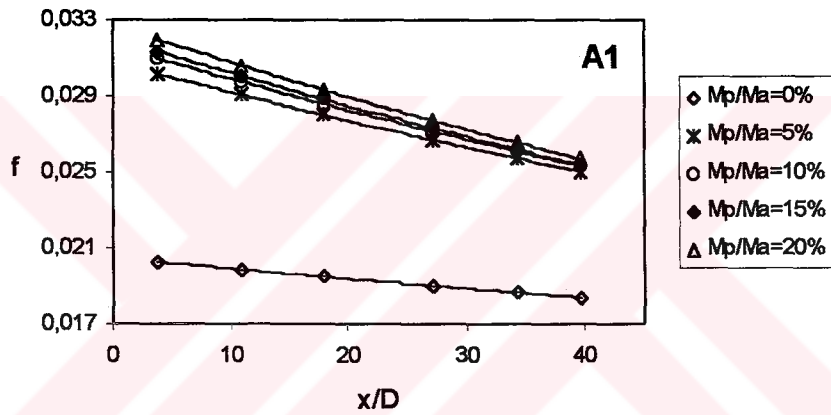


d) $\alpha=30^\circ$

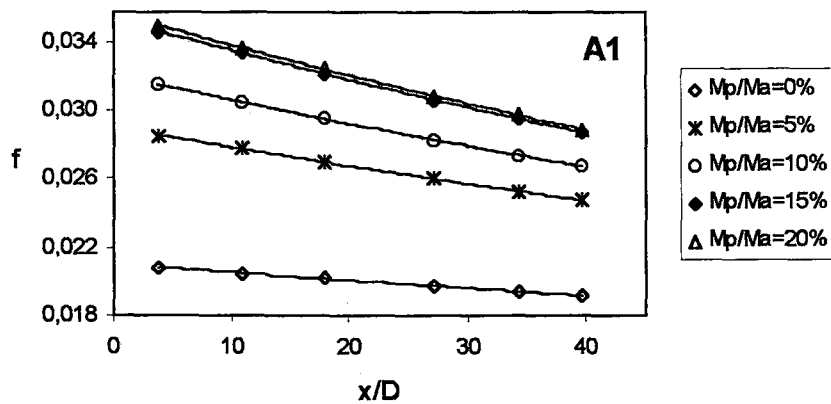
Figure 4.47. a, b, c, d Variation of friction factor f with x/D for F3 at $Re=70667$ along different test section inclinations.



a) $\alpha=0^\circ$ (Horizontal Line)



b) $\alpha=10^\circ$



c) $\alpha=20^\circ$

Figure 4.48.a, b, c Variation of friction factor, f with x/D for A1 at $Re=88333$ along different test section inclinations.

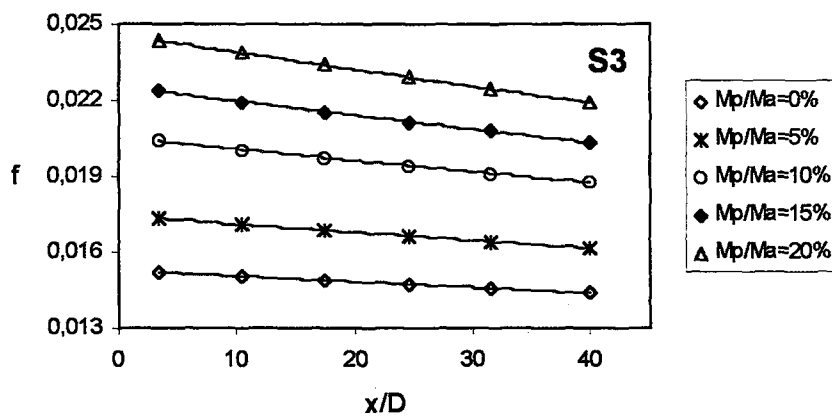
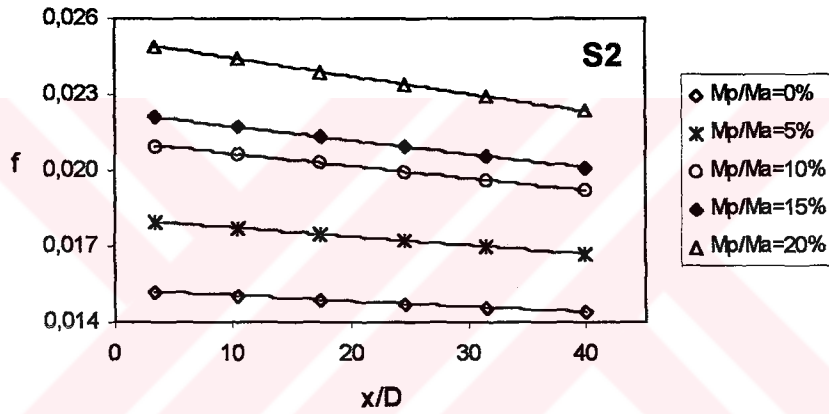
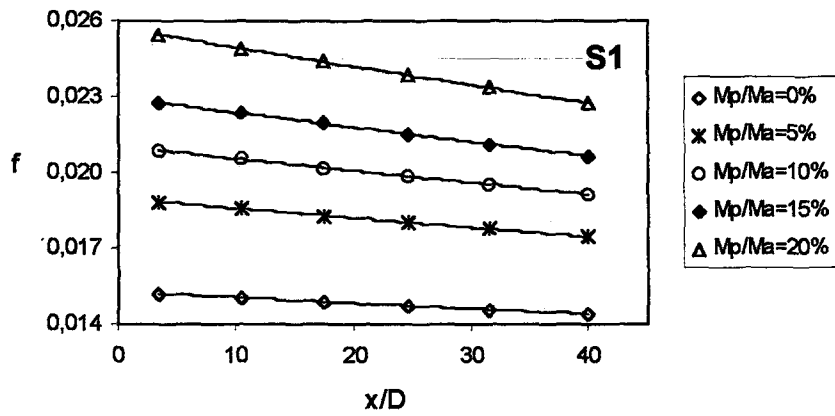


Figure 4.49 Variation of friction factor, f with x/D for S1, S2, S3 at $Re=88333$ along horizontal line.

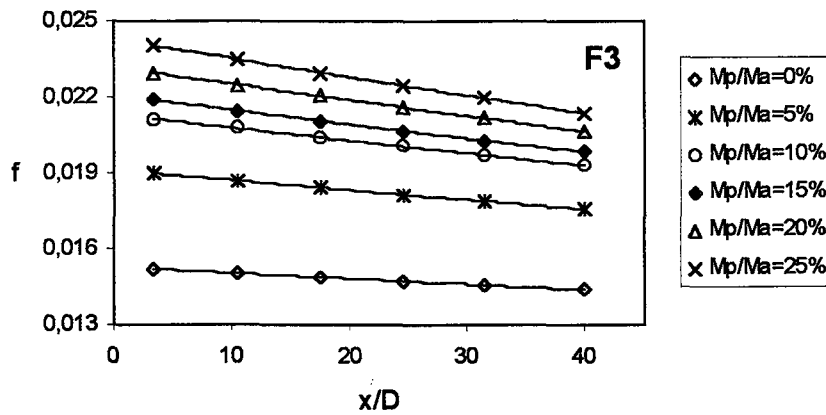
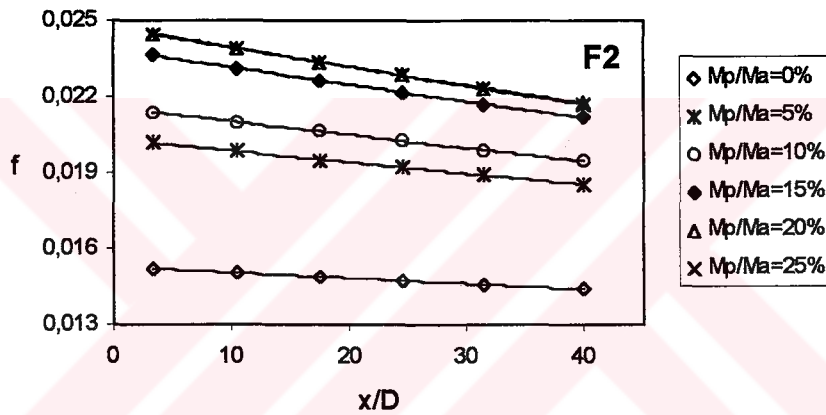
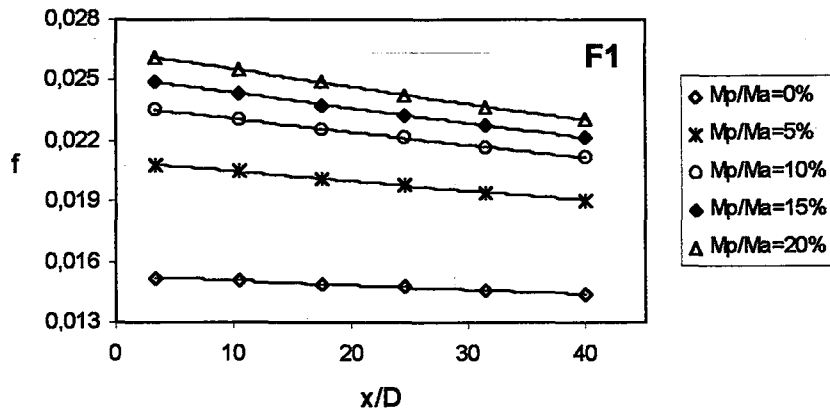


Figure 4.50 Variation of friction factor, f with x/D for F1, F2, F3 at $Re=88333$ along horizontal line.

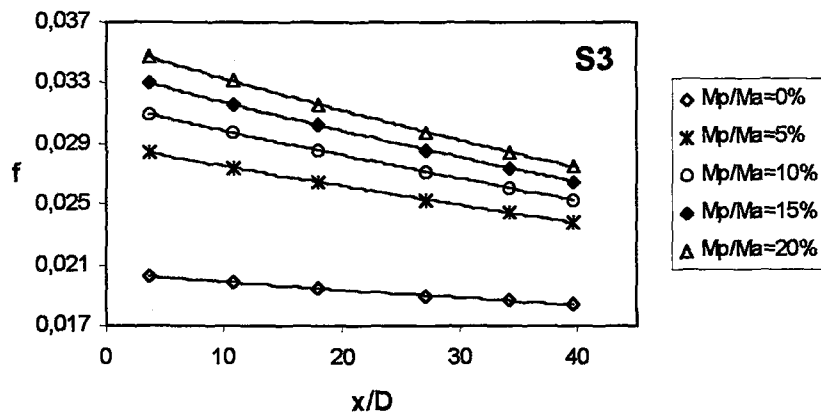
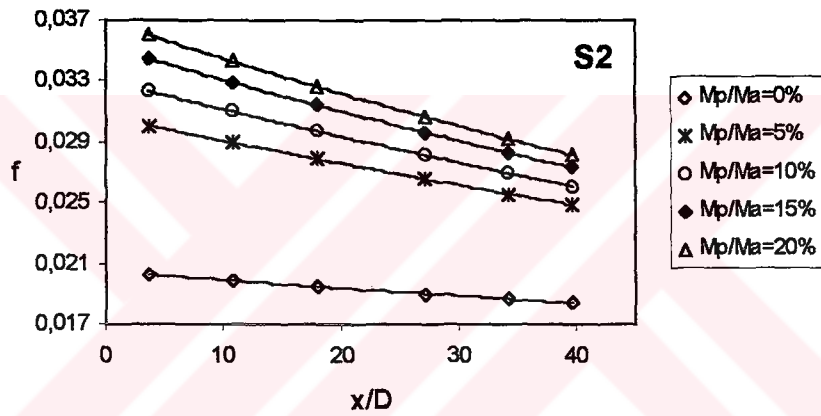
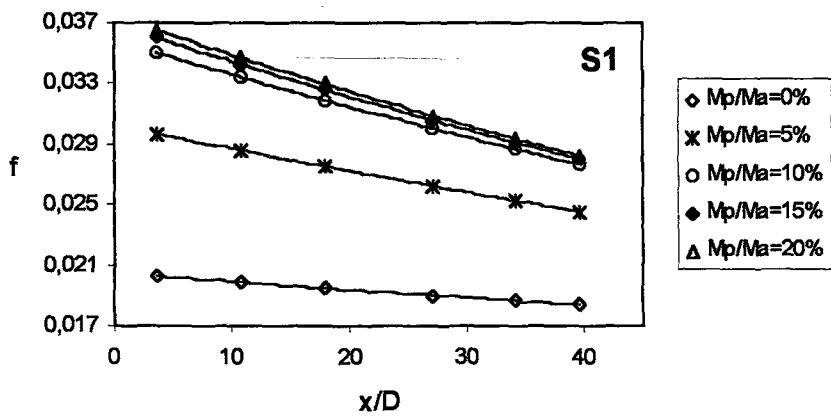


Figure 4.51 Variation of friction factor, f with x/D for S1, S2, S3 at $Re=88333$ along inclined line, $\alpha=10^\circ$.

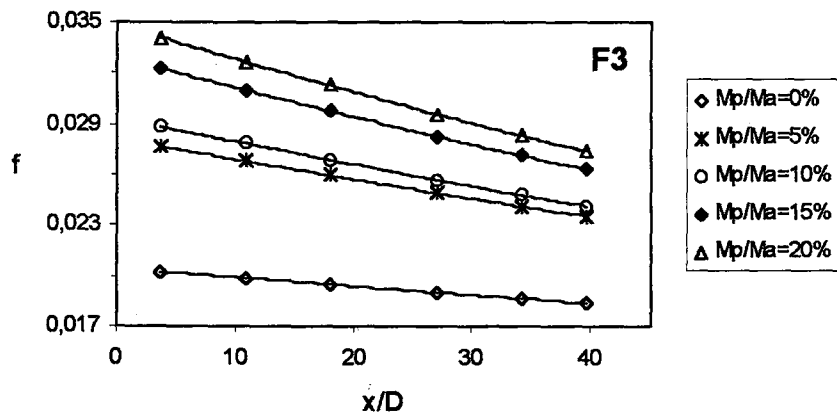
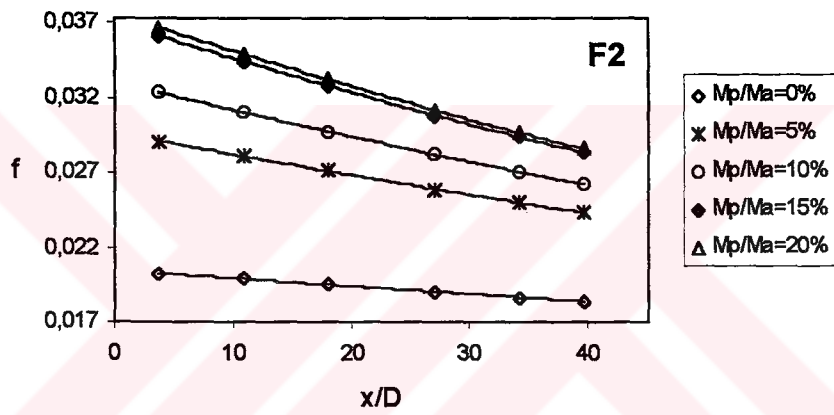
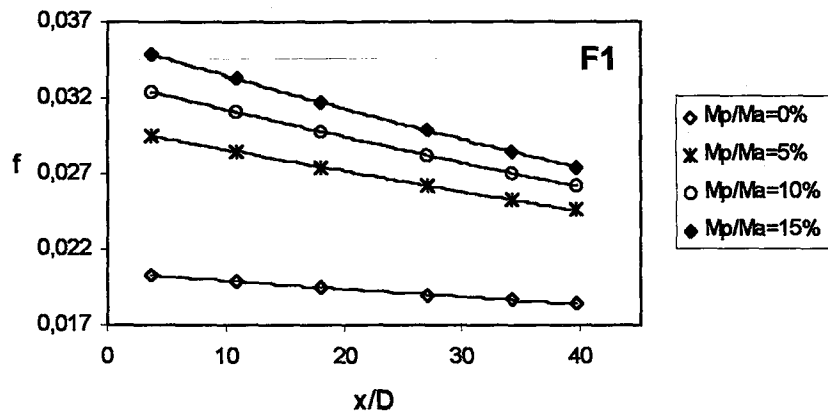


Figure 4.52 Variation of friction factor, f with x/D for F1, F2, F3 at $Re=88333$ along inclined line, $\alpha=10^\circ$.

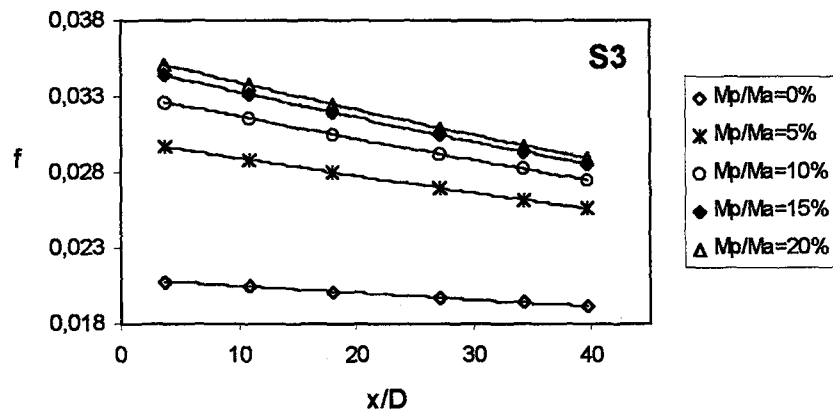
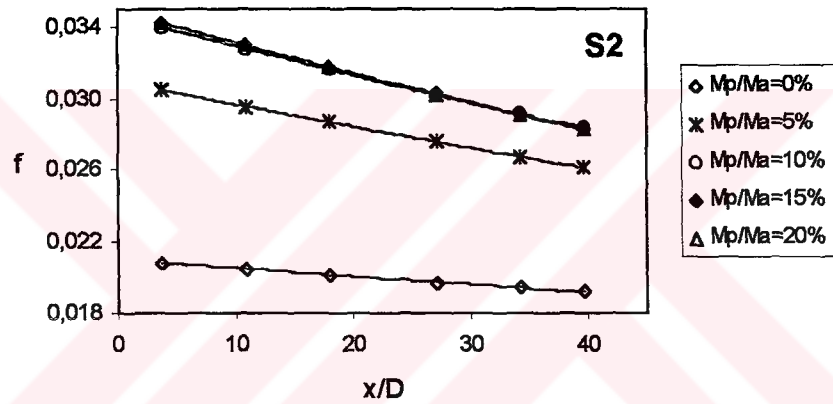
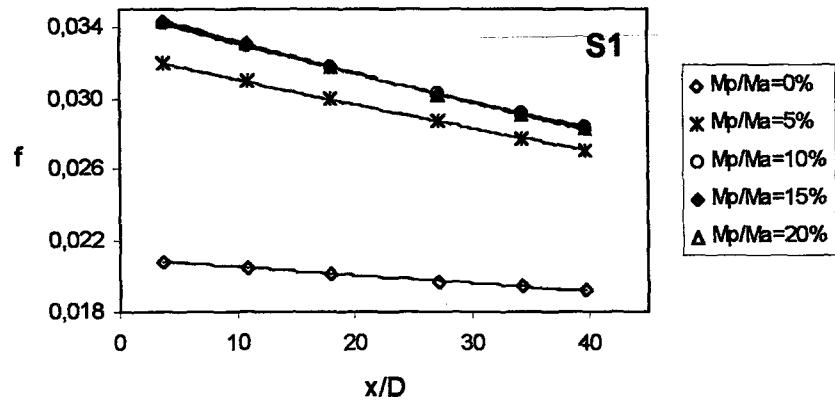


Figure 4.53 Variation of friction factor, f with x/D for S1, S2, S3 at $Re=88333$ along inclined line, $\alpha=20^\circ$.

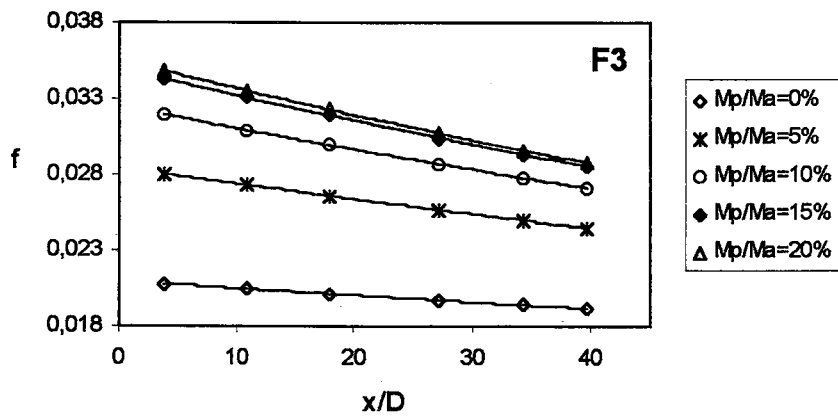
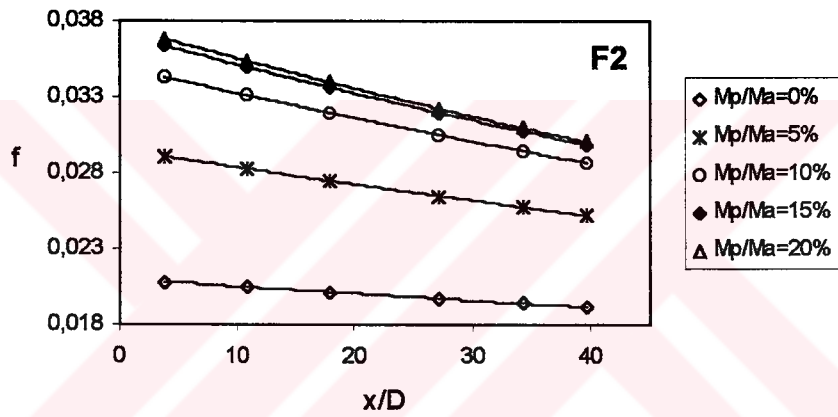
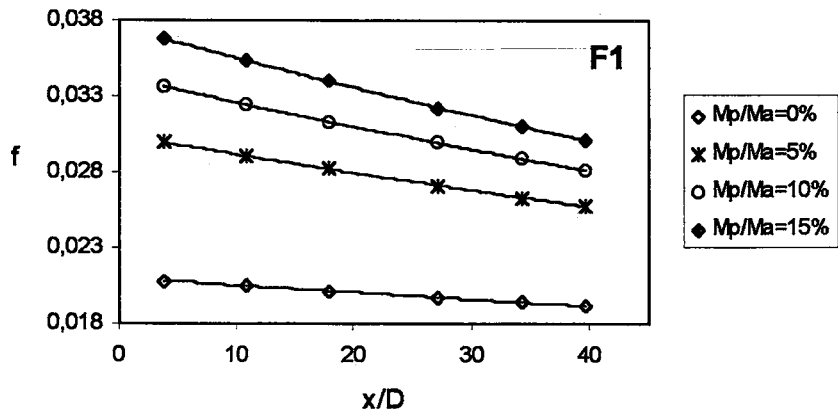
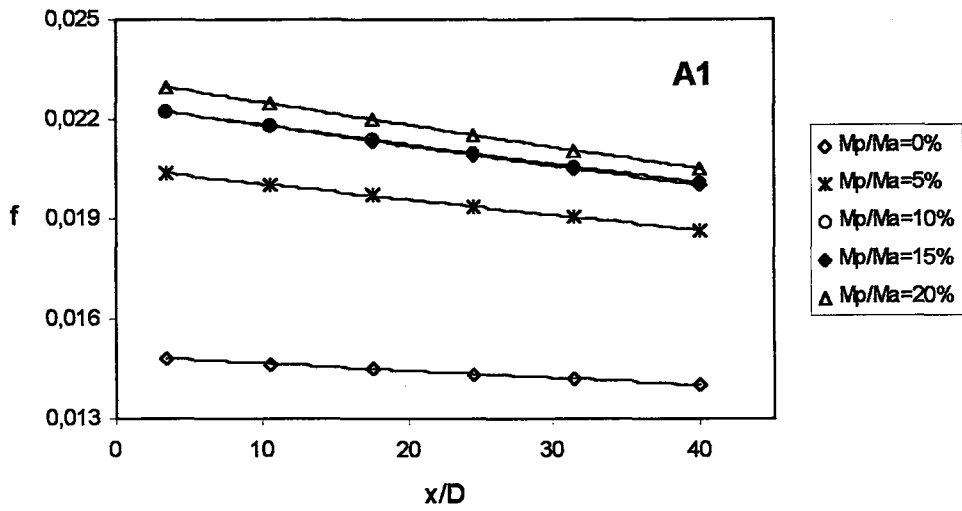
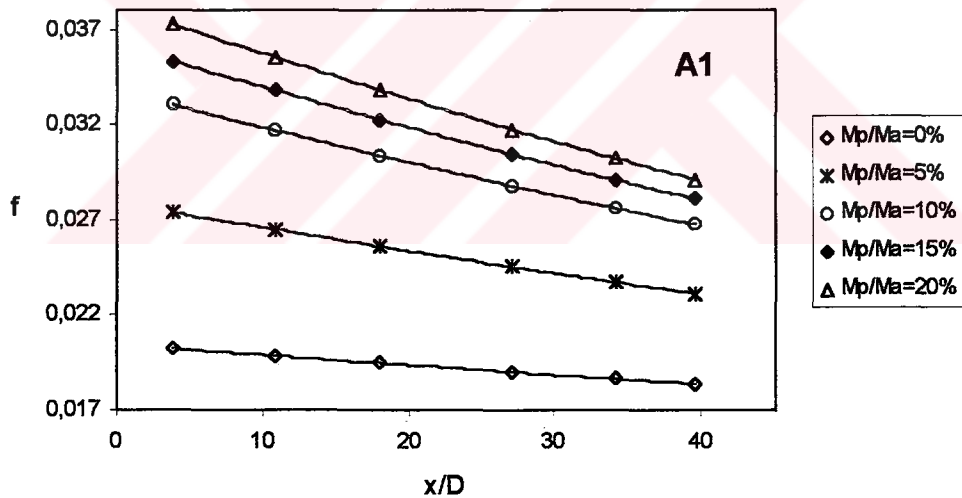


Figure 4.54 Variation of friction factor, f with x/D for F1, F2, F3 at $Re=88333$ along inclined line, $\alpha=20^\circ$.



a) $\alpha=0^\circ$ (Horizontal Line)



b) $\alpha=10^\circ$

Figure 4.55. a, b Variation of friction factor, f with x/D for A1 at $Re=98933$ along different test section inclinations.

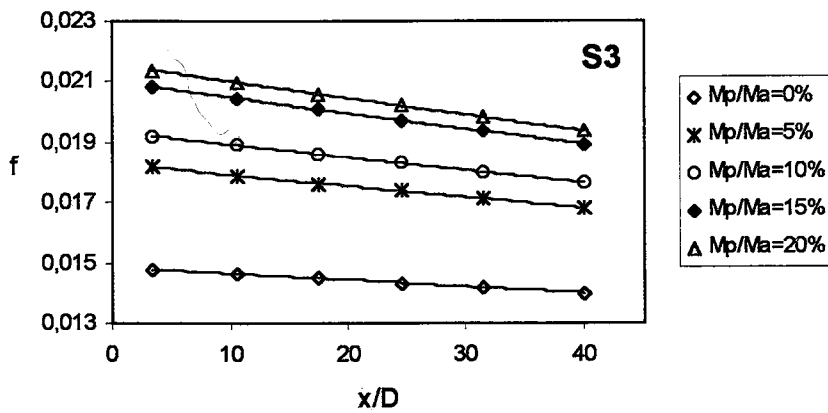
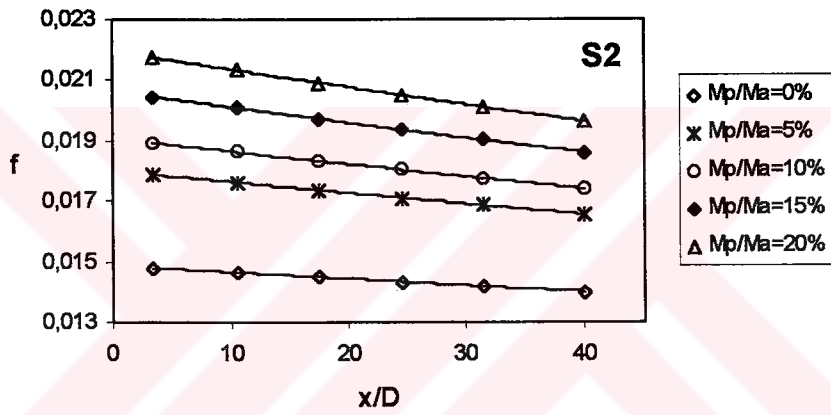
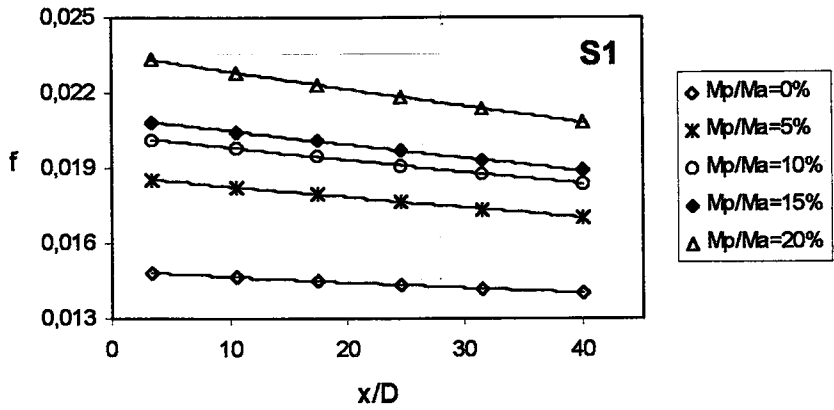


Figure 4.56 Variation of friction factor, f with x/D for S1, S2, S3 at $Re=98933$ along horizontal line.

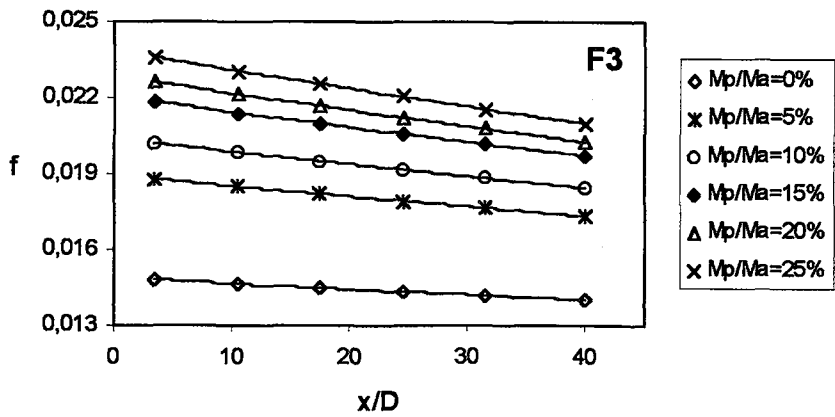
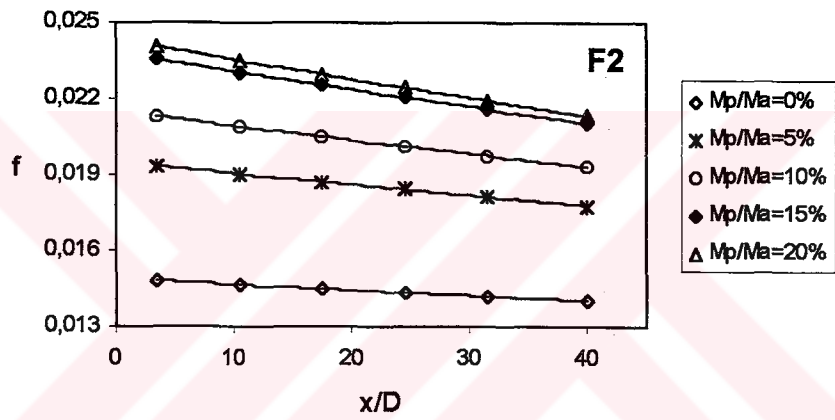
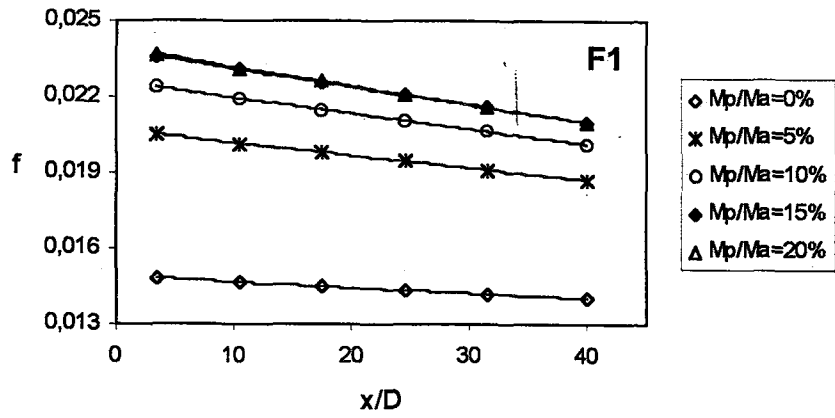


Figure 4.57 Variation of friction factor, f with x/D for F1, F2, F3 at $Re=98933$ along horizontal line.

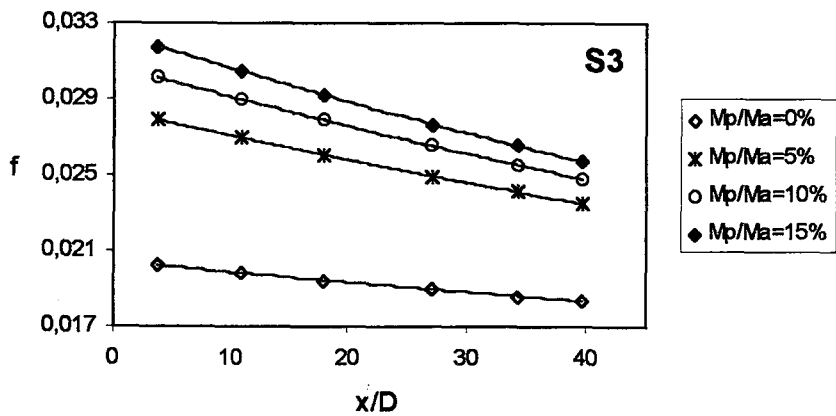
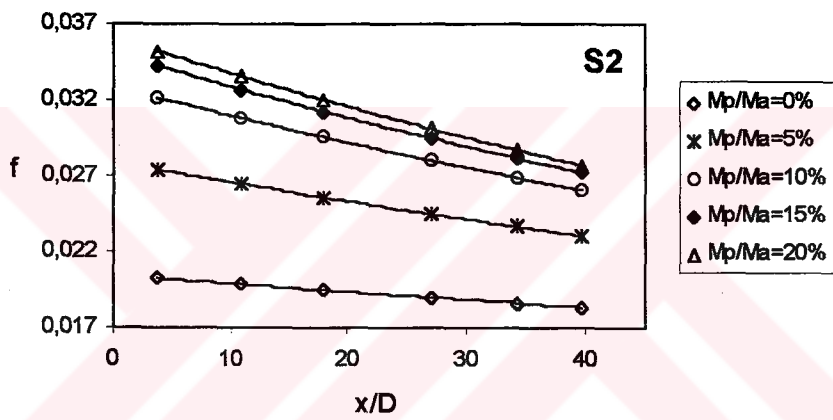
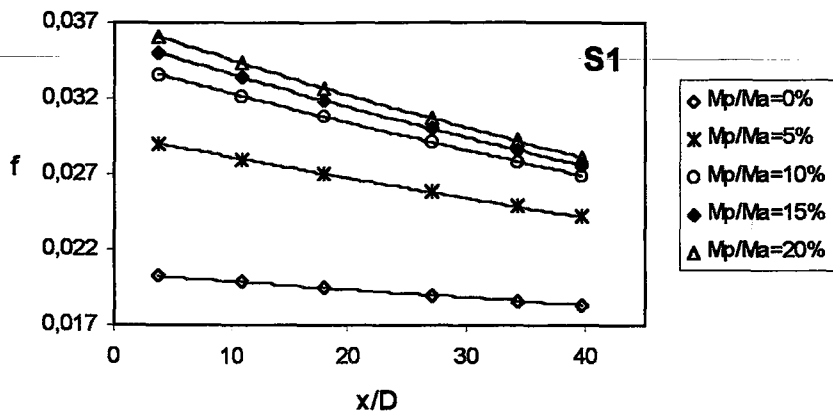


Figure 4.58 Variation of friction factor, f with x/D for S1, S2, S3 at $Re=98933$ along inclined line, $\alpha=10^\circ$.

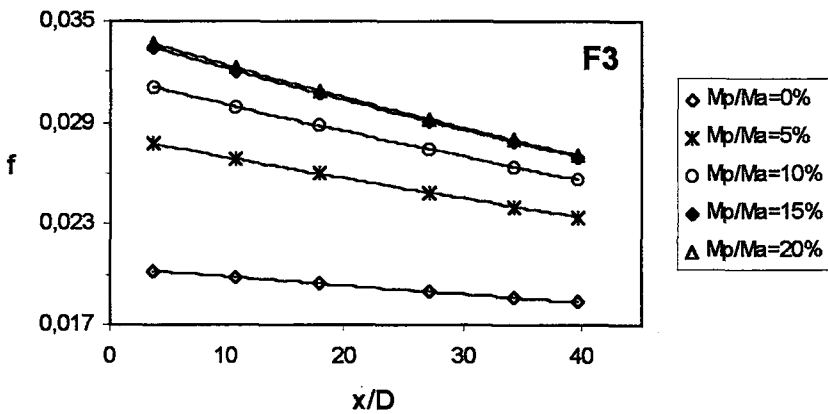
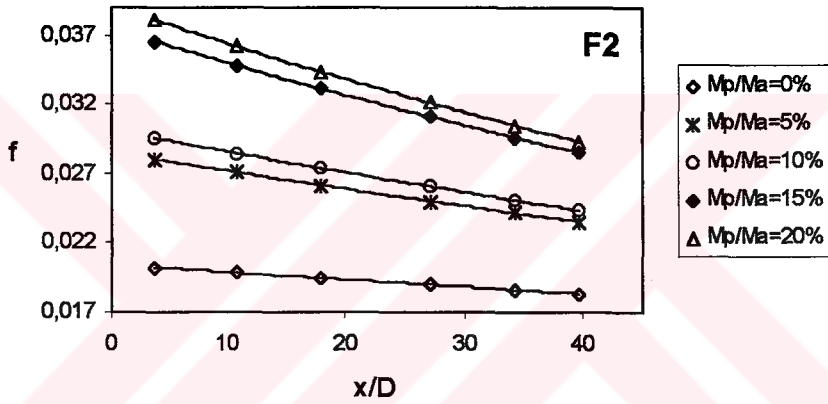
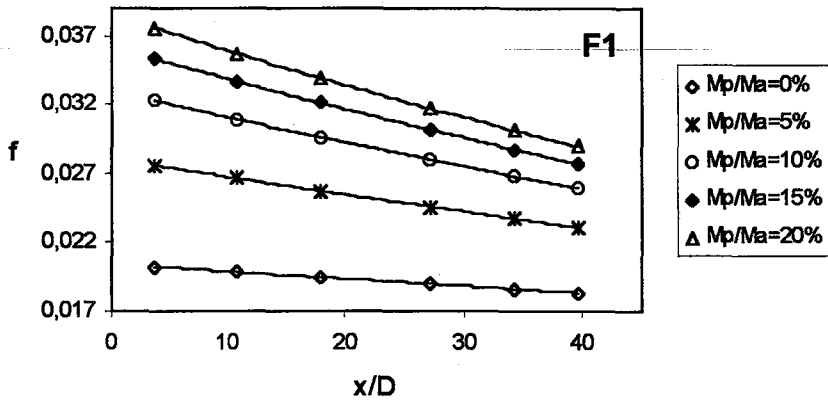
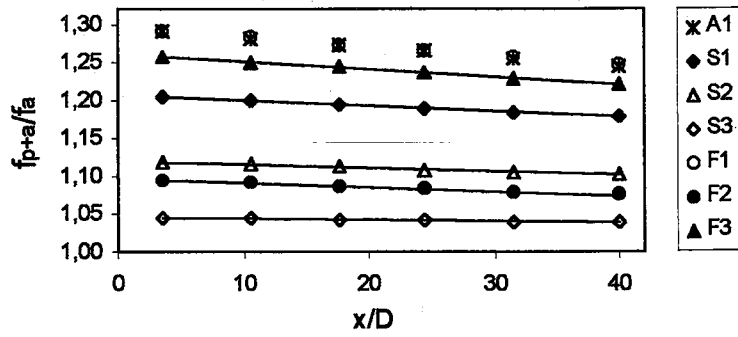
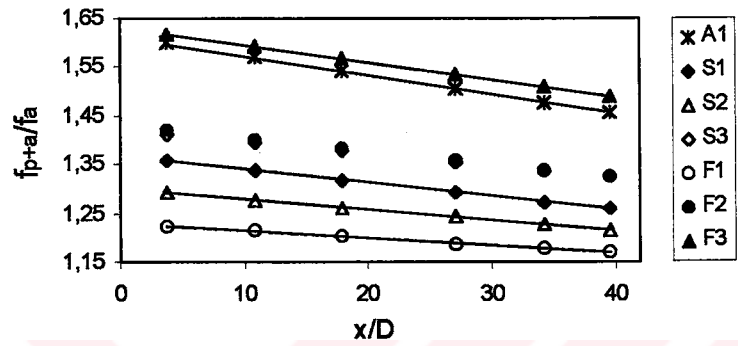


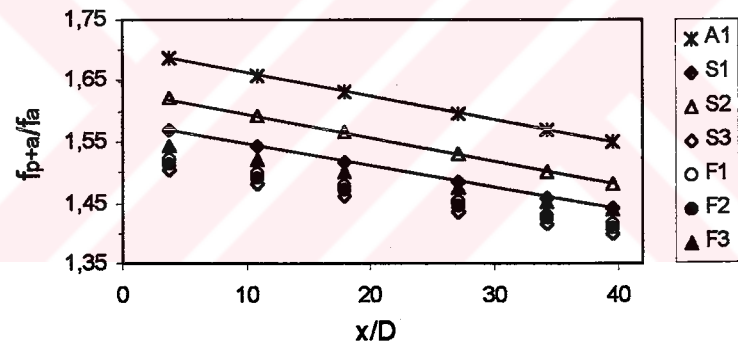
Figure 4.59 Variation of friction factor, f with x/D for F1, F2, F3 at $Re=98933$ along inclined line, $\alpha=10^\circ$.



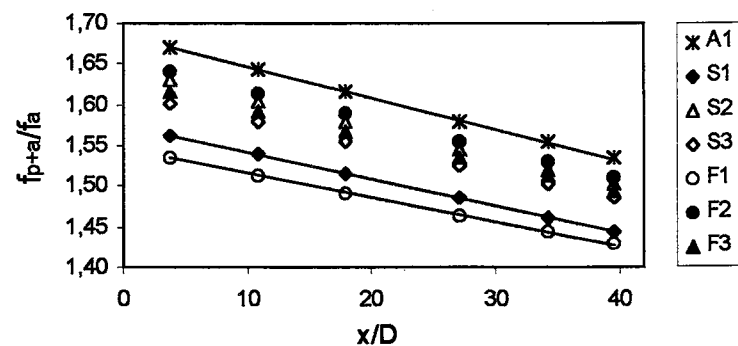
a) $\alpha = 0^\circ$



b) $\alpha = 10^\circ$

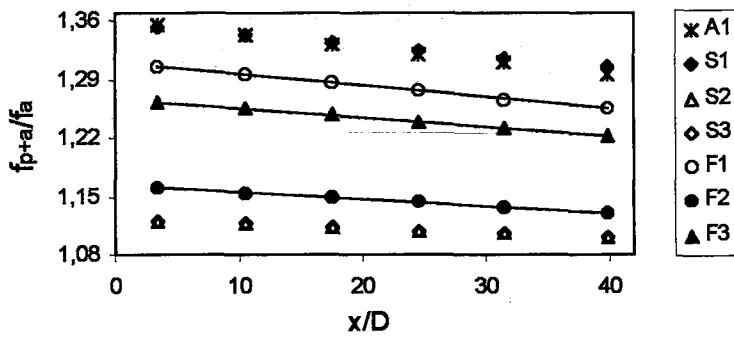


c) $\alpha = 20^\circ$

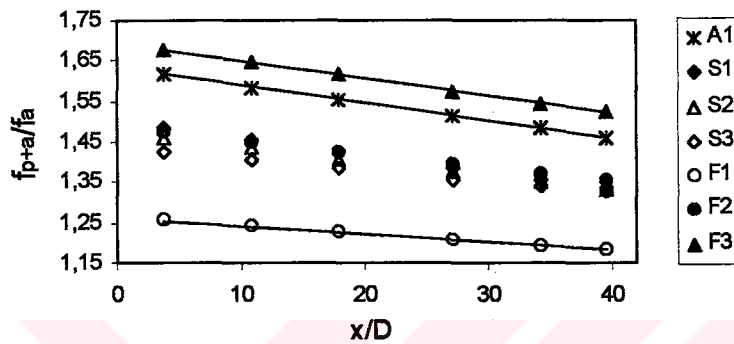


d) $\alpha = 30^\circ$

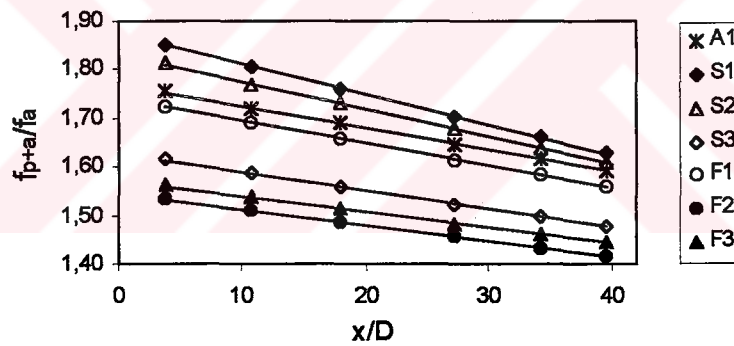
Figure 4.60. a, b, c, d Variation of f_{p+a}/f_a with x/D at $Re=53000$ and $M_p/M_a=5\%$ along different test section inclinations.



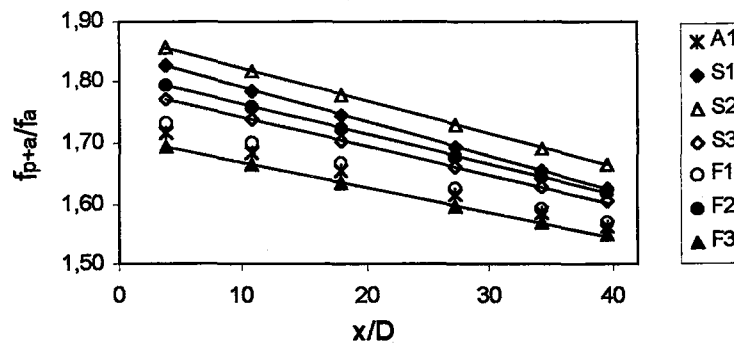
a) $\alpha=0^\circ$



b) $\alpha=10^\circ$

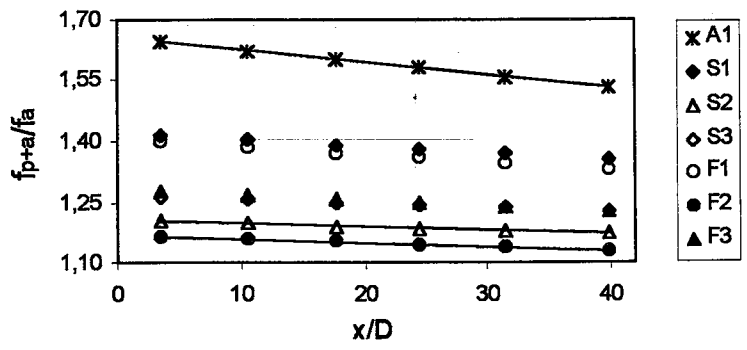


c) $\alpha=20^\circ$

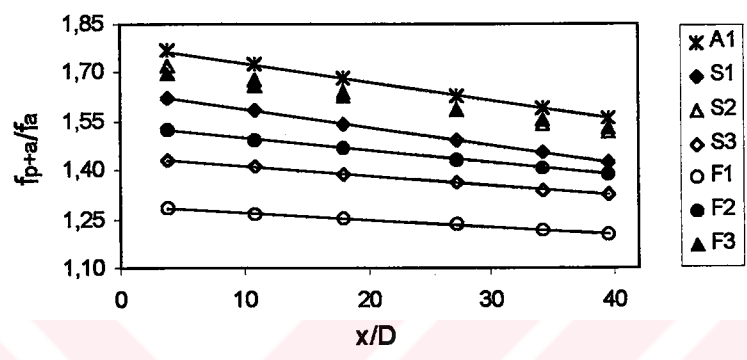


d) $\alpha=30^\circ$

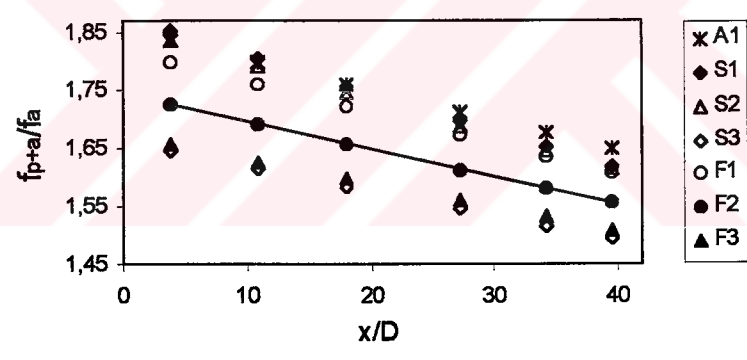
Figure 4.61. a,b,c,d Variation of f_{p+a}/f_a with x/D at $Re=53000$ and $M_p/M_a=10\%$ along different test section inclinations.



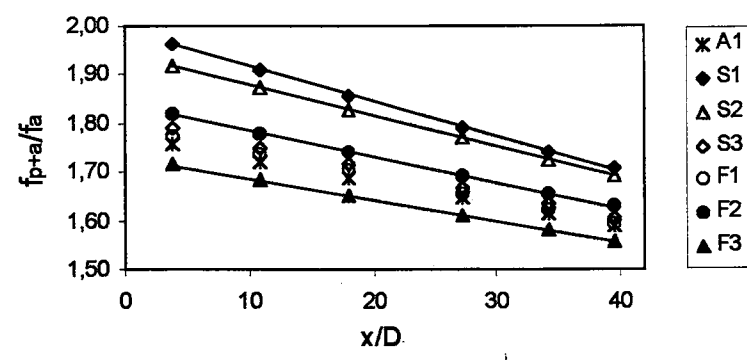
a) $\alpha=0^\circ$



b) $\alpha=10^\circ$

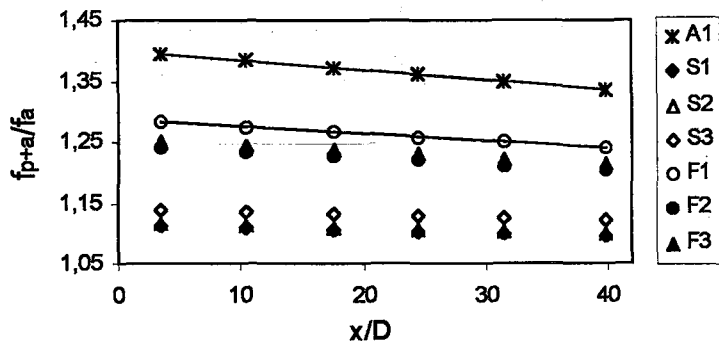


c) $\alpha=20^\circ$

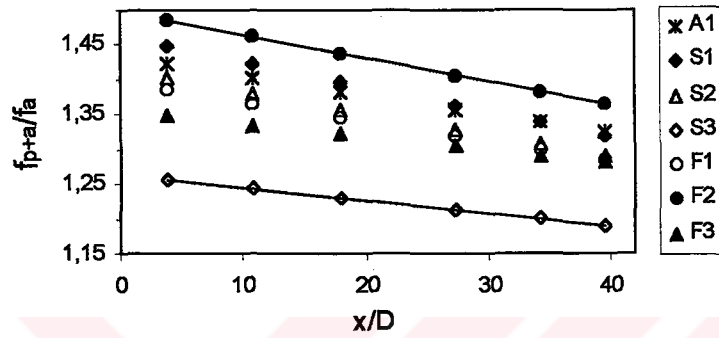


d) $\alpha=30^\circ$

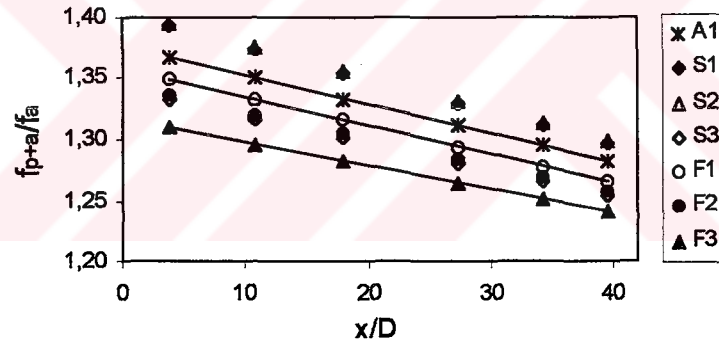
Figure 4.62.a,b,c,d Variation of f_{p+a}/f_a with x/D at $Re=53000$ and $M_p/M_a=15\%$ along different test section inclinations.



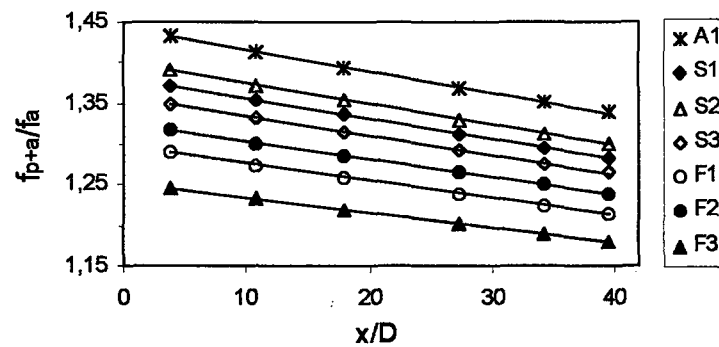
a) $\alpha = 0^\circ$



b) $\alpha = 10^\circ$

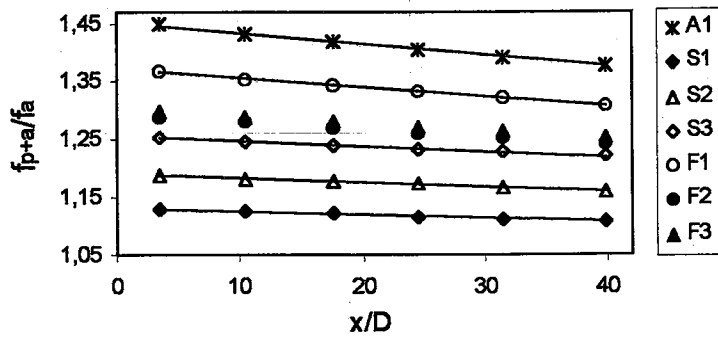


c) $\alpha = 20^\circ$

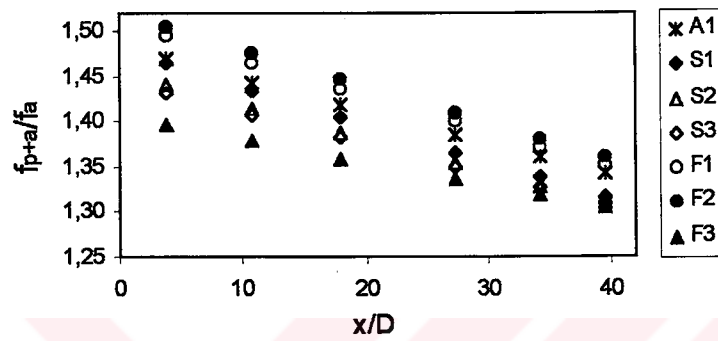


d) $\alpha = 30^\circ$

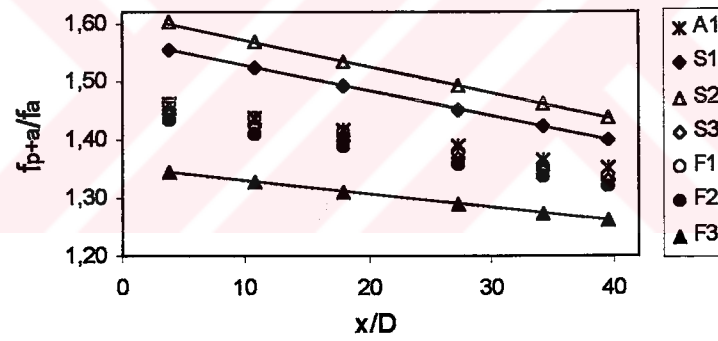
Figure 4.63.a,b,c,d Variation of f_{p+a}/f_a with x/D at $Re=70667$ and $M_p/M_a=5\%$ along different test section inclinations.



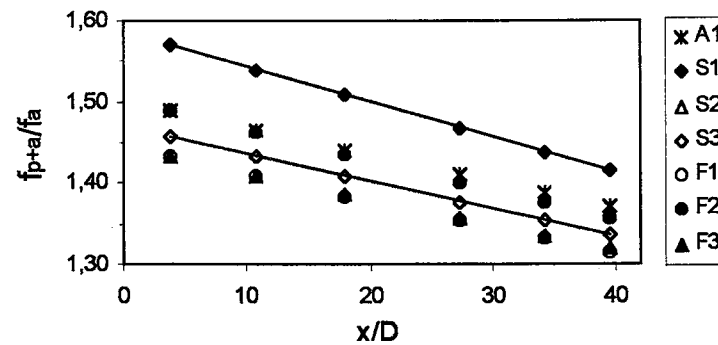
a) $\alpha=0^\circ$



b) $\alpha=10^\circ$

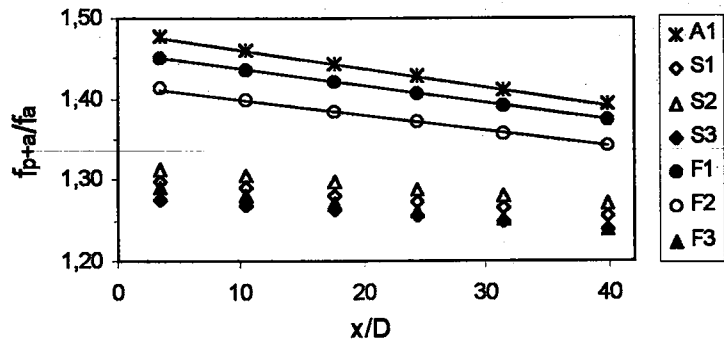


c) $\alpha=20^\circ$

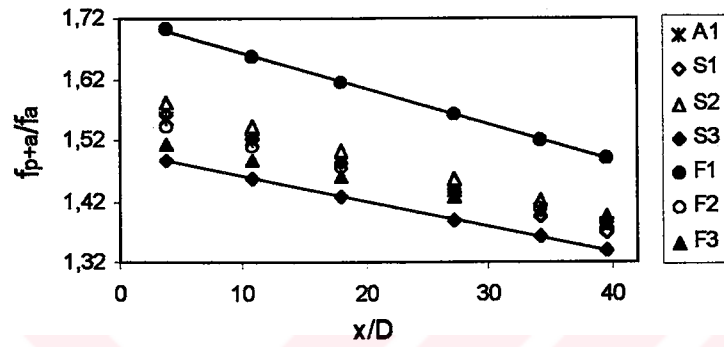


d) $\alpha=30^\circ$

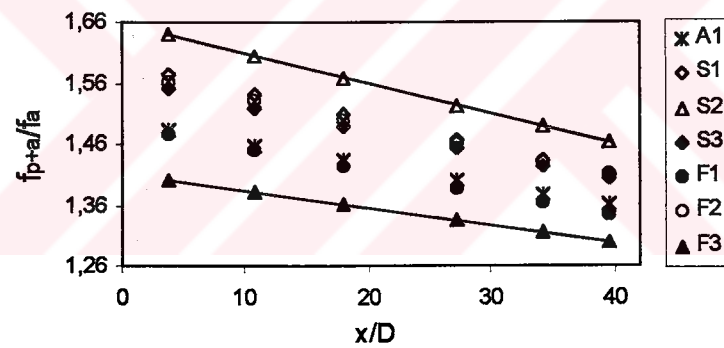
Figure 4.64. a,b,c,d Variation of f_{p+a}/f_a with x/D at $Re=70667$ and $M_p/M_a=10\%$ along different test section inclinations.



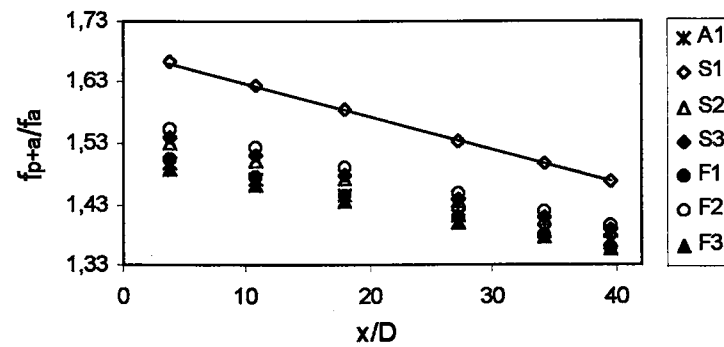
a) $\alpha=0^\circ$



b) $\alpha=10^\circ$

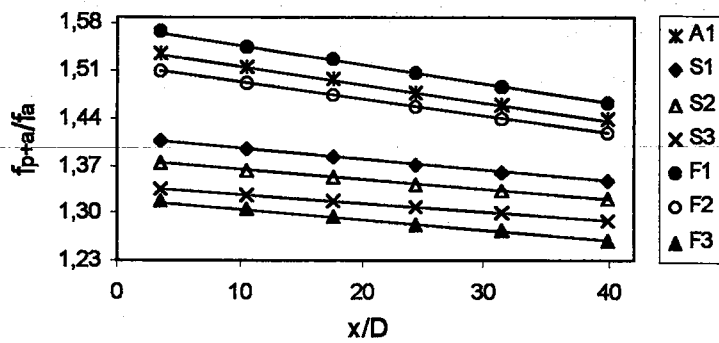


c) $\alpha=20^\circ$

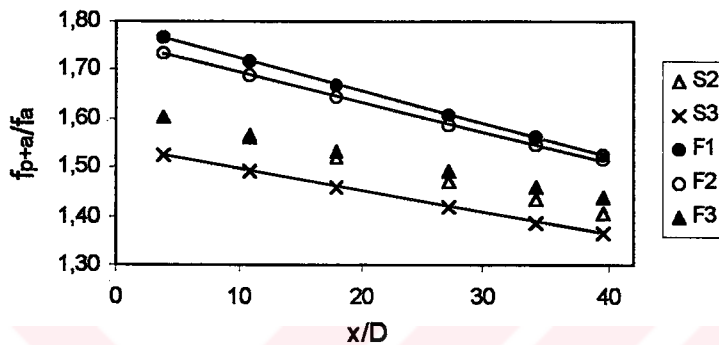


d) $\alpha=30^\circ$

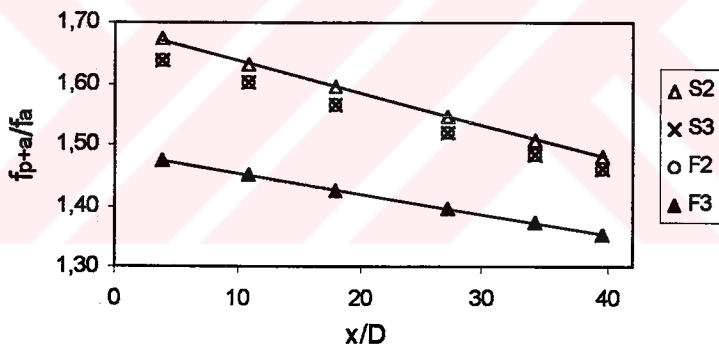
Figure 4.65.a,b,c,d Variation of f_{p+a}/f_a with x/D at $Re=70667$ and $M_p/M_a=15\%$ along different test section inclinations.



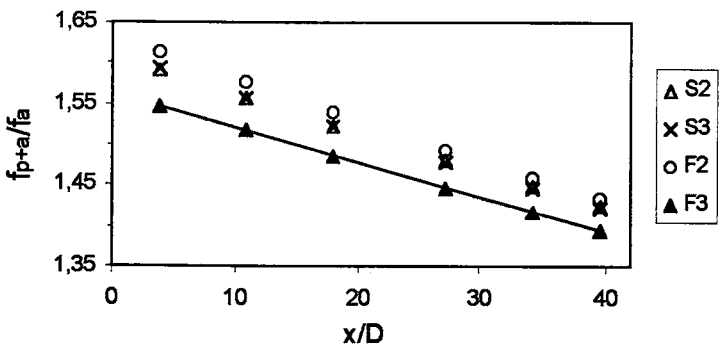
a) $\alpha = 0^\circ$



b) $\alpha = 10^\circ$

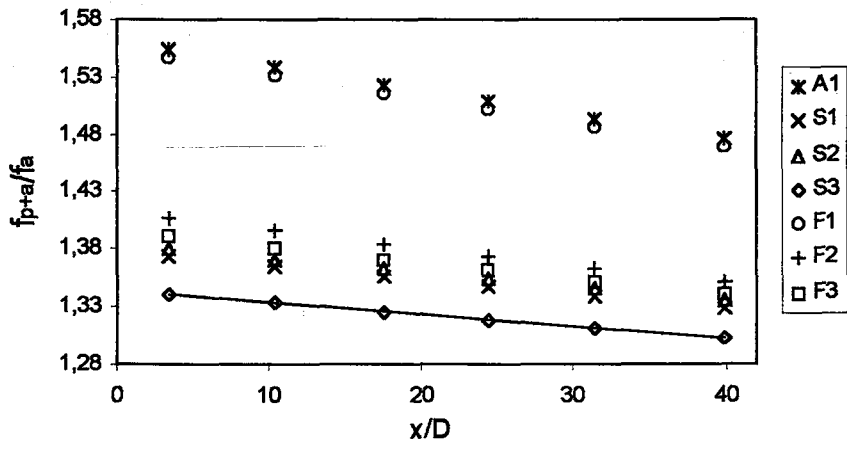


c) $\alpha = 20^\circ$

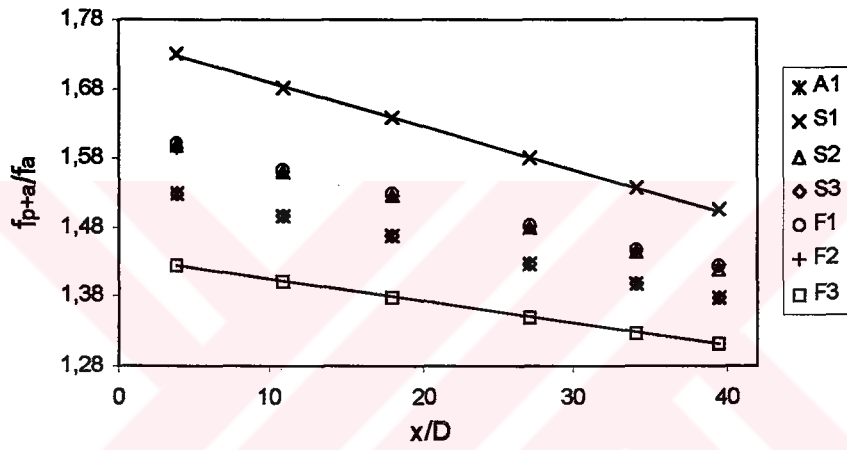


d) $\alpha = 30^\circ$

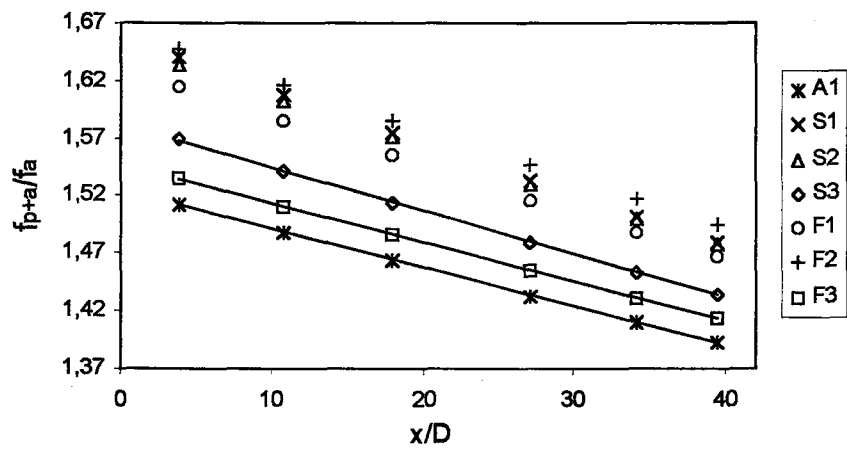
Figure 4.66.a,b,c,d Variation of f_{p+a}/f_a with x/D at $Re=70667$ and $M_p/M_a=20\%$ along different test section inclinations.



a) $\alpha=0^\circ$

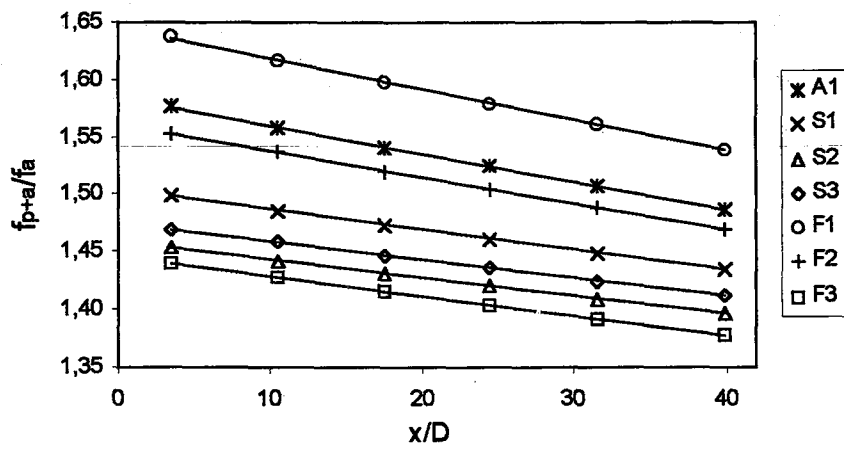


b) $\alpha=10^\circ$

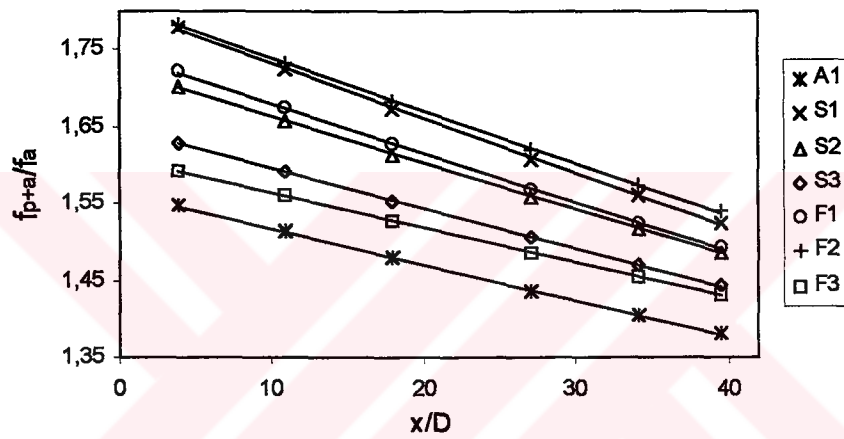


c) $\alpha=20^\circ$

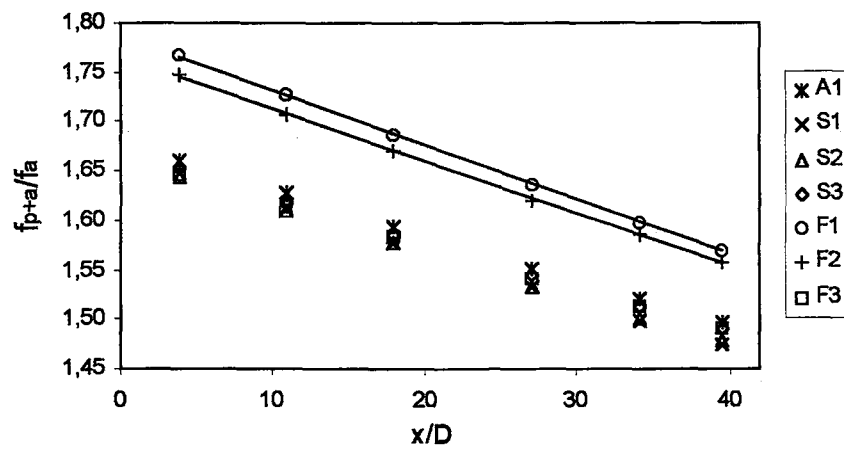
Figure 4.67. a, b, c Variation of f_{p+a}/f_a with x/D at $Re=88333$ and $M_p/M_a=10\%$ along different test section inclinations.



a) $\alpha=0^\circ$

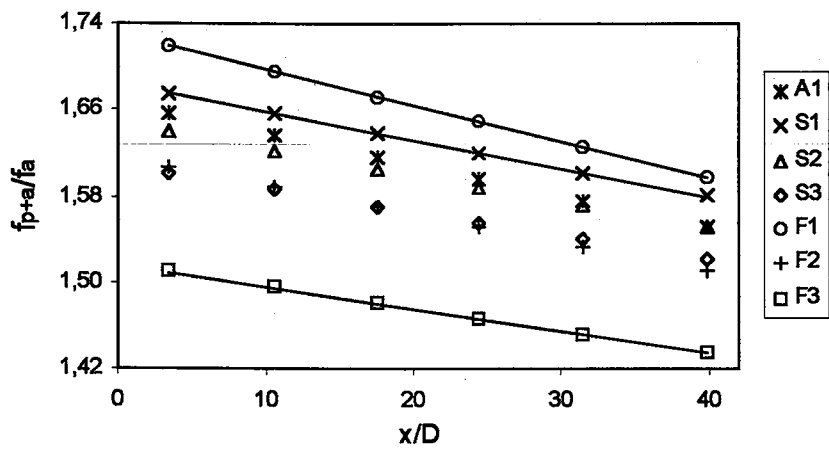


b) $\alpha=10^\circ$

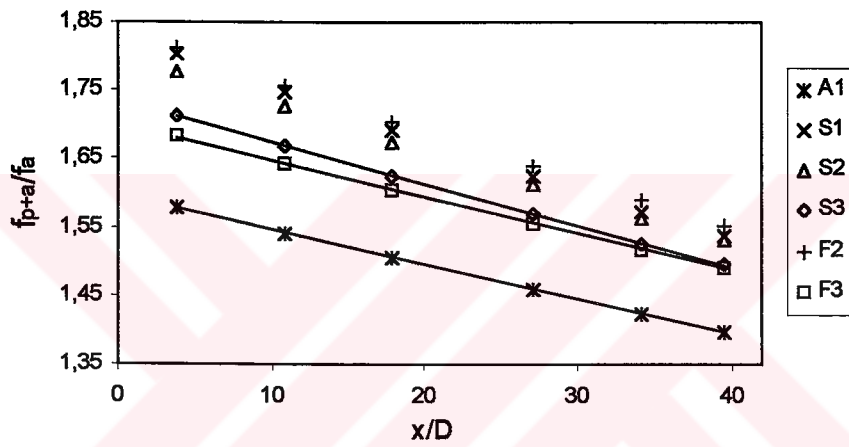


c) $\alpha=20^\circ$

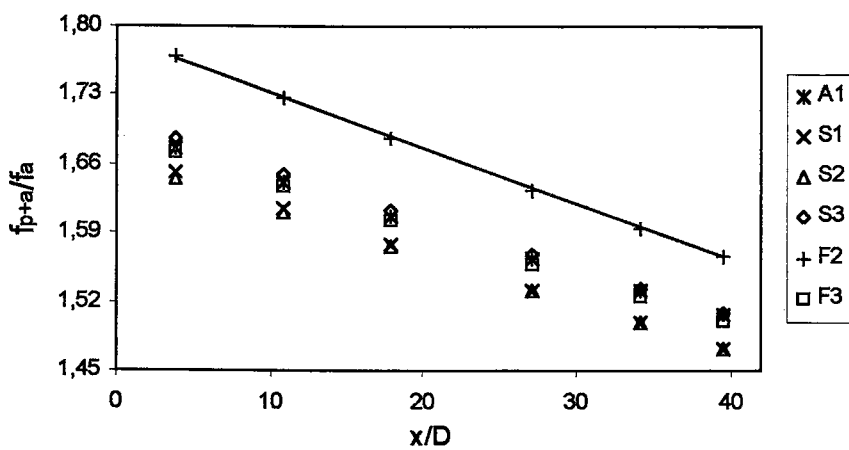
Figure 4.68.a,b,c Variation of f_{p+ra}/f_a with x/D at $Re=88333$ and $M_p/M_a=15\%$ along different test section inclinations.



a) $\alpha = 0^\circ$

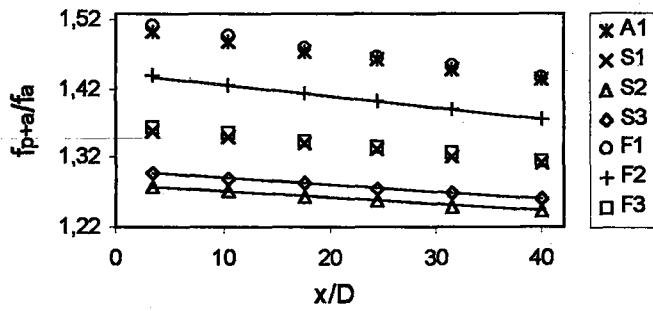


b) $\alpha = 10^\circ$

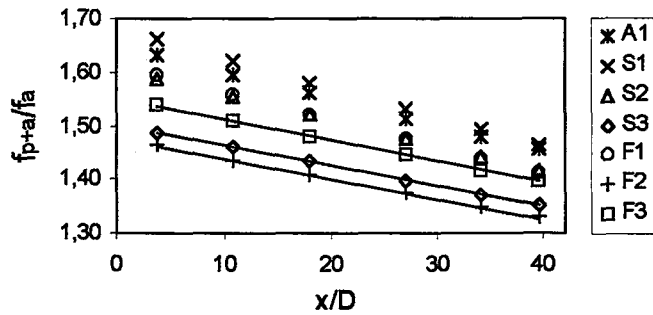


c) $\alpha = 20^\circ$

Figure 4.69.a,b,c Variation of f_{p+a}/f_a with x/D at $Re=88333$ and $M_p/M_a=20\%$ along different test section inclinations.

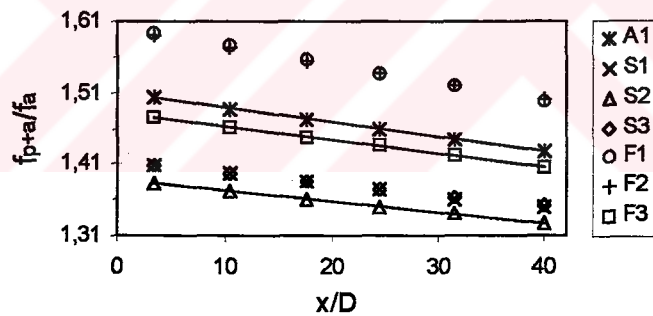


a) $\alpha=0^\circ$

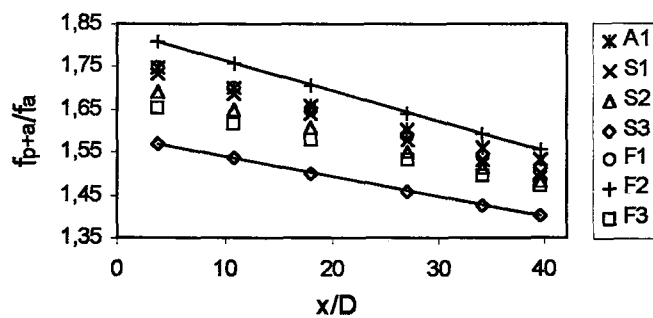


b) $\alpha=10^\circ$

Figure 4.70.a,b Variation of f_{p+a}/f_a with x/D at $Re=98933$ and $M_p/M_a=10\%$ along different test section inclinations.



a) $\alpha=0^\circ$



b) $\alpha=10^\circ$

Figure 4.71.a,b Variation of f_{p+a}/f_a with x/D at $Re=98933$ and $M_p/M_a=15\%$ along different test section inclinations.

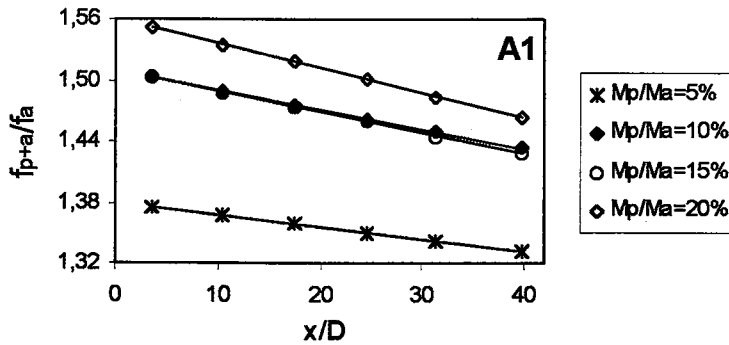
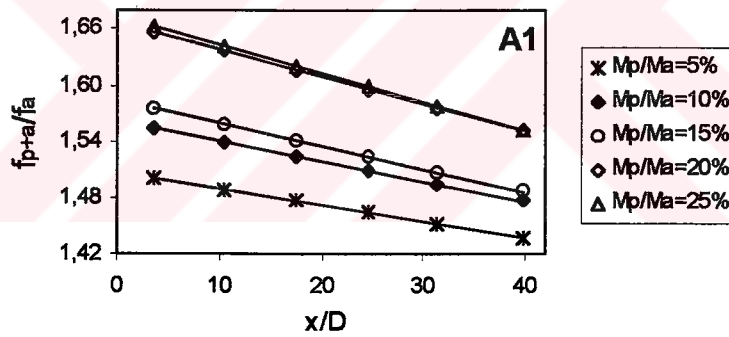
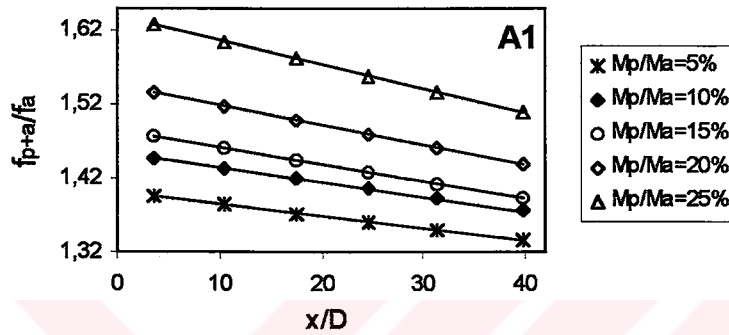
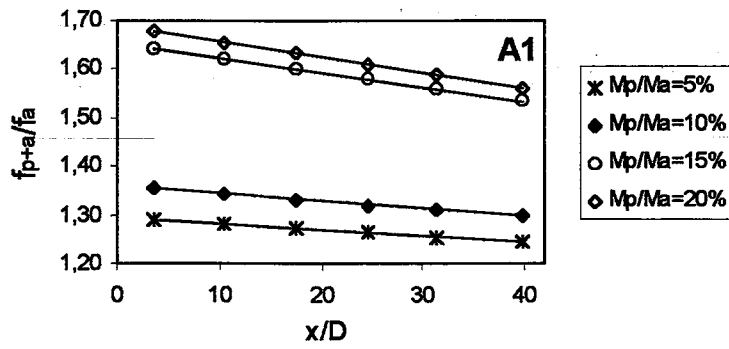
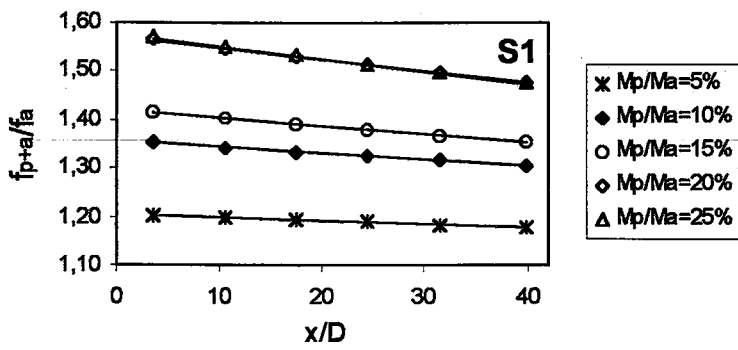
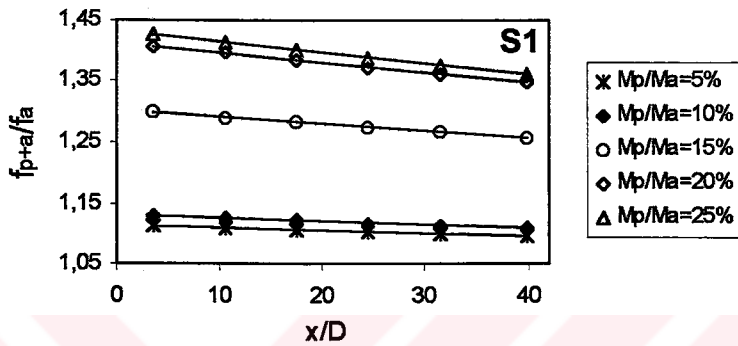


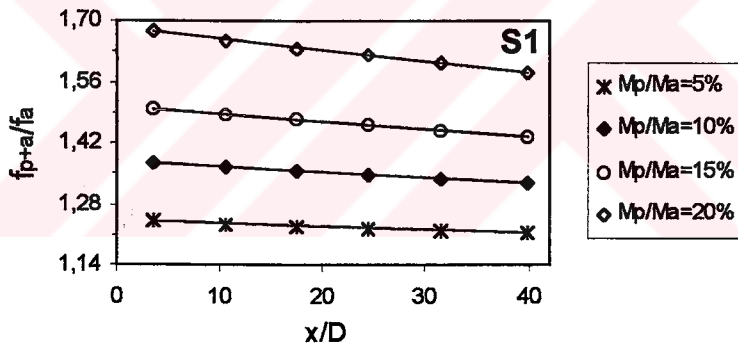
Figure 4.72. a,b,c,d Variation of f_{p+a}/f_a with x/D for A1 at different Re numbers along horizontal line.



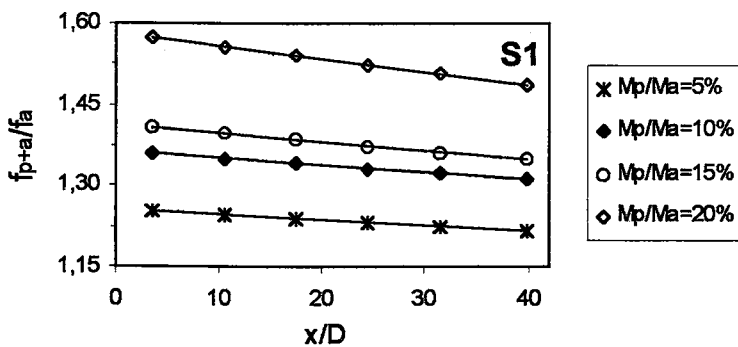
a) Re=53000



b) Re=70667

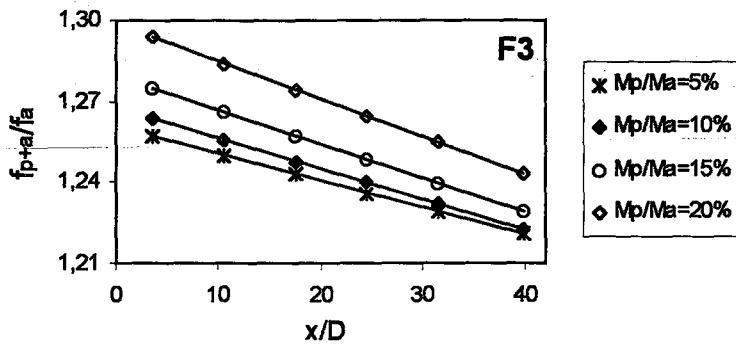


c) Re=88333

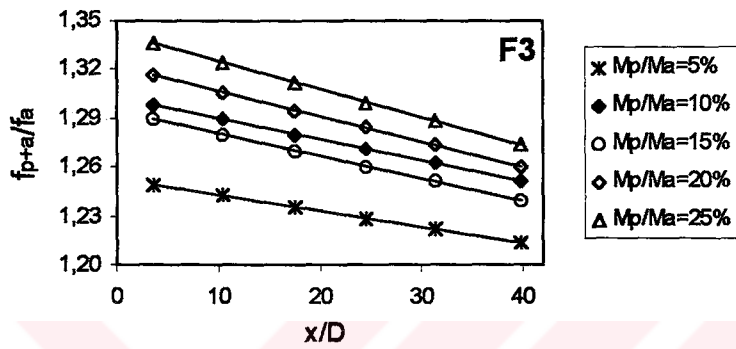


d) Re=98933

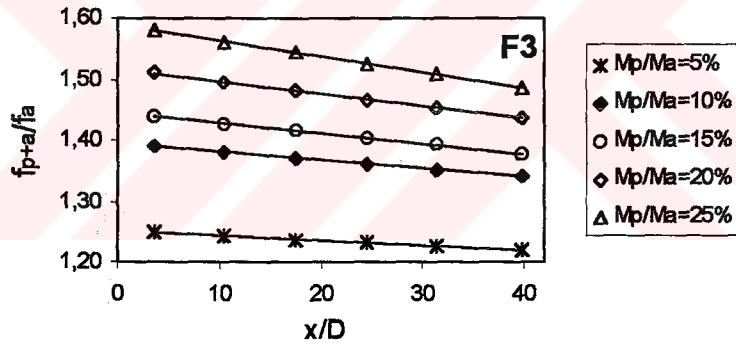
Figure 4.73.a,b,c,d Variation of f_{p+a}/f_a with x/D for S1 at different Re numbers along horizontal line.



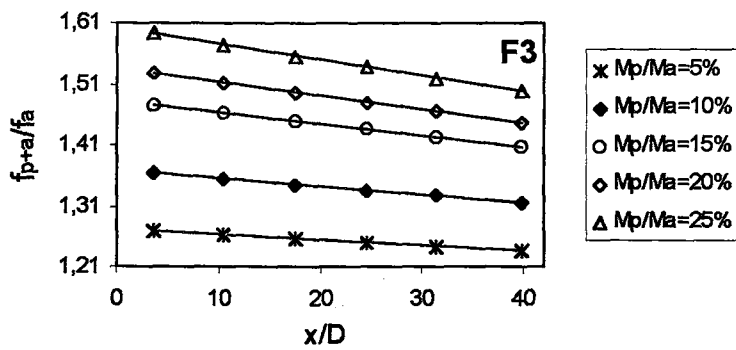
a) Re=53000



b) Re=70667

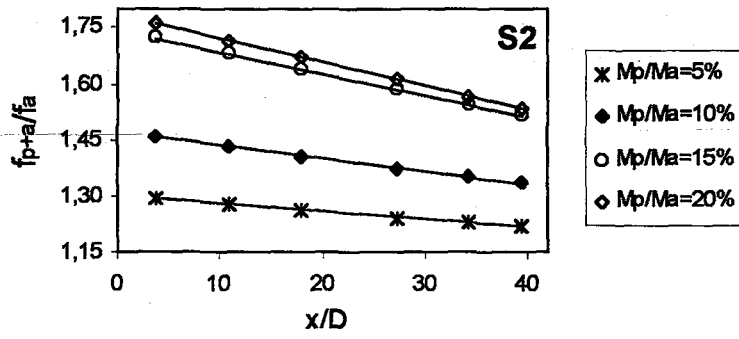


c) Re=88333

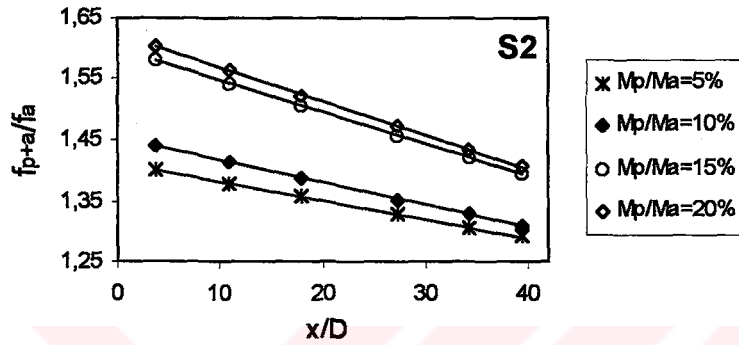


d) Re=98933

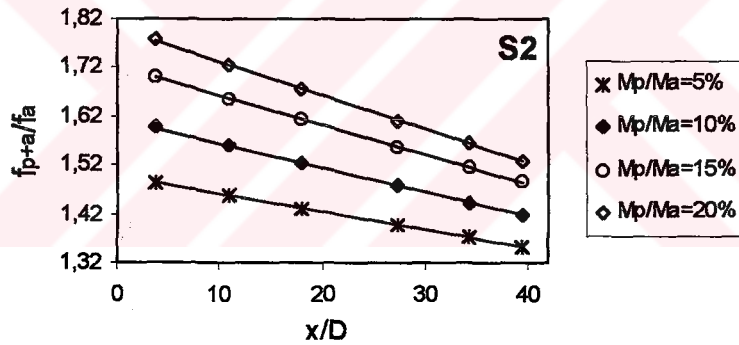
Figure 4.74.a,b,c,d Variation of f_{p+a}/f_a with x/D for F3 at different Re numbers along horizontal line.



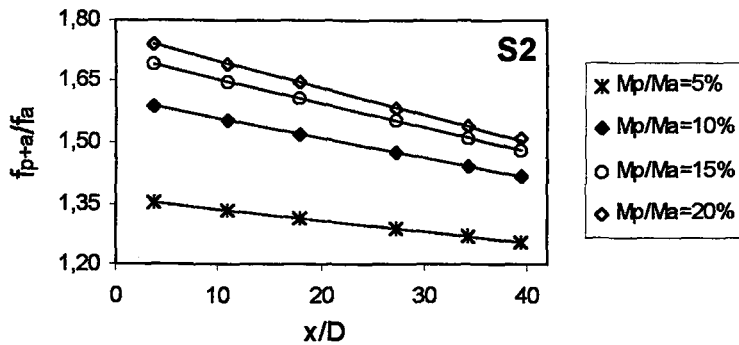
a) $Re=53000$



b) $Re=70667$

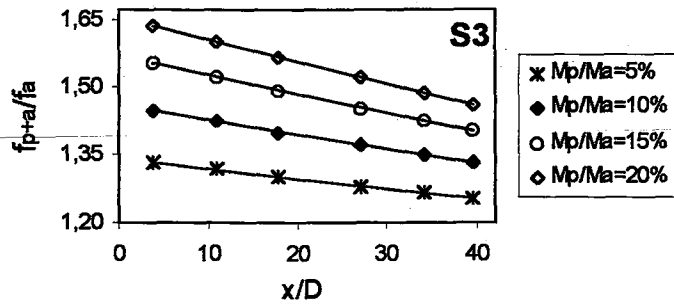


c) $Re=88333$

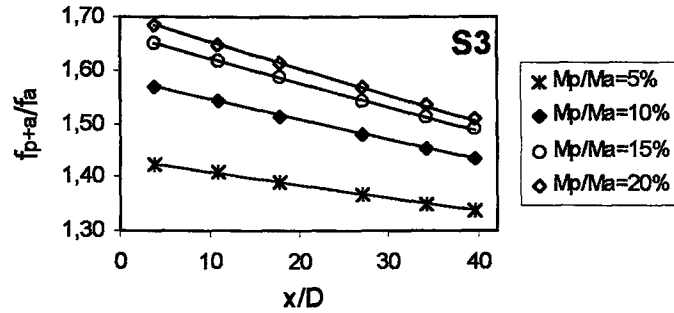


d) $Re=98933$

Figure 4.75.a,b,c,d Variation of f_{p+a}/f_a with x/D for S2 at different Re numbers along inclined line, $\alpha=10^\circ$.

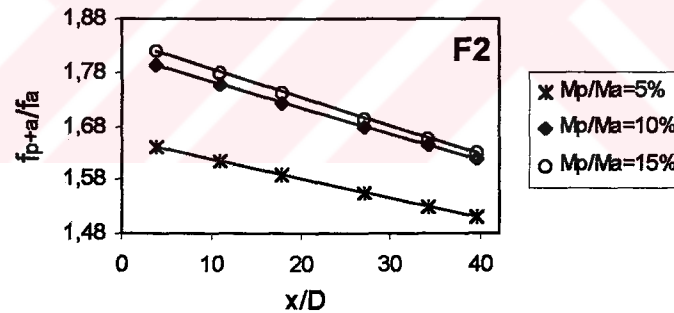


a) Re=70667

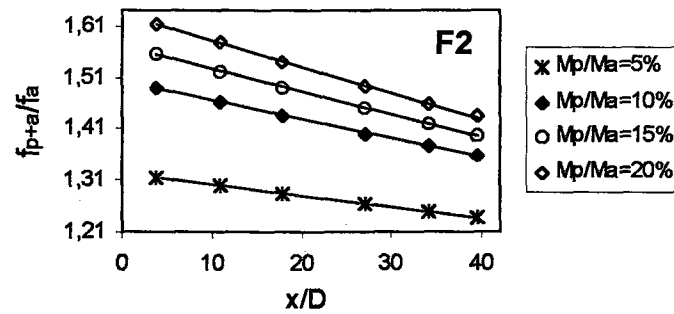


b) Re=88333

Figure 4.76.a,b Variation of f_{p+a}/f_a with x/D for S3 at different Re numbers along inclined line, $\alpha=20^\circ$.



a) Re=53000



b) Re=70667

Figure 4.77.a,b Variation of f_{p+a}/f_a with x/D for F2 at different Re numbers along inclined line, $\alpha=30^\circ$.

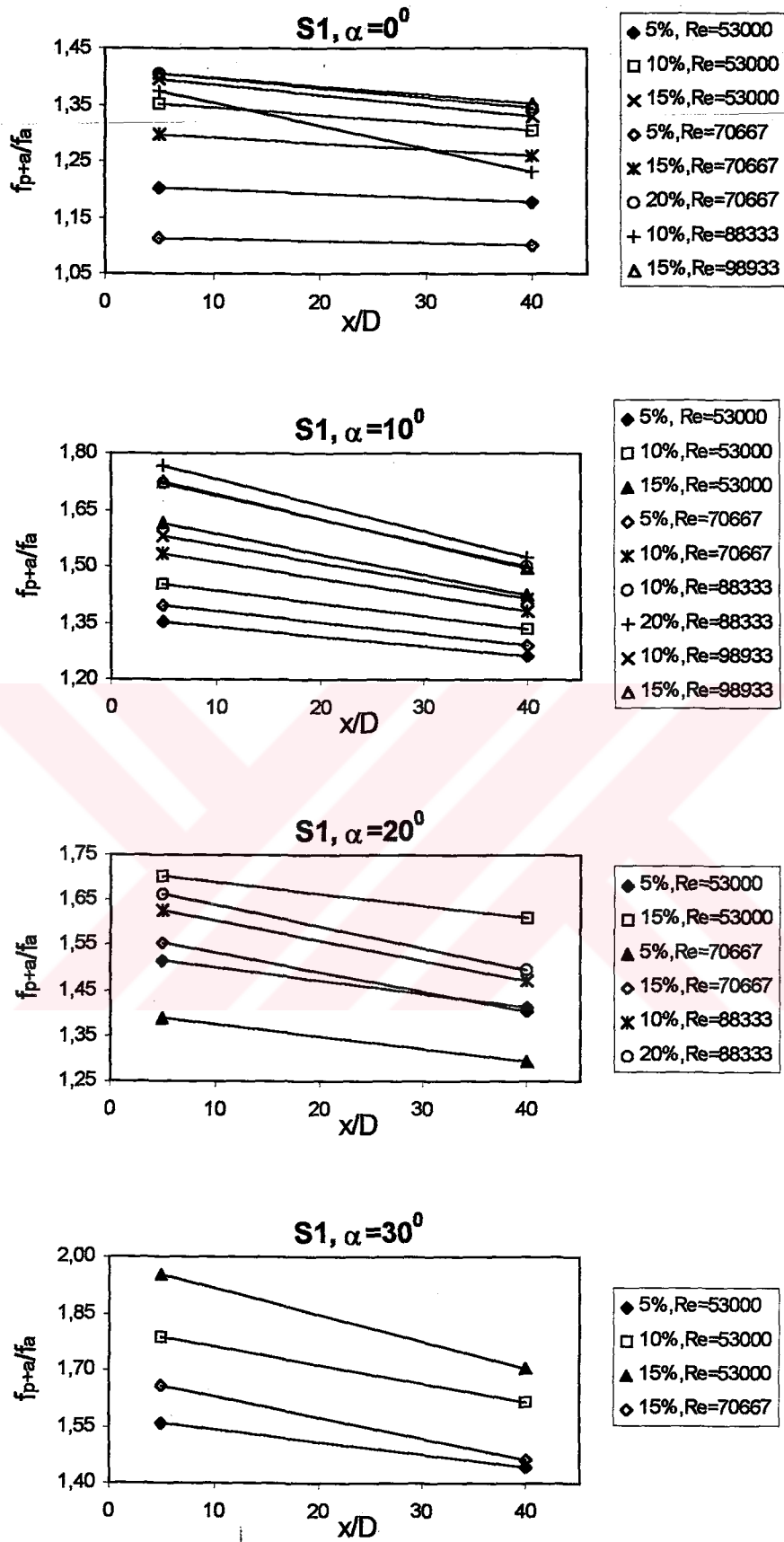


Figure 4.78 Variation of f_{p+a}/f_a with x/D for S1 along different test section inclinations.

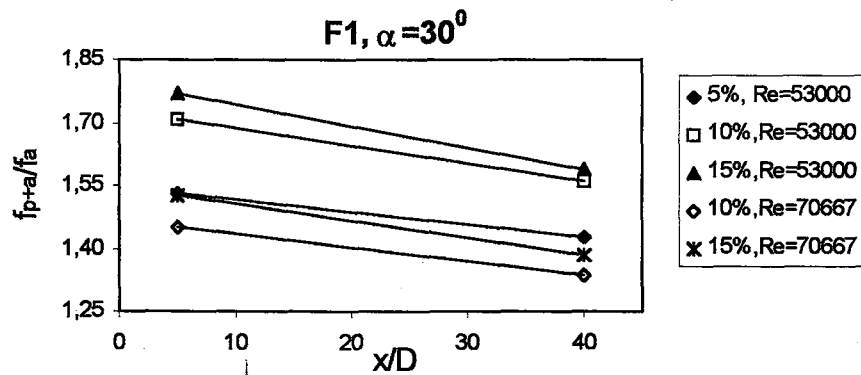
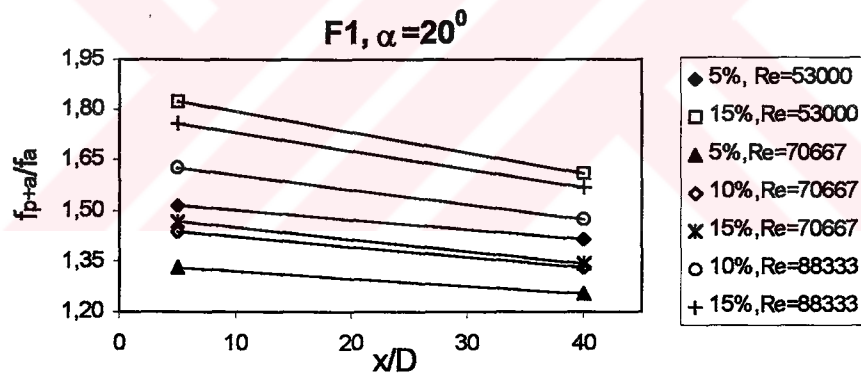
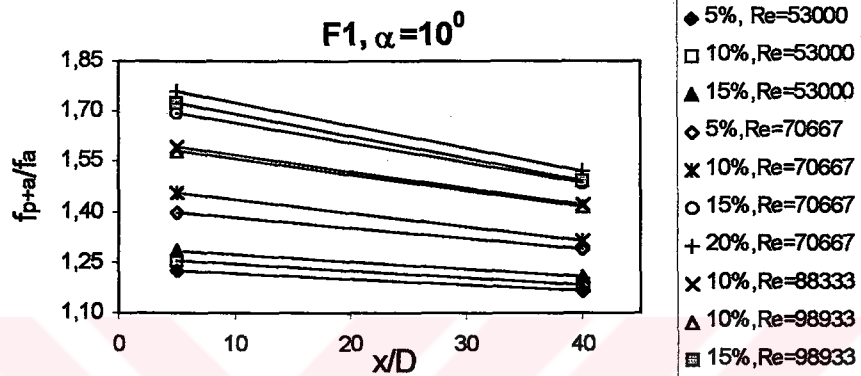
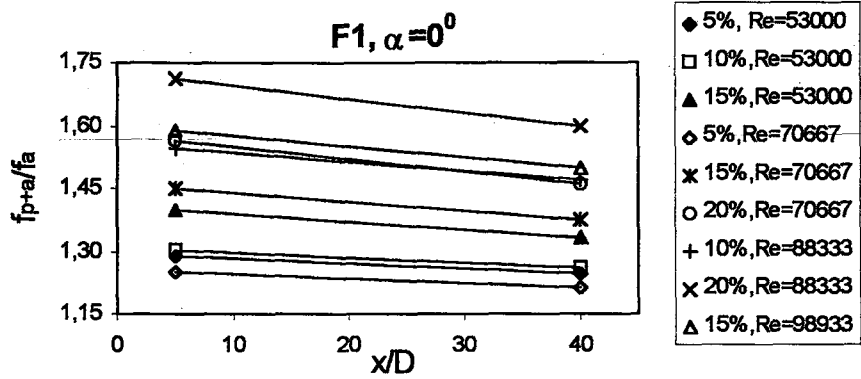
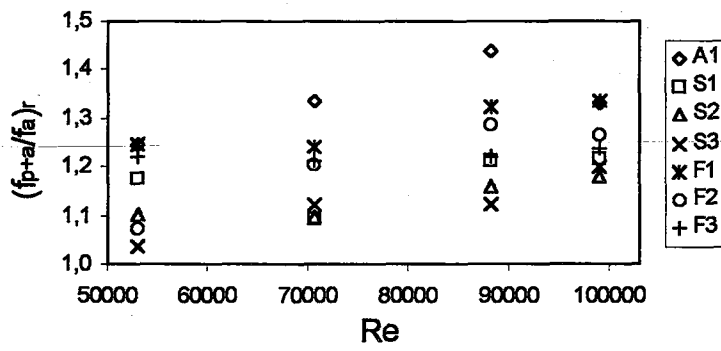
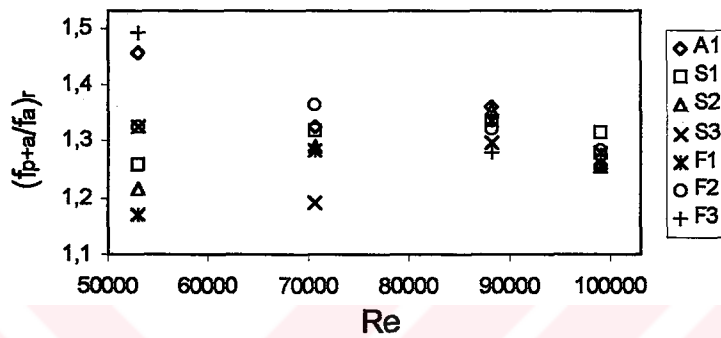


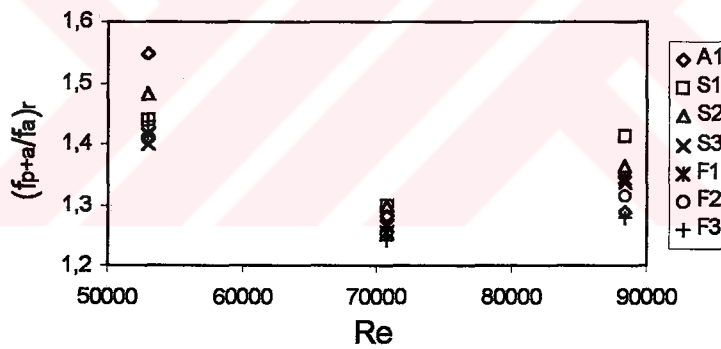
Figure 4.79 Variation of f_{p+a}/f_a with x/D for F1 along different test section inclinations.



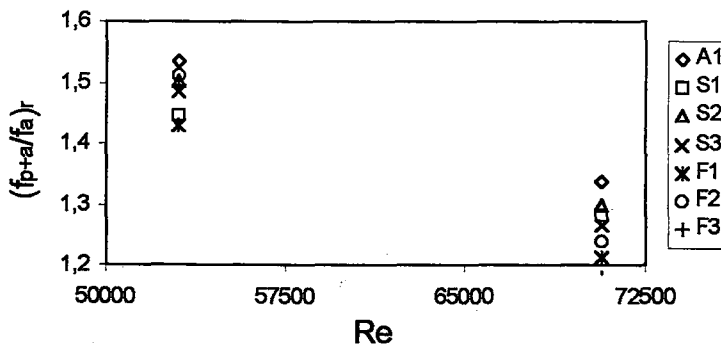
a) $\alpha=0^\circ$



b) $\alpha=10^\circ$

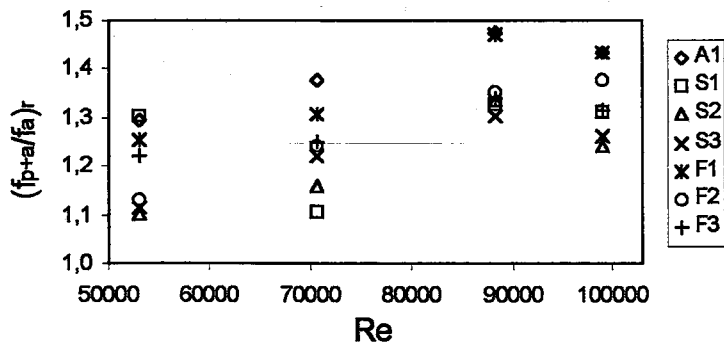


c) $\alpha=20^\circ$

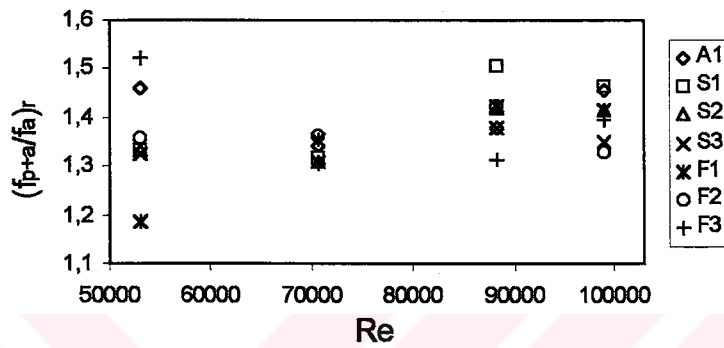


d) $\alpha=30^\circ$

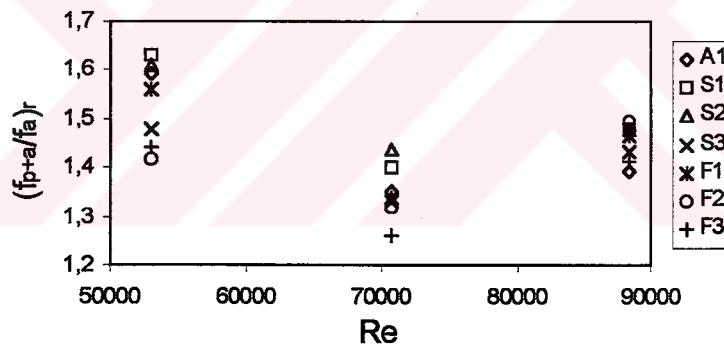
Figure 5.1.a,b,c,d Variation of $(f_{p+a}/f_a)_r$ with Re at $M_p/M_a=5\%$ along different test section inclinations.



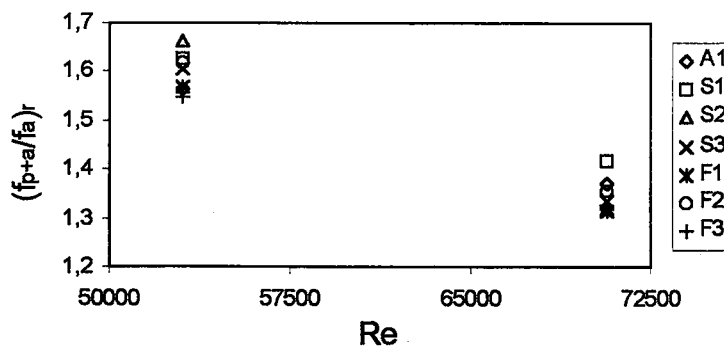
a) $\alpha=0^\circ$



b) $\alpha=10^\circ$

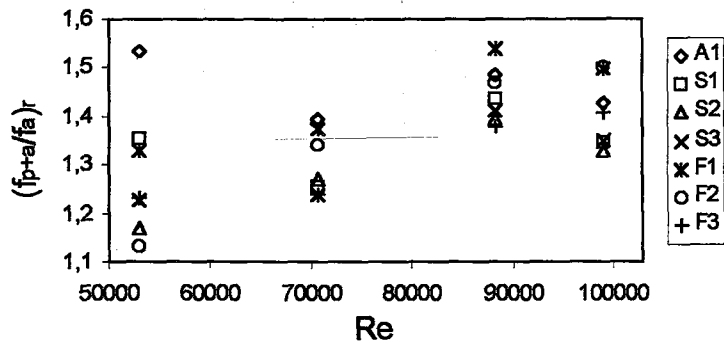


c) $\alpha=20^\circ$

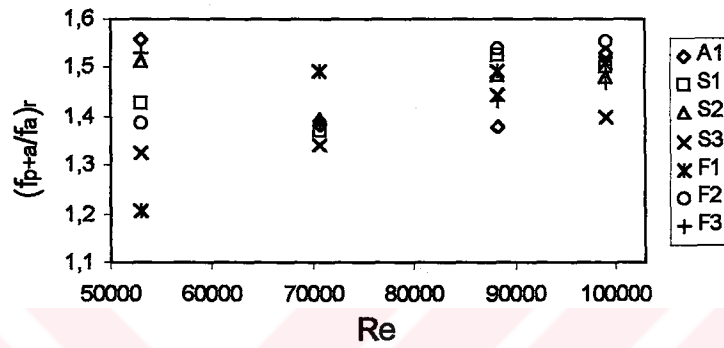


d) $\alpha=30^\circ$

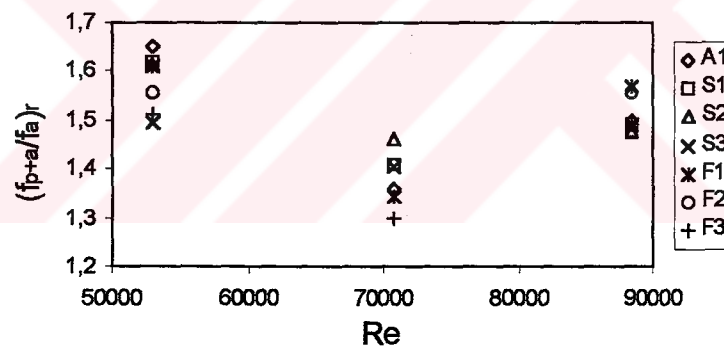
Figure 5.2.a,b,c,d Variation of $(f_{p+a}/f_a)_r$ with Re at $M_p/M_a=10\%$ along different test section inclinations.



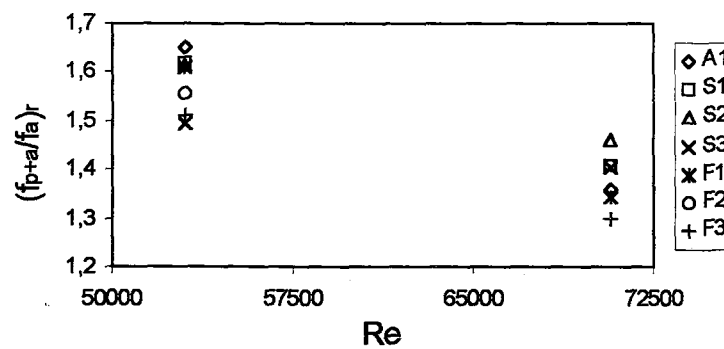
a) $\alpha=0^\circ$



b) $\alpha=10^\circ$



c) $\alpha=20^\circ$



d) $\alpha=30^\circ$

Figure 5.3.a,b,c,d Variation of $(f_{p+a}/f_a)_r$ with Re at $M_p/M_a=15\%$ along different test section inclinations.

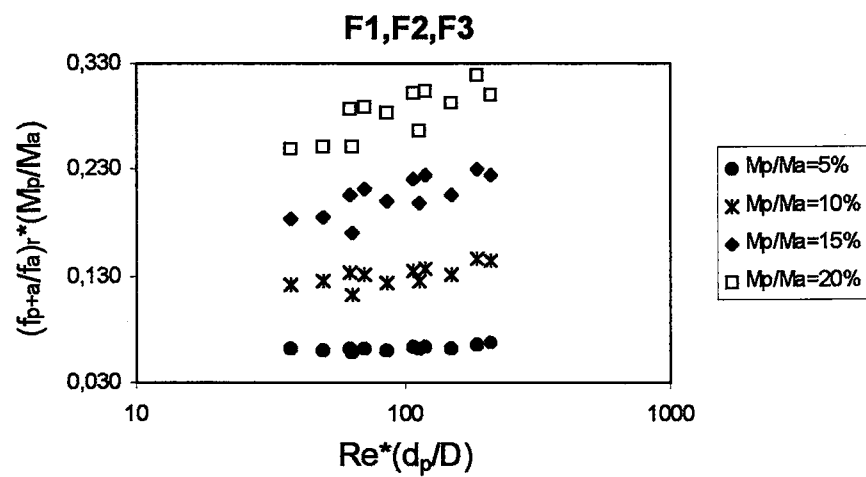
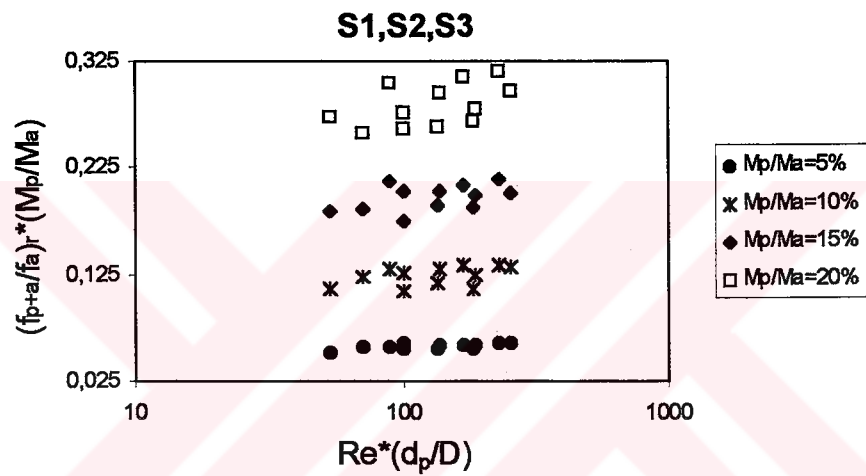
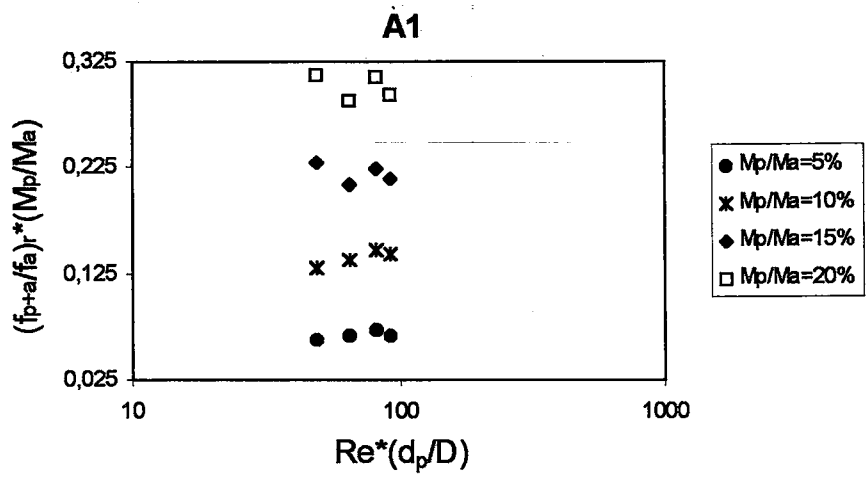
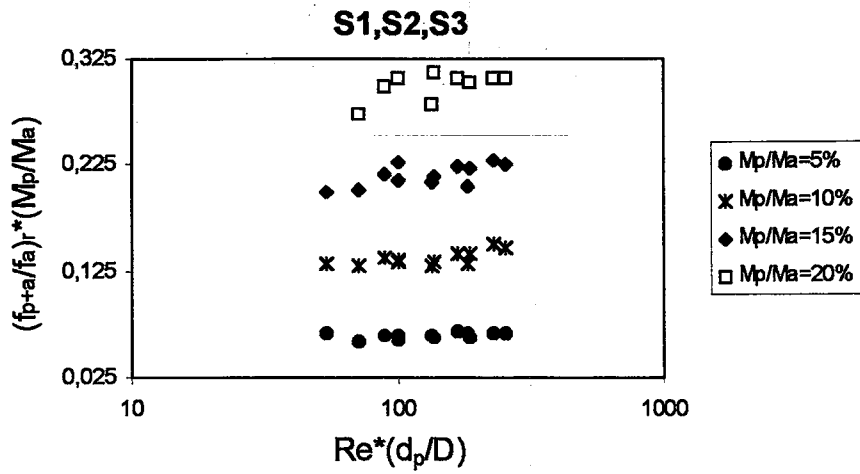
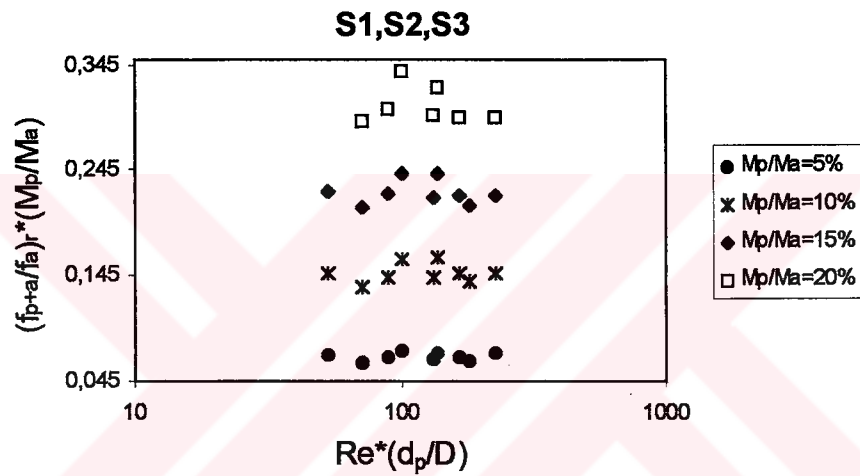


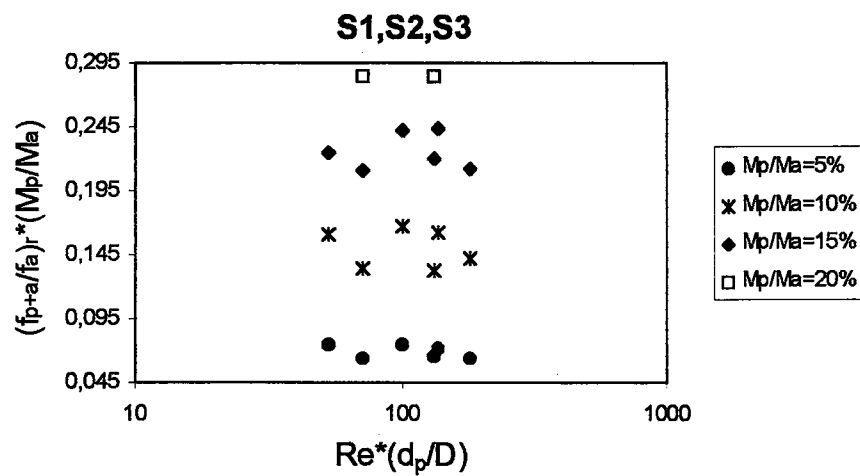
Figure 5.4 Variation of $(f_{p+a}/f_a)_r \cdot (M_p/M_a)$ with $Re^*(d_p/D)$ for A1; S1,S2,S3; and F1,F2,F3 along horizontal line, $\alpha=0^\circ$.



a) $\alpha=10^\circ$

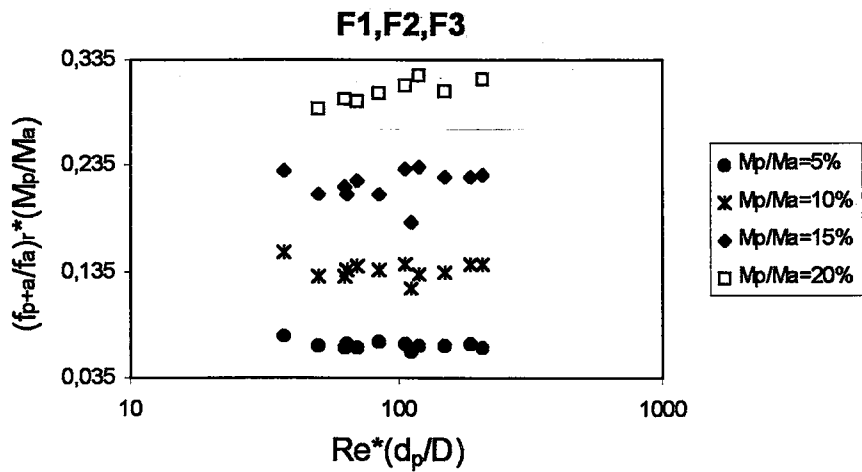


b) $\alpha=20^\circ$

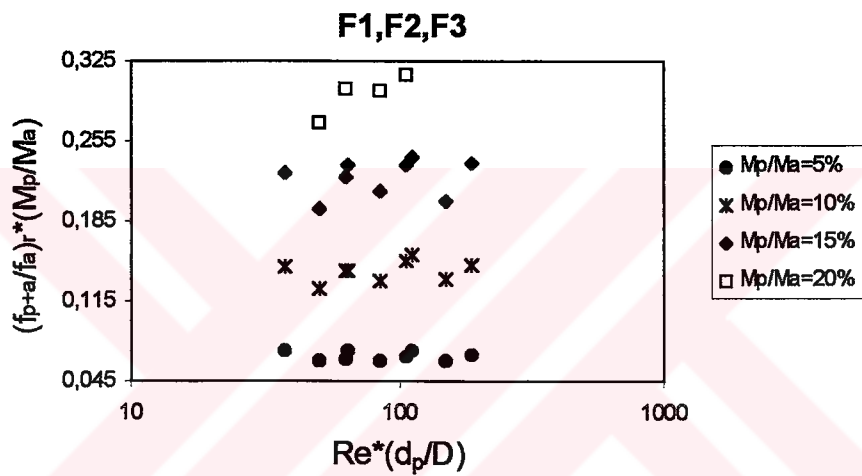


c) $\alpha=30^\circ$

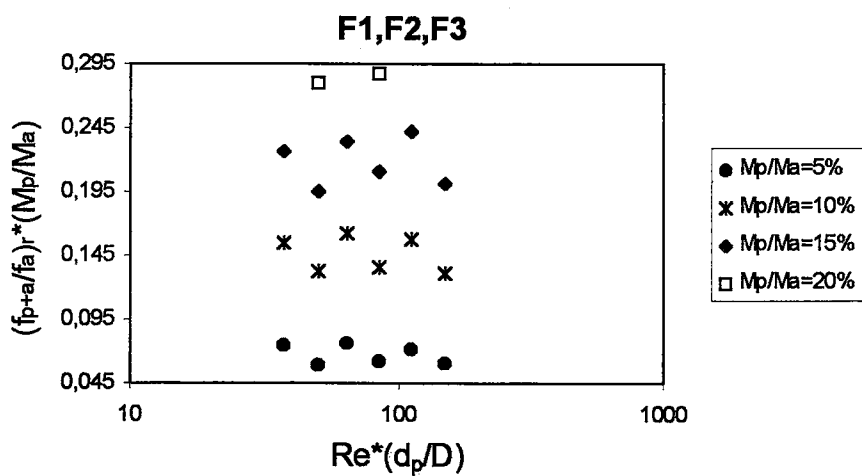
Figure 5.5.a,b,c Variation of $(f_{p+a}/f_a)_r \cdot (M_p/M_a)$ with $Re^*(d_p/D)$ for S1,S2,S3 along different test section inclinations.



a) $\alpha=10^\circ$



b) $\alpha=20^\circ$



c) $\alpha=30^\circ$

Figure 5.6.a,b,c Variation of $(f_{p+a}/f_a)_r \cdot (M_p/M_a)$ with $Re^*(d_p/D)$ for F1,F2,F3 along different test section inclinations.

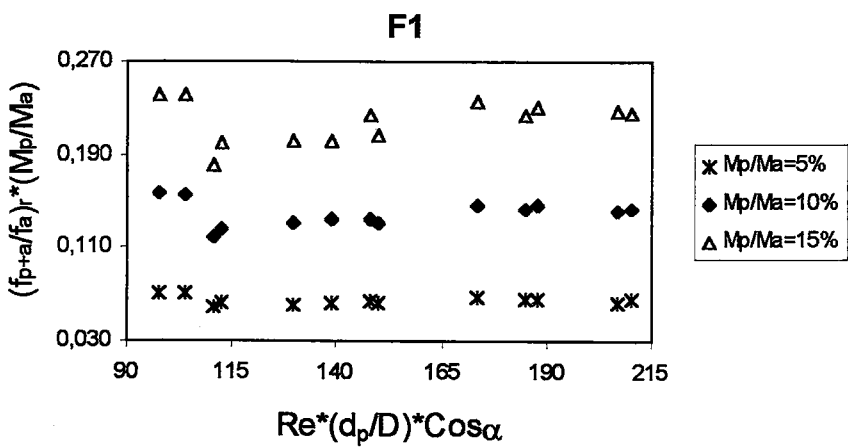
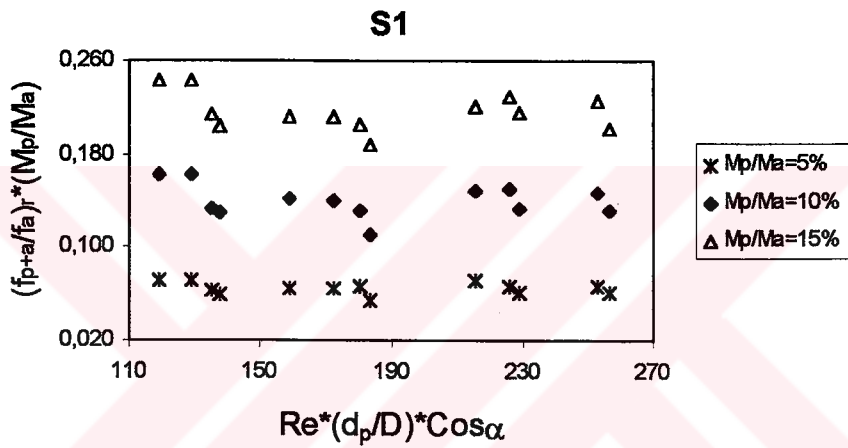
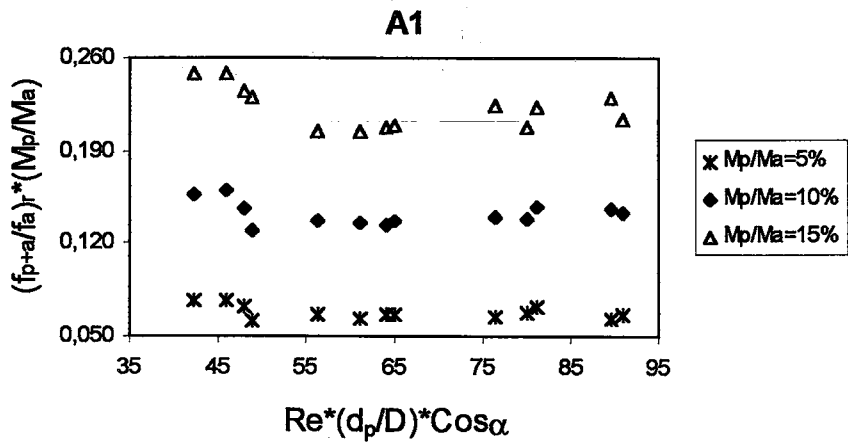


Figure 5.7 Variation of $(f_{p+a}/f_a)_r \cdot (M_p/M_a)$ with $Re \cdot (d_p/D) \cdot \cos \alpha$ for A1,S1,F1.

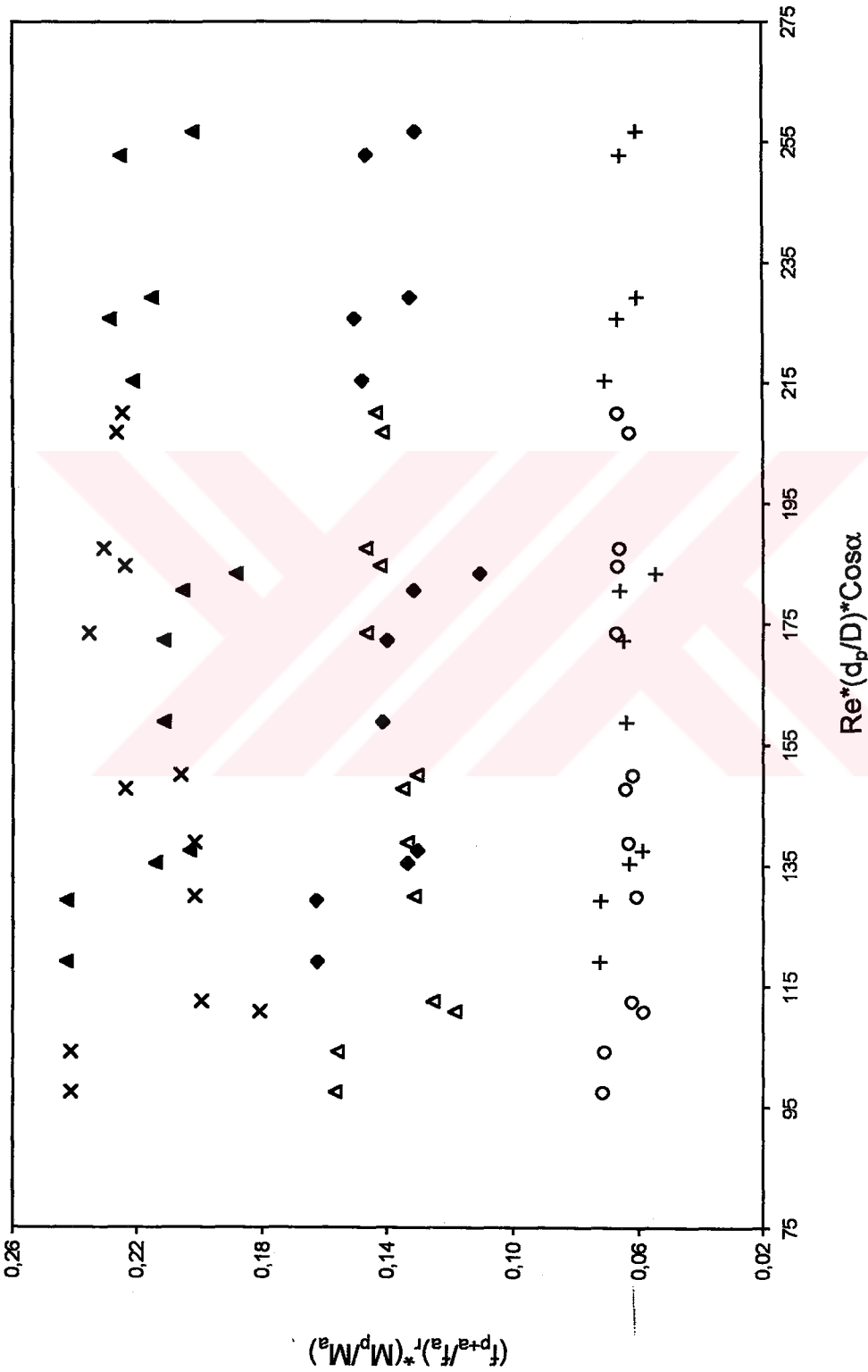


Figure 5.8 Variation of $(f_{p+a}/f_a)^r \cdot (M_p/M_a)$ with $Re \cdot (d_p/D) \cdot \cos \alpha$ for S1 & F1.

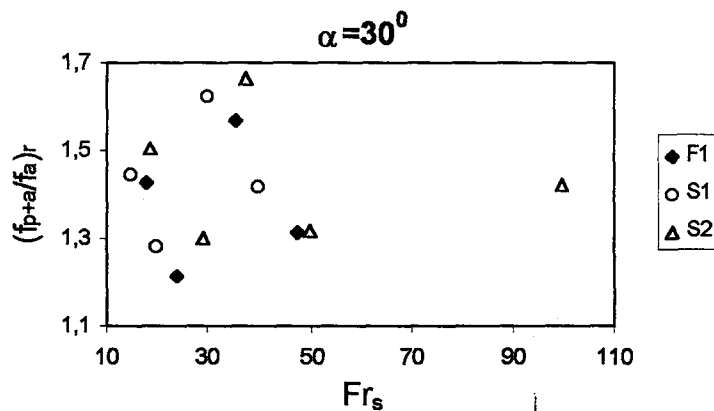
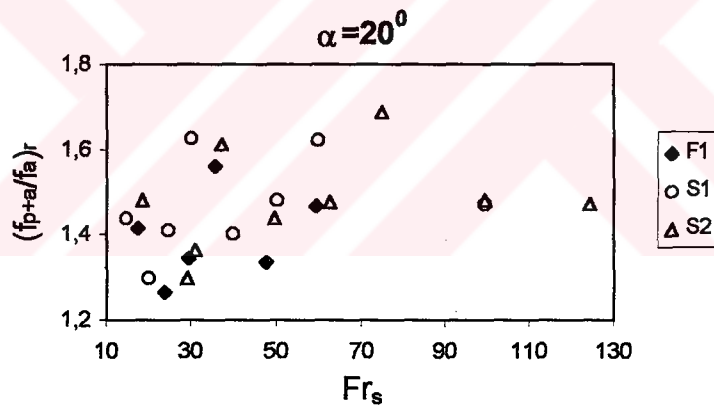
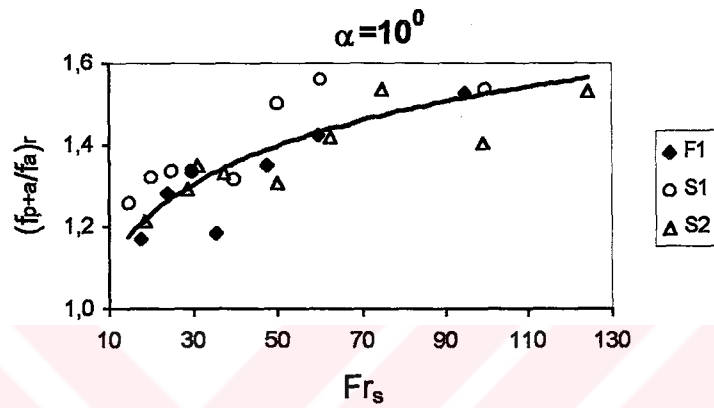
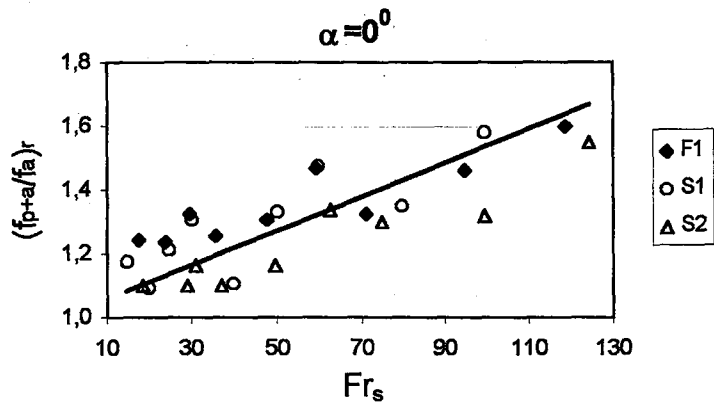


Figure 5.9 Variation of $(f_{p+a}/f_a)_r$ with Fr_s for $M_p/M_a=5,10,20\%$ along different test section inclinations.

F1&S1

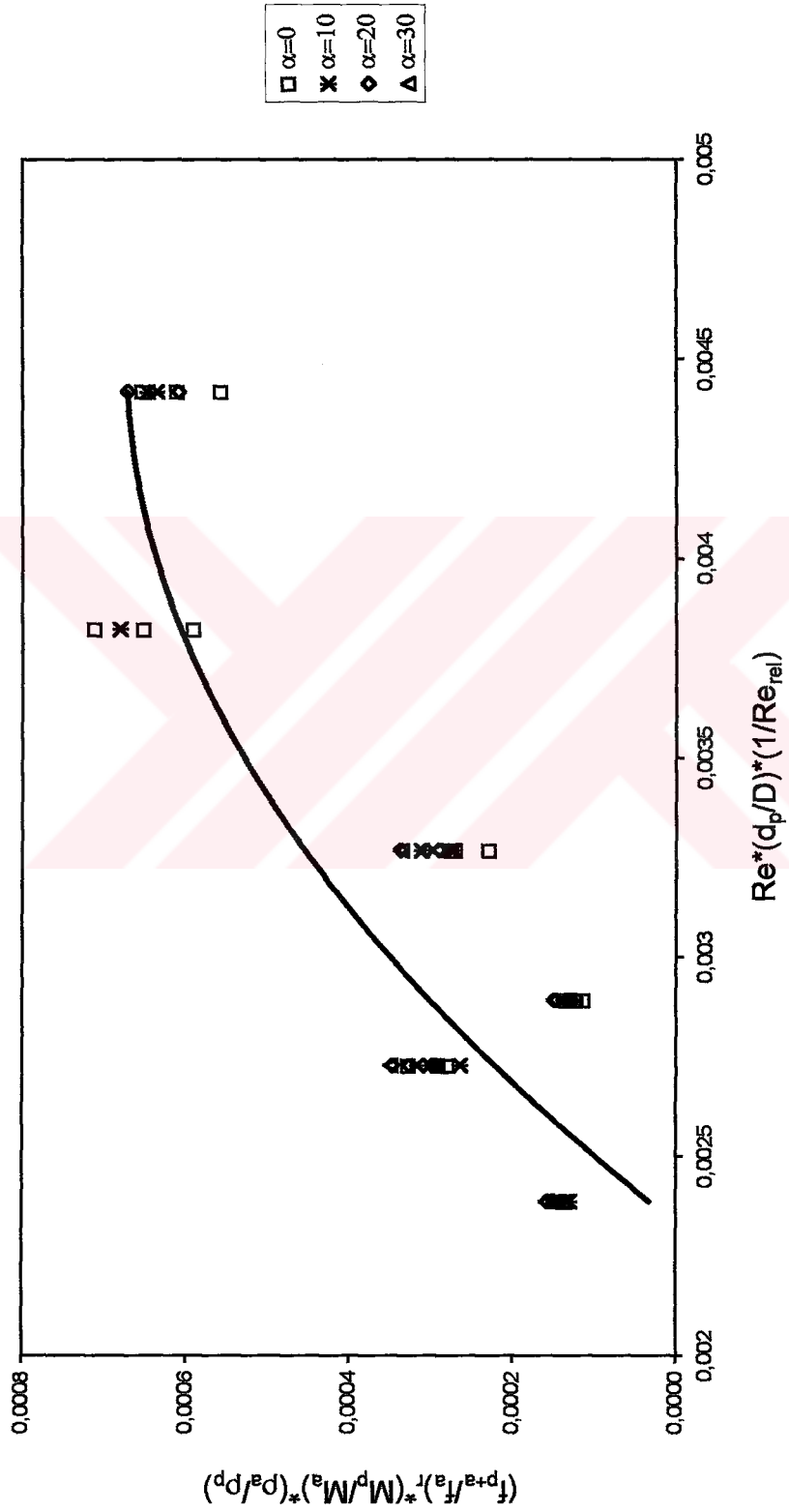


Figure 5.10 Variation of $(f_{p+s}/f_a) \cdot (M_p/M_a)^r \cdot (\rho_a/\rho_p)$ with $Re(d_p/D) \cdot (1/Re_{rel})$ for F1&S1 along different test section inclinations.